



THE HONG KONG  
POLYTECHNIC UNIVERSITY

香港理工大學

Pao Yue-kong Library

包玉剛圖書館

---

## Copyright Undertaking

This thesis is protected by copyright, with all rights reserved.

**By reading and using the thesis, the reader understands and agrees to the following terms:**

1. The reader will abide by the rules and legal ordinances governing copyright regarding the use of the thesis.
2. The reader will use the thesis for the purpose of research or private study only and not for distribution or further reproduction or any other purpose.
3. The reader agrees to indemnify and hold the University harmless from and against any loss, damage, cost, liability or expenses arising from copyright infringement or unauthorized usage.

### IMPORTANT

If you have reasons to believe that any materials in this thesis are deemed not suitable to be distributed in this form, or a copyright owner having difficulty with the material being included in our database, please contact [lbsys@polyu.edu.hk](mailto:lbsys@polyu.edu.hk) providing details. The Library will look into your claim and consider taking remedial action upon receipt of the written requests.

**SYNTHESIS OF ULTRA-LOW PT  
LOADING CATALYSTS FOR  
DIRECT LIQUID FUEL CELLS**

**LUK SIN YEE**

**Ph.D**

**The Hong Kong Polytechnic University**

**2018**

**The Hong Kong Polytechnic  
University**

**Department of Applied Biology and  
Chemical Technology**

**Synthesis of Ultra-low Pt Loading  
Catalysts for Direct Liquid Fuel Cells**

**LUK Sin Yee**

A thesis submitted in partial fulfillment

of the requirements for the degree of

Doctor of Philosophy

July 2017

## **CERTIFICATE OF ORIGINALITY**

I hereby declare that this thesis is my own work and that, to the best of my knowledge and belief, it reproduces no material previously published or written, nor material that has been accepted for the award of any other degree or diploma, except where due acknowledgement has been made in the text.

---

**Sin-Yee LUK**

July 2017

## **ABSTRACT**

Abstract of the thesis entitled

# **Synthesis of Ultra-low Pt Loading Catalysts for Direct Liquid Fuel Cells**

Submitted

by

LUK Sin Yee

for the degree of Doctor of Philosophy

at The Hong Kong Polytechnic University

in July 2017

Due to the depleting and limited supply of fossil fuel and the related environmental impacts, fuel cell technology is widely adopted to enhance efficiency and reduce pollution. In direct liquid fuel cells, platinum (Pt) and Pt-based electrocatalysts are reported to be the most effective catalyst in the literature but the massive commercialization is limited owing to its high cost and limited reserve. The aim of this project is to develop ultra-low Pt loading catalysts with improved Pt utilization and enhanced catalytic activity.

---

Platinum-gold core-shell (AuNP@Pt) nanostructures supported on multi-walled carbon nanotubes (MWCNTs) composites (AuNP@Pt/CNTs) were prepared by Pt halide ion adsorption onto gold nanoparticles (AuNPs) surface, followed by *in-situ* electrochemical reduction. Electrochemical studies show that different Pt halides show different adsorption affinity and different electrocatalytic activity towards the electrooxidations of formic acid and methanol. It is found that varying the concentrations of tetrahaloplatinate complex  $[\text{PtX}_4]^{2-}$  (X = Cl and Br) ion and tetraammineplatinum(II) nitrate  $(\text{Pt}(\text{NH}_3)_4(\text{NO}_3)_2)$  solutions from 0.02 mM to 5.12 mM could control the Pt coverage on gold nanoparticles supported on MWCNTs (AuNP/CNTs) composite while hexahaloplatinate complex ( $[\text{PtX}_6]^{2-}$ ) solutions could not. Also, varying immersion time with the concentrations of  $[\text{PtX}_4]^{2-}$  ion and  $\text{Pt}(\text{NH}_3)_4(\text{NO}_3)_2$  solutions could control the Pt coverage on AuNP/CNTs composite. The AuNP@Pt/CNTs composites prepared by different Pt halide ions with different Pt coverages show different electrocatalytic activity due to the different specific packing modes of the Pt atoms deposit on the AuNPs surface. The electrocatalytic studies show that the AuNP@Pt/CNTs composites with Pt coverage of lower than 30 % were active to direct oxidation of formic acid but inactive to methanol. The AuNP@Pt/CNTs composite prepared by tetrachloroplatinate complex ( $[\text{PtCl}_4]^{2-}$ ) solution with Pt coverage of higher than 30 % and prepared by tetrabromoplatinate complex ( $[\text{PtBr}_4]^{2-}$ ) solution with Pt coverage of higher than 80 % start becoming active to indirect oxidations of formic acid and methanol.

Pd@PdPt/CNTs alloy and Pt@Pd/CNTs phase-separate composites were synthesized from surfactant-free Pd/CNTs and Pt/CNTs composites respectively.

Both clean palladium (Pd) and Pt metal surfaces are available for surface modification to form alloy and phase-separate PdPt surfaces. The PdPt shell of Pd@PdPt/CNTs alloy catalysts were synthesized by the galvanic replacement reaction between Pd and  $[\text{PtCl}_4]^{2-}$  ions. The Pt@Pd/CNTs phase-separate composites were prepared by adsorption of tetrachloropalladate complex ( $[\text{PdCl}_4]^{2-}$ ) onto Pt surface followed by hydrogen reduction. Powder X-ray diffraction (XRD) suggests that both Pd@PdPt/CNTs alloy and Pt@Pd/CNTs phase-separate composites adopt a face-centred cubic (fcc) structure. X-ray photoelectron spectroscopy (XPS) analysis confirms the formation of PdPt alloy structure. Compared with monometallic Pd/CNTs and Pt/CNTs composites, the Pd@PdPt/CNTs alloy and Pt@Pd/CNTs phase-separate composites with particular Pd-to-Pt surface ratio exhibit enhanced catalytic activity towards the electrooxidations of ethanol and glycerol.

Hollow PtAg nanowires (NWs) composites were synthesized in the galvanic replacement reaction using silver nanowires (AgNWs) as sacrificial template and potassium tetrachloroplatinate(II) ( $\text{K}_2\text{PtCl}_4$ ) as metal precursor. The Pt-to-Ag atomic ratio from 1 : 3.0 to 3.5 : 1 and surface ratio from 1 : 8.0 to 1 : 3.5 of hollow PtAg NWs composites could be controlled by varying the amount of  $\text{K}_2\text{PtCl}_4$  present. Both XRD and XPS analyses confirm the alloying of Ag and Pt in hollow PtAg NWs. Electrochemical investigations show that the hollow PtAg NWs composites with specific Pt-to-Ag surface ratio exhibit enhanced catalytic activity towards the oxidations of methanol, ethanol, glycerol and formic acid when compared with Pt black composite.

## **PUBLICATIONS AND CONFERENCES**

### **Publications**

Fulin Zheng, **Sin-Yee Luk**, Tsz-Lung Kwong and Ka-Fu Yung\*, “Synthesis of hollow PtAg alloy nanospheres with excellent electrocatalytic performances towards methanol and formic acid oxidations”, *RSC Advances*, 2016, **50**, 44902 – 44907.

### **Conferences**

**Sin-Yee Luk**, Fulin Zheng and Ka-Fu Yung\*, “Synthesis of Hollow PtAg Nanospheres for Methanol and Formic Acid Electro-oxidations”, BIT's 6th Annual World Congress of Nano-S&T 2016 - BIT Congress Inc. – Singapore, 25 – 28 October 2016.

### **Symposia**

**Sin-Yee Luk** and Ka-Fu Yung\*, “Synthesis of Ultralow Platinum-Gold Nanostructures for Direct Liquid Fuel Cells”, The 21<sup>st</sup> Symposium on Chemistry Postgraduate Research in Hong Kong, 12 April 2014.

**Sin-Yee Luk** and Ka-Fu Yung\*, “Synthesis of Platinum-Gold Core-Shell Nanoparticles for Direct Liquid Fuel Cells”, The 22<sup>nd</sup> Symposium on Chemistry Postgraduate Research in Hong Kong, 18 April 2015.

**Sin-Yee Luk** and Ka-Fu Yung\*, “Synthesis of Platinum-Gold Core-Shell Nanoparticles for Direct Liquid Fuel Cells”, The 23<sup>rd</sup> Symposium on Chemistry Postgraduate Research in Hong Kong, 23 April 2016.

**Sin-Yee Luk** and Ka-Fu Yung\*, “Synthesis of Platinum-Gold Core-Shell Nanoparticles for Direct Liquid Fuel Cells”, The 24<sup>th</sup> Symposium on Chemistry Postgraduate Research in Hong Kong, 6 May 2017.

## **Acknowledgements**

First of all, I would like to express my sincere gratitude to my supervisor, Dr. Joseph Ka-Fu Yung for his valuable guidance and patience throughout my research. His support helped me not only exploring my research, but also accomplishing this thesis.

Besides my supervisor, I also greatly thank my co-supervisor, Prof. Fuk-Yee Kwong, as well for his support and advice throughout my research.

I would like to express my gratefulness to all members of Yung's group, Dr. Samuel T. -L. Kwong, Mr. Henry P. -C. Lau and Miss Christie Ng for their support.

Special thanks are also given to Dr. Karen Y. Gu and Dr. F. Zheng, for their guidance and valuable comments during my study.

I am obliged to the staff and the technicians of the Chemical Technology section of Department of Applied Biology and Chemical Technology, The Hong Kong Polytechnic University for their technical assistance throughout my course of study.

I would like to thank Dr. W. Lu for his kind support and assistance in conducting microscopic studies.

I would like to acknowledge the receipt of a postgraduate studentship (2013 – 2017) administrated by The Hong Kong Polytechnic University and a grant supporting my conference participation in BIT's 6th Annual World Congress of Nano-S&T 2016 - BIT Congress Inc in Singapore in October 2016.

Finally, I would like to offer my special thanks to my father, Mr Kui-Chun Luk and my mother, Ms Foon-Siu Cheung for their support and encouragement.

## **TABLE OF CONTENTS**

<b>CERTIFICATE OF ORIGINALITY.....</b>	<b>i</b>
<b>ABSTRACT.....</b>	<b>ii</b>
<b>PUBLICATIONS AND CONFERENCES.....</b>	<b>v</b>
<b>ACKNOWLEDGEMENTS.....</b>	<b>vii</b>
<b>TABLE OF CONTENTS.....</b>	<b>ix</b>
<b>ABBREVIATIONS.....</b>	<b>xiv</b>

---

**CHAPTER 1 Introduction**

1.1. An Overview of Fuel Cells .....	1
1.1.1 General background of fuel cells.....	1
1.1.2 Significance of fuel cells.....	3
1.2. Introduction of Several Types of Fuel Cells.....	5
1.2.1 Alkaline fuel cell.....	5
1.2.2 Proton exchange membrane fuel cell (hydrogen fuel cell).....	7
1.2.3 Phosphoric acid fuel cell.....	9
1.2.4 Molten carbonate fuel cell.....	11
1.2.5 Solid oxide fuel cell.....	13
1.2.6 Direct liquid fuel cells.....	15
1.3. Exploration on Pt and Pt-based Catalysts and its Applications in Direct Liquid Fuel Cells.....	22
1.3.1 Synthetic methods of Pt and Pt-based electrocatalysts.....	22
1.3.2 Applications in direct liquid fuel cells.....	33
1.4. Scope of thesis.....	41
REFERENCES.....	42

**CHAPTER 2 Synthesis of Platinum-Gold Core-Shell  
Nanoparticles for Direct Formic Acid and  
Methanol Fuel Cells**

2.1 Background.....	50
2.2 Results and Discussions.....	60

---

2.2.1	Synthesis of AuNPs and AuNP/CNTs.....	60
2.2.2	Exploration on different Pt halide solutions of different concentrations towards formic acid and methanol electrooxidations.....	70
2.2.3	Exploration on immersion time towards formic acid and methanol electrooxidations.....	113
2.3	Summary.....	138
	REFERENCES.....	140

### **CHAPTER 3 Synthesis of Pd@PdPt/CNTs Alloy and Pt@Pd/CNTs Phase-separate Catalysts for Direct Liquid Fuel Cells**

3.1	Background.....	145
3.2	Results and Discussions.....	154
3.2.1	Synthesis of Pd@PdPt/CNTs alloy catalysts.....	154
3.2.2	Synthesis of Pt@Pd/CNTs phase-separate catalysts.....	167
3.2.3	Elemental and surface composition analysis.....	182
3.2.4	Electrochemical characterizations and electrocatalytic studies.....	199
3.2.4.1	Cyclic voltammetry in sulfuric acid.....	199
3.2.4.2	Electrooxidation of methanol and its related chronoamperometric test.....	206
3.2.4.3	Electrooxidation of ethanol and its related chronoamperometric test.....	215

3.2.4.4	Electrooxidation of glycerol and its related chronoamperometric test.....	225
3.2.4.5	Accelerated durability test in sulfuric acid.....	234
3.3	Summary.....	238
	REFERENCES .....	240

## **CHAPTER 4 Synthesis of Hollow PtAg Nanowires for Direct Liquid Fuel Cells**

4.1	Background.....	244
4.2	Results and Discussions.....	253
4.2.1	Synthesis of AgNWs and PtAg NWs.....	253
4.2.2	Electrochemical characterizations and electrocatalytic studies..	285
4.2.2.1	Cyclic voltammetry in sulfuric acid.....	285
4.2.2.2	Electrooxidation of methanol and its related chronoamperometric test.....	289
4.2.2.3	Electrooxidation of ethanol and its related chronoamperometric test.....	294
4.2.2.4	Electrooxidation of glycerol and its related chronoamperometric test.....	299
4.2.2.5	Electrooxidation of formic acid and its related chronoamperometric test.....	305
4.3	Summary.....	310
	REFERENCES .....	311

---

<b>CHAPTER 5 CONCLUSIONS.....</b>	<b>316</b>
 <b>CHAPTER 6 Experimental Section</b>	
6.1 General Section.....	319
6.1.1 Materials.....	319
6.1.2 Physical characterization techniques.....	320
6.2 Experimental Catalysts Preparation.....	323
6.2.1 Catalysts preparation for Chapter 2.....	323
6.2.2 Catalysts preparation for Chapter 3.....	324
6.2.3 Catalysts preparation for Chapter 4.....	326
6.3 Electrochemical Characterizations and Electrocatalytic Studies.....	327
6.3.1 Electrochemical characterizations and electrocatalytic studies for Chapter 2.....	328
6.3.2 Electrochemical characterizations and electrocatalytic studies for Chapter 3.....	330
6.3.3 Electrochemical characterizations and electrocatalytic studies for Chapter 4.....	332
REFERENCES .....	334

## **ABBREVIATIONS AND SYMBOLS**

### **Abbreviations**

ADT	Accelerated durability test
CNTs	Carbon nanotubes
CV	Cyclic voltammetry
ECSA	Electrochemically active surface area
EDX	Energy dispersive X-ray
EtOH	Ethanol
EG	Ethylene glycol
HM-TEM	High magnification transmission electron microscopy
HR-TEM	High resolution transmission electron microscopy
ICP-OES	Inductively coupled plasma optical emission spectroscopy
i-t test	Chronoamperometric test
LM-TEM	Low magnification transmission electron microscopy
MeOH	Methanol
MWCNTs	Multi-walled carbon nanotubes
ORR	Oxygen reduction reaction
PVP	Polyvinylpyrrolidone
SAED	Selective area electron diffraction
SCE	Saturated calomel electrode
SEM	Scanning electron microscopy
SHE	Standard hydrogen electrode

STM	Scanning tunneling microscopy
TEM	Transmission electron microscopy
UV	Ultra-violet
XPS	X-ray photoelectron spectroscopy
XRD	Powder X-ray diffraction

# Chapter 1

## Introduction

### 1.1 An Overview of Fuel Cells

#### 1.1.1 General background of fuel cells

Fuel cell is an electrochemical device converting the chemical energy into electrical energy. It consists of two electrodes (anode and cathode) and electrolyte. The anodic reaction in fuel cells is the oxidation of fuels while the cathodic reaction is usually oxygen reduction reaction (ORR). The charges can move in the electrolyte between the two sides of fuel cell. The electrons move from the anode to cathode via the external circuit.[1]

The history of fuel cells development is briefly described. In 1800, the British scientists Sir Anthony Carlisle and William Nicholson discovered the electrolysis of water into hydrogen and oxygen.[2] In 1838, Sir William Robert Grove introduced the concept of hydrogen fuel cell and created a gas battery. Two platinum (Pt) electrodes were immersed in sulfuric acid. The other two electrodes were sealed in two respective containers of hydrogen and oxygen and both containers contain water. It was found that there was a current flow between the electrodes and the water level rose in both tubes. He also studied the connection of electrodes in series resulting in a higher voltage drop, creating a gas battery.[3] In 1889, Ludwig Mond and Carl Langer described Mond process which is the process for obtaining nickel (Ni).[4] In 1893, the components of fuel cell including electrodes, electrolyte, oxidizing and reducing agents, anions and cations were described by Friedrich Wilhelm Ostwald.[5] He also further solved

the confusion of Grove's gas battery. In 1896, the first fuel cell with applications was developed by William W. Jacques.[6]

In 1921, the first molten carbonate fuel cell was built by Emil Baur. He also researched solid oxide fuel cell with high operating temperature during the thirties.[7] In 1933, Thomas Francis Bacon developed a hydrogen fuel cell which converted hydrogen and air directly into electricity through a series of electrochemical reactions. In 1939, Bacon also started exploring alkaline fuel cell. He also developed a fuel cell for the submarines in Royal Navy during World War II. In 1950, teflon was developed and used in fuel cells. In 1955, the ion-exchange polystyrene sulphated membrane was developed by Thomas Grubb. In 1958, scientists G. H. J. Broers and J. A. Ketelaar were investigating the molten carbonate fuel cells. In 1959, the team organized by General Electric Company (GE) and led by Harry Ihring researched solid oxide fuel cell. In 1961, G.V. Elmore and H.A. Tanner developed a phosphoric acid fuel cell. In 1990, a direct methanol fuel cell was developed by the Jet Propulsion Laboratory of NASA and the University of Southern California.[2]

Nowadays, fuel cells are used in a wide range of applications in the fields of stationary applications, transport, portable applications and micro power.[2] The applications of stationary fuel cells include hospitals, shelters, elderly care centers, hotels and schools.[8] They are also used in landfills and wastewater plants.[9] The transport includes buses, motorcycles,[10] the auxiliary power units (APUS) in the long-haul trucks[11] and mining trains.[12] For the portable applications, fuel cells can be used instead of diesel generators in the places which do not have electrical power supply such as camping area.[2]

### 1.1.2 Significance of fuel cells

One of the reasons for fuel cells is the depletion of fossil fuels. Our energy needs mostly depend on fossil fuels. Since the fossil fuel is running out, it is essential to seek for an alternative way for our energy sources.

Another reason is that the impacts from using fossil fuels are induced in terms of environmental hazards and health problems. Greenhouse effect is a major consequence. A large amount of carbon dioxide ( $\text{CO}_2$ ) is produced by burning fossil fuel, causing an imbalance level of  $\text{CO}_2$ . Apart from increasing  $\text{CO}_2$  level, acid rain is also caused. The combustion of sulfur-containing natural resources such as coal, oil and diesel can create sulfur dioxide ( $\text{SO}_2$ ).[13]

In addition to environmental hazards, human health problems are caused. A variety of pollutants including nitrous oxides ( $\text{NO}_x$ ), sulfuric oxides ( $\text{SO}_2$ ), carbon dioxide ( $\text{CO}_2$ ) and particulate matter are emitted. Nitrous oxides ( $\text{NO}_x$ ) and hydrocarbons increase the ozone levels in the lower atmosphere, which is toxic to humans. Sulfur dioxide ( $\text{SO}_2$ ) created from sulfuric oxides ( $\text{SO}_x$ ) causes the respiratory inflammation. The particulate matters are airborne particles which are emitted from the vehicle engines and power plants. Those particles are able to enter into the lungs and remain for a long period of time.[13]

Fuel cell is an important technology to alleviate the depletion of fossil fuels and pollution from using fossil fuel with numerous advantages. First, the energy source is clean. Using hydrogen as fuel, only water is produced which is clean to the environment. Moreover, fuel cells have higher efficiency. They are able to extract energy from fuel with 40 % to 70 % efficiency while the traditional

internal combustion engines extract energy from fuel with around 30 % efficiency by converting the chemical energy into mechanical energy and finally into electrical energy. Besides, the recharge of fuel cells is much faster and does not damage the cell when compared with batteries. Also, fuel cells have unlimited life. The batteries are dead when the chemicals in the cell are used up. Fuel cells can be kept using owing to the constant flow of chemicals.[14]

## 1.2 Introduction of Several Types of Fuel Cells

### 1.2.1 Alkaline fuel cell

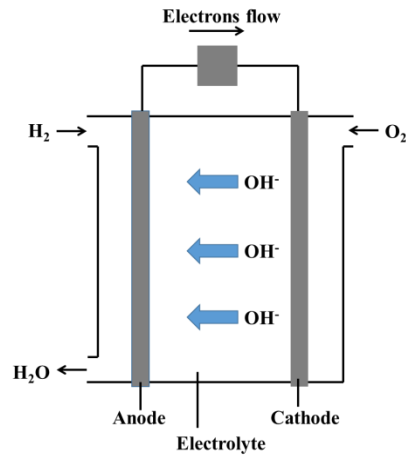
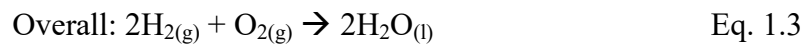
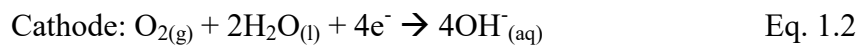
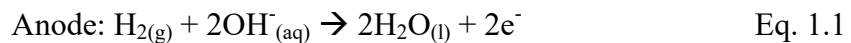


Figure 1.1 Schematic diagram of an alkaline fuel cell.

Figure 1.1 presents the schematic diagram of an alkaline fuel cell (AFC). In an AFC, hydrogen is fuel and oxidized at anode while ORR occurs at cathode. An alkaline electrolyte is used such as potassium hydroxide (KOH). The hydroxide ions ( $\text{OH}^-$  ions) produced from ORR move through the alkaline electrolyte from cathode to anode where hydrogen oxidation takes place. Water is finally produced.



The electrical efficiency of AFC is highest among all the fuel cells because ORR is faster than that in acidic fuel cells due to better kinetics.[13] Also, the catalyst for AFC is Ni which is an inexpensive metal. However, the electrolyte KOH usually absorbs  $\text{CO}_2$  and converts to potassium carbonate ( $\text{K}_2\text{CO}_3$ ) which poisons the fuel cell. Therefore, very pure hydrogen and oxygen are needed, which may

increase the operating costs.[15]

The AFCs are commonly used in the Space Shuttles for energy production. Water is also produced as drinking water for astronauts.[13] They are also used in transportation applications such as submarines and boats.[15]

### 1.2.2 Proton exchange membrane fuel cell (hydrogen fuel cell)

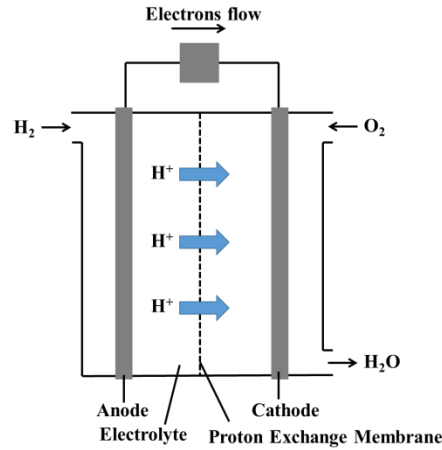
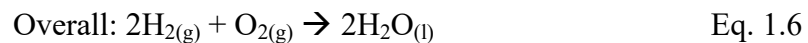
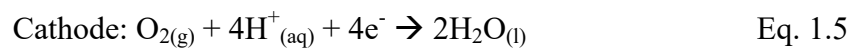
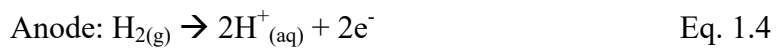


Figure 1.2 Schematic diagram of a proton exchange membrane fuel cell.

In a proton exchange membrane fuel cell (PEMFC) as shown in Figure 1.2, a proton-conducting polymer membrane is used as electrolyte. Nafion membranes with high acidity and concurrently conductivity are commonly used. Hydrogen is oxidized and protons and electrons are produced at anode. The protons pass through the membrane and the electrons move through the external circuit. Oxygen is fed to cathode and reacts with the protons generated from the hydrogen oxidation reaction to form water.



The PEMFCs is lightweight and of compact package due to high power density. Also, the conversion efficiency of PEMFCs is high. However, hydrogen storage and the cost for building hydrogen fueling stations are still challenges.

The PEMFCs are applied in portable appliances such as automobiles. They are also used in space shuttles for electricity and heat. Clean drinking water is also generated for astronauts.[14]

### 1.2.3 Phosphoric acid fuel cell

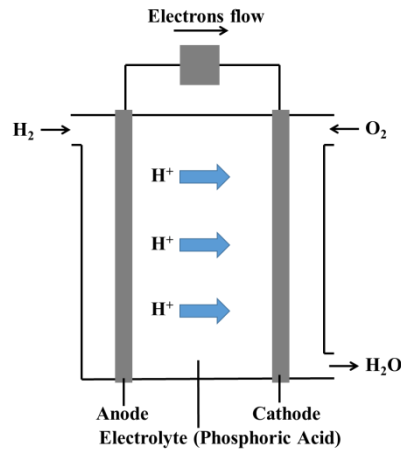
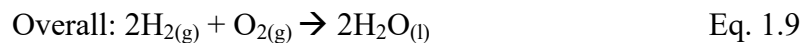
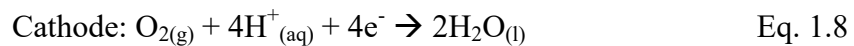
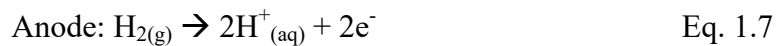


Figure 1.3 Schematic diagram of a phosphoric acid fuel cell.

In phosphoric acid fuel cell (PAFC) as displayed in Figure 1.3, phosphoric acid ( $\text{H}_3\text{PO}_4$ ) is an electrolyte. Hydrogen is pumped to anode for the oxidation. The protons pass through the  $\text{H}_3\text{PO}_4$  electrolyte and the electrons travel through the external circuit to the cathode. Oxygen is reduced at cathode by reacting with protons and electrons.



The PAFCs include numerous advantages. For instance, its construction is simple with thermal, chemical and electrochemical stability. The volatility of the electrolyte is low at the operating temperatures between 150 °C to 200 °C. However, the cost of the PAFCs is high. The PAFCs uses air instead of pure oxygen, resulting in a decrease in the current density. The stack bipolar plates are needed to increase the electrode area in order to raise the activity of the ORR.[15] Also, expensive and rare Pt is required for ORR.

The PAFCs are developed for power plants which supply electricity, heat and water to cities, shopping malls and hospitals.[13]

### 1.2.4 Molten carbonate fuel cell

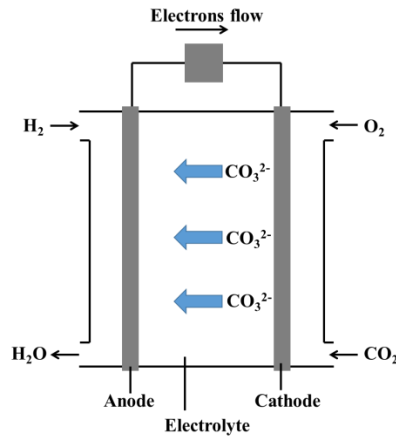
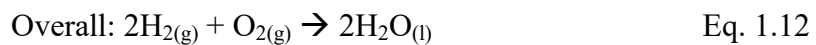
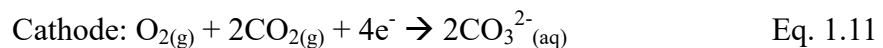
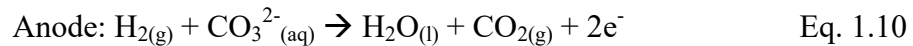


Figure 1.4 Schematic diagram of a molten carbonate fuel cell.

In molten carbonate fuel cell (MCFC) as shown in Figure 1.4, the electrolyte is the molten carbonate which is stabilized in an alumina-based matrix. Hydrogen oxidation occurs at the anode by reacting with the carbonate ions from the molten carbonate electrolyte. Water and carbon dioxide are produced. At cathode, oxygen is reduced with the carbon dioxide produced at anode. Carbonate ions are formed and return to the electrolyte. The final product of this reaction is water.



One of the advantages is that the carbon dioxide produced in the oxidation reaction is consumed at cathode. That means no carbon dioxide is produced. Also, since the MCFCs work at high operating temperature ranging from 600 °C to 700 °C, methane is reformed internally. The high operating temperature also increases the activity of ORR. Hence, inexpensive catalysts such as nickel(II) oxide (NiO) cathodes can be used. However, the materials of higher stability and corrosion

resistance but higher cost are required due to high operating temperature.[13]

Also, reaching to the high operating temperature requires longer time.[15]

The MCFCs are applied in the power conversion units for the stationary power.[13]

### 1.2.5 Solid oxide fuel cell

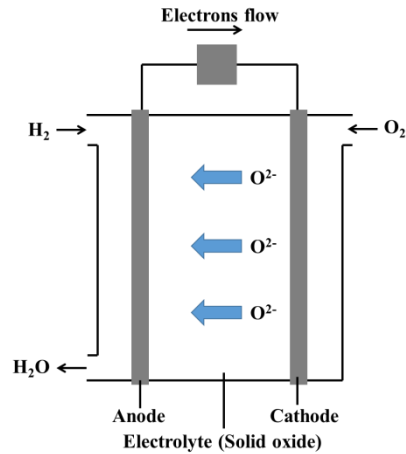
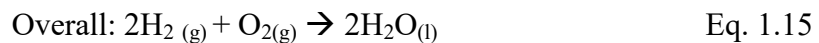
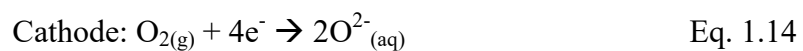
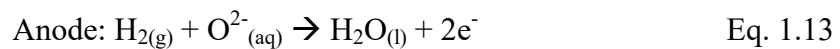


Figure 1.5 Schematic diagram of a solid oxide fuel cell.

In solid oxide fuel cell (SOFC) as shown in Figure 1.5, a solid oxide is used as an electrolyte. The commonly used electrolyte is yttria stabilized zirconia because it is highly chemically and thermally stable.[15] Hydrogen which is pumped to anode react with oxygen ions ( $O^{2-}$  ions) forming water and electrons. Those electrons move through the external circuit to the cathode for the reduction of oxygen at cathode. Oxygen is fed to the cathode side. Oxygen receives electrons from the external circuit forming  $O^{2-}$  ions.  $O^{2-}$  ions travel to the anode through the electrolyte.



The SOFCs are more stable than the MCFCs. The SOFCs employ solid electrolyte while the MCFCs use liquid electrolyte. Hence, no leakage happens in the SOFCs. Also, high operating temperature allows internal reforming of methane to hydrogen directly over anode catalyst. However, owing to high

operating temperature, materials of high thermal and chemical stability and longer set-up time are required.[13]

The SOFCs are applied in stationary power applications,[13] transportation and military market sectors.[16]

## 1.2.6 Direct liquid fuel cells

### Direct methanol fuel cell

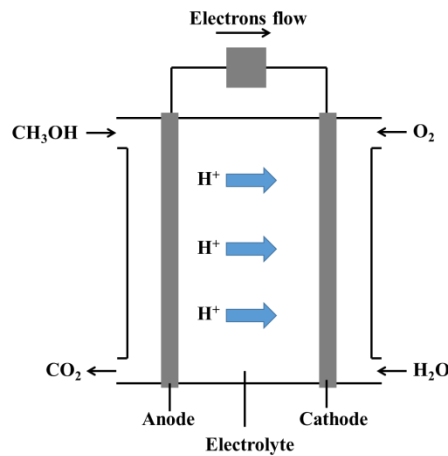
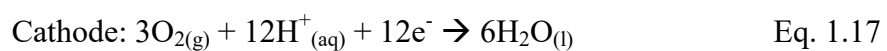
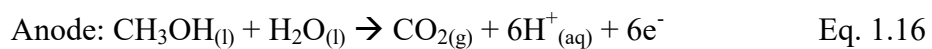


Figure 1.6 Schematic diagram of a direct methanol fuel cell.

In direct methanol fuel cell (DMFC) as shown in Figure 1.6, methanol is fed into the fuel cell and used directly without internal reforming of methane to hydrogen. At anode, methanol is oxidized to carbon dioxide through consecutive stripping of protons and electrons. The protons move from anode to cathode through the electrolyte. The electrons move through the external circuit to cathode. At cathode, oxygen is reduced to water. The final products are carbon dioxide and water.



The DMFCs have many advantages including easy and safe handling, storage and transportation of methanol, high energy density and low cost.

However, methanol is toxic.[17] Besides, methanol crossover occurs. Methanol

moves from anode to cathode through the electrolyte membrane. Methanol is oxidized at cathode directly due to the presence of oxygen, causing a decrease in the cell potential. As a consequence, fuel and the cell efficiency are lost.[18]

The DMFCs are applied in power sources in automobiles, buildings and factories.[19]

## Direct ethanol fuel cell

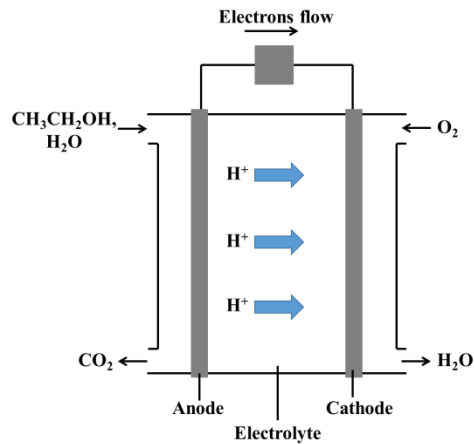
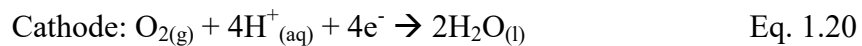
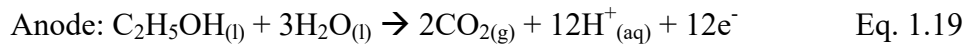


Figure 1.7 Schematic diagram of a direct ethanol fuel cell.

In direct ethanol fuel cell (DEFC) as displayed in Figure 1.7, ethanol reacts with water at anode giving out carbon dioxide, protons and electrons. At cathode, oxygen is reduced with protons and electrons to form water.



Ethanol is less toxic, less expensive and equips high energy density. However, it is difficult to achieve the complete oxidation of ethanol because the C-C bond of ethanol is required to be broken down at low temperatures. Hence, the anodic oxidation of the ethanol oxidation becomes sluggish. The performance of the DEFCs is affected.

The DEFCs still have a wide range of applications including electric vehicles, mobile phones and laptops.[20]

## Direct glycerol fuel cell

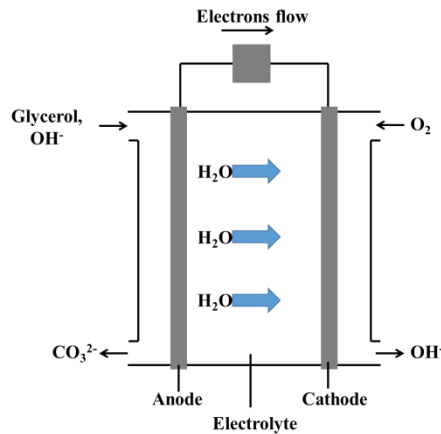
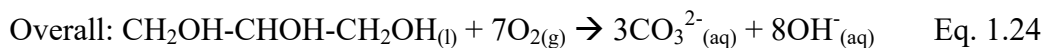
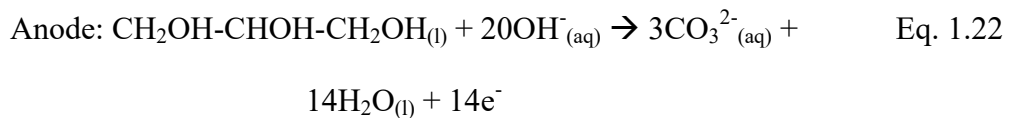


Figure 1.8 Schematic diagram of direct glycerol fuel cell.

In direct glycerol fuel cell (DGFC) as shown in Figure 1.8, glycerol is oxidized to carbonate ( $\text{CO}_3^{2-}$ ) ions with water and electrons at anode. At cathode, ORR occurs with the electron forming hydroxide ( $\text{OH}^-$ ) ions. The final products are carbonate ions and hydroxide ions.



Glycerol is less toxic, not volatile and not flammable when compared with methanol. Also, since it is a byproduct of biodiesel production, it is an inexpensive material from industry. It also has a relatively high theoretical energy density ( $6.4 \text{ kWh L}^{-1}$ ).<sup>[21]</sup> The partial oxidation of glycerol to mesoxalate generates 10 electrons without C-C bond breaking. 71.5 % of the whole existing energy can be achieved. The complete oxidation of glycerol to carbonate ion generates 14 electrons.<sup>[22]</sup> However, poisonous intermediates are produced on

the surface of the catalysts at low potentials. The performance of the fuel cell system will be affected.

## Direct formic acid fuel cell

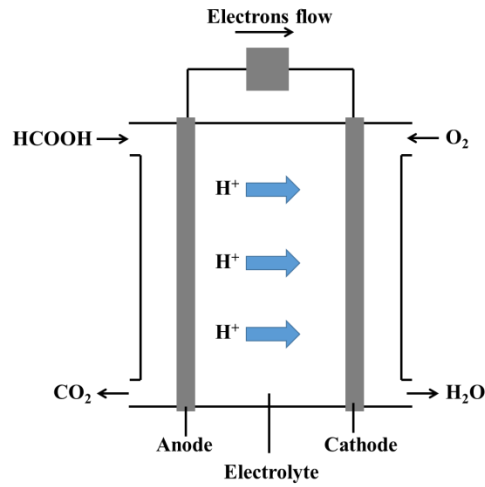
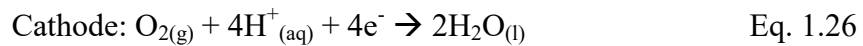


Figure 1.9 Schematic diagram of direct formic acid fuel cell.

In direct formic acid fuel cell (DFAFC) as displayed in Figure 1.9, at anode, formic acid is oxidized to carbon dioxide with the generation of protons and electrons. At cathode, ORR occurs with the electrons produced by the oxidation of formic acid. Finally, carbon dioxide and water are formed.



The toxicity of formic acid is low.[23] Also, the crossover through Nafion membranes of formic acid is smaller than methanol. Thus, highly concentrated fuel solutions and thinner membranes can be used in the DFAFCs.[24] The DFAFCs have a higher electromotive force, which is calculated from the Gibbs free energy, than hydrogen and direct methanol fuel cells. The major drawback of the DFACs is that the energy density of formic acid is quite low ( $2104 \text{ Wh L}^{-1}$ ) when compared with methanol ( $4900 \text{ Wh L}^{-1}$ ). However, this drawback can be

solved by using formic acid of high concentration.[17, 25]

The DFAFCs are applied in portable power systems such as laptop computer. [25, 26]

### **1.3 Exploration on Pt and Pt-based catalysts and its Applications in Direct Liquid Fuel Cells**

#### **1.3.1 Synthetic methods of Pt and Pt-based electrocatalysts**

##### **Hydrothermal and solvothermal method**

Hydrothermal and solvothermal methods are commonly used to synthesize Pt and Pt-based electrocatalysts. Both methods are performed under high temperature and high pressure. They also take place in close systems such as Teflon lined autoclaves enclosed in stainless steel. One difference between hydrothermal and solvothermal methods is that hydrothermal methods take place in aqueous solvents while solvothermal methods take place in non-aqueous solvents. Different metal precursors are used for synthesizing of Pt and Pt-based electrocatalysts.  $\text{H}_2\text{PtCl}_6 \cdot 6\text{H}_2\text{O}$  is usually used in hydrothermal method[27, 28] while platinum acetylacetonate ( $\text{Pt}(\text{acac})_2$ ) is used in solvothermal methods.[29, 30]

For example, nanoporous Pt catalysts were synthesized onto titanium support under hydrothermal methods using  $\text{H}_2\text{PtCl}_6 \cdot 6\text{H}_2\text{O}$  as metal precursor. Scanning electron microscopy (SEM) showed the Pt particle sizes ranging from 50 nm to 500 nm and also in the form of network. They exhibited strong and sensitive amperometric responses to glucose due to its large electrochemically active surface area (ECSA).[28]

PtFe nanowires were synthesized under solvothermal methods using  $\text{Pt}(\text{acac})_2$  as metal precursor. The mixture of  $\text{Pt}(\text{acac})_2$  and other chemicals including glycerol, 1,2-hexandecandiol, ethylenediamine and  $\text{Fe}(\text{CO})_5$  was heated in a Teflon autoclave inside a stainless steel. The as-synthesized PtFe nanowires were 2  $\mu\text{m}$

in length and 30 nm to 50 nm in diameter as displayed by transmission electron microscopy (TEM). They were also annealed at different temperatures to study the change of morphology and magnetic properties.[30]

Both hydrothermal and solvothermal methods consist of many advantages including simplicity, high reproducibility, low cost and short reaction time. Besides, the composition and morphology of Pt and Pt-based electrocatalysts can be easily controlled by varying the reaction parameters such as precursors, pH and temperature. It is easy to synthesize Pt,[31, 32] Pt-based binary,[29, 30] Pt-based ternary catalysts.[27] The morphology of Pt and Pt-based electrocatalysts ranges from nanoparticles,[31] nanowires[29, 30] to nanodendrites.[33] Moreover, the methods are suitable for large scale production. However, one disadvantage is that the use of autoclaves is required for dealing with the extreme experimental conditions of high temperature and high pressure.

### **Sol-gel method**

The sol-gel method is a wet-chemical method of synthesizing solid materials from small molecules. This method usually involves the hydrolysis and polycondensation of hydrolysable precursors such as metal alkoxides, followed by drying to products. Hydrogen hexachloroplatinate(IV) hexahydrate ( $\text{H}_2\text{PtCl}_6 \cdot 6\text{H}_2\text{O}$ ) is mostly used as metal precursor.[34-37] In some studies, organometallic precursor such as  $\text{Pt}(\text{acac})_2$  is also used.[38, 39]

For instance, nanostructured platinum/yttria-stabilized zirconia (Pt/YSZ) cement composite was synthesized using  $\text{H}_2\text{PtCl}_6 \cdot 6\text{H}_2\text{O}$  as metal precursor. The morphology and size of nanostructure Pt/YSZ were further studied by changing reaction parameters including Pt/YSZ ratio, gelling procedure and calcination temperature.[34] One research group prepared Pt deposited on silica films using  $\text{Pt}(\text{acac})_2$  as metal precursor. The mixture of  $\text{Pt}(\text{acac})_2$ , ethanol, 3-(2-aminoethylamino)propyltrimethoxysilane (AEAPTS), tetraethoxysilane (TEOS) and ammonium hydroxide ( $\text{NH}_4\text{OH}$ ) was heated at 70 °C for 3 days, followed by deposition on silica films. Hydrogen reduction was conducted at 500 °C for 2 days, forming Pt nanoparticles with average diameter of 22 nm. The Pt nanoparticles are in homogenous distribution on silica films due to the surrounding silica matrix. The Pt nanoparticles were also found to have larger average size with increasing reduction temperature.[38]

Sol-gel method is a helpful technique synthesizing the Pt and Pt-based electrocatalysts with uniform size and distribution. In addition, it is useful to prepare the catalyst with supports such as carbon,[36, 40], aluminum,[37, 39] titanium[41] and silicates.[35, 42, 43] Besides, this method is also usually

adopted to prepare binary Pt-based electrocatalysts such as PtAg,[44] PtRu[45] and PtSn.[46]

### **Physical synthetic method**

Apart from hydrothermal and solvothermal methods and sol-gel method, physical synthetic methods are also developed. Physical synthetic methods only involve the physical change of metal precursor without chemical change. They include a variety of techniques including sputtering ion,[47, 48] electron beam deposition,[49, 50] laser ablation [51, 52] and other types of irradiation such as gamma ( $\gamma$ ),[53, 54] UV-visible,[55, 56] microwave [57, 58] and ultrasonic irradiation.[59]

Different metal sources were used in different physical techniques. In sputtering, 99.95 % Pt plate was used as sputtering target [60] while Pt hydrocarbonate such as (Methylcyclopentadienyl)trimethylplatinum ( $C_9H_{16}Pt$ ) [61] and trimethyl(methylcyclopentadienyl)platinum(IV) ( $(CH_3)_3CH_3C_5H_4Pt$ ) [62] were used in ion or electron beam deposition.

For instance, Pt nanoparticles were deposited on carbon nanofibers (CNFs) in a polygonal barrel sputtering system with 99.95 % Pt plate was used as sputtering target. Under optimized deposition condition with the presence of columnar stainless steel, the Pt nanoparticles were deposited onto CNFs with uniform size and distribution.[60] Under ion or electron beam deposition,  $C_9H_{16}Pt$  was used as metal precursor in a dual beam system for Pt deposition. The volume of Pt nanorods was controlled by varying the reaction time, accelerating voltages and beam currents.[61]

For irradiation methods, potassium tetrachloroplatinate(II) ( $K_2PtCl_4$ ) [58] and  $H_2PtCl_6 \cdot 6H_2O$  [63, 64] were used as metal precursor. For example, PtNi

nanoparticles supported on carbon (PtNi/C) composite was synthesized by using  $K_2PtCl_4$  and  $NiCl_2 \cdot 6H_2O$  were used as metal precursor, poly(n-vinyl-2-pyrrolidone) (PVP) as a stabilizing agent under microwave heating. The PtNi nanoparticles, with the size ranging from 2.9 nm to 5.6 nm, were smaller in size and more uniformly distributed under microwave heating when compared with conventional heating.[58]

In physical methods, the morphology, composition and properties of products can be easily controlled by varying the experimental conditions, reagents and stabilizing agent concentrations. However, additional instruments are usually required, which may hinder the commercialization of the products.

### **Electrochemical deposition**

Electrochemical deposition is another technique for synthesizing Pt and Pt-based electrocatalysts.[65-68] In this technique, a two- or three-electrode electrochemical cell is used. The working electrode and reference electrode are involved in the two-electrode electrochemical cell and one more electrode, counter electrode, is involved in three-electrode electrochemical cell. In the electrochemical cell, the electrolyte acts a conducting medium and the source of Pt. By controlling the electrode potential or the current in the cell, Pt ions are deposited and reduced on the working electrode. Electrochemical deposition includes a variety of techniques including cyclic voltammetry (CV),[69] potential step experiments,[70] potential pulse experiments,[71] chronopotentiometry,[72] chronoamperometry [73] and current pulse experiments.[74]

For instance, CV is used to deposit Pt nanoparticles on multi-walled carbon nanotubes (MWCNTs). This deposition involves three steps. The first step was to functionalize the MWCNTs with different functional groups such as quinoid (=O), carbonyl (C=O) and carboxyl (-COOH) by electrochemical treatment. The second step was oxidize the tetrachloroplatinate complex ( $[\text{PtCl}_4]^{2-}$ ) into Pt(IV) complex by conducting CV. The final step was to convert Pt(IV) complex to Pt nanoparticles on MWCNTs. The effect of the cycling numbers of the second step towards the deposition of Pt nanoparticles onto MWCNTs and their catalytic activities towards the oxidation of methanol was studied. The Pt nanoparticles were more dispersed on MWCNTs with the increasing cycle numbers and the highest catalytic activity was achieved at 190 cycles.[69]

Potential step technique is also used to deposit Pt nanoparticles on MWCNTs

with the potential steps from 0.5 V to 0.7 V. The effect of number of potential step cycles and the width of the potential steps towards the morphology of Pt nanoparticles and their catalytic activities towards ORR was investigated. It was found that the width of the potential steps has no effect on the size of Pt nanoparticles. Besides, the Pt nanoparticles became larger in size with the morphology of snowflake at 200 potential step cycles and exhibited high electrocatalytic activity towards ORR.[70]

By varying the deposition techniques, metal precursor and electrode supporting substrate, Pt and Pt-based electrocatalysts of different morphologies and compositions are easily controlled.

For example, 3D flowerlike Pt nanoparticles clusters on carbon nanotubes (CNTs) were synthesized by a three-step electrochemical process including functionalization of CNTs by electrochemical treatment, electrochemical oxidation of Pt(II) complex to Pt(IV) complex by potential step deposition and transformation of Pt(IV) to Pt nanoparticles on MWCNTs. The flowerlike Pt nanoparticles were synthesized in potential step deposition while spherical Pt nanoparticles were synthesized in CV.[75]

Apart from different morphologies, Pt-based electrocatalysts with different compositions are also studied. The alloyed PtPb nanoparticles on MWCNTs (PtPb/CNTs) was synthesized via potential step deposition in a solution of potassium hexachloroplatinate(IV) ( $K_2PtCl_6$ ) and lead(II) nitrate ( $Pb(NO_3)_2$ ). The as-synthesized PtPb/CNTs is ranging from 10 nm to 40 nm in size with the morphology of snowflake.[76]

Electrochemical deposition is a simple method for synthesizing Pt and Pt-based electrocatalysts of different morphologies, compositions and electrocatalytic activity by changing deposition conditions and other parameters.

### **Electroless deposition**

In addition to electrochemical deposition, electroless deposition is also commonly used to synthesize Pt and Pt-based electrocatalysts. This method involves the reduction of metal ions onto inert substrate without external current source. It takes place in acidic, alkaline or neutral medium, and in open systems with the use of reducing agents.

The shape and size of Pt and Pt-based electrocatalysts can be controlled by controlling the metal precursors, reducing agents such as ethylene glycol (EG), [77, 78] sodium borohydride ( $\text{NaBH}_4$ ) [79, 80] and hydrazine [81] and stabilizing agents such as citric acid [82] and PVP.[83]

For instance, the Pt nanoparticles on carbon nanotubes (CNTs) and carbon nanofibers (CNFs) (Pt/CNTs and Pt/CNFs) were synthesized with EG as reducing agent. The synthetic steps include the chemical treatment of CNTs and CNFs by nitric acid and sulfuric acid, dispersion of CNTs and CNFs in the mixture of EG and water by sonication, addition of  $\text{K}_2\text{PtCl}_6$  followed by sonication, and refluxing the mixture. The Pt nanoparticles were from 2.3 nm to 3.9 nm in size. The Pt/CNTs achieved highest ECSA due to small particle size and high dispersion.[84]

The Pt nanoparticles were synthesized with the use of CA as a stabilizing agent and  $\text{NaBH}_4$  as a reducing agent. The mixture of CA and  $\text{H}_2\text{PtCl}_6$  was firstly sonicated, followed by the addition of Vulcan XC-72. The mixture was stirred with continuous addition of  $\text{NH}_4\text{OH}$ . Finally,  $\text{NaBH}_4$  was added to reduce Pt ions. By controlling the ratios of CA-to- $\text{H}_2\text{PtCl}_6$ , from 1 : 1 to 1 : 4, the Pt

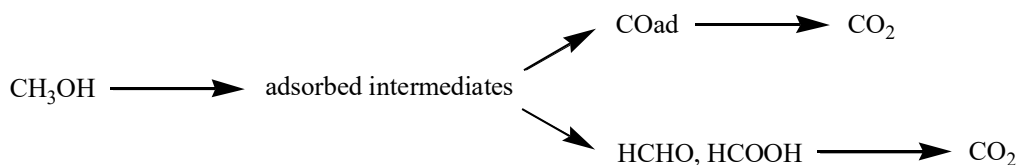
nanoparticles with the sizes ranging from 3.82 nm to 6.41 nm were synthesized. The Pt nanoparticle, with the size of 3.82 nm, synthesized with the CA-to- $\text{H}_2\text{PtCl}_6$  ratio of 2 : 1 achieved highest ECSA.[82]

Electroless deposition is an economical approach for synthesizing Pt and Pt-based electrocatalysts. The morphology and electrocatalytic activity can be controlled by tuning the experimental conditions such as the reaction temperature and concentrations of metal precursors, reducing agents and stabilizing agents.

### 1.3.2 Applications in direct liquids fuel cells

#### Methanol oxidation on Pt-based electrocatalysts

Methanol oxidation takes place in direct methanol fuel cell (DMFC). The reaction involves the generation of 6 electrons.[85]



Scheme 1.1 Schematic representation of the mechanism of methanol oxidation.[85]

It is generally believed that methanol oxidation takes place on Pt catalyst under dual path mechanism involving direct and indirect pathways as shown in the Scheme 1.1.[86]

The methanol molecules first adsorb on the Pt catalyst and become adsorbed intermediates. In the direct pathway, the adsorbed intermediates become soluble intermediates such as formaldehyde (HCHO) and formic acid (HCOOH). These soluble intermediates are directly oxidized to form  $\text{CO}_2$  by OH species generated from the dissociation of water. In the indirect pathway, the adsorbed intermediates dehydrogenate through several steps to form  $\text{CO}_{\text{ads}}$  intermediates which cause poisoning to Pt catalysts and blocking the active sites. The  $\text{CO}_{\text{ads}}$  intermediates are oxidized to form  $\text{CO}_2$  by OH species.[87, 88]

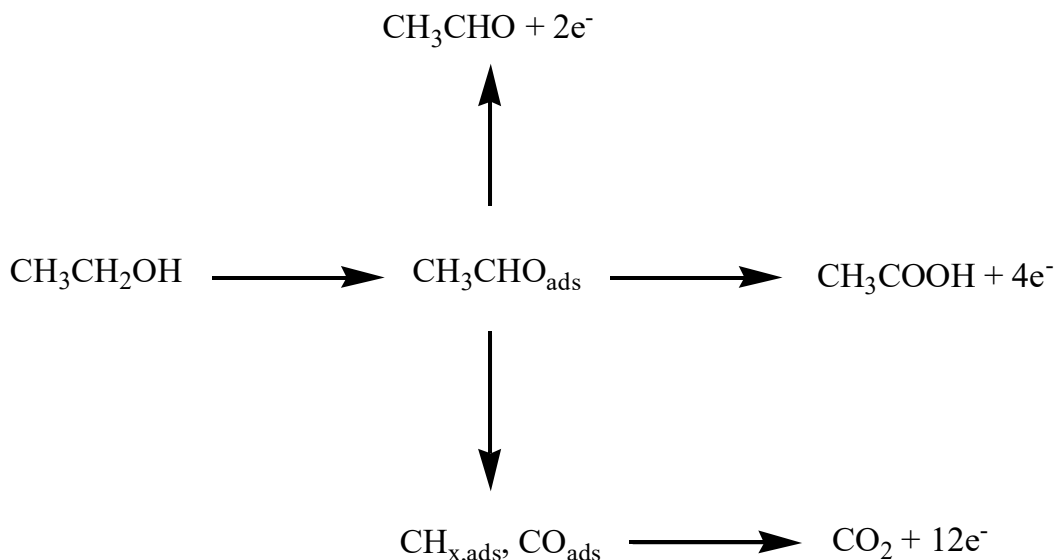
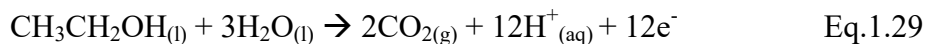
In methanol oxidation, indirect pathway is a dominant path with the formation of

$\text{CO}_{\text{ads}}$ . This is related to the energy barriers for breaking bond in the order of O-H < C-H < C-O, suggesting the methanol is oxidized via the bond cleavage of O-H bond dominantly.[69] However, the rate of indirect methanol oxidation will be different in different electrolytes. The experiments from other literatures suggest that sulfuric acid favors direct methanol oxidation while the perchloric acid favors indirect methanol oxidation because the electrolyte anions exhibit different adsorption affinity to Pt.[88, 89]

Many research groups investigated PtRu bimetallic electrocatalysts for the oxidation of methanol instead of pure Pt. It is suggested that  $\text{OH}^-$  ions, which are generated from the activation of water, adsorb on Ru and oxidized  $\text{CO}_{\text{ads}}$  intermediate on Pt surface.[90] Another group suggested that Ru is more likely to adsorb  $\text{CO}_{\text{ads}}$  than Pt. Hence, less  $\text{CO}_{\text{ads}}$  adsorb on Pt and the CO poisoning to Pt is reduced.[91]

### Ethanol oxidation on Pt-based electrocatalysts

Ethanol oxidation takes place in direct ethanol fuel cell (DEFC). The reaction involves the generation of 12 electrons.[92]



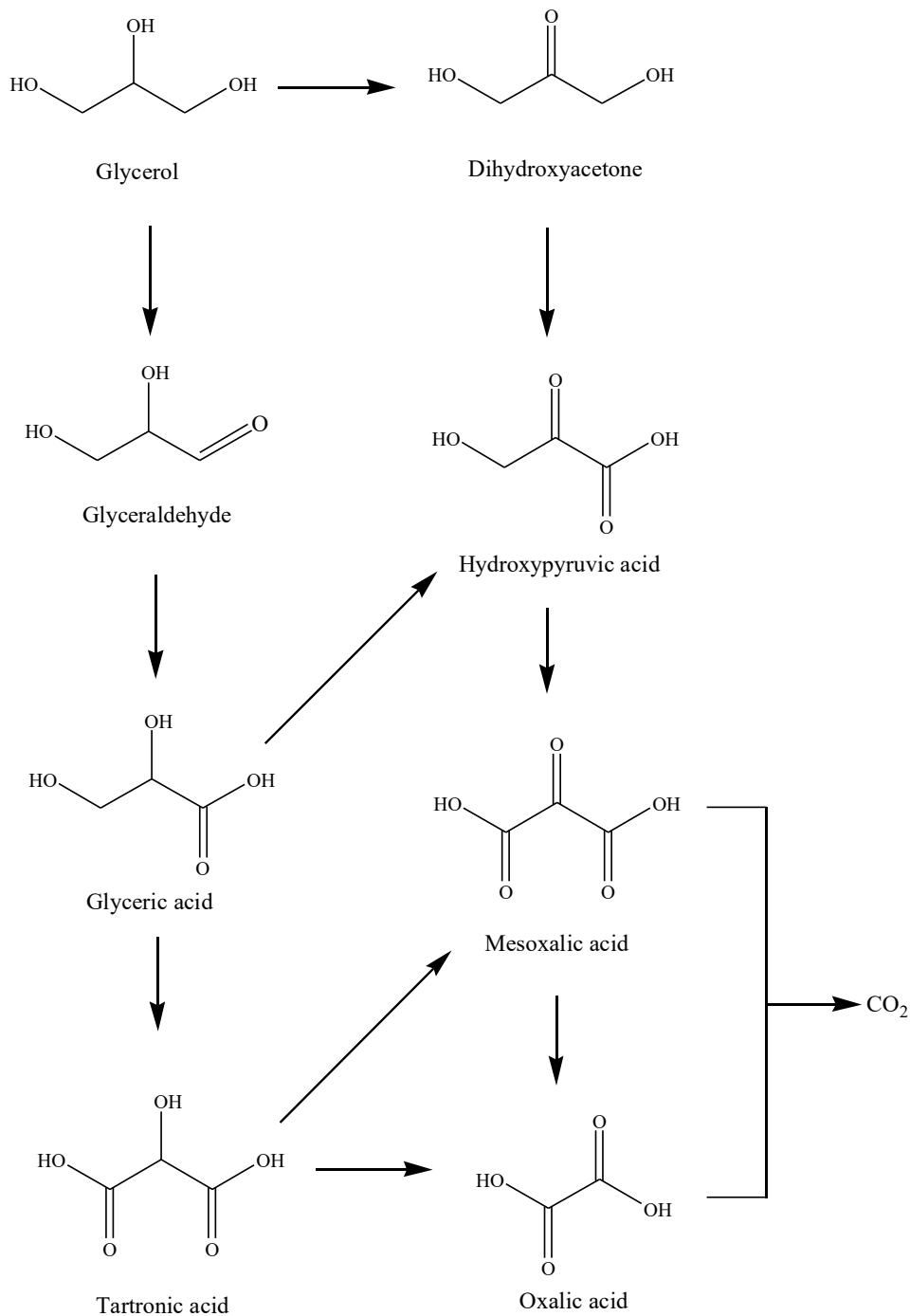
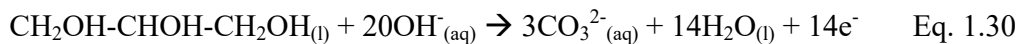
Scheme 1.2 Schematic representation of the mechanism of ethanol oxidation.[93]

The ethanol oxidation occurs in two main pathways which are complete oxidation with the formation of carbon dioxide (CO<sub>2</sub>) and partial oxidation with the formation of acetaldehyde (CH<sub>3</sub>CHO) and acetic acid (CH<sub>3</sub>COOH) as shown in Scheme 1.2. However, the complete oxidation of ethanol is difficult due to the difficulty of C-C bond cleavage. As a result, ethanol is partially oxidized to CH<sub>3</sub>CHO and CH<sub>3</sub>COOH with fewer electrons formed, which lowers the overall electron density.[93] Also, the CO and other intermediates strongly adsorb on Pt surface. This causes poisoning to Pt catalysts and blocking the active sites from ethanol molecule, resulting in lower catalytic activity.

Hence, many research groups investigate more efficient Pt-based electrocatalysts by incorporating metals such as Sn,[94, 95] Ni,[96] Ru [97, 98] and Pd [99, 100] into Pt to reduce CO poisoning effect, thereby enhancing the catalytic activity.

### Glycerol oxidation on Pt-based electrocatalysts

Glycerol oxidation takes place in direct glycerol fuel cell (DGFC). The reaction involves the generation of 14 electrons. [21]

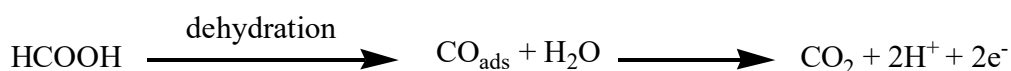
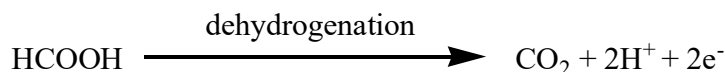
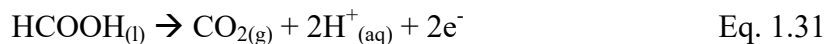


Scheme 1.3 Schematic representation of the mechanism of glycerol oxidation.[101]

In the general mechanism displayed in Scheme 1.3, there are two pathways for the oxidation of glycerol. In primary alcohol oxidation, glycerol is oxidized to glyceraldehyde which is further oxidized to glyceric acid, tartronic acid and oxalic acid. In secondary alcohol oxidation, glycerol is oxidized to dihydroxyacetone which is oxidized to hydroxypyruvic acid and mesoxalic acid. The oxalic acid and mesoxalic acid are oxidized to CO<sub>2</sub>. [101] CO<sub>2</sub> is generated in form of carbonate (CO<sub>3</sub><sup>2-</sup>) in alkaline medium. [102] Many research groups studied using monometallic Au, [21, 103] Pd [104, 105] and Pt [106] as anode electrocatalysts for glycerol oxidation. [107]

### Formic acid oxidation on Pt-based electrocatalysts

Formic acid oxidation takes place in direct formic acid fuel cell (DFAFC). The reaction involves the generation of 2 electrons.[17]

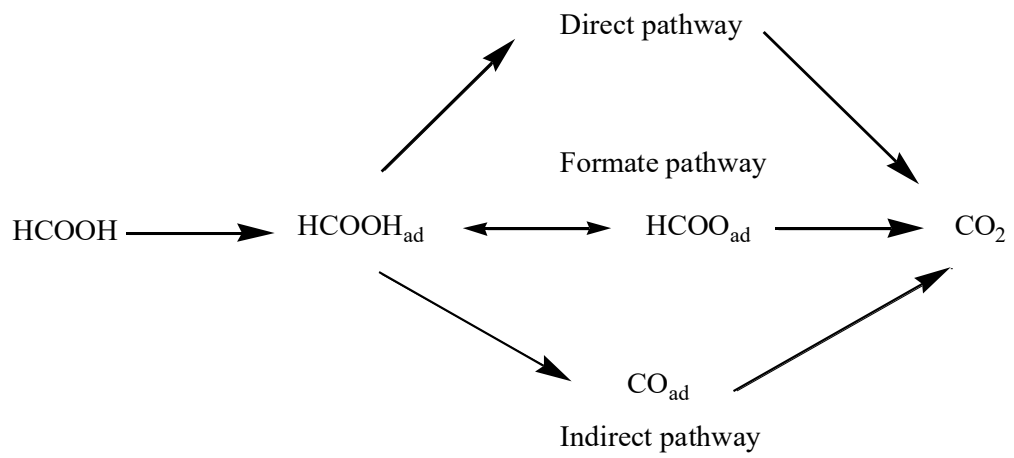


Scheme 1.4 Schematic representation of the mechanism of formic acid oxidation.[25]

It is generally accepted that formic acid oxidation is under “parallel or dual pathway mechanism” with two pathways on Pt as shown in Scheme 1.4. The two pathways are direct and indirect oxidations, which are also called dehydrogenation and dehydration respectively. The direct oxidation (dehydrogenation) means that formic acid is directly oxidized to CO<sub>2</sub> while the indirect oxidation (dehydration) means that formic acid is oxidized to adsorbed CO intermediate which is finally oxidized to CO<sub>2</sub>. The CO<sub>ads</sub> causes poisoning to Pt and blocks the Pt active sites from the direct oxidation of formic acid.[17, 25, 108] Hence, many studies on developing the Pt-based catalysts enhancing dehydrogenation and lowering dehydration were performed.

In addition to dual-path mechanism, a formate pathway for the oxidation formic acid, as shown in the Scheme 1.5, is proposed as studied by *in-situ* IR spectroscopy. The formic acid is dehydrogenated adsorbed formate with a

bridged bond which is then oxidized to  $\text{CO}_2$ . [109]



Scheme 1.5 Schematic representation of the mechanism of formic acid oxidation. [109]

## 1.4 Scope of thesis

Since the massive application of Pt is constrained by its high cost and limited availability, the objective of the research is to develop low-Pt-content catalysts with improved Pt utilization and enhanced catalytic activity for applications in direct liquid fuel cell.

In Chapter 2, low-dose Pt submonolayer on gold nanoparticles supported on CNTs (AuNP/CNTs) composites by using halides as bridging agent were developed by halide ion adsorption followed by *in-situ* electrochemical reduction. Their electrocatalytic activities towards oxidations of formic acid and methanol were studied. In Chapter 3, Pd@PdPt/CNTs alloy and Pt@Pd/CNTs phase-separate composites were developed from the surfactant-free Pd/CNTs and Pt/CNTs composites by galvanic replacement reaction between palladium (Pd) and  $[\text{PtCl}_4]^{2-}$  ions, and adsorption of tetrachloropalladate complex ( $[\text{PdCl}_4]^{2-}$ ) on Pt surface followed by hydrogen reduction respectively. Their electrocatalytic activities towards oxidations of methanol, ethanol and glycerol were studied. In Chapter 4, hollow PtAg nanowires (PtAg NWs) were prepared by galvanic replacement reaction between silver nanowires (AgNWs) and  $[\text{PtCl}_4]^{2-}$  ions. The electrocatalytic activities towards oxidations of methanol, ethanol, glycerol and formic acid were studied.

## REFERENCES

- [1] A. Rabis, P. Rodriguez, T.J. Schmidt, *Acs Catalysis*, 2 (2012) 864-890.
- [2] J.M. Andújar, F. Segura, *Renewable and sustainable energy reviews*, 13 (2009) 2309-2322.
- [3] P.G. Grimes, *IEEE Aerospace and Electronic Systems Magazine*, 15 (2000) 7-10.
- [4] P. Chaurasia, Y. Ando, T. Tanaka, *Energy conversion and management*, 44 (2003) 611-628.
- [5] A.B. Stambouli, E. Traversa, *Renewable and sustainable energy reviews*, 6 (2002) 433-455.
- [6] A. Appleby, *Journal of Power Sources*, 29 (1990) 3-11.
- [7] C. Stone, A.E. Morrison, *Solid State Ionics*, 152 (2002) 1-13.
- [8] J.-H. Lee, S.-T. Baek, H.-J. Jung, H.-H. Kang, J.-M. Chung, I.-Y. Suh, *Electrical Machines and Systems, 2007. ICEMS. International Conference on, IEEE2007*, pp. 354-358.
- [9] R.J. Spiegel, J. Preston, *Waste management*, 23 (2003) 709-717.
- [10] *Fuel Cells Bulletin*, 2005 (2005) 1.
- [11] U. Second, *Fuel Cells Bulletin*, 1 (2003).
- [12] A. Miller, K. Hess, D. Barnes, T. Erickson, *Journal of Power Sources*, 173 (2007) 935-942.
- [13] L. Carrette, K.A. Friedrich, U. Stimming, *ChemPhysChem*, 1 (2000) 162-193.
- [14] C.-J. Zhong, J. Luo, P.N. Njoki, D. Mott, B. Wanjala, R. Loukrakpam, S. Lim, L. Wang, B. Fang, Z. Xu, *Energy & Environmental Science*, 1 (2008) 454-466.
- [15] S. Mekhilef, R. Saidur, A. Safari, *Renewable and Sustainable Energy*

Reviews, 16 (2012) 981-989.

[16] S.C. Singhal, Solid State Ionics, 152 (2002) 405-410.

[17] X. Yu, P.G. Pickup, Journal of Power Sources, 182 (2008) 124-132.

[18] A.B.A.A. Nassr, I. Sinev, W. Grünert, M. Bron, Applied Catalysis B: Environmental, 142 (2013) 849-860.

[19] Y. Hu, P. Wu, Y. Yin, H. Zhang, C. Cai, Applied Catalysis B: Environmental, 111 (2012) 208-217.

[20] Z.-B. Wang, G.-P. Yin, Y.-G. Lin, Journal of Power Sources, 170 (2007) 242-250.

[21] Z. Zhang, L. Xin, W. Li, international journal of hydrogen energy, 37 (2012) 9393-9401.

[22] E. Habibi, H. Razmi, international journal of hydrogen energy, 37 (2012) 16800-16809.

[23] C. Rice, S. Ha, R. Masel, A. Wieckowski, Journal of Power Sources, 115 (2003) 229-235.

[24] Y.-W. Rhee, S.Y. Ha, R.I. Masel, Journal of Power Sources, 117 (2003) 35-38.

[25] J. Xu, T. Zhao, Z. Liang, Journal of Power Sources, 185 (2008) 857-861.

[26] C.M. Miesse, W.S. Jung, K.-J. Jeong, J.K. Lee, J. Lee, J. Han, S.P. Yoon, S.W. Nam, T.-H. Lim, S.-A. Hong, Journal of Power Sources, 162 (2006) 532-540.

[27] Q. Yi, L. Li, W. Yu, Z. Zhou, X. Liu, G. Xu, Journal of Alloys and Compounds, 466 (2008) 52-58.

[28] P. Holt-Hindle, S. Nigro, M. Asmussen, A. Chen, Electrochemistry Communications, 10 (2008) 1438-1441.

[29] Z. Zhang, D.A. Blom, Z. Gai, J.R. Thompson, J. Shen, S. Dai, Journal of the

- American Chemical Society, 125 (2003) 7528-7529.
- [30] Y. Hou, H. Kondoh, R. Che, M. Takeguchi, T. Ohta, *Small*, 2 (2006) 235-238.
- [31] D.U. Hong, C.-H. Han, S.H. Park, I.-J. Kim, J. Gwak, S.-D. Han, H.J. Kim, *Current Applied Physics*, 9 (2009) 172-178.
- [32] X. Peng, K. Koczkur, S. Nigro, A. Chen, *Chemical communications*, (2004) 2872-2873.
- [33] Z.-C. Zhang, J.-F. Hui, Z.-G. Guo, Q.-Y. Yu, B. Xu, X. Zhang, Z.-C. Liu, C.-M. Xu, J.-S. Gao, X. Wang, *Nanoscale*, 4 (2012) 2633-2639.
- [34] H. Shiga, T. Okubo, M. Sadakata, *Industrial & engineering chemistry research*, 35 (1996) 4479-4486.
- [35] D.S. Bae, K.S. Han, J.H. Adair, *Journal of the American Ceramic Society*, 85 (2002) 1321-1323.
- [36] M. Yang, Y. Yang, Y. Liu, G. Shen, R. Yu, *Biosensors and Bioelectronics*, 21 (2006) 1125-1131.
- [37] R.J. Bass, T.M. Dunn, Y.-C. Lin, K.L. Hohn, *Industrial & Engineering Chemistry Research*, 47 (2008) 7184-7189.
- [38] M. Malenovska, S. Martinez, M.A. Neouze, U. Schubert, *European journal of inorganic chemistry*, 2007 (2007) 2609-2611.
- [39] L. Hu, K.A. Boateng, J.M. Hill, *Journal of Molecular Catalysis A: Chemical*, 259 (2006) 51-60.
- [40] X. Kang, Z. Mai, X. Zou, P. Cai, J. Mo, *Talanta*, 74 (2008) 879-886.
- [41] G. Facchin, G. Carturan, R. Campostrini, S. Gialanella, L. Lutterotti, L. Armelao, G. Marci, L. Palmisano, A. Sclafani, *Journal of sol-gel science and technology*, 18 (2000) 29-59.
- [42] B.K. Jena, C.R. Raj, *The Journal of Physical Chemistry C*, 112 (2008)

3496-3502.

[43] L.W. Beakley, S.E. Yost, R. Cheng, B.D. Chandler, *Applied Catalysis A: General*, 292 (2005) 124-129.

[44] K.M.K. Yu, D. Thompsett, S.C. Tsang, *Chemical Communications*, (2003) 1522-1523.

[45] J.Y. Kim, Z. Yang, C.-C. Chang, T. Valdez, S. Narayanan, P. Kumta, *Journal of the Electrochemical Society*, 150 (2003) A1421-A1431.

[46] K. Balakrishnan, R.D. Gonzalez, *Langmuir*, 10 (1994) 2487-2490.

[47] C.-H. Wan, Q.-H. Zhuang, *International Journal of Hydrogen Energy*, 32 (2007) 4402-4411.

[48] K.-W. Park, Y.-J. Song, J.-M. Lee, S.-B. Han, *Electrochemistry communications*, 9 (2007) 2111-2115.

[49] A. Reguer, F. Bedu, D. Tonneau, H. Dallaporta, M. Prestigiacomo, A. Houel, P. Sudraud, *Journal of Vacuum Science & Technology B: Microelectronics and Nanometer Structures Processing, Measurement, and Phenomena*, 26 (2008) 175-180.

[50] B.J. Inkson, G. Dehm, Y. Peng, *Nanotechnology*, 18 (2007) 415601.

[51] R. Dolbec, E. Irissou, M. Chaker, D. Guay, F. Rosei, M. El Khakani, *Physical Review B*, 70 (2004) 201406.

[52] A. Serventi, R. Dolbec, M. El Khakani, R. Saint-Jacques, D. Rickerby, *Journal of Physics and Chemistry of Solids*, 64 (2003) 2097-2103.

[53] S.-D. Oh, K.R. Yoon, S.-H. Choi, A. Gopalan, K.-P. Lee, S.-H. Sohn, H.-D. Kang, I.S. Choi, *Journal of Non-Crystalline Solids*, 352 (2006) 355-360.

[54] H. Wang, X. Sun, Y. Ye, S. Qiu, *Journal of Power Sources*, 161 (2006) 839-842.

[55] E. Ozkaraoglu, I. Tunc, S. Suzer, *Polymer*, 50 (2009) 462-466.

- [56] S. Shironita, K. Mori, T. Shimizu, T. Ohmichi, N. Mimura, H. Yamashita, *Applied Surface Science*, 254 (2008) 7604-7607.
- [57] N.N. Mallikarjuna, R.S. Varma, *Crystal growth & design*, 7 (2007) 686-690.
- [58] T. Deivaraj, W. Chen, J.Y. Lee, *Journal of Materials Chemistry*, 13 (2003) 2555-2560.
- [59] R.A. Caruso, M. Ashokkumar, F. Grieser, *Colloids and Surfaces A: Physicochemical and Engineering Aspects*, 169 (2000) 219-225.
- [60] H. Yamamoto, K. Hirakawa, T. Abe, *Materials Letters*, 62 (2008) 2118-2121.
- [61] H. Plank, C. Gspan, M. Dienstleder, G. Kothleitner, F. Hofer, *Nanotechnology*, 19 (2008) 485302.
- [62] Z.-M. Liao, J. Xu, X.-Z. Zhang, D.-P. Yu, *Nanotechnology*, 19 (2008) 305402.
- [63] J.-E. Park, M. Atobe, T. Fuchigami, *Electrochimica Acta*, 51 (2005) 849-854.
- [64] X. Luo, T. Imae, *Journal of Materials Chemistry*, 17 (2007) 567-571.
- [65] Y. Zhao, E. Yifeng, L. Fan, Y. Qiu, S. Yang, *Electrochimica acta*, 52 (2007) 5873-5878.
- [66] A. Bauer, E.L. Gyenge, C.W. Oloman, *Journal of power sources*, 167 (2007) 281-287.
- [67] G. Sine, I. Duo, B.E. Roustom, G. Foti, C. Comninellis, *Journal of applied electrochemistry*, 36 (2006) 847-862.
- [68] L. Plyasova, I.Y. Molina, A. Gavrilov, S. Cherepanova, O. Cherstiouk, N. Rudina, E. Savinova, G. Tsirlina, *Electrochimica Acta*, 51 (2006) 4477-4488.
- [69] Y. Zhao, L. Fan, H. Zhong, Y. Li, *Microchimica Acta*, 158 (2007) 327-334.
- [70] H.-F. Cui, J.-S. Ye, W.-D. Zhang, J. Wang, F.-S. Sheu, *Journal of*

- Electroanalytical Chemistry, 577 (2005) 295-302.
- [71] J.N. Tiwari, F.-M. Pan, R.N. Tiwari, S. Nandi, Chemical Communications, (2008) 6516-6518.
- [72] C. Paoletti, A. Cemmi, L. Giorgi, R. Giorgi, L. Pilloni, E. Serra, M. Pasquali, Journal of Power Sources, 183 (2008) 84-91.
- [73] G.-Y. Zhao, H.-L. Li, Applied Surface Science, 254 (2008) 3232-3235.
- [74] Y.-J. Song, J.-K. Oh, K.-W. Park, Nanotechnology, 19 (2008) 355602.
- [75] Y. Zhao, L. Fan, H. Zhong, Y. Li, S. Yang, Advanced functional materials, 17 (2007) 1537-1541.
- [76] H.-F. Cui, J.-S. Ye, W.-D. Zhang, C.-M. Li, J.H. Luong, F.-S. Sheu, Analytica chimica acta, 594 (2007) 175-183.
- [77] H. Nitani, T. Nakagawa, H. Daimon, Y. Kurobe, T. Ono, Y. Honda, A. Koizumi, S. Seino, T.A. Yamamoto, Applied Catalysis A: General, 326 (2007) 194-201.
- [78] Z. Liu, X.Y. Ling, B. Guo, L. Hong, J.Y. Lee, Journal of power sources, 167 (2007) 272-280.
- [79] F. Matsumoto, C. Roychowdhury, F.J. DiSalvo, H.D. Abruña, Journal of The Electrochemical Society, 155 (2008) B148-B154.
- [80] D. Nagao, Y. Shimazaki, Y. Kobayashi, M. Konno, Colloids and Surfaces A: Physicochemical and Engineering Aspects, 273 (2006) 97-100.
- [81] S. Chu, H. Kawamura, M. Mori, Journal of The Electrochemical Society, 155 (2008) D414-D418.
- [82] J. Guo, T. Zhao, J. Prabhuram, C. Wong, Electrochimica Acta, 50 (2005) 1973-1983.
- [83] T. Herricks, J. Chen, Y. Xia, Nano Letters, 4 (2004) 2367-2371.
- [84] S.L. Knupp, W. Li, O. Paschos, T.M. Murray, J. Snyder, P. Haldar, Carbon,

46 (2008) 1276-1284.

[85] T. Iwasita, *Electrochimica Acta*, 47 (2002) 3663-3674.

[86] E. Herrero, W. Chrzanowski, A. Wieckowski, *The Journal of Physical Chemistry*, 99 (1995) 10423-10424.

[87] J.-M. Léger, *Journal of Applied Electrochemistry*, 31 (2001) 767-771.

[88] M. Neurock, M. Janik, A. Wieckowski, *Faraday discussions*, 140 (2009) 363-378.

[89] D. Cao, G.-Q. Lu, A. Wieckowski, S.A. Wasileski, M. Neurock, *The Journal of Physical Chemistry B*, 109 (2005) 11622-11633.

[90] A. Tripković, K.D. Popović, B. Grgur, B. Blizanac, P. Ross, N. Marković, *Electrochimica Acta*, 47 (2002) 3707-3714.

[91] Z. Liu, X.Y. Ling, X. Su, J.Y. Lee, *The Journal of Physical Chemistry B*, 108 (2004) 8234-8240.

[92] S. Song, P. Tsiakaras, *Applied Catalysis B: Environmental*, 63 (2006) 187-193.

[93] A.B. Delpuech, M. Jacquot, M. Chatenet, C. Cremers, *Physical Chemistry Chemical Physics*, 18 (2016) 25169-25175.

[94] L. Jiang, G. Sun, S. Sun, J. Liu, S. Tang, H. Li, B. Zhou, Q. Xin, *Electrochimica Acta*, 50 (2005) 5384-5389.

[95] D.R.M.d. Godoi, J. Perez, H. Villullas, *Journal of Power Sources*, 195 (2010) 3394-3401.

[96] D. Soundararajan, J. Park, K. Kim, J. Ko, *Current Applied Physics*, 12 (2012) 854-859.

[97] E.V. Spinacé, A.O. Neto, T.R. Vasconcelos, M. Linardi, *Journal of Power Sources*, 137 (2004) 17-23.

[98] Y. Zhao, X. Yang, L. Zhan, S. Ou, J. Tian, *Journal of Materials Chemistry*,

21 (2011) 4257-4263.

[99] F. Ren, H. Wang, C. Zhai, M. Zhu, R. Yue, Y. Du, P. Yang, J. Xu, W. Lu, ACS applied materials & interfaces, 6 (2014) 3607-3614.

[100] X. Chen, Z. Cai, X. Chen, M. Oyama, Journal of Materials Chemistry A, 2 (2014) 315-320.

[101] S. Carrettin, P. McMorn, P. Johnston, K. Griffin, C.J. Kiely, G.J. Hutchings, Physical Chemistry Chemical Physics, 5 (2003) 1329-1336.

[102] Y. Kwon, K.J.P. Schouten, M. Koper, ChemCatChem, 3 (2011) 1176-1185.

[103] H. Wang, L. Thia, N. Li, X. Ge, Z. Liu, X. Wang, Applied Catalysis B: Environmental, 166 (2015) 25-31.

[104] M. Simões, S. Baranton, C. Coutanceau, Applied Catalysis B: Environmental, 93 (2010) 354-362.

[105] A. Dector, F. Cuevas-Muñiz, M. Guerra-Balcázar, L.A. Godínez, J. Ledesma-García, L. Arriaga, International Journal of Hydrogen Energy, 38 (2013) 12617-12622.

[106] Z. Zhang, L. Xin, W. Li, Applied Catalysis B: Environmental, 119 (2012) 40-48.

[107] Z. Zhang, L. Xin, J. Qi, D.J. Chadderton, W. Li, Applied Catalysis B: Environmental, 136 (2013) 29-39.

[108] K.A. Schwarz, R. Sundararaman, T.P. Moffat, T.C. Allison, Physical Chemistry Chemical Physics, 17 (2015) 20805-20813.

[109] Y.X. Chen, M. Heinen, Z. Jusys, R.J. Behm, Angewandte Chemie International Edition, 45 (2006) 981-985.

## Chapter 2

# Synthesis of Platinum-Gold Core-Shell Nanoparticles for Direct Formic Acid and Methanol Fuel Cells

### 2.1 Background

#### Overview of CNTs

Carbon nanotubes (CNTs), which were discovered in the early 90s, are commonly applied in the fields of nanoscience and nanotechnology such as nanostructured electronic devices,[1] biochemical sensors,[2] catalyst supports [3] and chemically sensitive tips for scanning probe microscopy.[4]

CNTs are nanostructures of rolling graphene sheets, with the hexagonal arrangement of  $sp^2$  hybridized carbon, into the shape of cylinder.[5, 6] The tubes are usually few nanometers in radius and 20 cm in length.[7] As displayed in Figure 2.1, there are three types of CNTs which are single-walled carbon nanotube (SWCNT), double-walled carbon nanotube (DWCNT) and multi-walled carbon nanotube (MWCNT). SWCNT, DWCNT and MWCNT consist of one graphene sheet, two graphene sheets, and several graphene sheets respectively.[4]

The synthesis of CNTs involves the decomposition of carbon source such as graphite and hydrocarbon by metal catalysts such as iron (Fe), cobalt (Co), nickel (Ni) and yttrium (Y), followed by the removal of metal catalyst remained in purification step.[6]

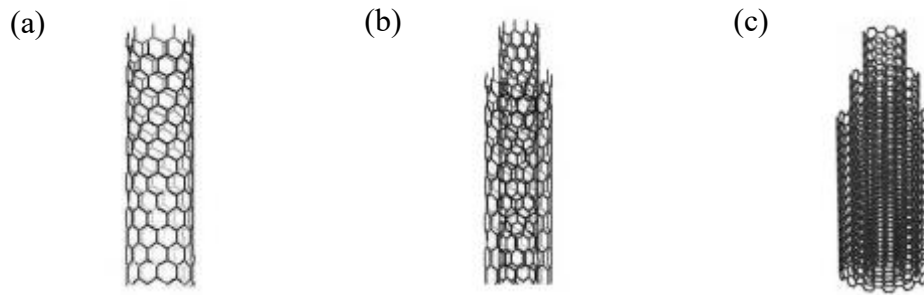


Figure 2.1 (a) SWCNT, (b) DWCNT and (c) MWCNT.[8]

### **Physical and chemical properties of CNTs**

CNTs have a wide range of properties in terms of electrical, thermal properties and strength based on different physical designs of the tube. There are three designs including armchair, chiral and zigzag depending how the graphene sheet rolls into the tube as shown in Figure 2.2. The graphene sheet rolling from its corner or edge results in different designs. The rolling structure can be described by a chiral vector  $(n, m)$ . The electrical conductivity is determined by the design of CNTs. It is stated that the CNTs is highly conductive when  $n - m$  is a multiple of 3. That means the Armchair ( $n = m$ ) CNTs is highly conducting while chiral ( $n \neq m$ ) and zigzag ( $m = 0$ ) CNTs are semi-conducting.[4] Also, CNTs have high tensile strength due to  $sp^2$  between carbon atoms. These bonds are stronger than  $sp^3$  bonds, thus providing tensile strength. Besides, CNTs can withstand high temperature due to the high tensile strength, showing high thermal conductivity.[9]

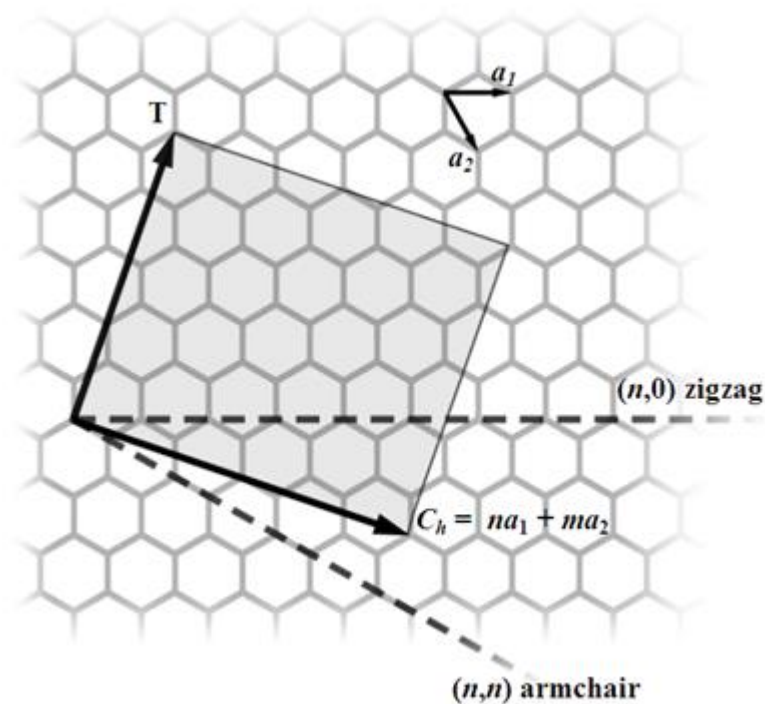


Figure 2.2 Diagram of showing how the graphene sheet rolls into the tube.[10]

### **Modification of CNTs**

It is general that CNTs keep aggregating owing to their hydrophobic force. Therefore, the metal particles poorly disperse when using CNTs as catalysts supports, affecting the catalytic activity. To achieve the uniform dispersion of metal particles on CNTs, modification of the CNTs surface is required for producing anchoring sites.[6] There are two types of functionalization which are covalent and non-covalent modifications. Covalent modification introduces the functional groups such as hydroxyl (-OH), carboxyl (-COOH) and carbonyl (-C=O) by different oxidants such as nitric acid (HNO<sub>3</sub>),[11] sulfuric acid (H<sub>2</sub>SO<sub>4</sub>),[12] and hydrogen peroxide (H<sub>2</sub>O<sub>2</sub>) [13] or electrochemical methods.[14, 15] The functional groups are able to form covalent bond with another molecule.

Non-covalent modifications introduce the functional groups without affecting the electronic network of CNTs. For instance, benzyl mercaptain was introduced to CNTs and attracted to CNTs by  $\pi$ - $\pi$  interaction. The thiol groups of benzyl mercaptain act as functional groups for anchoring Pt nanoparticles due to the formation of Pt-S bonds as shown in Figure 2.3.[16]

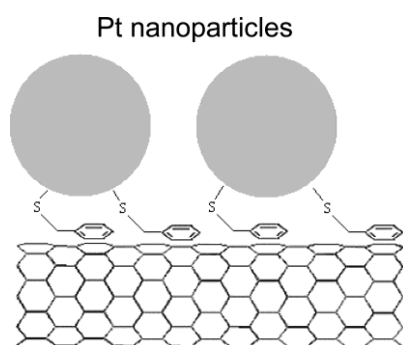


Figure 2.3 Non-covalent modification of CNTs.[16]

### **Applications of CNTs in fuel cell**

One of the applications of CNTs is to act as supporting material to metal nanoparticles in heterogeneous catalysis in fuel cells. Pt-based electrocatalysts are widely used as heterogeneous catalysts and active in fuel cells. However, Pt is a rare and precious metal. The massive commercialization is constrained by its limited availability. To reduce the cost of Pt-based catalysts, low-Pt-content electrocatalysts have to be developed.

CNTs are commonly applied to support Pt nanoparticles, which is able to increase the utilization of Pt. Besides, the catalytic activity is enhanced by increasing the surface area-to-volume ratio of Pt nanoparticles. Moreover, since CNTs anchor the Pt nanoparticles, the aggregation of Pt nanoparticles during the

oxidations of fuels is reduced resulting in enhanced stability.[17]

For instance, Pt supported on CNTs (Pt/CNTs) was synthesized under the reduction of potassium tetrachloroplatinate(II) ( $K_2PtCl_4$ ) with ethylene glycol (EG) as a reducing agent onto sonochemically treated CNTs. They were synthesized with different Pt loadings of 10 %, 20 % and 30 % and their Pt average sizes were  $2.78 \pm 0.60$  nm,  $3.57 \pm 0.78$  nm and  $4.46 \pm 1.33$  nm respectively as displayed in Figure 2.4. The electrochemical studies show that Pt/CNTs with lowest Pt loading (10 %) exhibit highest specific mass activity in 0.1 M  $H_2SO_4$  solution.[18]

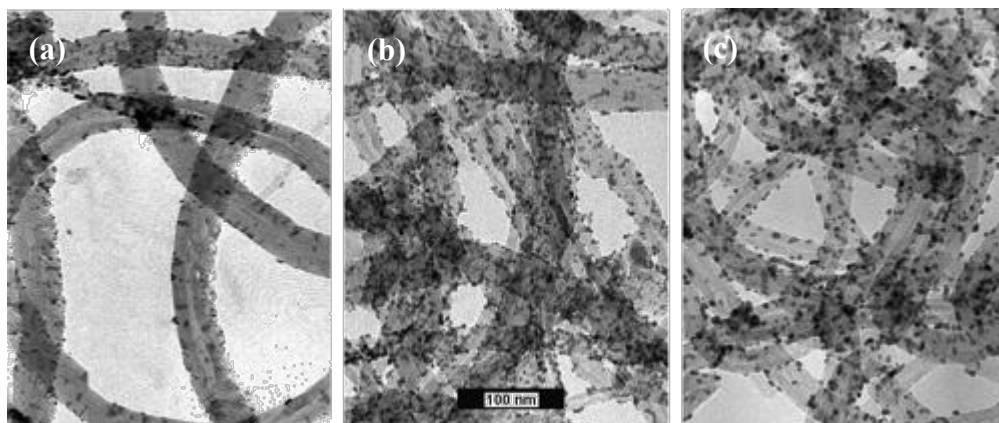


Figure 2.4 TEM images of Pt/CNTs with Pt loadings of (a) 10 %, (b) 20 % and (c) 30 %.[18]

### **Development of Au@Pt core-shell electrocatalysts for formic acid and methanol electrooxidations**

Pt is a commonly used metal catalyst for formic acid oxidation. However, the  $CO_{ads}$ , which is generated in the oxidation of formic acid, causes poisoning to Pt. To raise the catalyst performance with low dose of Pt, extensive research on alloying Pt with other metals is investigated. The enhanced activity and stability

are usually attributed to bifunctional effect and electronic effect. For instance, the alloy of FePt nanoparticles of Fe-to-Pt molar ratio in 1: 1 exhibited enhanced catalytic activity and stability towards the oxidation of formic acid.[19] Nevertheless, alloying is still affected by many factors and thus cannot be well-controlled. Also, the Pt utilization cannot be raised significantly because the use of Pt in alloy is still high.

Hence, another way to develop low-Pt-content electrocatalysts for improving the catalytic efficiency of Pt is investigated. The method is to decorate Pt nanoparticles onto metal core especially gold (Au) forming Au@Pt core-shell structure. It is mentioned that Au possesses its inherent catalytic activity, contributing to the enhanced activity of Au@Pt catalysts. Also, Au is oxidized at higher potential than other metals such as Fe and titanium (Ti). The chance of Au dissolution during the oxidation of fuels is greatly reduced.[20]

For example, submonolayer Pt-decorated Au nanoparticles on carbon black support with different Pt-to-Au ratios were developed. The electrochemical characterizations show that the catalyst with low Pt content exhibit enhanced catalytic activity towards the direct oxidation of formic acid when compared with commercial Pt/C catalyst.[21] The Au@Pt core-shell structure supported on carbon nanotubes (Au@Pt/CNTs) with controllable Pt coverage was also developed by ion adsorption followed by *in-situ* electrochemical reduction. Compared with commercial Pt/C catalyst, the Au@Pt/CNTs with low Pt coverage under 30 % exhibit enhanced catalytic activity towards the direct oxidation of formic acid.[22]

The Au@Pt core-shell catalyst was also applied in the oxidation of methanol. The Au@Pt supported on carbon with controllable Pt shell thickness was investigated. The electrochemical characterizations show that Au@Pt/C catalyst with the complete Pt shell exhibit higher catalytic activity than commercial Pt/C catalyst towards the oxidation of methanol. This confirms that Au@Pt core-shell greatly enhances the utilization of Pt.[23]

<b>Catalyst</b>	<b>Morphology</b>	<b>Pt-to-Au atomic ratio</b>	<b>Fuel</b>	<b>Synthetic method</b>	<b>Specific area activity</b>	<b>Specific mass activity</b>	<b>Ref.</b>
Pt-around-Au/C	Nanoparticle	-	0.5 M HCOOH + 0.5 M H <sub>2</sub> SO <sub>4</sub>	Electrostatic self-assembly.	~ 20 mAcm <sup>-2</sup>	-	[24]
PtAu/C	Nanoparticle	-	0.5 M HCOOH + 0.5 M H <sub>2</sub> SO <sub>4</sub>	Co-reduction	-	1180 mA mg <sub>metal</sub> <sup>-1</sup>	[25]
PtAu bimetallic heteronanostructures	Nanoparticle	0.63 : 1	0.5 M HCOOH + 0.5 M H <sub>2</sub> SO <sub>4</sub>	Thermal treatment	-	359 mA mg <sub>metal</sub> <sup>-1</sup>	[26]
Pt-Au/C Pt-Modified Au Nanoparticles	Nanoparticle	0.25 : 1	1.0 M HCOOH + 0.5 M H <sub>2</sub> SO <sub>4</sub>	Successive reduction	0.33 mAcm <sup>-2</sup>	105.91 mA mg <sub>metal</sub> <sup>-1</sup> 534.68 mA mg <sub>Pt</sub> <sup>-1</sup>	[27]
Pt-Au/C Pt-Modified Au Nanoparticles	Nanoparticle	0.75 : 1	1.0 M HCOOH + 0.5 M H <sub>2</sub> SO <sub>4</sub>	Successive reduction	0.21 mAcm <sup>-2</sup>	60.60 mA mg <sub>metal</sub> <sup>-1</sup> 143.96 mA mg <sub>Pt</sub> <sup>-1</sup>	[27]
Au@Pt	Nanobranh	39 : 4	0.5 M HCOOH + 0.5 M H <sub>2</sub> SO <sub>4</sub>	H <sub>2</sub> reduction	-	137.1 mA mg <sub>Pt</sub> <sup>-1</sup>	[28]
Au <sub>80</sub> Pt <sub>20</sub>	Nanoporous	80 : 20	0.5 M HCOOH + 0.5 M H <sub>2</sub> SO <sub>4</sub>	Dealloying	1.6 mAcm <sup>-2</sup>	-	[29]

Au <sub>40</sub> Pt <sub>60</sub>	Nanoporous	60 : 40	0.5 M HCOOH + 0.5 M H <sub>2</sub> SO <sub>4</sub>	Dealloying	-	560.8 mA mg <sub>Pt</sub> <sup>-1</sup>	[30]
Au <sub>40</sub> Pt <sub>60</sub>	Nanoporous	60 : 40	0.5 M HCOOH + 0.5 M H <sub>2</sub> SO <sub>4</sub>	Dealloying	-	320.6 mA mg <sub>Pt</sub> <sup>-1</sup>	[31]
Au@Pt	Honeycomb nanosphere	12.5 : 1	2.0 M HCOOH + 0.5 M H <sub>2</sub> SO <sub>4</sub>	Seed-mediated method	3.33 mA cm <sup>-2</sup>	234.9 mA mg <sub>Pt</sub> <sup>-1</sup>	[32]
Submonolayer Pt-decorated Au nanostructure	Nanoparticle	1 : 10	0.1 M MeOH + 0.5 M H <sub>2</sub> SO <sub>4</sub>	Successive reduction	~ 12 mA cm <sup>-2</sup>	-	[33]
Au <sub>core</sub> -Pt <sub>shell</sub>	Nanoparticle	-	2.0 M MeOH + 0.1 M H <sub>2</sub> SO <sub>4</sub>	UPD	~ 0.4 mA cm <sup>-2</sup>	-	[34]
Au@Pt core-shell	Nanosturctured Pt dendritic shell	1 : 1	0.5 M MeOH + 0.5 M H <sub>2</sub> SO <sub>4</sub>	Co-reduction	-	115 mA mg <sup>-1</sup>	[35]

Table 2.1

Comparison of the previously reported PtAu-based catalysts with respect to their catalytic activities for formic acid and methanol oxidations.

### **Aim of the project**

Following the previous success of our research group on developing low-dose Pt submonolayer on AuNPs/CNTs composite by using halides as bridging agent,[22] the objective of this project is to investigate the adsorption of different amount of different Pt halide solutions on AuNPs/CNTs composite and the later formation of submonolayer Pt layer, resulting in forming AuNP@Pt/CNTs composites with different loadings of Pt submonolayer. The change in the adsorption affinity of different Pt halide solutions is also studied, followed by investigating their electrocatalytic activities towards the electrooxidations of formic acid and methanol.

## 2.2 Results and Discussions

### 2.2.1 Synthesis of AuNPs and AuNP/CNTs

In the synthetic process of AuNPs, sodium borohydride ( $\text{NaBH}_4$ ) acts as a reducing agent to reduce chloroaurate ( $[\text{AuCl}_4]^{2-}$ ) ions to metallic gold (Au).[36] Sodium citrate acts as a stabilizing agent to prevent the aggregation of AuNPs.[25] The UV-Vis spectrum of AuNPs is shown in Figure 2.5. It displays an absorption peak at 504 nm due to collective dipole resonance or surface plasmon resonance (SPR) of the AuNPs formed.[33, 37]

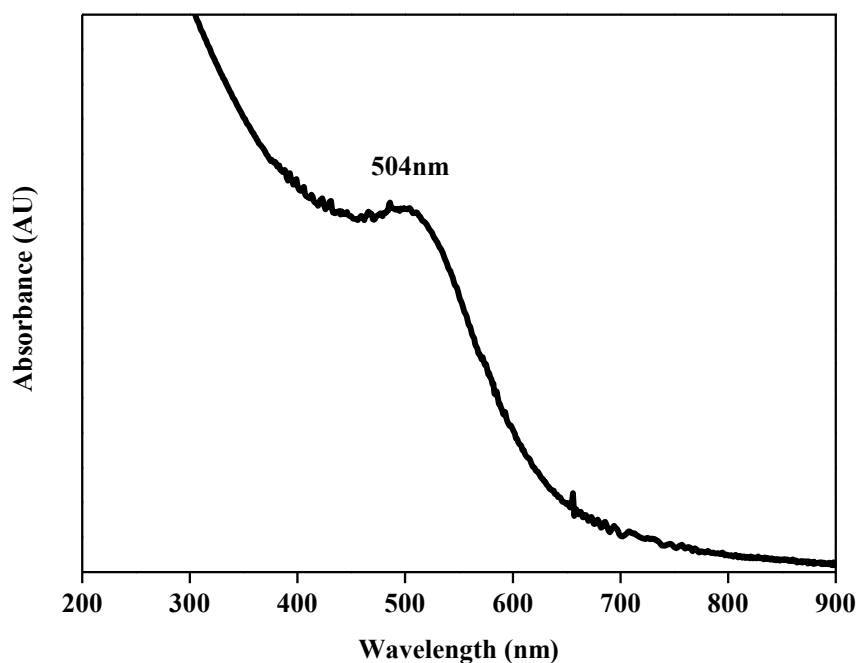


Figure 2.5 UV-Vis spectrum of AuNPs solution.

AuNPs/CNTs composite was synthesized by depositing as-synthesized AuNPs onto multi-walled carbon nanotubes (MWCNTs). Before depositing AuNPs, it is necessary to functionalize MWCNTs by oxidizing with conc.  $\text{HNO}_3$  to produce functional groups such as carboxyl groups and hydroxyl groups on the surface of MWCNTs. The functional groups were characterized by infrared (IR) spectroscopy.[38] However, the IR modes were too weak to be observed. Raman spectroscopy was also conducted. The ratio between D-band from disorder in CNTs sidewall structure and G-band from highly ordered CNTs sidewalls ( $I_D:I_G$ ) was determined. The  $I_D:I_G$  ratio (0.86) is not high, suggesting that the structure is not changed significantly and the main structural feature of MWCNTs was kept.[38] The decoration of AuNPs onto MWCNTs was facilitated because the functional groups can act as anchor sites for metal particles.[39, 40] The functional groups can also improve the dispersion of MWCNTs in water.[11, 41] Figure 2.6 displays the dispersion of raw MWCNTs and acid-treated MWCNTs in water. After 4 h, the raw MWCNTs aggregated and acid-treated MWCNTs still remain dispersed. It is believed that the introduction of carboxyl groups and hydroxyl groups increases the hydrophilicity of MWCNTs, thus improving its dispersion. The pH value of the dispersion of acid-treated MWCNTs (5.78) is lower than that of raw CNTs (6.48), suggesting that the carboxyl groups may exist on the surface of acid-treated MWCNTs.

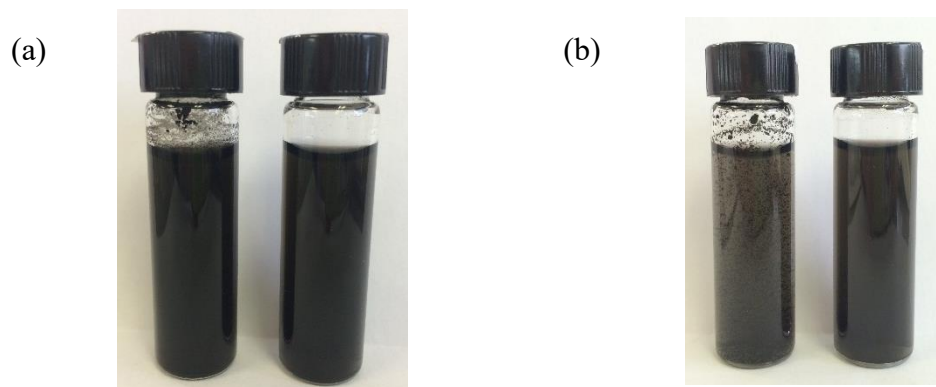


Figure 2.6 Photographs of (a) freshly prepared MWCNTs and (b) after 4 h dispersion in water: raw MWCNTs (left) and acid-treated MWCNTs (right).

After functionalizing MWCNTs, AuNPs were deposited onto MWCNTs. Transmission electron microscopy (TEM) was conducted to investigate the morphology of AuNP/CNTs composite and confirm the deposition of AuNPs onto MWCNTs. As displayed in Figure 2.7 (a) and (b), the AuNPs were synthesized in spherical morphology with the average size of  $5.4 \pm 2.0$  nm and successfully deposited on the MWCNTs. The non-uniform AuNPs distribution on MWCNTs is due to the surface modification. In order to retain the main structural features of MWCNTs, mild acid treatment was conducted. Hence, the AuNPs only anchored on defect sites. The structure of AuNP/CNTs composite was also analyzed by selective area electron diffraction (SAED) and high resolution transmission electron microscopy (HR-TEM) as shown in Figure 2.7 (c) and (d) respectively. Figure 2.7 (c) shows that the diffraction rings obtained from (002) and (004) crystal planes which are compatible to the d-spacing of graphite. It is suggested that the CNTs are adopting hexagonal structure with a P63/mmc(194) space group (JCPDS Card no. 00-001-0646). Other diffraction rings obtained from (111), (200), (220) and (311) crystal planes are compatible to the d-spacing of gold (Au). It is suggested that the AuNPs are adopting a face-centered cubic (fcc) structure with a Fm-3m(225) space group (JCPDS Card no.01-071-4615). From Figure 2.7 (d), the crystal plane with d-spacing of 2.95 Å is found which corresponds to the (111) crystal plane of gold.

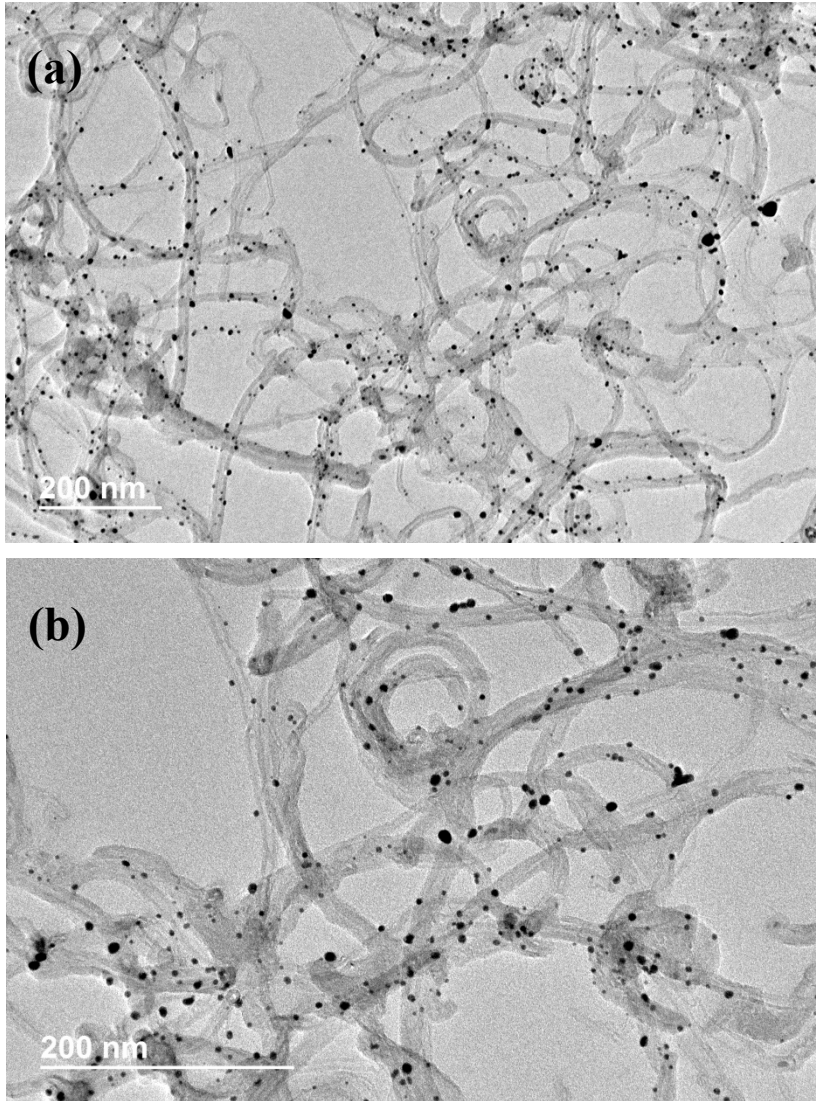


Figure 2.7 (a) LM-TEM and (b) HM-TEM images of AuNP/CNTs composite.

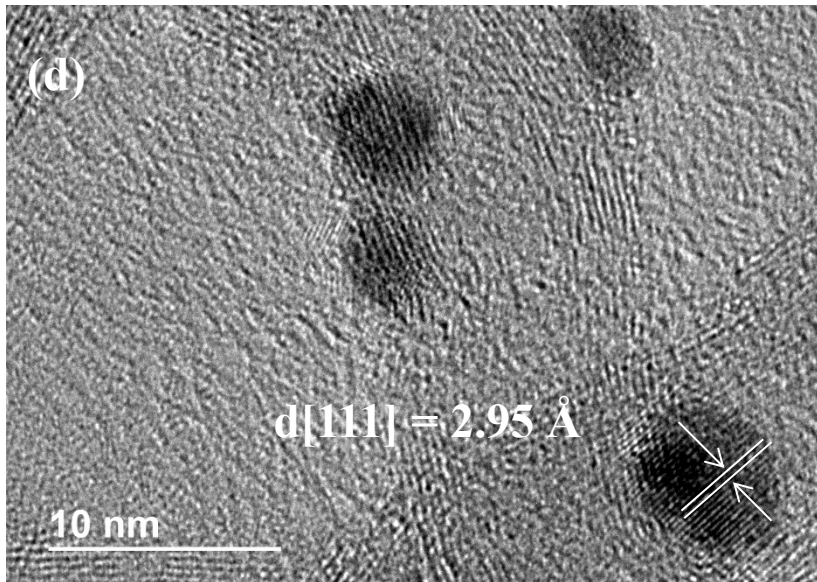
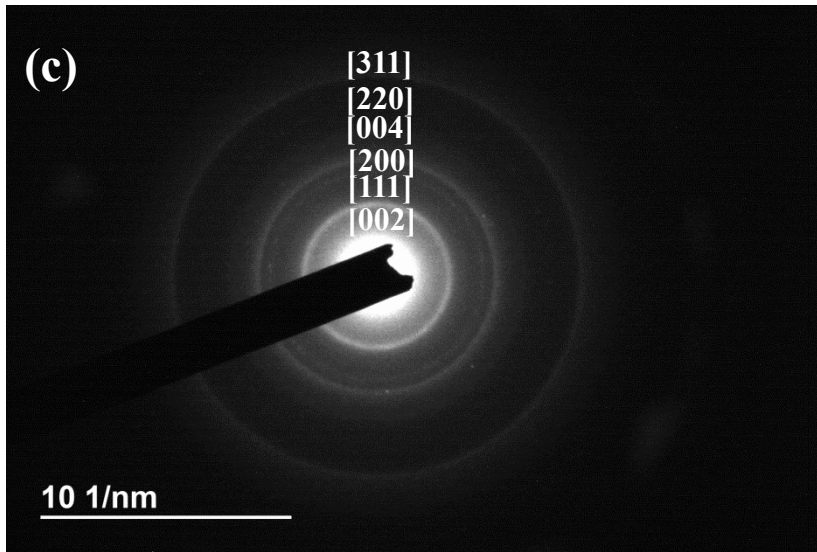


Figure 2.7 (c) SAED and (d) HR-TEM images of AuNP/CNTs composite.

To further study the crystalline structure, the AuNP/CNTs composite was characterized by XRD analysis. The XRD pattern of AuNP/CNTs composite is shown in Figure 2.8. AuNP/CNTs composite exhibits two sets of diffraction peaks. One diffraction peak at  $2\theta$  value of  $26.4^\circ$  is characteristic of the hexagonal structure with a P63/mmc(194) space group, corresponding the (002) crystal plane of graphite (JCPDS Card no. 00-001-0646).[42] The other diffraction peaks at  $2\theta$  values of  $38.2^\circ$ ,  $44.2^\circ$ ,  $64.6^\circ$  and  $77.8^\circ$  are characteristic of a fcc structure with a Fm-3m(225) space group, corresponding to the (111), (200), (220) and (311) crystal planes of gold respectively (JCPDS Card no. 01-071-4615).[42] This further confirms the fcc crystalline structure of AuNPs as suggested by TEM analysis.

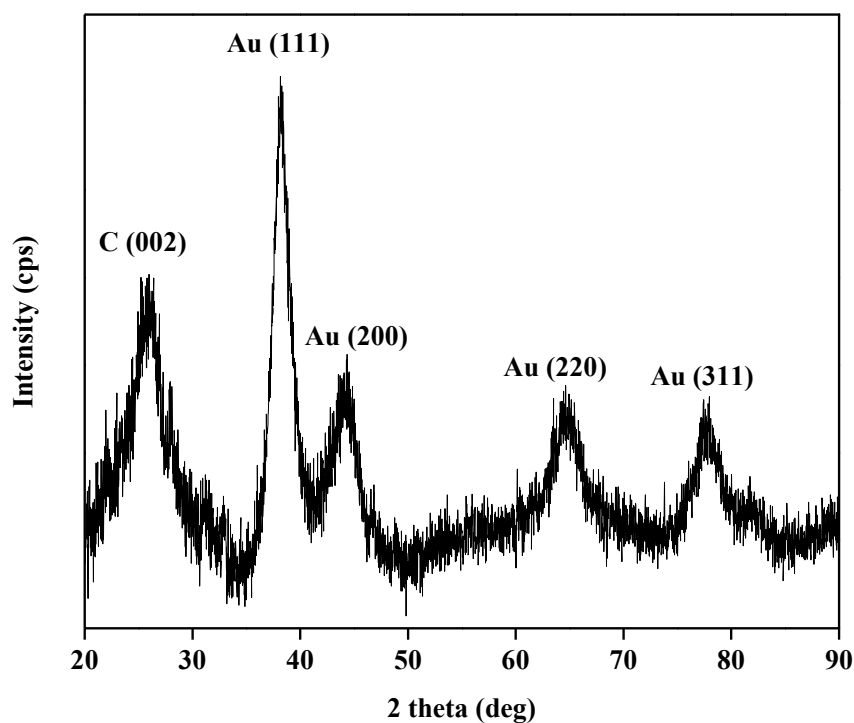


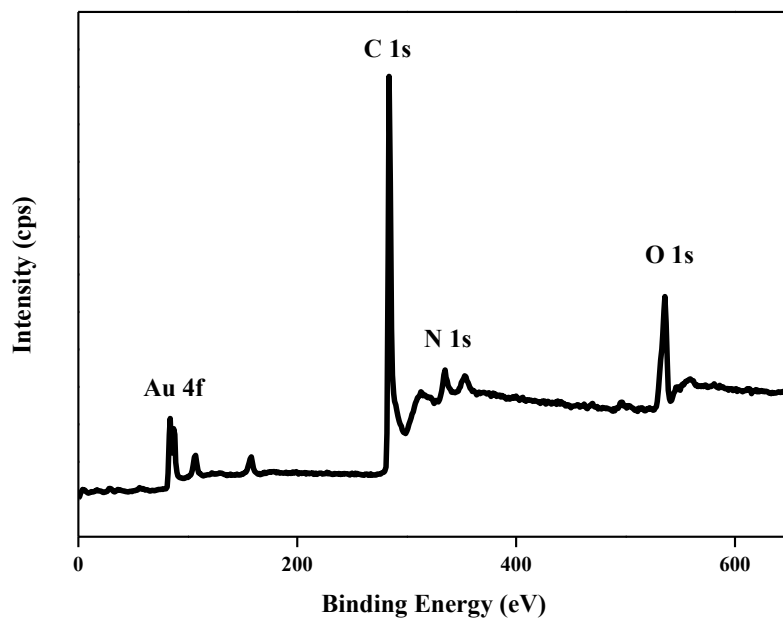
Figure 2.8 XRD pattern of AuNP/CNTs composite.

X-ray photoelectron spectroscopy (XPS) was also conducted to further confirm the existence of AuNPs on the catalyst surface and explore the metallic state of AuNPs. Figure 2.9 (a) illustrates the predominant XPS peaks at 84 eV, 284 eV and 536 eV coming from Au, C and O elements in the spectrum respectively. The further deconvolution of Au 4f region is shown in Figure 2.9 (b). The more intense doublets at 87.7 eV and 84.1 eV correspond to the metallic Au(0) 4f<sub>5/2</sub> and 4f<sub>7/2</sub> while the less intense doublets at 88.9 eV and 85.3 eV correspond to the oxidized Au(III) 4f<sub>5/2</sub> and 4f<sub>7/2</sub> respectively.[43] As summarized in Table 2.2, the amount of Au species was calculated from the relative intensities of these two doublets. The XPS results suggest that the predominant surface species on the catalysts is metallic Au(0). This further confirms the successful reduction of [AuCl<sub>4</sub>]<sup>-</sup> ions to metallic AuNPs.

Catalysts	Species	Binding	Relative	Binding	Relative
		energy (eV) (Au 4f <sub>5/2</sub> )	intensity (%)	energy (eV) (Au 4f <sub>7/2</sub> )	intensity (%)
AuNP/CNTs	Au(0)	87.7	80	84.1	87
	Au(III)	88.9	20	85.3	13

Table 2.2 Binding energies and relative intensities of different gold species of AuNP/CNTs composite.

(a)



(b)

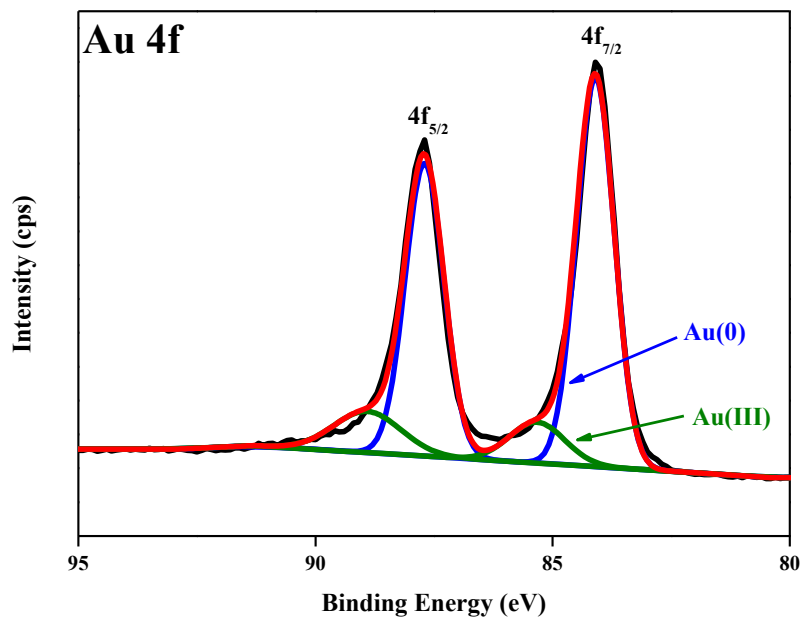


Figure 2.9 (a) Overall XPS spectrum and (b) Au 4f region of AuNP/CNTs composite.

The Au loading on MWCNTs was investigated by inductively coupled plasma optical emission spectrometry (ICP-OES). It is found that the Au loading is 16.2 %, which is slightly lower than the theoretical Au loading of 17.5 %.

## 2.2.2 Exploration on different Pt halide solutions of different concentrations towards formic acid and methanol electrooxidations

### Cyclic voltammetry of AuNP/CNTs composite in N<sub>2</sub>-purged sulfuric acid

Figure 2.10 displays the cyclic voltammogram (CV) of AuNP/CNTs composite on the GCE in N<sub>2</sub>-purged 0.1 M H<sub>2</sub>SO<sub>4</sub> solution in the potential region from -0.24 V to 1.5 V with a scan rate of 50 mVs<sup>-1</sup>. The broad anodic peak at higher than 1.1 V is ascribed to the oxidation of gold while the cathodic peak at around 0.8 V to 0.9 V is ascribed to the reduction of gold oxide.[44]

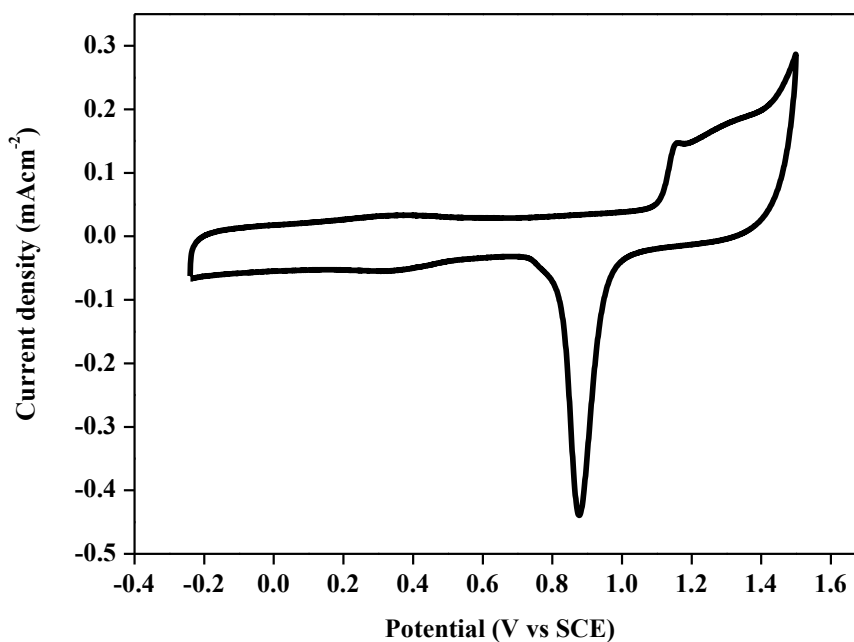


Figure 2.10 CV of AuNP/CNTs composite in N<sub>2</sub>-purged 0.1 M H<sub>2</sub>SO<sub>4</sub> solution. Scan rate, 50 mVs<sup>-1</sup>.

## **Cyclic voltammetry of AuNP@Pt/CNTs composites in N<sub>2</sub>-purged sulfuric acid**

After conducting CV of AuNP/CNTs composite, the GCE coated with AuNP/CNTs composite was immersed into 5.12 mM K<sub>2</sub>PtCl<sub>4</sub> solution for 10 min to prepare AuNP@Pt/CNTs composite. The immersion process allows the adsorption of Pt halide ions on AuNPs surface, followed by *in-situ* electrochemical reduction. Gold is used as catalyst support due to its high spatial and electrochemical stability to synthesize AuNP@Pt/CNTs composites. This can maximize the Pt active sites and minimize the use of Pt.

Figure 2.11 shows the CVs of AuNP/CNTs and AuNP@Pt/CNTs composites in N<sub>2</sub>-purged 0.1 M H<sub>2</sub>SO<sub>4</sub> solution in the potential region from -0.24 V to 1.5 V with a scan rate of 50 mVs<sup>-1</sup>. The CV of AuNP@Pt/CNTs shows weak typical characteristics of hydrogen adsorption and desorption peaks. Also, the cathodic peak associated with the reduction of gold oxide decreases due to the adsorption of Pt on AuNPs surface. Another cathodic peak at around 0.3 V appears indicating the reduction of Pt oxide.[45] High angle annular dark-field scanning transmission electron microscope-energy dispersive spectroscopy (HAADF-STEM-EDS) mapping was conducted. [36, 46, 47] However, Pt was not shown due to the low Pt content.

To determine electrochemically active surface area (ECSA) of catalysts, there are many methods including oxygen adsorption from solution, hydrogen adsorption from solution (H<sub>UPD</sub>), adsorption of probe molecules from solution such as CO stripping and underpotential deposition of copper (Cu<sub>UPD</sub>) with different advantages and limitations.

The oxygen adsorption from solution is used with metals showing well-developed regions for oxide monolayer formation and reduction. This method can be used with metals showing no  $H_{\text{ads/des}}$  peaks such as Au and absorbing hydrogen such as Pd.[48] However, the overlapping of oxygen and hydrogen adsorption may occur.

$H_{\text{UPD}}$  is used with the transition metals showing hydrogen adsorption in potential regions prior to massive  $H_2$  evolution. Nevertheless, this method cannot be used with metals showing no  $H_{\text{ads/des}}$  peaks such as Au and absorbing hydrogen such as Pd. Also, the H atoms deposited on metals diffuse to the surface of catalyst support which is hydrogen spillover.[48] The ECSA of metals may be overstated and hence, the specific area activity may be underestimated.

For adsorption of probe molecules from solution, a probe molecule such as CO and  $I_2$  is adsorbed on the solid in solution and the extent of adsorption is determined analytically from the depletion in the solution. The absorbing species may produce micelles in solution and at the surface.[48]

$Cu_{\text{UPD}}$  is used when better separation between H and O adsorption cannot be achieved such as Ru. This method is better than  $H_{\text{UPD}}$  because of no spillover effects.[48] However, UPD may be incomplete on very small particles. The ECSA may be underestimated and specific area activity may be overestimated.[49] UPD may also have undesired effect due to retention of some UPD atoms on the surface.[48]

In this study, the catalyst with clean metal surface is important for catalysis. Both methods including adsorption of probe molecules and Cu<sub>UPD</sub> may cause the retention of some atoms on the catalyst surface. Also, Au has no H<sub>ads/des</sub> peaks. Hence, the method of oxygen adsorption from solution was adopted to determine the ECSA of catalysts in this chapter.

The areas under the cathodic peaks for the reduction of gold oxide before immersion and Pt oxide after immersion are used to determine the electrochemically active surface area (ECSA) of Au and Pt, and thus to estimate Pt coverage. The ECSA of Au and Pt can be calculated by the following equations.

$$ECSA_{Au} = Q_{Au}/400 \mu Ccm^{-2} \quad \text{Eq. 2.1}$$

$$ECSA_{Pt} = Q_{Pt}/420 \mu Ccm^{-2} \quad \text{Eq. 2.2}$$

The Pt coverage  $\Theta_{Pt}$  was calculated by the following equation:

$$\Theta_{Pt} = ECSA_{Pt}/ECSA_{Au} = (Q_{Pt}/420 \mu Ccm^{-2})/(Q_{Au}/400 \mu Ccm^{-2}) \quad \text{Eq. 2.3}$$

where  $Q_{Au}$  and  $Q_{Pt}$  are the surface oxide reduction charges of plain Au and Pt respectively.[50, 51]

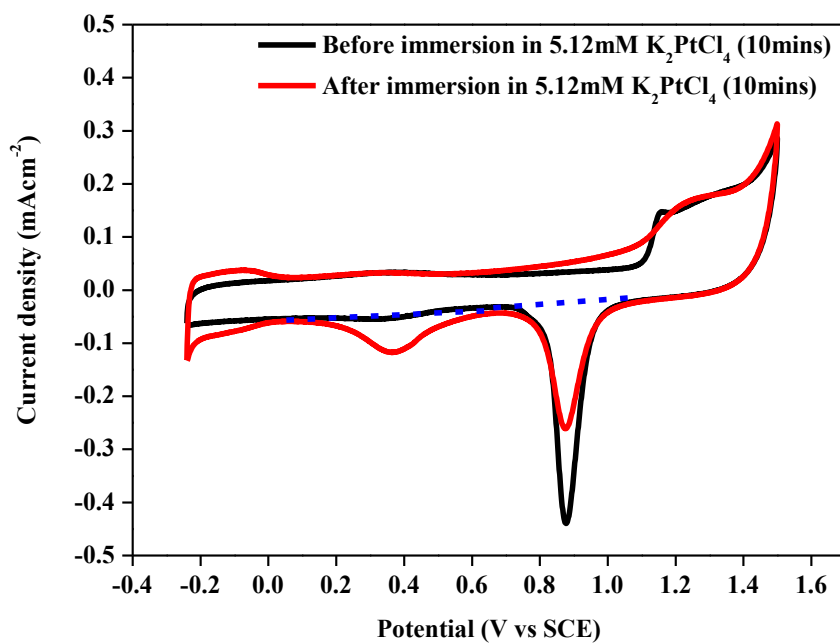


Figure 2.11 CVs of AuNP/CNTs and AuNP@Pt/CNTs composites in N<sub>2</sub>-purged 0.1 M H<sub>2</sub>SO<sub>4</sub> solution. Scan rate, 50 mVs<sup>-1</sup>.

To confirm the adsorption of Pt halide ions occurs onto AuNPs surface only, CV was performed by immersing the GCE coated with MWCNTs in 5.12 mM  $\text{K}_2\text{PtCl}_4$  + 0.1 M  $\text{H}_2\text{SO}_4$  solution, followed by *in-situ* electrochemical reduction. As displayed in Figure 2.12, no obvious change is observed for the CVs of MWCNTs before immersion and after immersion in 5.12 mM  $\text{K}_2\text{PtCl}_4$  solution. It is confirmed that Pt halides ions do not directly adsorb on MWCNTs surface.

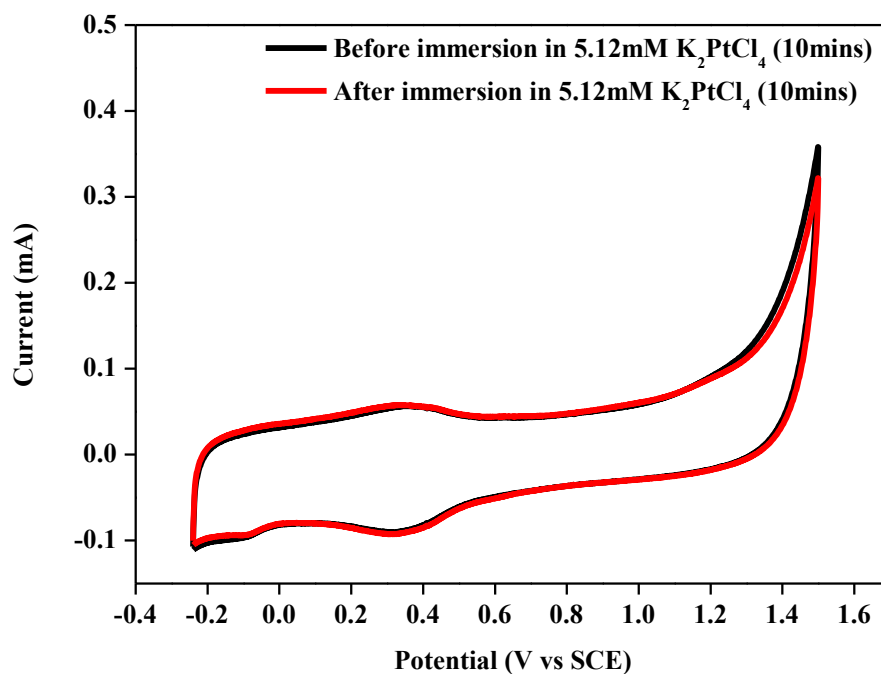


Figure 2.12 CVs of MWCNTs before and after immersion in 5.12 mM  $\text{K}_2\text{PtCl}_4$  + 0.1 M  $\text{H}_2\text{SO}_4$  solution. Scan rate,  $50 \text{ mVs}^{-1}$ .

To confirm the existence of Pt on AuNP/CNTs composite, the CV of Pt on activated charcoal (Pt/C) in N<sub>2</sub>-purged 0.1 M H<sub>2</sub>SO<sub>4</sub> solution was conducted. In Figure 2.13, the CV of Pt/C shows the cathodic peak at around 0.3 V suggesting the reduction of Pt oxide.

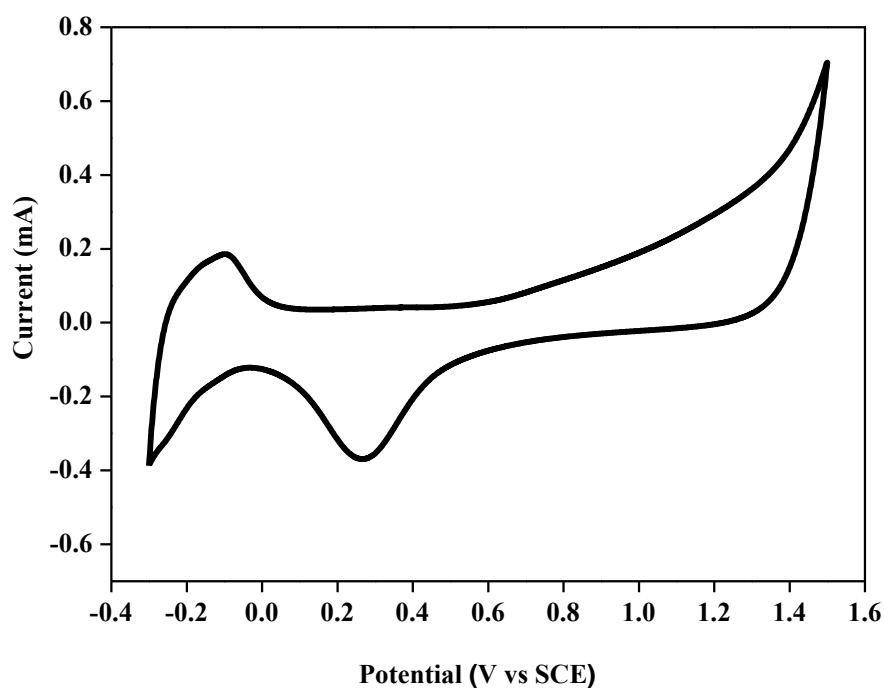


Figure 2.13 CV of Pt/C in N<sub>2</sub>-purged 0.1 M H<sub>2</sub>SO<sub>4</sub> solution. Scan rate, 50 mVs<sup>-1</sup>.

### Pt coverage

The AuNP@Pt/CNTs composites were prepared by immersing the GCE coated with AuNP/CNTs composite into Pt halide solutions ( $K_2PtCl_4$ ,  $K_2PtCl_6$ ,  $Na_2PtCl_4$ ,  $Na_2PtCl_6 \cdot 6H_2O$ ,  $K_2PtBr_4$ ,  $K_2PtBr_6$ ,  $Pt(NH_3)_4(NO_3)_2$ ) with the concentrations ranging from 0.02 mM to 5.12 mM for 10 min. The immersion process allows the adsorption of Pt halide ions on AuNPs surface, followed by *in-situ* electrochemical reduction. Table 2.3 presents the Pt coverage of AuNP@Pt/CNTs composites prepared by immersion in different Pt halide solutions of different concentrations. Figure 2.14 displays a linear relationship between the concentrations of Pt halide solutions and Pt coverage.

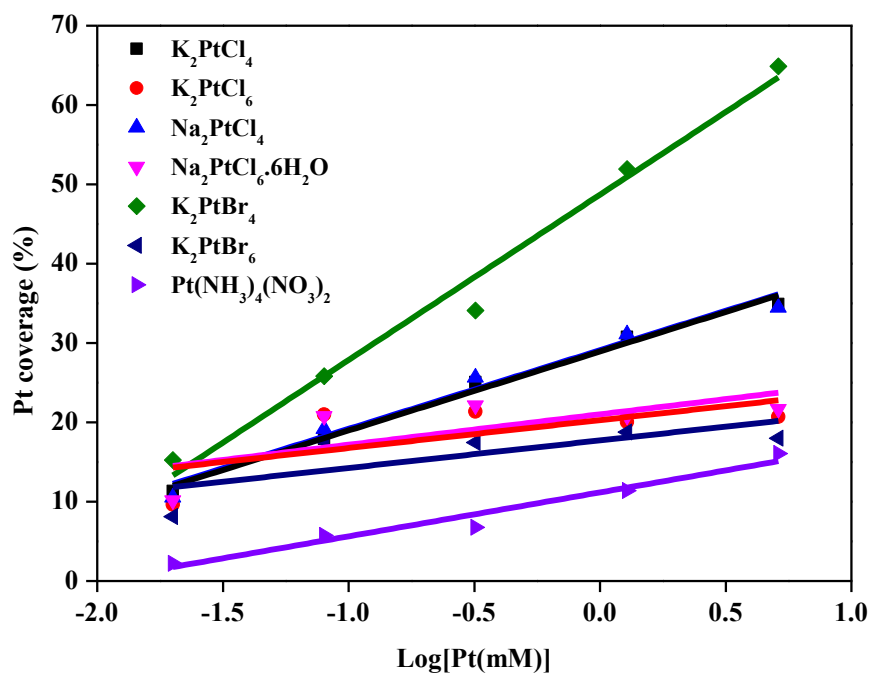


Figure 2.14 The relationship between Pt halide solutions of different concentrations and Pt coverage.

Concentration of Pt halides (mM)	Pt coverage (%)						
	K <sub>2</sub> PtCl <sub>4</sub>	K <sub>2</sub> PtCl <sub>6</sub>	Na <sub>2</sub> PtCl <sub>4</sub>	Na <sub>2</sub> PtCl <sub>6</sub> ·6H <sub>2</sub> O	K <sub>2</sub> PtBr <sub>4</sub>	K <sub>2</sub> PtBr <sub>6</sub>	Pt(NH <sub>3</sub> ) <sub>4</sub> (NO <sub>3</sub> ) <sub>2</sub>
0.02	9.7	11.3	10.5	10.2	15.2	8.1	2.2
0.08	17.9	21.0	19.2	20.8	25.8	17.6	5.7
0.32	25.1	21.4	25.7	22.1	34.1	17.5	6.8
1.28	30.8	20.1	31.1	20.8	51.9	18.8	11.4
5.12	34.9	20.7	34.5	21.7	64.9	18.0	16.1

Table 2.3 Summary of the Pt coverage of AuNP@Pt/CNTs composites prepared by immersion in different Pt halide solutions of concentrations from 0.02 mM to 5.12 mM.

There is a significant difference in the Pt coverages obtained by  $K_2PtCl_4$  and  $K_2PtCl_6$  solutions at the same concentrations. It is found that increasing the concentration of  $K_2PtCl_4$  solution from 0.02 mM to 5.12 mM could increase the Pt coverage from 9.8 % to 34.9 %. When the concentration of  $K_2PtCl_4$  solution increases, more Pt halide ions adsorb on AuNPs, thus increasing the Pt coverage.

The Pt coverage increases from 11.3 % to 21.0 % with the increase of the concentration of  $K_2PtCl_6$  solution from 0.02 mM to 0.08 mM. However, the Pt coverage could not further increase with further increasing to 5.12 mM. Similar Pt coverages around 20 % were achieved and reached plateau.

The Pt coverage obtained from  $K_2PtCl_6$  solution differs from  $K_2PtCl_4$  solution at the same concentrations. This may be due to the different coordination geometries of  $[PtCl_4]^{2-}$  (square planar) and  $[PtCl_6]^{2-}$  (octahedral) ions, resulting in different ion adsorption mode. According to the *in-situ* STM images of  $[PtCl_4]^{2-}$  ions adsorbed on Au(111) and Au(100) studied by Nagahara et al.[52] and Waibel et al. respectively,[53]  $[PtCl_4]^{2-}$  ions adsorb through all four  $Cl^-$  ions, stabilizing  $[PtCl_4]^{2-}$  ions on Au surface. As revealed by the model for the surface structure of  $[PtCl_6]^{2-}$  ions on Au(111) surface proposed by Uosaki et al.,[54]  $[PtCl_6]^{2-}$  ions adsorbed through one to two  $Cl^-$  ions. It is deduced that  $[PtCl_6]^{2-}$  ions are weakly adsorbed on Au surface when compared with  $[PtCl_4]^{2-}$  ions. Thus,  $[PtCl_6]^{2-}$  ions are easily removed from Au surface during washing.[52, 55] As a consequence, fewer  $[PtCl_6]^{2-}$  ions adsorb on AuNPs when compared with  $[PtCl_4]^{2-}$  ions at the same concentrations, resulting in lower Pt coverage.

Apart from investigating different coordination geometries, the effect of cations on Pt coverage was explored.  $\text{Na}_2\text{PtCl}_4$  and  $\text{Na}_2\text{PtCl}_6 \cdot 6\text{H}_2\text{O}$  solutions were compared with  $\text{K}_2\text{PtCl}_4$  and  $\text{K}_2\text{PtCl}_6$  solutions respectively. It is observed that similar Pt coverages were achieved by immersing the GCE coated with AuNP/CNTs composite in  $[\text{PtCl}_4]^{2-}$  ( $\text{K}_2\text{PtCl}_4$  and  $\text{Na}_2\text{PtCl}_4$ ) and  $[\text{PtCl}_6]^{2-}$  ( $\text{K}_2\text{PtCl}_6$  and  $\text{Na}_2\text{PtCl}_6 \cdot 6\text{H}_2\text{O}$ ) ion solutions respectively at the same concentrations. This suggests that the adsorption mode of Pt halide ions on AuNPs is independent of the cations and solely dependent of Pt halide ions.

After studying the effect of cations in Pt halide solutions on Pt coverages, the effect of halide in anions of Pt halide solutions was explored.  $\text{K}_2\text{PtBr}_4$  and  $\text{K}_2\text{PtBr}_6$  solutions were compared with  $\text{K}_2\text{PtCl}_4$  and  $\text{K}_2\text{PtCl}_6$  solutions respectively.

Compared with  $\text{K}_2\text{PtCl}_4$  solution, both Pt coverages can be raised by increasing the concentration of  $[\text{PtX}_4]^{2-}$  ( $\text{X} = \text{Cl}$  or  $\text{Br}$ ) solutions from 0.02 mM to 5.12 mM. However, a significant difference in Pt coverage is found between  $\text{K}_2\text{PtCl}_4$  and  $\text{K}_2\text{PtBr}_4$  solutions. At the same concentrations, the Pt coverage obtained by  $\text{K}_2\text{PtBr}_4$  solution is higher than  $\text{K}_2\text{PtCl}_4$  solution. Also, the deviation of Pt coverages between  $\text{K}_2\text{PtCl}_4$  and  $\text{K}_2\text{PtBr}_4$  solutions increases when the concentration of the solutions increases.

In accordance with *in-situ* STM image  $[\text{PtBr}_4]^{2-}$  ions adsorbed on Au(111) studied by Nagahara et al.,[52]  $[\text{PtBr}_4]^{2-}$  adsorb through all four  $\text{Br}^-$  ions. It is proposed that both  $[\text{PtCl}_4]^{2-}$  and  $[\text{PtBr}_4]^{2-}$  ions have same ion adsorption mode. Hence, the significant difference in Pt coverage between  $\text{K}_2\text{PtCl}_4$  and  $\text{K}_2\text{PtBr}_4$  solutions

could be attributed to stronger affinity of Br than Cl.[52, 56, 57] Hence, more  $[\text{PtBr}_4]^{2-}$  ions adsorb on AuNPs surface by bromide adsorption than chloride adsorption and fewer  $[\text{PtBr}_4]^{2-}$  ions are washed away, resulting in higher Pt coverage at the same concentrations of Pt halide solutions.

Compared with  $\text{K}_2\text{PtCl}_6$  solution, both Pt coverages can only increase by increasing the concentration of  $[\text{PtX}_6]^{2-}$  ( $\text{X} = \text{Cl}$  or  $\text{Br}$ ) solutions from 0.02 mM to 0.08 mM. Also, further increasing the concentration of  $[\text{PtX}_6]^{2-}$  ( $\text{X} = \text{Cl}$  or  $\text{Br}$ ) solutions from 0.08 mM to 5.12 mM could not further increase the Pt coverage. A slight difference is found between  $\text{K}_2\text{PtCl}_6$  and  $\text{K}_2\text{PtBr}_6$  solutions. The Pt coverage obtained by  $\text{K}_2\text{PtBr}_6$  solution is slightly lower than  $\text{K}_2\text{PtCl}_6$  solution at the same concentrations. For the octahedral structure of  $[\text{PtX}_6]^{2-}$  ion, the Br group, due to its larger size than Cl, may slightly hinder the ion adsorption process by steric effect.

To further confirm the importance of halide during the ion adsorption onto AuNPs surface,  $\text{Pt}(\text{NH}_3)_4(\text{NO}_3)_2$  was used. It is found that the Pt coverages obtained by  $\text{Pt}(\text{NH}_3)_4(\text{NO}_3)_2$  solution are lower than those obtained by other Pt halide solutions at the same concentrations. Compared with  $[\text{PtX}_4]^{2-}$  ions ( $\text{X} = \text{Cl}$  or  $\text{Br}$ ),  $[\text{Pt}(\text{NH}_3)_4]^{2+}$  ion is also square planar in coordination geometry structure. This probably results in similar ion adsorption mode, which will be further confirmed in progress. Also, it is believed that the positively charged  $[\text{Pt}(\text{NH}_3)_4]^{2+}$  ion may hinder the ion adsorption process but could control the relatively low Pt coverage of AuNP@Pt/CNTs composite.

The electrochemical results suggests that by simply changing different Pt halide

solutions with different concentrations, a wide range of Pt coverage from 2.2 % to 64.9 % on the surface of AuNP/CNTs composite can be easily controlled.

### **Electrooxidation of formic acid**

The electrocatalysis of formic acid (HCOOH) was performed by conducting the cyclic voltammetry (CV) of AuNP@Pt/CNTs composites on GCE in 0.025 M HCOOH + 0.1 M H<sub>2</sub>SO<sub>4</sub> solution in the potential region from -0.2 V to 0.9 V with a scan rate of 50 mVs<sup>-1</sup>. It is known that CNTs and Au are not active towards the oxidation of formic acid.[21, 25, 26, 36] The specific area activity towards the oxidation of formic acid is calculated by normalizing current to the ECSA of Pt of AuNP@Pt/CNTs composites. The relationship between Pt coverage and specific area activity towards the oxidation of formic acid is presented in Table 2.4. It is observed that the specific area activity towards the oxidation of formic acid reaches threshold value when the concentration of Pt halide solution is 0.08 mM. For Pt(NH<sub>3</sub>)<sub>4</sub>(NO<sub>3</sub>)<sub>2</sub> solution, the specific area activity towards the oxidation of formic acid reaches threshold value when the concentration of Pt halide solution is 1.28 mM.

Concentration of Pt halides (mM)	K <sub>2</sub> PtCl <sub>4</sub>		K <sub>2</sub> PtCl <sub>6</sub>		Na <sub>2</sub> PtCl <sub>4</sub>		Na <sub>2</sub> PtCl <sub>6</sub> ·6H <sub>2</sub> O		K <sub>2</sub> PtBr <sub>4</sub>		K <sub>2</sub> PtBr <sub>6</sub>		Pt(NH <sub>3</sub> ) <sub>4</sub> (NO <sub>3</sub> ) <sub>2</sub>	
	Pt	Specific	Pt	Specific	Pt	Specific	Pt	Specific	Pt	Specific	Pt	Specific	Pt	Specific
	coverage	area	coverage	area	coverage	area	coverage	area	coverage	area	coverage	area	coverage	area
	(%)	activity (mAcm <sup>-2</sup> )	(%)	activity (mAcm <sup>-2</sup> )	(%)	activity (mAcm <sup>-2</sup> )	(%)	activity (mAcm <sup>-2</sup> )	(%)	activity (mAcm <sup>-2</sup> )	(%)	activity (mAcm <sup>-2</sup> )	(%)	activity (mAcm <sup>-2</sup> )
0.02	9.7	1.39	11.3	1.30	10.5	1.40	10.2	1.47	15.2	0.93	8.1	0.78	2.2	0.18
0.08	17.4	1.52	21.0	1.42	19.2	1.44	20.8	1.60	25.8	1.04	17.6	1.08	5.7	0.93
0.32	25.1	1.19	21.4	1.55	25.7	1.15	22.1	1.47	34.1	0.75	17.5	1.18	6.8	1.20
1.28	30.8	0.89	20.1	1.42	31.1	0.84	20.8	1.38	51.9	0.48	18.8	1.23	11.4	1.79
5.12	34.9	0.84	20.7	1.31	34.5	0.80	21.7	1.61	64.9	0.37	18.0	1.06	16.1	1.51

Table 2.4 Summary of Pt coverage by different Pt halide solutions of concentrations from 0.02 mM to 5.12 mM and the corresponding specific area activity towards the oxidation of formic acid.

Figure 2.15 shows the CVs of AuNP@Pt/CNTs composite prepared by  $K_2PtCl_4$  solution towards the oxidation of formic acid. It is known that the oxidation of formic acid follows a dual-path mechanism.[21, 58] In positive-going scan, there is an oxidative peak at around 0.2 V to 0.3 V as ascribed to the dehydrogenation which is the direct oxidation of formic acid to form  $CO_2$ .

The specific area activity towards the direct oxidation of formic acid increases from  $1.39 \text{ mAcm}^{-2}$  to  $1.52 \text{ mAcm}^{-2}$  when the Pt coverage increases from 9.7 % to 17.9 %. The increase in Pt coverage indicates that more Pt deposit on AuNPs and more Pt sites are available for the oxidation of formic acid. When Pt coverage increases from 17.9 % to 34.7 %, a decreasing specific area activity from  $1.52 \text{ mAcm}^{-2}$  to  $0.84 \text{ mAcm}^{-2}$  towards the direct oxidation of formic acid is achieved. The trend of decreasing specific area activity towards the direct oxidation of formic acid under increasing Pt coverage is due to ensemble effect.[21] Dehydrogenation does not require continuous neighboring Pt sites while dehydration, which is indirect oxidation of formic acid, requires at least two adjacent Pt sites. Higher Pt coverage indicates higher availability of adjacent Pt sites for dehydration, reducing the specific area activity of dehydrogenation.[21, 24] It is believed that the oxidation of formic acid on AuNP@Pt/CNTs composite prepared from  $K_2PtCl_4$  solution with the concentrations from 0.02 mM to 5.12 mM mainly follows the dehydrogenation towards the oxidation of formic acid.

In backward scan, there is an oxidative peak at around 0.4 V indicating the oxidation of  $CO_{ads}$  produced in dehydration. It can be seen that the specific area activity of peak in backward scan is lower than that in forward scan, indicating that the amount of  $CO_{ads}$  is not significant.[21, 59]

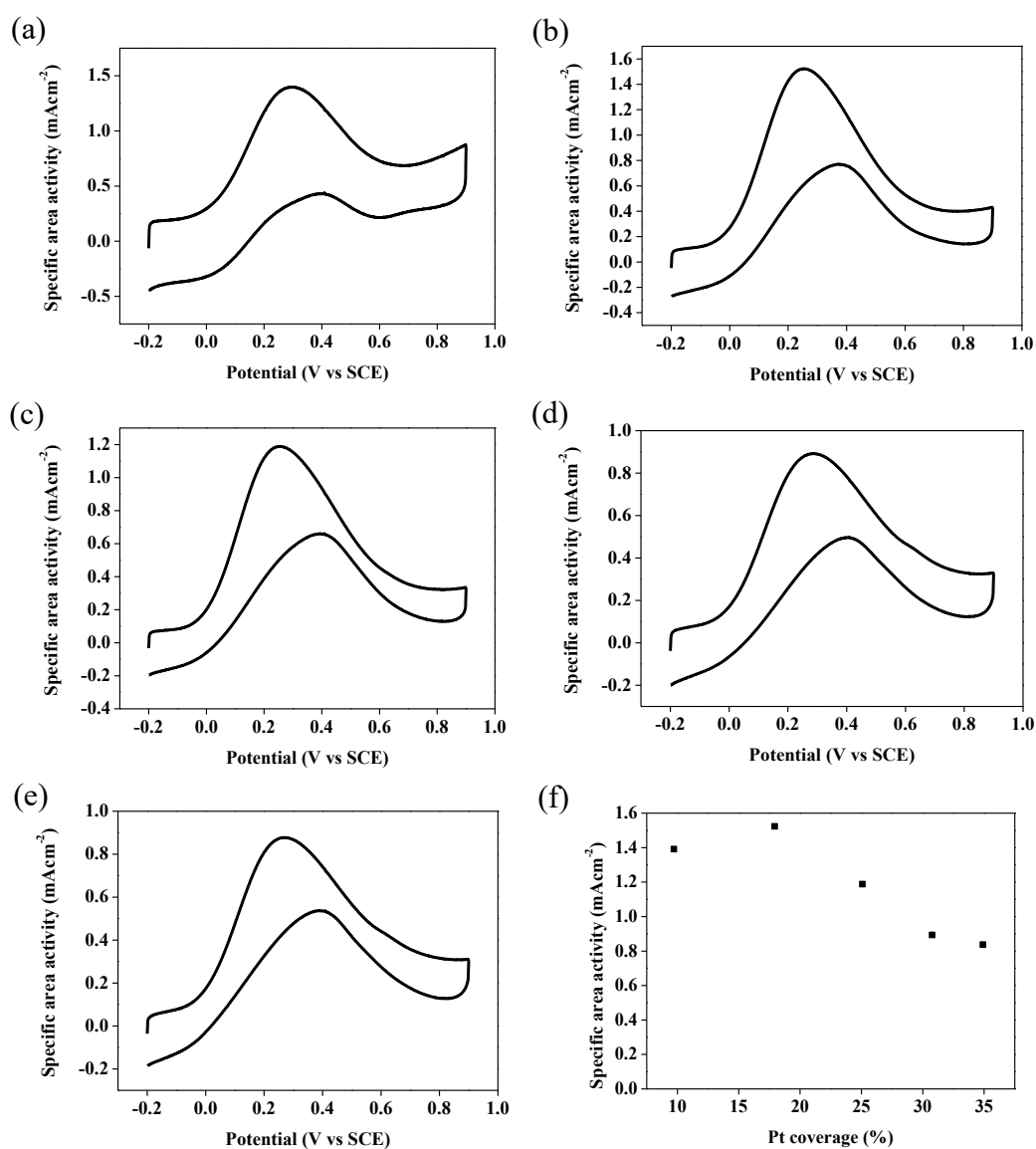


Figure 2.15 CVs of AuNP@Pt/CNTs composite prepared by  $K_2PtCl_4$  solution with Pt coverage of (a) 9.7 %, (b) 17.9 %, (c) 25.1 %, (d) 30.8 % and (e) 34.7 % in 0.025 M HCOOH + 0.1 M  $H_2SO_4$  solution. Scan rate, 50  $mVs^{-1}$ . (f) The relationship between Pt coverage and the electrocatalytic activity towards the oxidation of HCOOH.

Figure 2.16 shows the CVs of AuNP@Pt/CNTs composite prepared by  $K_2PtCl_6$  solution towards the oxidation of formic acid. The specific area activity towards the direct oxidation of formic acid increases from  $1.30 \text{ mAcm}^{-2}$  to  $1.42 \text{ mAcm}^{-2}$  when the Pt coverage increases from 11.3 % to 21.0 % because more Pt active sites are available for the oxidation of formic acid. Under similar Pt coverages of around 20 %, similar specific area activities of around  $1.4 \text{ mAcm}^{-2}$  towards the direct oxidation of formic acid are achieved, which suggests that it follows the direct oxidation of formic acid.

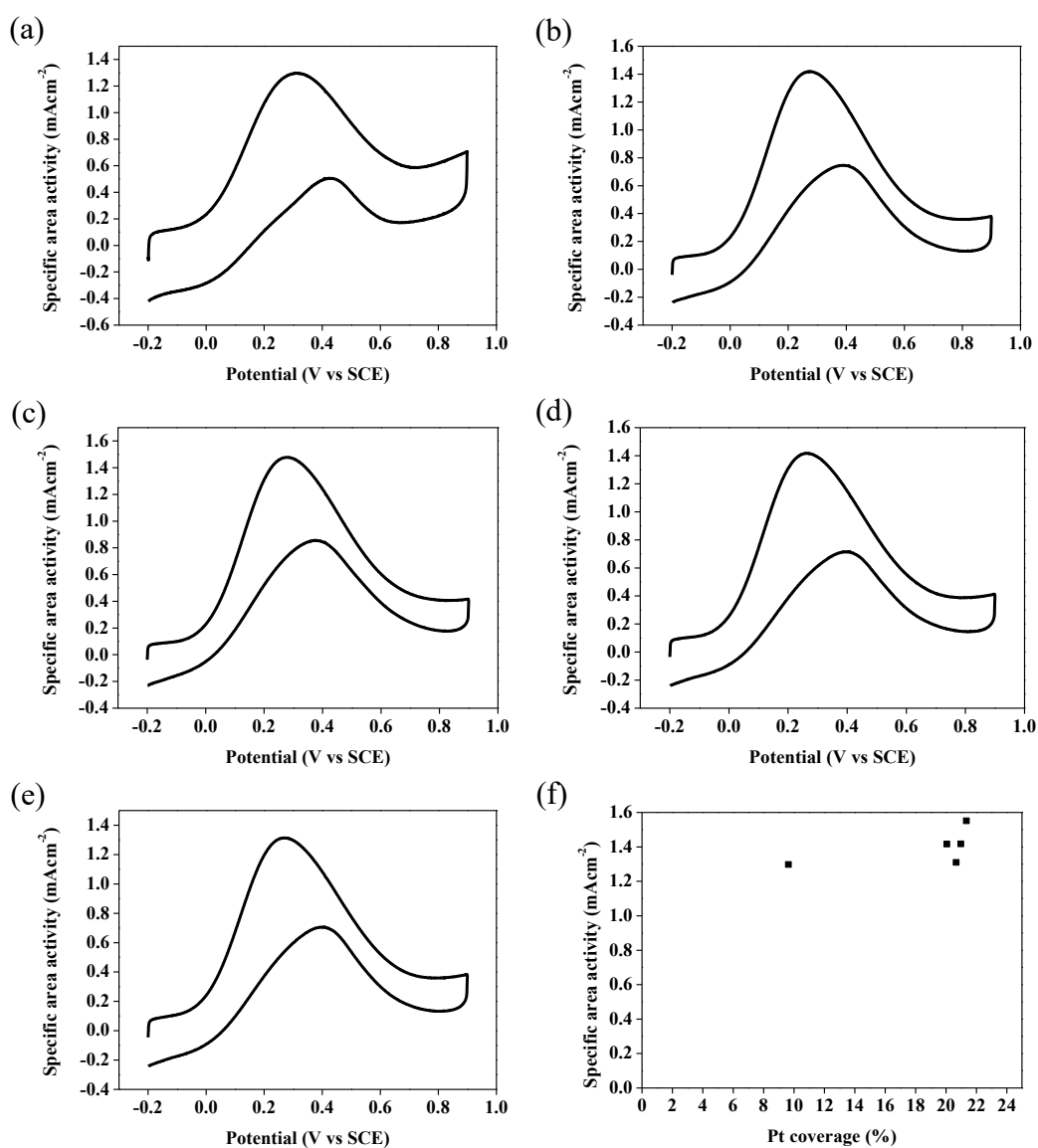


Figure 2.16 CVs of AuNP@Pt/CNTs composite prepared by  $K_2PtCl_6$  solution with Pt coverage of (a) 11.3 %, (b) 21.0 %, (c) 21.4 %, (d) 20.1 % and (e) 20.7 % in 0.025 M HCOOH + 0.1 M  $H_2SO_4$  solution. Scan rate, 50  $mVs^{-1}$ . (f) The relationship between Pt coverage and the electrocatalytic activity towards the oxidation of HCOOH.

Figure 2.17 presents the relationship between Pt coverage and the electrocatalytic activity towards the oxidation of formic acid by AuNP@Pt/CNTs composite prepared by  $K_2PtCl_4$  and  $K_2PtCl_6$  solutions. A significant difference of electrocatalytic activities towards the direct oxidation of formic acid between AuNP@Pt/CNTs composite prepared by  $K_2PtCl_4$  and  $K_2PtCl_6$  solutions is observed. Both specific area activities towards the direct oxidation of formic acid of AuNP@Pt/CNTs composite prepared by  $K_2PtCl_4$  and  $K_2PtCl_6$  solutions increases. When the concentration further increases, they show different electrocatalytic activities. For  $K_2PtCl_4$ , the specific area activity decreases due to increasing Pt ensemble site while for  $K_2PtCl_6$ , the specific area activity remains at similar level due to the similar resultant Pt coverages

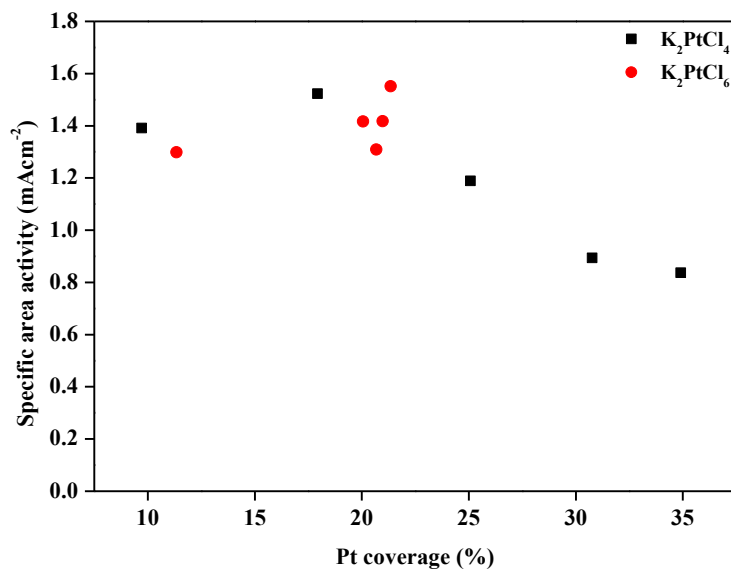


Figure 2.17 The relationship between Pt coverage and the electrocatalytic activity towards the oxidation of HCOOH by AuNP@Pt/CNTs composite prepared by  $K_2PtCl_4$  and  $K_2PtCl_6$  solutions.

Figure 2.18 and Figure 2.19 show the CVs of AuNP@Pt/CNTs composites prepared by Na<sub>2</sub>PtCl<sub>4</sub> and Na<sub>2</sub>PtCl<sub>6</sub>·6H<sub>2</sub>O solutions towards the oxidation of formic acid respectively. Their catalytic performances are similar to that prepared by K<sub>2</sub>PtCl<sub>4</sub> and K<sub>2</sub>PtCl<sub>6</sub> solutions due to similar Pt coverages achieved at the same concentrations respectively. As shown in previous study, the Pt coverage is relatively independent of the cations present. Thus, their resultant catalytic activities are also not affected.

For AuNP@Pt/CNTs composite prepared by Na<sub>2</sub>PtCl<sub>4</sub> solution, their specific area activity towards the direct oxidation of formic acid increases from 1.40 mAcm<sup>-2</sup> to 1.44 mAcm<sup>-2</sup> when the Pt coverage increases from 10.5 % to 19.2 % due to the increasing availability of Pt active sites. When the Pt coverage increases from 19.2 % to 34.5 %, a decreasing specific area activity from 1.44 mAcm<sup>-2</sup> to 0.80 mAcm<sup>-2</sup> towards the direct oxidation of formic acid is achieved. The trend of first increase and then decrease for specific area activity of formic acid oxidation by AuNP@Pt/CNTs composite prepared from Na<sub>2</sub>PtCl<sub>4</sub> solution is similar to that of K<sub>2</sub>PtCl<sub>4</sub> due to similar Pt coverages achieved at the same concentrations. For AuNP@Pt/CNTs composite prepared by Na<sub>2</sub>PtCl<sub>6</sub>·6H<sub>2</sub>O solution, their specific area activity towards the direct oxidation of formic acid increases from 1.47 mAcm<sup>-2</sup> to 1.60 mAcm<sup>-2</sup> when the Pt coverage increases from 10.2 % to 20.8 % owing to the increase of Pt active sites. For Pt coverages at around 20 %, similar specific area activities of 1.4 mAcm<sup>-2</sup> towards the direct oxidation of formic acid were achieved. The trend of first increase and then decrease for specific area activity of formic acid oxidation by is similar to that K<sub>2</sub>PtCl<sub>6</sub> as the resultant Pt coverage is similar. Both AuNP@Pt/CNTs composites prepared by Na<sub>2</sub>PtCl<sub>4</sub> and Na<sub>2</sub>PtCl<sub>6</sub>·6H<sub>2</sub>O solutions achieve catalytic performances towards the oxidation

of formic acid when compared with  $\text{K}_2\text{PtCl}_4$  and  $\text{K}_2\text{PtCl}_6$  solutions. They mainly follow the direct pathway of formic acid oxidation.

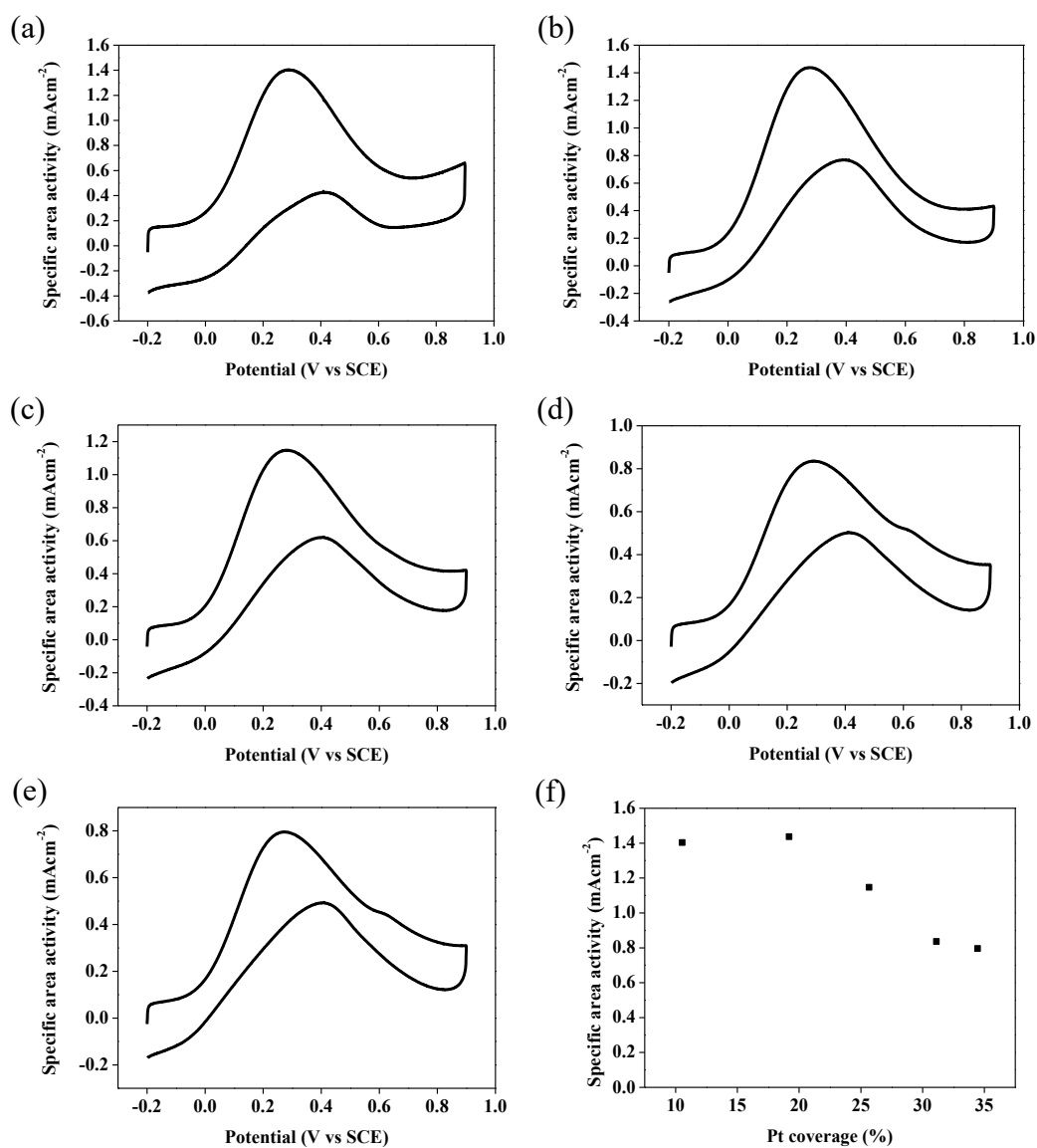


Figure 2.18 CVs of AuNP@Pt/CNTs composite prepared by Na<sub>2</sub>PtCl<sub>4</sub> solution with Pt coverage of (a) 10.5 %, (b) 19.2 %, (c) 25.7 %, (d) 31.1% and (e) 34.5 % in 0.025 M HCOOH + 0.1 M H<sub>2</sub>SO<sub>4</sub> solution. Scan rate, 50 mVs<sup>-1</sup>. (g) The relationship between Pt coverage and the electrocatalytic activity towards the oxidation of HCOOH.

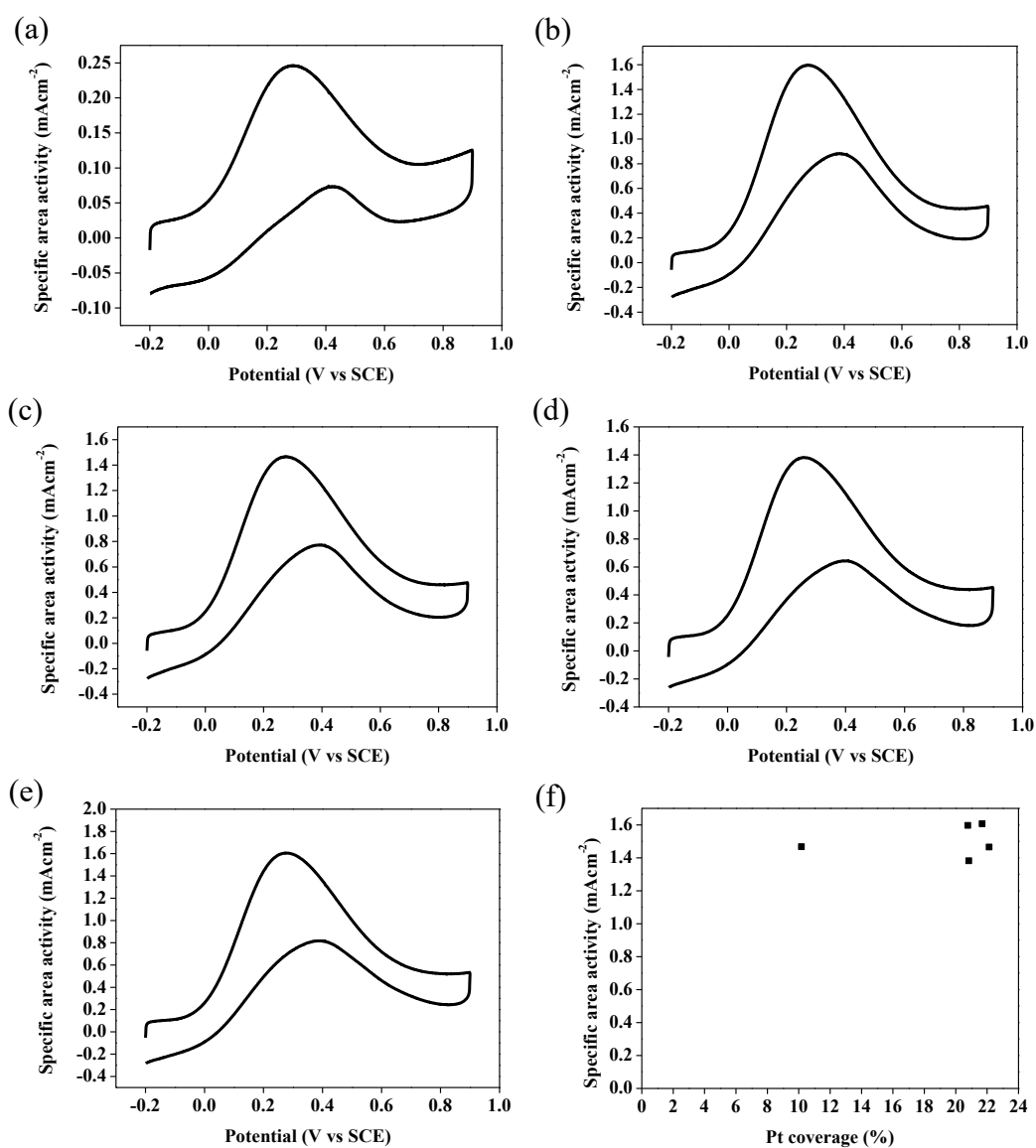


Figure 2.19 CVs of AuNP@Pt/CNTs composite prepared by Na<sub>2</sub>PtCl<sub>6</sub>·6H<sub>2</sub>O solution with Pt coverage of (a) 10.2 %, (b) 20.8 %, (c) 22.1 %, (d) 20.8 % and (e) 21.7 % in 0.025 M HCOOH + 0.1 M H<sub>2</sub>SO<sub>4</sub> solution. Scan rate, 50 mVs<sup>-1</sup>. (f) The relationship between Pt coverage and the electrocatalytic activity towards the oxidation of HCOOH.

Figure 2.20 and Figure 2.22 show the CVs of AuNP@Pt/CNTs composites prepared by  $K_2PtBr_4$  and  $K_2PtBr_6$  solutions towards the oxidation of formic acid respectively. In positive-going scan, there is an oxidative peak at around 0.3 to 0.4V as ascribed to the dehydrogenation, which is slightly positive-shifted when compared with  $K_2PtCl_4$  and  $K_2PtCl_6$  solutions. It is indicated that the oxidation of formic acid by the AuNP@Pt/CNTs composites prepared by  $K_2PtBr_4$  and  $K_2PtBr_6$  solutions are more difficult when compared with  $K_2PtCl_4$  and  $K_2PtCl_6$  solutions. According to the XPS analysis, Br atoms exist on AuNP@Pt/CNTs composites. The Br atoms may bind strongly with the surface atoms which may lower the catalytic activity of the resultant catalyst.

For AuNP@Pt/CNTs composite prepared by  $K_2PtBr_4$  solution, their specific area activity towards the direct oxidation of formic acid increases from  $0.93 \text{ mAcm}^{-2}$  to  $1.04 \text{ mAcm}^{-2}$  when the Pt coverage increases from 15.2 % to 25.8 % because Pt active sites increase for formic acid oxidation. Under an increase of Pt coverage from 25.8 % to 64.9 %, a decreasing specific area activity from  $1.04 \text{ mAcm}^{-2}$  to  $0.37 \text{ mAcm}^{-2}$  towards the direct oxidation of formic acid is achieved due to ensemble effect.[21] With the Pt coverage of 51.9 % or above, a shoulder peak at around 0.6 V appears indicating the dehydration as shown in Figure 2.20 (e) and (f).[21] It is believed that the direct pathway of formic acid oxidation is still a dominant pathway for AuNP@Pt/CNTs composite prepared by  $K_2PtBr_4$  solution.

Also, as displayed in Figure 2.21, their specific area activity towards the direct oxidation of formic acid is lower because higher Pt coverage enhances ensemble effect when compared with AuNP@Pt/CNTs composite prepared by  $K_2PtCl_4$

solution.[21]

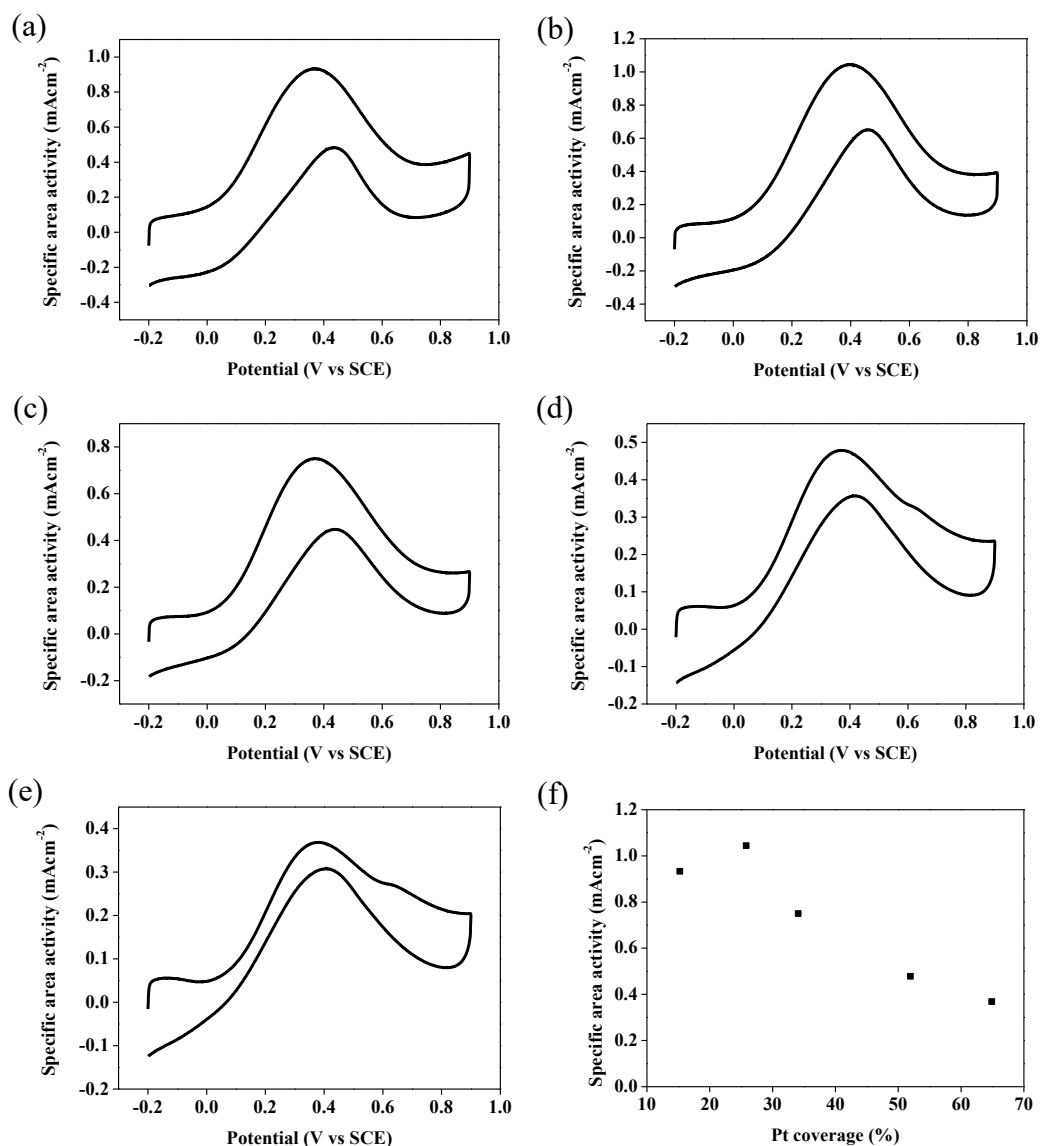


Figure 2.20 CVs of AuNP@Pt/CNTs composite prepared by K<sub>2</sub>PtBr<sub>4</sub> solution with Pt coverage of (a) 15.2 %, (b) 25.8 %, (c) 34.1 %, (d) 51.9 % and (e) 64.9 % in 0.025 M HCOOH + 0.1 M H<sub>2</sub>SO<sub>4</sub> solution. Scan rate, 50 mVs<sup>-1</sup>. (f) The relationship between Pt coverage and the electrocatalytic activity towards the oxidation of HCOOH.

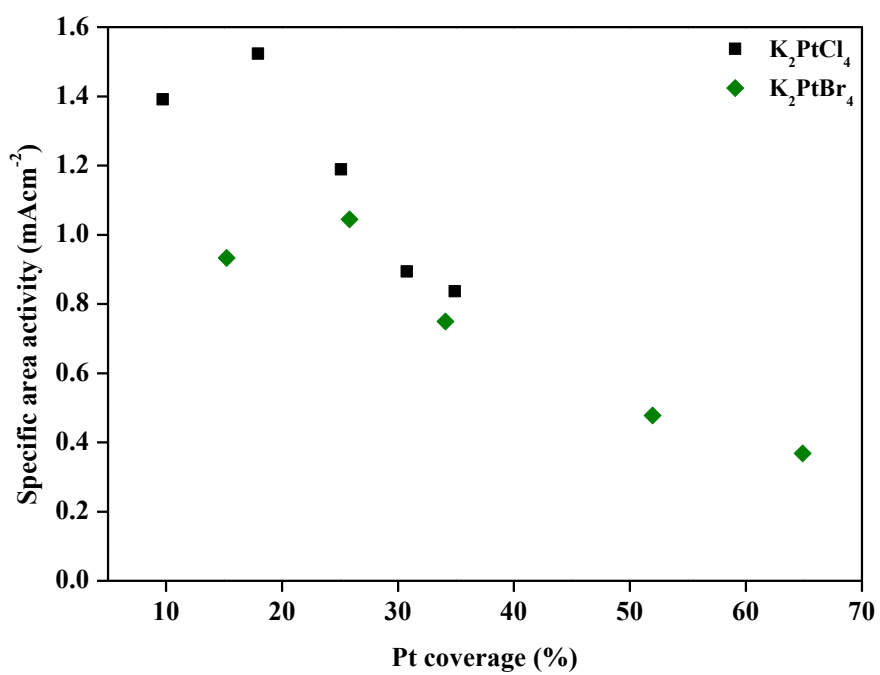


Figure 2.21 The relationship between Pt coverage and the electrocatalytic activity towards the oxidation of HCOOH by AuNP@Pt/CNTs composite prepared by K<sub>2</sub>PtCl<sub>4</sub> and K<sub>2</sub>PtBr<sub>4</sub> solutions.

For AuNP@Pt/CNTs composite prepared by  $K_2PtBr_6$  solution, their specific area activity towards the direct oxidation of formic acid increases from  $0.78 \text{ mAcm}^{-2}$  to  $1.08 \text{ mAcm}^{-2}$  when the Pt coverage increases from 8.1 % to 17.6 % because Pt active sites increase for formic acid oxidation. Under similar Pt coverages of around 17 % to 18 %, similar specific area activities of around  $1.1 \text{ mAcm}^{-2}$  towards the direct oxidation of formic acid were achieved. It is believed that AuNP@Pt/CNTs composites prepared by  $K_2PtBr_6$  solution mainly follow the direct oxidation of formic acid.

Besides, as displayed in Figure 2.23, AuNP@Pt/CNTs composite prepared by  $K_2PtBr_6$  solution have lower Pt coverage but still lower specific area activity towards the direct oxidation of formic acid when compared with  $K_2PtCl_6$  solution. The existence of Br, as confirmed by XPS analysis, may affect the electrocatalytic activity of AuNP@Pt/CNTs composite prepared by  $K_2PtBr_6$  solution.

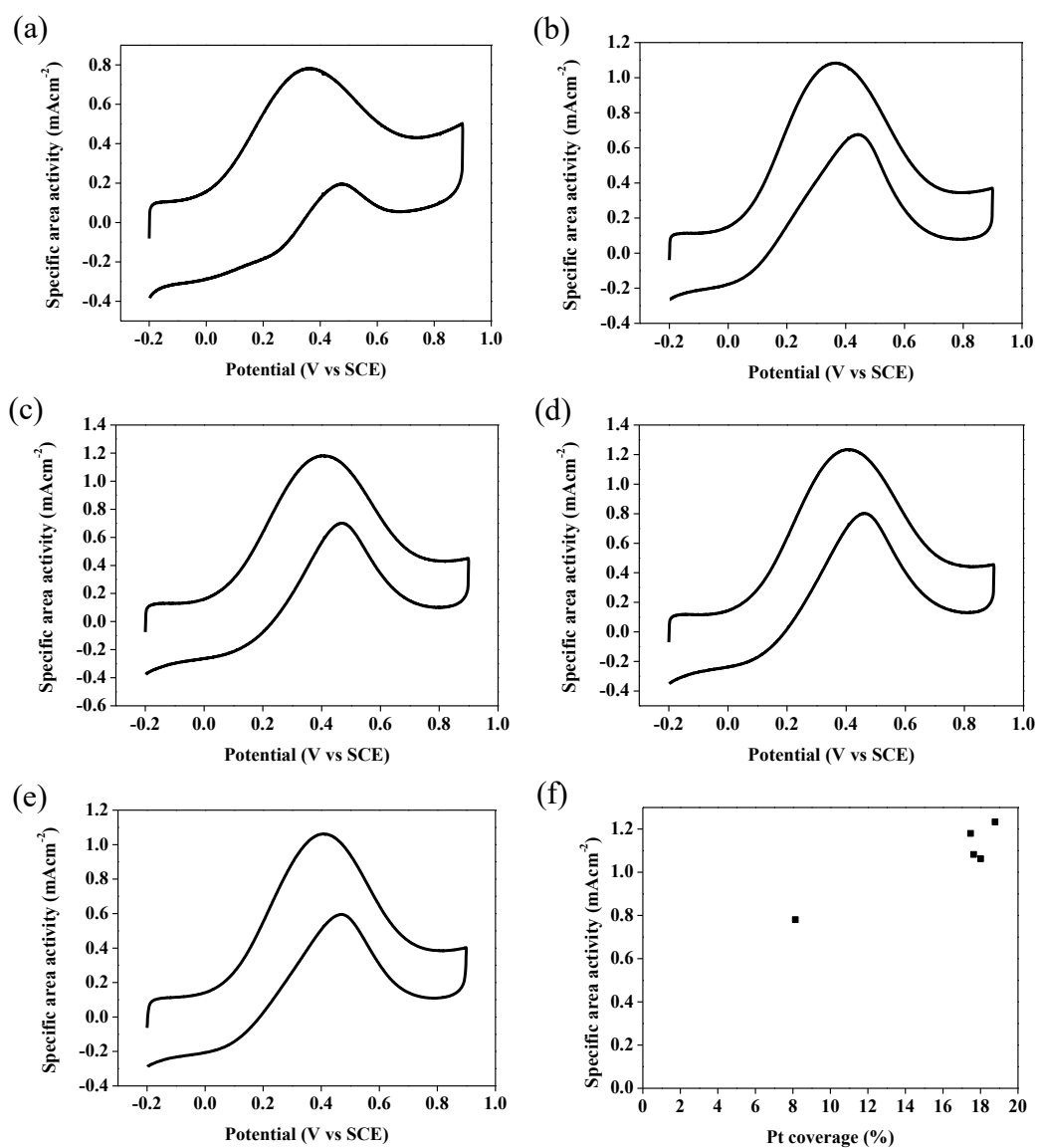


Figure 2.22 CVs of AuNP@Pt/CNTs composite prepared by  $K_2PtBr_6$  solution with Pt coverage of (a) 8.1 %, (b) 17.4 %, (c) 17.5 %, (d) 18.8 % and (e) 18.0 % in 0.025 M HCOOH + 0.1 M  $H_2SO_4$  solution. Scan rate, 50  $mVs^{-1}$ . (f) The relationship between Pt coverage and the electrocatalytic activity towards the oxidation of HCOOH.

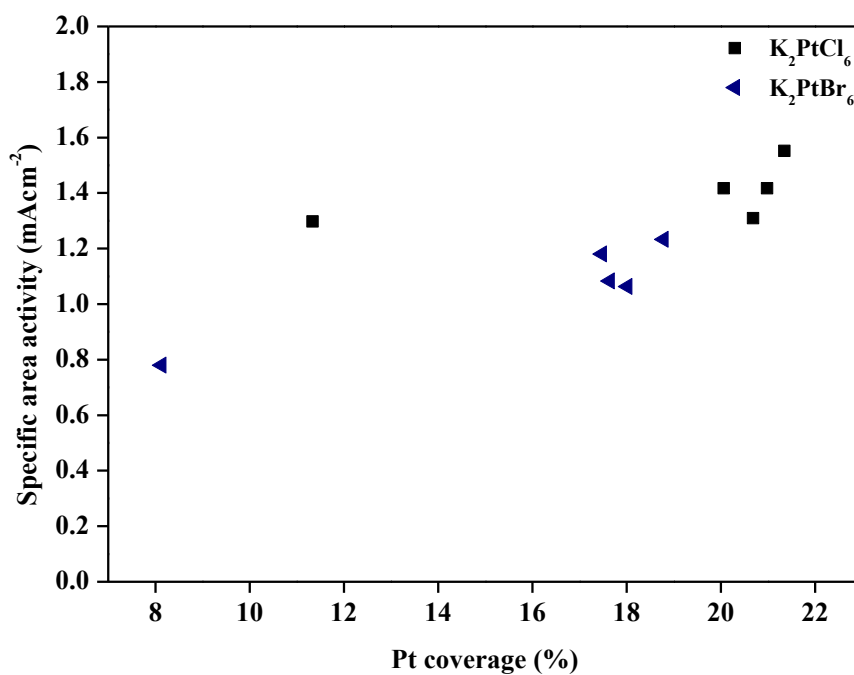


Figure 2.23 The relationship between Pt coverage and the electrocatalytic activity towards the oxidation of HCOOH by AuNP@Pt/CNTs composite prepared by K<sub>2</sub>PtCl<sub>6</sub> and K<sub>2</sub>PtBr<sub>6</sub> solutions.

Figure 2.24 shows the CVs of AuNP@Pt/CNTs composite prepared by  $\text{Pt}(\text{NH}_3)_4(\text{NO}_3)_2$  solution towards the oxidation of formic acid. Their specific area activity towards the direct oxidation of formic acid increases from  $0.18 \text{ mAcm}^{-2}$  to  $1.79 \text{ mAcm}^{-2}$  when the Pt coverage increases from 2.2 % to 11.4 % because the Pt active sites increase for the oxidation of formic acid. When the Pt coverage increases from 11.4 % to 16.1 %, a decrease of specific area activity from  $1.79 \text{ mAcm}^{-2}$  to  $1.51 \text{ mAcm}^{-2}$  towards the direct oxidation of formic acid is achieved due to ensemble effect.[21] The low Pt coverage results in Pt isolated states which facilitate the direct oxidation of formic acid. With the increasing Pt coverage, AuNPs cannot accommodate Pt isolated state and ensemble Pt sites start to appear, resulting in a decreasing specific area activity.

Since  $\text{Pt}(\text{NH}_3)_4(\text{NO}_3)_2$  solution was used to prepare AuNP@Pt/CNTs composite with low Pt coverage, the catalytic activity towards the direct oxidation of formic acid could be optimized by comparing with  $\text{K}_2\text{PtCl}_4$  solution. As displayed in Figure 2.25 (a), by finding the intersection point of two linear fit lines, the Pt coverage and specific area activity are optimized to 12.1 % and  $1.48 \text{ mAcm}^{-2}$  respectively. Since the R-square of the two linear fit lines are low, the linear fit lines are re-plotted by neglecting the first data point of  $\text{K}_2\text{PtCl}_4$  and the last data point of  $\text{Pt}(\text{NH}_3)_4(\text{NO}_3)_2$  as displayed in Figure 2.25 (b). Only the upward trend of  $\text{Pt}(\text{NH}_3)_4(\text{NO}_3)_2$  data points and the downward trend of  $\text{K}_2\text{PtCl}_4$  data points are considered. By finding the intersection point of two re-plotted linear fit lines, the Pt coverage and specific area activity are optimized to 11.0 % and  $1.80 \text{ mAcm}^{-2}$  respectively.

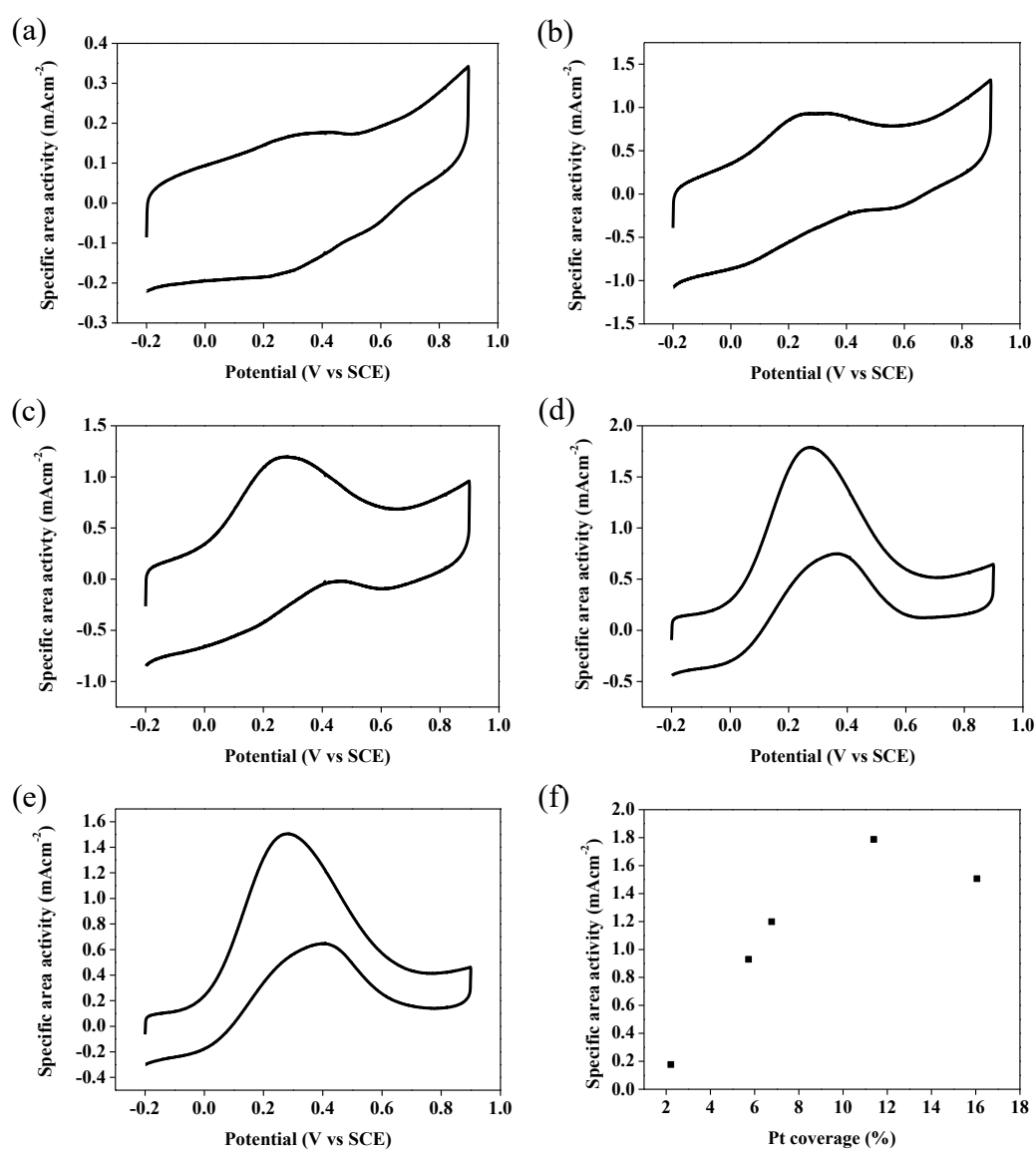


Figure 2.24 CVs of AuNP@Pt/CNTs composite prepared by  $\text{Pt}(\text{NH}_3)_4(\text{NO}_3)_2$  solution with Pt coverage of (a) 2.2 %, (b) 5.7 %, (c) 6.8 %, (d) 11.4 % and (e) 16.1 % in 0.025 M  $\text{HCOOH}$  + 0.1 M  $\text{H}_2\text{SO}_4$  solution. Scan rate,  $50 \text{ mVs}^{-1}$ . (f) The relationship between Pt coverage and the electrocatalytic activity towards the oxidation of  $\text{HCOOH}$ .

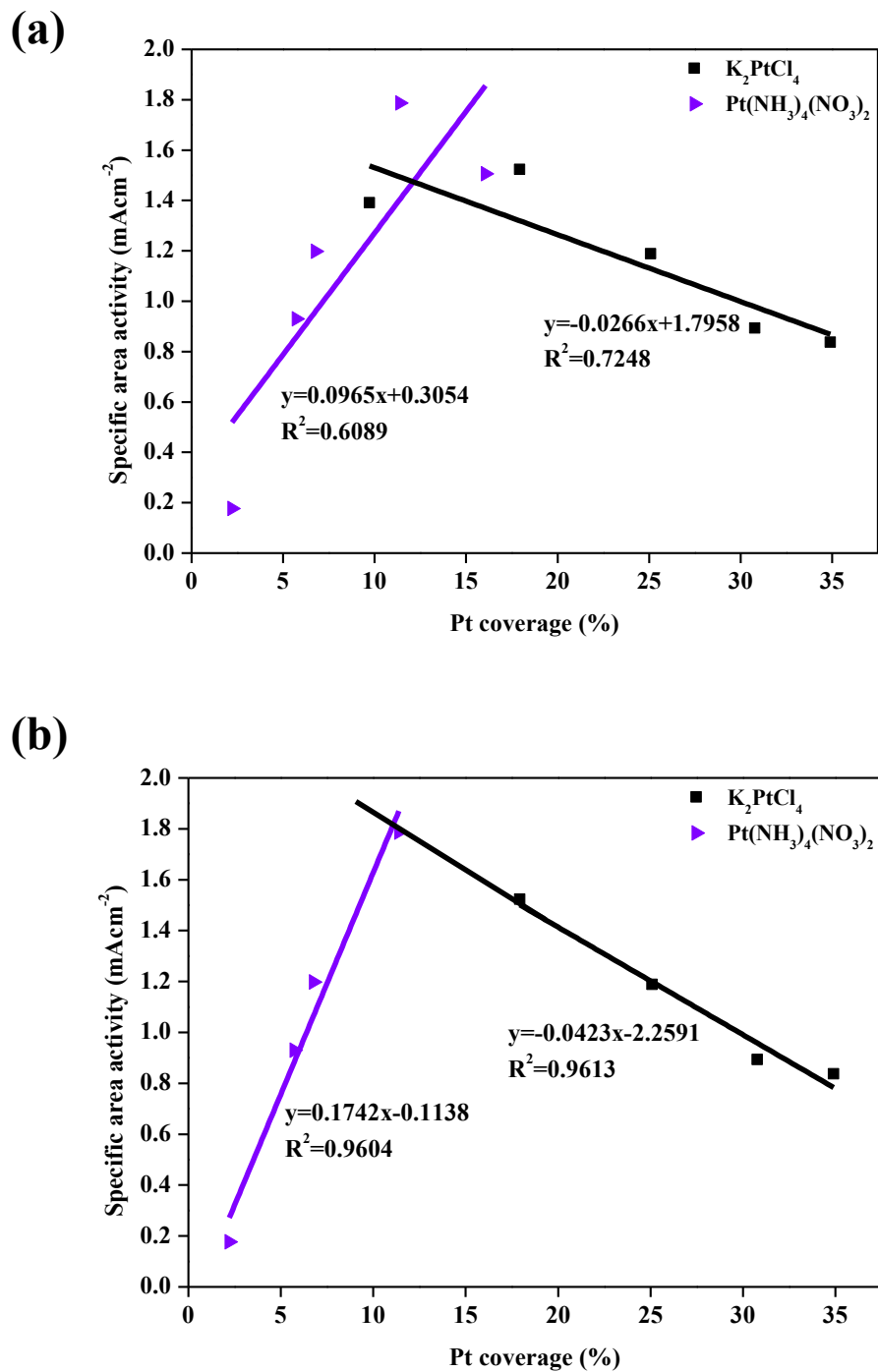


Figure 2.25 (a) The relationship and (b) the re-plotted relationship between Pt coverage and the electrocatalytic activity towards the oxidation of HCOOH by AuNP@Pt/CNTs composites prepared by  $K_2PtCl_4$  and  $Pt(NH_3)_4(NO_3)_2$  solutions.

The specific area activity was determined to study the intrinsic activity of catalysts. Apart from specific area activity, specific mass activity of the AuNP@Pt/CNTs prepared by K<sub>2</sub>PtCl<sub>4</sub> solution towards formic acid oxidation was also explored. However, there is a large discrepancy and the data has to be verified in progress. The specific mass activity of AuNP@Pt/CNTs prepared by K<sub>2</sub>PtCl<sub>4</sub> solution is roughly estimated. Compared with the PtAu-based catalysts reported in the literatures, AuNP@Pt/CNTs composite prepared by K<sub>2</sub>PtCl<sub>4</sub> solution shows higher specific mass activity towards the direct oxidation of formic acid. The utilization of Pt is enhanced.

Conc. of K <sub>2</sub> PtCl <sub>4</sub> (mM)	Pt coverage (%)	Pt loading by ICP-OES (wt%)	Specific area activity (mAcm <sup>-2</sup> )	Specific mass activity (mA <sub>mgPt</sub> <sup>-1</sup> )
0.02	9.7	0.45	1.39	1255.6
0.08	17.9	0.54	1.52	2310.2
0.32	25.1	0.63	1.19	1908.7
1.28	30.8	0.92	0.89	1084.2
5.12	34.9	1.30	0.84	750.0

Table 2.5 The electrocatalytic performance of AuNP@Pt/CNTs composite prepared by K<sub>2</sub>PtCl<sub>4</sub> solution towards direct formic acid oxidation.

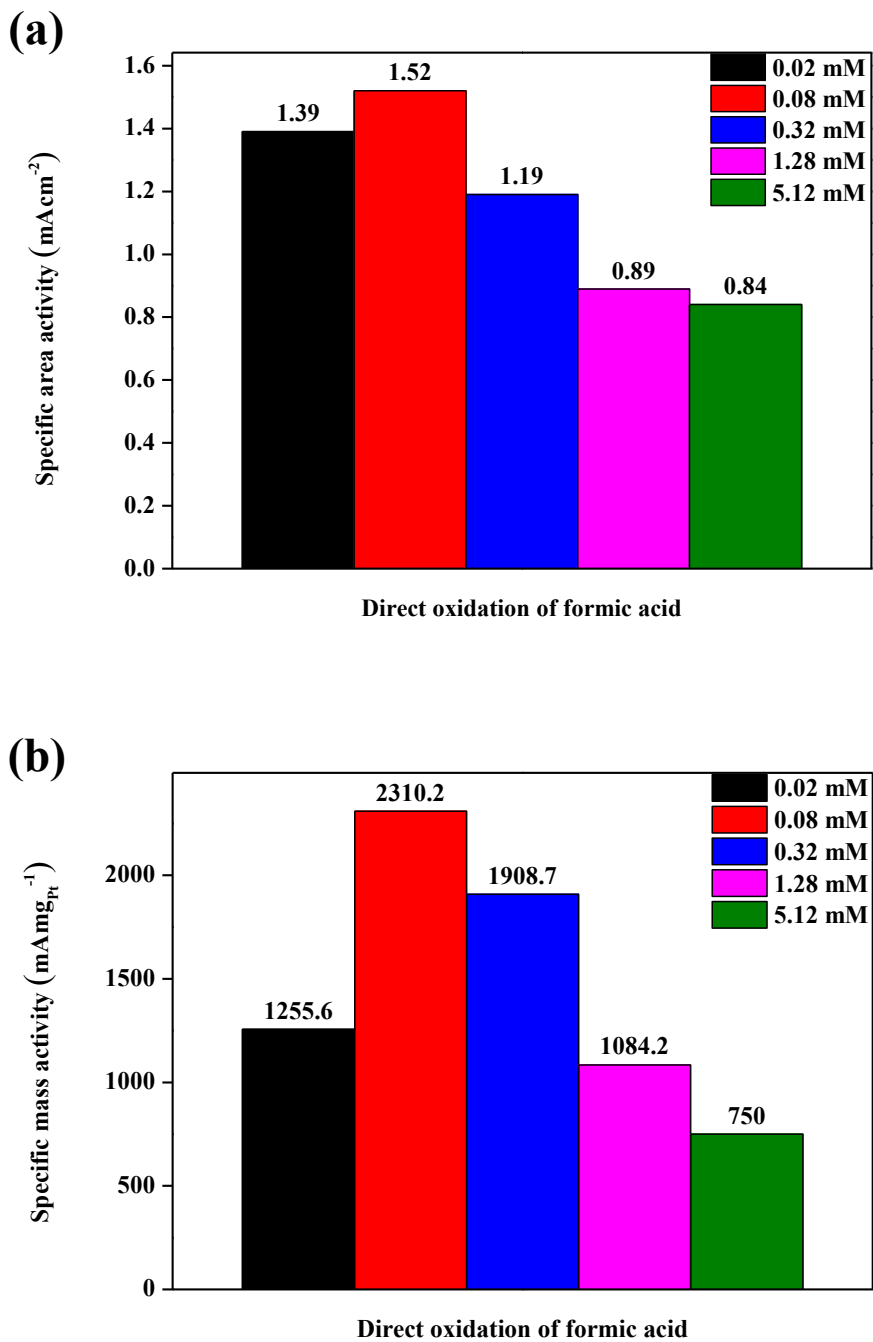


Figure 2.26

(a) The specific area activities and (b) specific mass activities of AuNP@Pt/CNTs composite prepared by K<sub>2</sub>PtCl<sub>4</sub> solution with Pt coverage of 9.7 %, 17.9 %, 25.1 %, 30.8 % and 34.7 % towards direct formic acid oxidation.

### **Chronoamperometric test of formic acid oxidation**

To study the stability of AuNP@Pt/CNTs composites towards the oxidation of formic acid, chronoamperometric tests were performed. Figure 2.27 displays the chronoamperometric curves of AuNP@Pt/CNTs composites with similar Pt coverages prepared by different Pt halide solutions in 0.025 M HCOOH + 0.1 M H<sub>2</sub>SO<sub>4</sub> solution at a fixed potential of 0.15 V for 3600 s.

Initially, the current densities decrease rapidly. During the oxidation of formic acid, the intermediate species, which is adsorbed carbon monoxide (CO<sub>ads</sub>), is produced and accumulate on the Pt surfaces. The Pt active sites are blocked from the oxidation of formic acid.[33, 36] Thus, the current densities then decay gradually.

As shown in the Table 2.6, it is found that the current densities retained by K<sub>2</sub>PtBr<sub>4</sub> and K<sub>2</sub>PtBr<sub>6</sub> solutions after chronoamperometric tests were slightly higher suggesting their slightly higher stability towards the oxidation of formic acid. According to XPS analysis as presented by Figure 2.28, the existence of Br is confirmed, which suggests its substantial binding on Au surface after reduction. This may help reducing the rearrangement of Pt during chronoamperometric tests.[52, 60]

Figure 2.28 (a) and (b) display the Pt 4f region of the XPS spectrum of AuNP@Pt/CNTs composites prepared by K<sub>2</sub>PtBr<sub>4</sub> and K<sub>2</sub>PtBr<sub>6</sub> solutions respectively. In Figure 2.28 (a), the Pt 4f region of the XPS spectrum is curve-fitted into two doublets assigned to metallic Pt(0) and oxidized Pt(II). The more intense doublets at 73.0 eV and 71.2 eV correspond to the metallic Pt(0)

$4f_{5/2}$  and  $4f_{7/2}$  respectively while the less intense doublets at 76.4 eV and 74.6 eV correspond to the Pt(II)  $4f_{5/2}$  and  $4f_{7/2}$  respectively. The predominant surface species is metallic Pt(0). The peak at 68.1 eV is attributed to Br  $3d_{5/2}$  region, suggesting the existence of Br.

In Figure 2.28 (b), the Pt 4f region of the XPS spectrum is curve-fitted into two doublets assigned to metallic Pt(0) and oxidized Pt(II). The more intense doublets at 74.3 eV and 71.1 eV correspond to the metallic Pt(0)  $4f_{5/2}$  and  $4f_{7/2}$  respectively while the less intense doublets at 75.9 eV and 72.7 eV correspond to the Pt(II)  $4f_{5/2}$  and  $4f_{7/2}$  respectively. The predominant surface species is metallic Pt(0). The peak at 68.0 eV is attributed to Br  $3d_{5/2}$  region, suggesting the existence of Br.

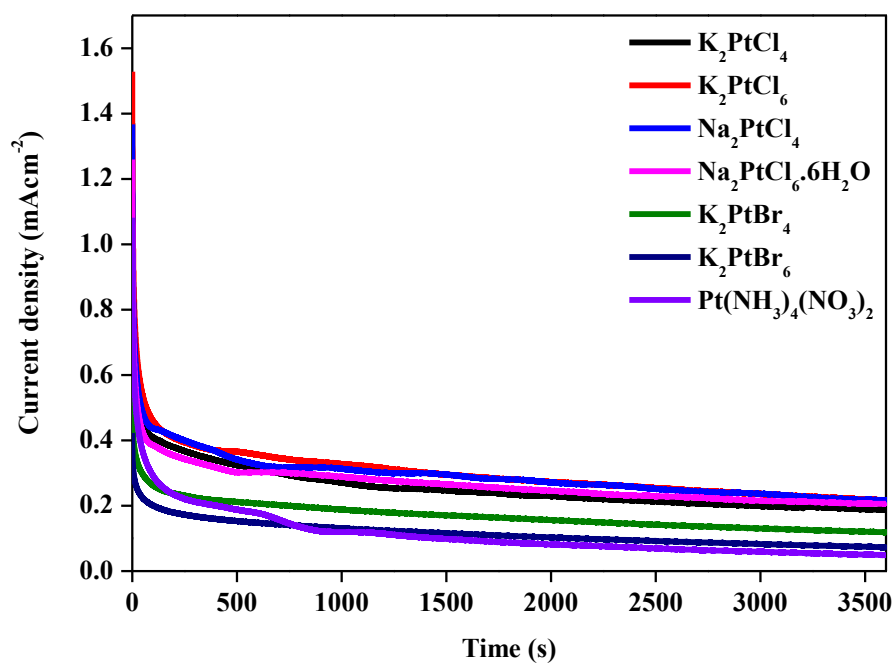
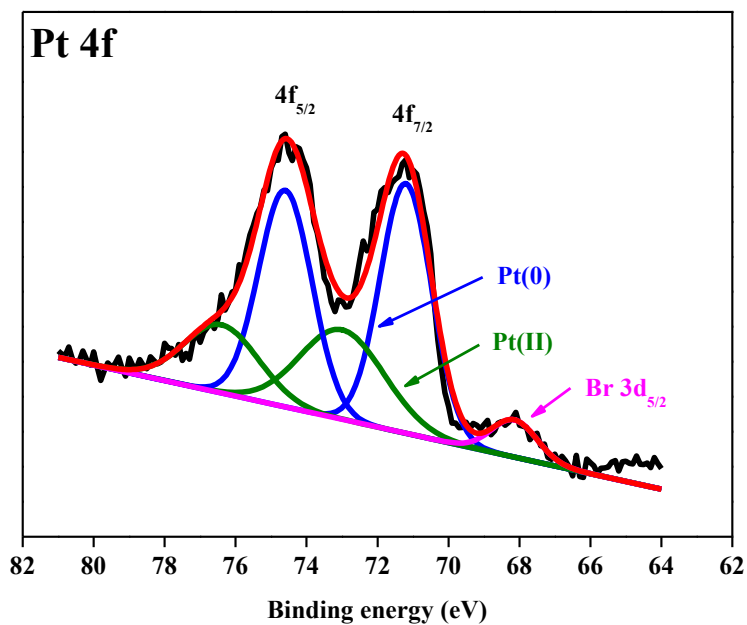


Figure 2.27 Chronoamperometric curves of AuNP@Pt/CNTs composites in 0.025 M HCOOH + 0.1 M H<sub>2</sub>SO<sub>4</sub> solution at a fixed potential of 0.15 V for 3600 s.

Pt halide solutions	Pt coverage (%)	Current density retained after chronoamperometric test (%)
$K_2PtCl_4$	17.9	13.6
$K_2PtCl_6$	21.0	14.2
$Na_2PtCl_4$	19.2	15.9
$Na_2PtCl_6 \cdot 6H_2O$	20.8	16.3
$K_2PtBr_4$	25.8	22.2
$K_2PtBr_6$	17.6	19.8
$Pt(NH_3)_4(NO_3)_2$	16.1	4.6

Table 2.6 Summary of current density retained after chronoamperometric test towards the oxidation of formic acid of AuNP@Pt/CNTs composites prepared with different Pt halide solutions.

(a)



(b)

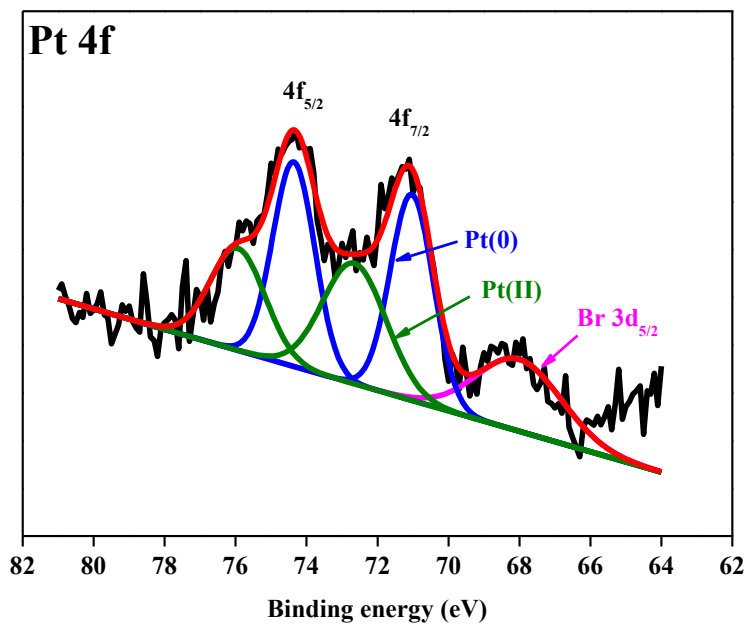


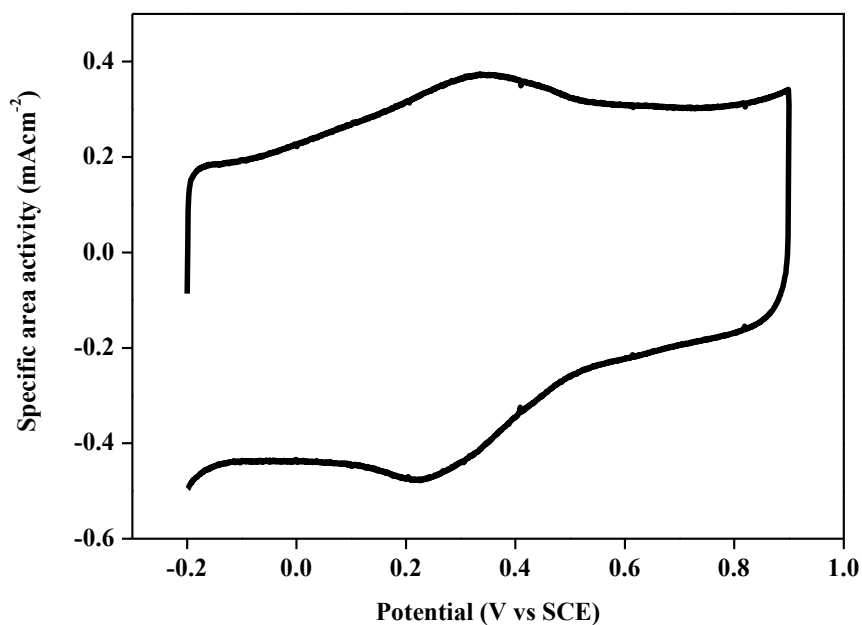
Figure 2.28

XPS spectra of Pt 4f region of AuNP@Pt/CNTs composites prepared by (a)  $K_2PtBr_4$  and (b)  $K_2PtBr_6$  solutions.

### **Electrooxidation of methanol**

The electrooxidation of methanol (MeOH) was investigated by conducting CV of AuNP@Pt/CNTs composites coated on GCE in 0.1 M MeOH + 0.1M H<sub>2</sub>SO<sub>4</sub> solution in the potential region from -0.2 V to 0.9 V with a scan rate of 50 mVs<sup>-1</sup>. It is known that CNTs and Au are not active towards the oxidation of methanol.[61] T The specific area activity towards the oxidation of methanol is calculated by normalizing current to the ECSA of Pt of AuNP@Pt/CNTs composites. Figure 2.29 (a) shows the CV of AuNP@Pt/CNTs composite prepared by 0.02 mM K<sub>2</sub>PtCl<sub>4</sub> solution, with the Pt coverage of 9.7 % which is not active to the oxidation of methanol. The AuNP@Pt/CNTs composites with different Pt coverages prepared by K<sub>2</sub>PtCl<sub>6</sub>, Na<sub>2</sub>PtCl<sub>4</sub>, Na<sub>2</sub>PtCl<sub>6</sub>·6H<sub>2</sub>O, K<sub>2</sub>PtBr<sub>4</sub>, K<sub>2</sub>PtBr<sub>6</sub> and Pt(NH<sub>3</sub>)<sub>4</sub>(NO<sub>3</sub>)<sub>2</sub> exhibit similar CV graphs, indicating that they are also inactive to the oxidation of methanol. Figure 2.29 (b) shows the AuNP@Pt/CNTs composite prepared by K<sub>2</sub>PtCl<sub>4</sub> solution with the Pt coverage of 34.7 % become slightly active towards the oxidation of methanol. For K<sub>2</sub>PtBr<sub>4</sub> solution, the AuNP/CNTs composites with high Pt coverage ranging from 34.1 % to 64.9 % are still inactive to the oxidation of methanol, which exhibit similar CV to Figure 2.29 (a). It is possible that Br may exist on the surface of catalyst, which may interrupt the availability of continuous Pt sites for the oxidation of methanol, resulting in inactive signals to methanol oxidation.

(a)



(b)

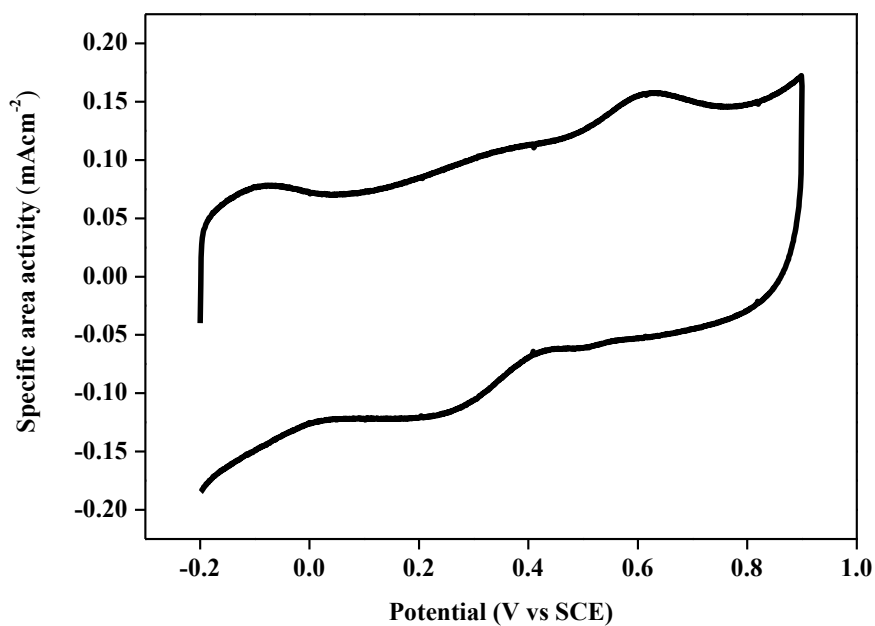


Figure 2.29

CV of AuNP@Pt/CNTs composite prepared by  $K_2PtCl_4$  solution with Pt coverage of (a) 9.7 % and (b) 34.7 % in 0.1 M MeOH + 0.1 M  $H_2SO_4$  solution. Scan rate, 50  $mVs^{-1}$ .

As shown in the results of electrochemical characterizations, varying the concentrations of  $[\text{PtX}_4]^{2-}$  ion ( $\text{X} = \text{Cl}$  or  $\text{Br}$ ) and  $\text{Pt}(\text{NH}_3)_4(\text{NO}_3)_2$  solutions could control the Pt coverage on AuNP/CNTs composite while  $[\text{PtX}_6]^{2-}$  ion solutions could not. Besides, the Pt coverage achieved by  $[\text{PtBr}_4]^{2-}$  ion solution is higher than that achieved by  $[\text{PtCl}_4]^{2-}$  ion solution. It is also found that the AuNP@Pt/CNTs composites with low Pt coverage are active towards the direct oxidation of formic acid but inactive towards the oxidation of methanol. However, it is not a must that AuNP@Pt/CNTs composites with high Pt coverage exhibit activity towards the indirect oxidation of formic acid and the oxidation of methanol. The  $[\text{PtCl}_4]^{2-}$  and  $[\text{PtBr}_4]^{2-}$  ions have same coordination geometries of square planar but exhibit different adsorption affinity and electrocatalytic activity towards the oxidations of formic acid and methanol. For  $[\text{PtCl}_4]^{2-}$  ions solutions, the AuNP@Pt/CNTs composites with the Pt coverage of greater 30 % start becoming active to indirect oxidations of formic acid and methanol. For  $[\text{PtBr}_4]^{2-}$  ions solutions, the AuNP@Pt/CNTs composites are slightly active to indirect oxidation of formic acid but still inactive to the oxidation of methanol even the Pt coverage reaches around 50 %. It is possible that the existence of Br may interrupt the Pt neighboring continuous sites for the oxidation of methanol.

### **2.2.3 Exploration on immersion time towards formic acid and methanol electrooxidations**

Apart from varying the concentrations of Pt halide solutions, the effect of increasing immersion time on Pt coverage and the related specific area activity towards the oxidations of formic acid and methanol were also explored. The AuNP@Pt/CNTs composites were prepared by immersing the GCE coated with AuNP/CNTs composite in Pt halide solutions with the low concentration of 0.08 mM under longer immersion time of 60 min, 120 min and 240 min.

It is general that the Pt coverage increases slightly when the immersion time increases from 10 min to 120 min as presented in Figure 2.30 and Table 2.7. More Pt halide ions deposit on the surface of AuNPs with the increasing immersion time.[62] However, the Pt coverage does not further increase significantly when the immersion time further increases to 240 min. This suggests that the Pt coverage reaches plateau with the Pt halide solutions concentration of 0.08 mM immersion time of 120 min.[20]

Immersion time (min)	Pt coverage (%)						
	K <sub>2</sub> PtCl <sub>4</sub>	K <sub>2</sub> PtCl <sub>6</sub>	Na <sub>2</sub> PtCl <sub>4</sub>	Na <sub>2</sub> PtCl <sub>6</sub> ·6H <sub>2</sub> O	K <sub>2</sub> PtBr <sub>4</sub>	K <sub>2</sub> PtBr <sub>6</sub>	Pt(NH <sub>3</sub> ) <sub>4</sub> (NO <sub>3</sub> ) <sub>2</sub>
10	17.9	21.0	19.2	20.8	25.8	17.6	5.7
60	25.0	22.1	25.4	21.5	33.2	21.2	6.3
120	24.9	23.1	28.0	22.0	40.2	26.4	8.0
240	26.1	20.4	28.0	21.4	37.5	23.4	8.0

Table 2.7 Summary of the Pt coverage of AuNP@Pt/CNTs composites prepared by immersion in different Pt halide solutions with concentration of 0.08 mM under different immersion times.

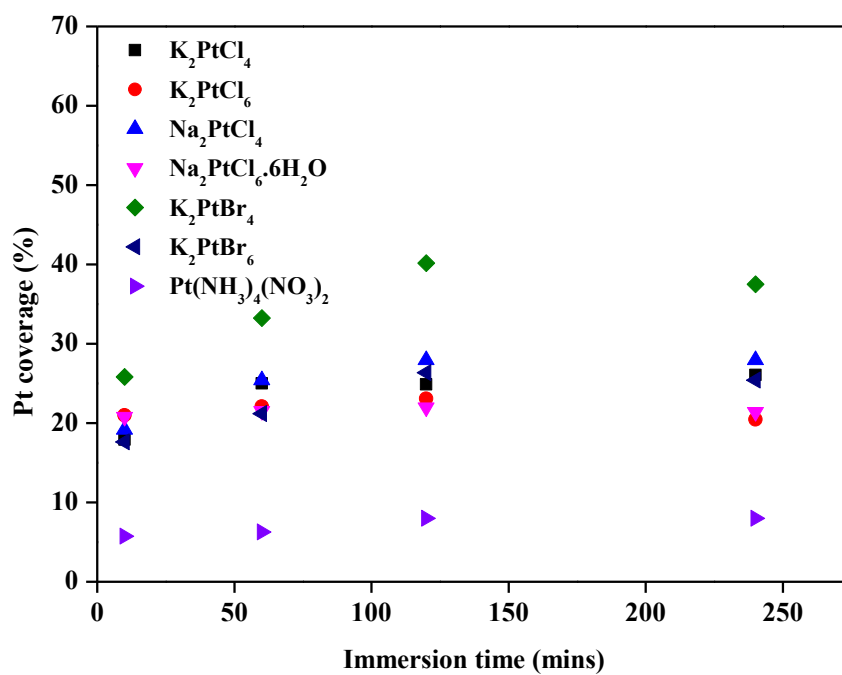


Figure 2.30 The relationship between the immersion time and Pt coverage.

The previous electrochemical results show that the Pt coverage does not increase significantly by immersing the GCE coated with the AuNP/CNTs composite in Pt halide solutions with the low concentration of 0.08 mM under longer immersion time of 60 min, 120 min and 240 min. It is suggested that the concentration of Pt halide solution is the limiting factor to control Pt coverage. Also, it is found that the Pt coverage can be controlled by  $[\text{PtX}_4]^{2-}$  ( $X = \text{Cl}$  or  $\text{Br}$ ) and  $\text{Pt}(\text{NH}_3)_4(\text{NO}_3)_2$  solutions of different concentrations. Hence, slightly higher concentration of Pt halide solutions of 5.12 mM was used under longer immersion time of 60 min, 120 min and 240 min to study the Pt coverage and the related specific area activity towards the oxidations of formic acid and methanol.

As shown in Figure 2.31 and Table 2.8, switching the concentration of Pt halide solutions from 0.08 mM to 5.12 mM, the Pt coverage increases significantly when the immersion time increases. This is because more Pt halide ions deposit on the surface of AuNPs with the increasing immersion time.[62] The magnitude of Pt coverage increase by  $\text{K}_2\text{PtBr}_4$  solution is highest while that by  $\text{Pt}(\text{NH}_3)_4(\text{NO}_3)_2$  solution is lowest.

Immersion time (min)	Pt coverage (%)			
	K <sub>2</sub> PtCl <sub>4</sub>	Na <sub>2</sub> PtCl <sub>4</sub>	K <sub>2</sub> PtBr <sub>4</sub>	Pt(NH <sub>3</sub> ) <sub>4</sub> (NO <sub>3</sub> ) <sub>2</sub>
10	34.9	34.5	64.9	16.1
60	39.4	37.2	80.8	20.0
120	49.9	49.5	90.2	31.7
240	58.5	60.4	117.3	34.3

Table 2.8 Summary of the Pt coverage of AuNP@Pt/CNTs composites prepared by immersion in different Pt halide solutions with concentration of 5.12 mM under different immersion times.

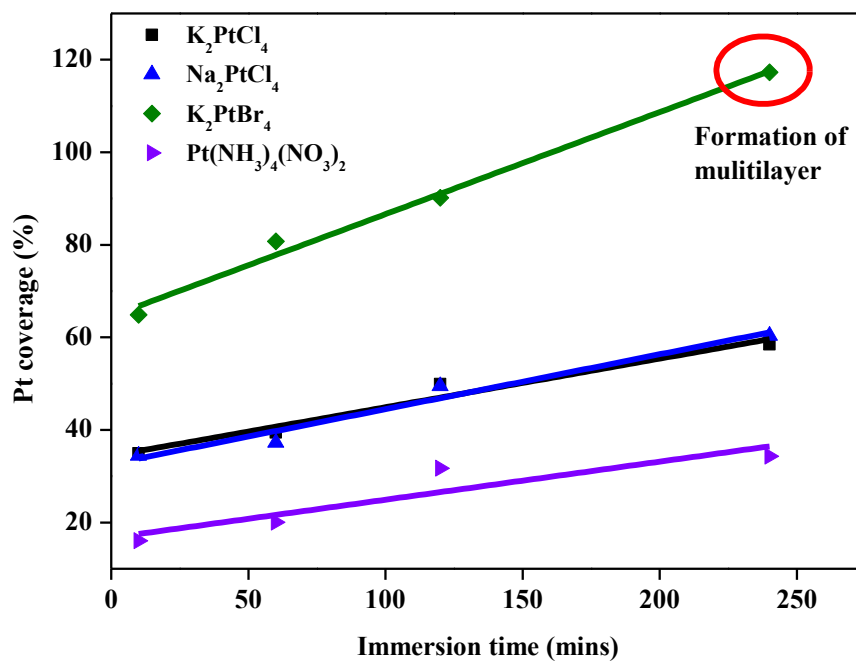


Figure 2.31 The relationship between the immersion time and Pt coverage.

Both Pt coverages achieved by  $K_2PtCl_4$  and  $Na_2PtCl_4$  solutions under the same immersion time are comparable because the adsorption of Pt halide ions on AuNPs is independent of the cations and solely dependent of Pt halide ions as proved before. For AuNP/CNTs composites prepared by  $K_2PtCl_4$  and  $Na_2PtCl_4$  solutions, the Pt coverage increases from 34.9 % to 58.5 % and from 34.5 % to 60.4 % respectively when the immersion time increases from 10 min to 240 min.

Compared with  $K_2PtCl_4$  solution, Pt coverage achieved by  $K_2PtBr_4$  is higher, ranging from 64.9 % to 117.3 %, under the same immersion time due to the stronger affinity of Br than Cl.[52, 56] Besides, under the immersion time of 240 min, the Pt coverage obtained is higher than 100 %. For other Pt halide ions adsorption, the difference between the decrease in cathodic peak of the Au oxide reduction and the increase in cathodic peak of the Pt oxide reduction is within 5 %. Thus, it is proposed that  $[PtBr_4]^{2-}$  ions may deposit onto the AuNPs surface in the form of multilayer structure.[52]

For AuNP@Pt/CNTs composite prepared by  $Pt(NH_3)_4(NO_3)_2$  solution, the magnitude of Pt coverage increase is low, which is ranging from 16.1 % to 34.3 %. This may be due to the positively charged  $[Pt(NH_3)_4]^{2+}$  ion hindering the ion adsorption process.

### Electrooxidation of formic acid

The electrocatalysis of formic acid oxidation was performed by conducting CV of AuNP@Pt/CNTs composites on GCE in 0.025M HCOOH + 0.1M H<sub>2</sub>SO<sub>4</sub> solution in the potential region from -0.2 V to 0.9 V with a scan rate of 50 mVs<sup>-1</sup>. It is known that CNTs and Au are not active towards the oxidation of formic acid.[21, 25, 26, 36] The specific area activity towards the oxidation of formic acid is calculated by normalizing current to the ECSA of Pt of AuNP@Pt/CNTs composites. The relationship between Pt coverage and specific area activity towards the oxidation of formic acid is presented in Table 2.9 and Figure 2.32. From Figure 2.32, the specific area activity towards the oxidation of formic acid decreases with increasing Pt coverage due to ensemble effect.[21]

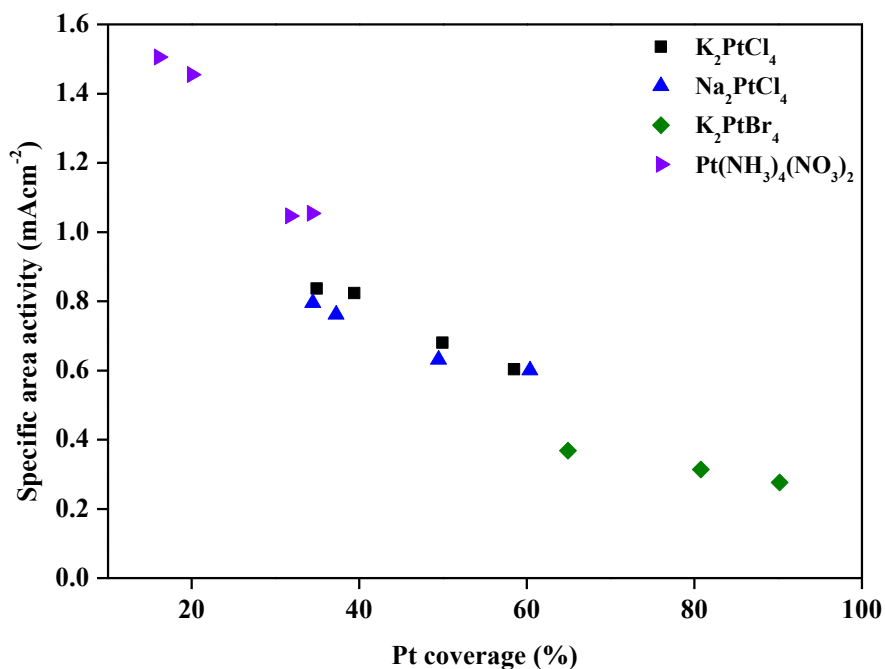


Figure 2.32 The relationship between Pt coverage and specific area activity towards the oxidation of formic acid.

Concentration of Pt halides (mM)	Immersion time (min)	K <sub>2</sub> PtCl <sub>4</sub>		Na <sub>2</sub> PtCl <sub>4</sub>		K <sub>2</sub> PtBr <sub>4</sub>		Pt(NH <sub>3</sub> ) <sub>4</sub> (NO <sub>3</sub> ) <sub>2</sub>	
		Pt coverage (%)	Specific area activity (mAcm <sup>-2</sup> )	Pt coverage (%)	Specific area activity (mAcm <sup>-2</sup> )	Pt coverage (%)	Specific area activity (mAcm <sup>-2</sup> )	Pt coverage (%)	Specific area activity (mAcm <sup>-2</sup> )
5.12	10	34.9	0.84	34.5	0.80	64.9	0.37	16.1	1.51
	60	39.4	0.82	37.2	0.76	80.8	0.31	20.0	1.46
	120	49.9	0.68	49.5	0.63	90.2	0.28	31.7	1.05
	240	58.5	0.60	60.4	0.60	117.3	0.19	34.3	1.05

Table 2.9 Summary of Pt coverage by different Pt halide solutions with concentration of 5.12 mM under different immersion times and the corresponding specific area activity towards the oxidation of formic acid.

Figure 2.33 and Figure 2.34 present the CVs of both AuNP@Pt/CNTs composites prepared by  $K_2PtCl_4$  and  $Na_2PtCl_4$  solutions towards the oxidation of formic acid respectively. They achieve comparable catalytic activities towards the oxidation of formic acid due to similar Pt coverage achieved under same immersion time. For AuNP/CNTs composites prepared by  $K_2PtCl_4$  and  $Na_2PtCl_4$  solutions, the specific area activity decreases from  $0.84 \text{ mAcm}^{-2}$  to  $0.60 \text{ mAcm}^{-2}$ ; and from  $0.80 \text{ mAcm}^{-2}$  to  $0.61 \text{ mAcm}^{-2}$  under increasing Pt coverage from 34.9 % to 58.5 %; and from 34.5 % to 60.4 % respectively when the immersion time increases from 10 min to 240 min. Also, the shoulder peak at around 0.6 V indicating the indirect oxidation of formic acid becomes prominent for both AuNP@Pt/CNTs composites. These can be attributed to the ensemble effect.[21, 24]

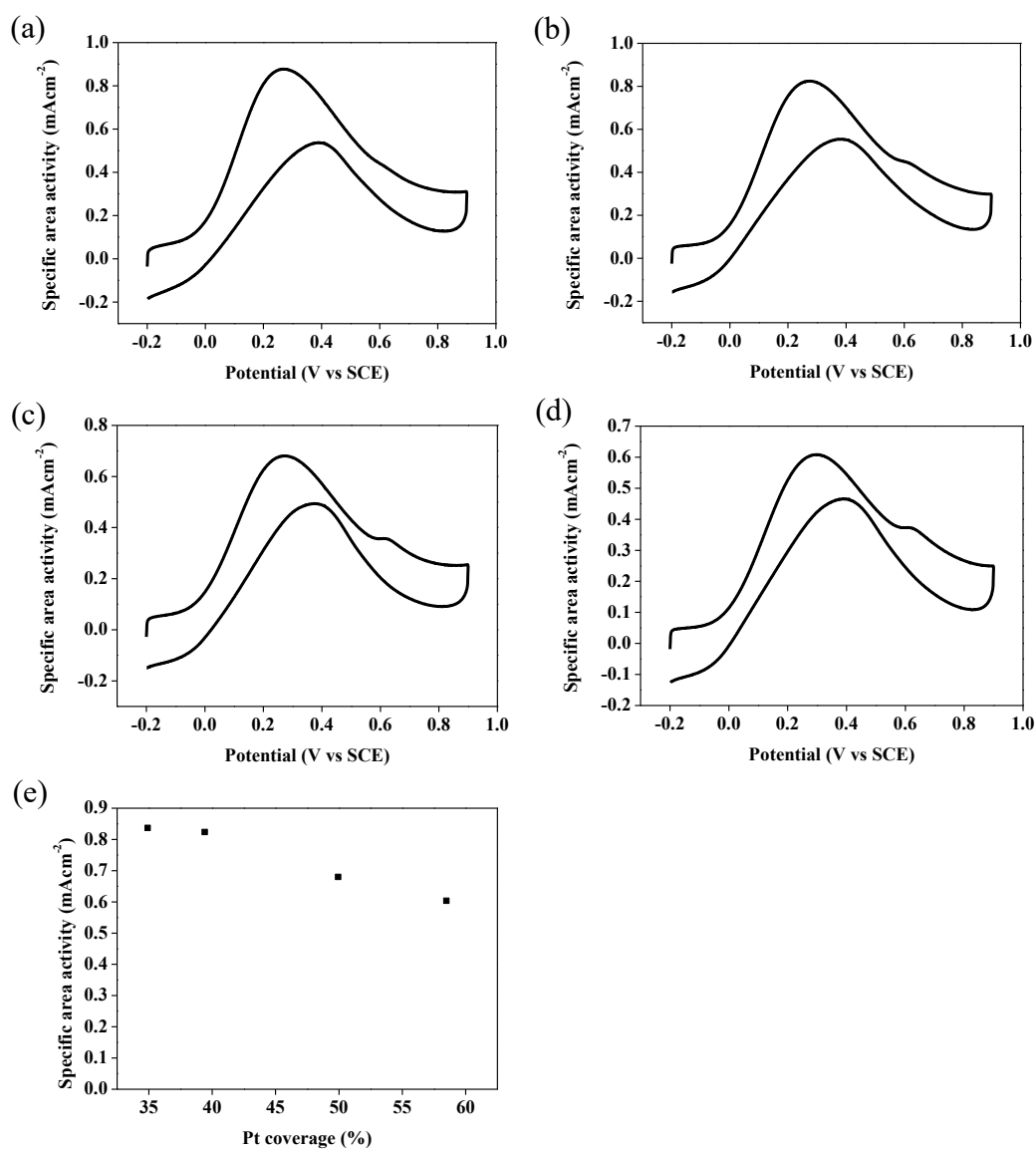


Figure 2.33 CVs of AuNP@Pt/CNTs composite prepared by  $K_2PtCl_4$  solution with Pt coverage of (a) 34.9 %, (b) 39.4 %, (c) 49.9 % and (d) 58.5 % in 0.025 M HCOOH + 0.1 M  $H_2SO_4$  solution. Scan rate,  $50\text{ mVs}^{-1}$ . (e) The relationship between Pt coverage and the electrocatalytic activity towards the oxidation of HCOOH.

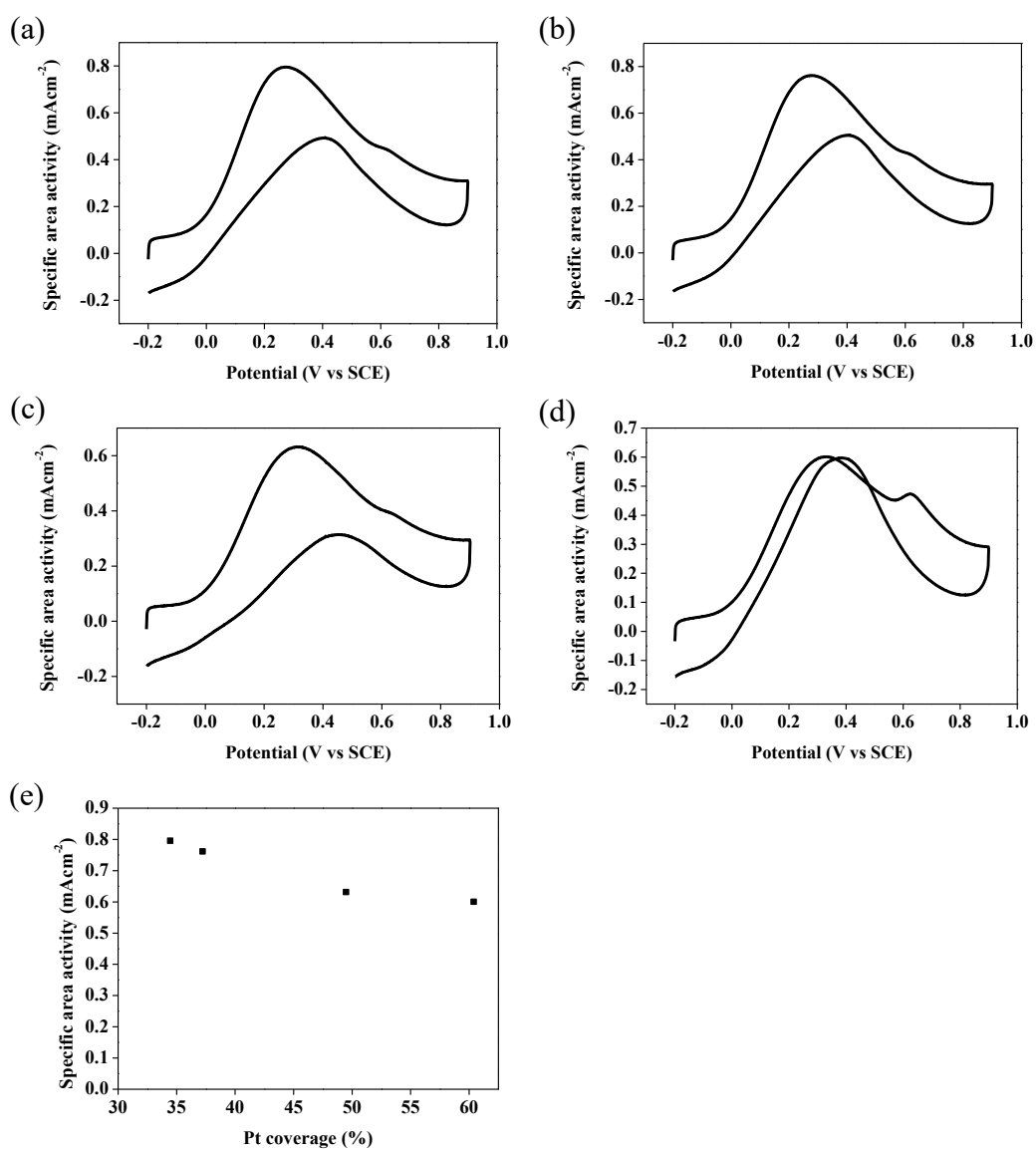


Figure 2.34 CVs of AuNP@Pt/CNTs composite prepared by  $\text{Na}_2\text{PtCl}_4$  solution with Pt coverage of (a) 34.5 %, (b) 37.2 %, (c) 49.5 % and (d) 60.4 % in 0.025 M  $\text{HCOOH}$  + 0.1 M  $\text{H}_2\text{SO}_4$  solution. Scan rate,  $50 \text{ mVs}^{-1}$ . (e) The relationship between Pt coverage and the electrocatalytic activity towards the oxidation of  $\text{HCOOH}$ .

Figure 2.35 displays the AuNP@Pt/CNTs composite prepared by  $K_2PtBr_4$  solution towards the oxidation of formic acid. They achieve lower catalytic activity towards the direct oxidation of formic acid when compared with  $K_2PtCl_4$  solution under the same immersion time. Under increasing Pt coverage from 64.9 % to 117.3 %, a decreasing specific area activity is achieved towards the direct oxidation of formic acid from  $0.37 \text{ mAcm}^{-2}$  to  $0.19 \text{ mAcm}^{-2}$ . Higher Pt coverage of AuNP@Pt/CNTs composite prepared by  $K_2PtBr_4$  solution enhances ensemble effect which lowers the catalytic activity towards the direct oxidation of formic acid. Also, the signal of indirect oxidation of formic acid indicated by the shoulder peak at around 0.6 V becomes stronger under increasing Pt coverage due to ensemble effect.[21, 24]

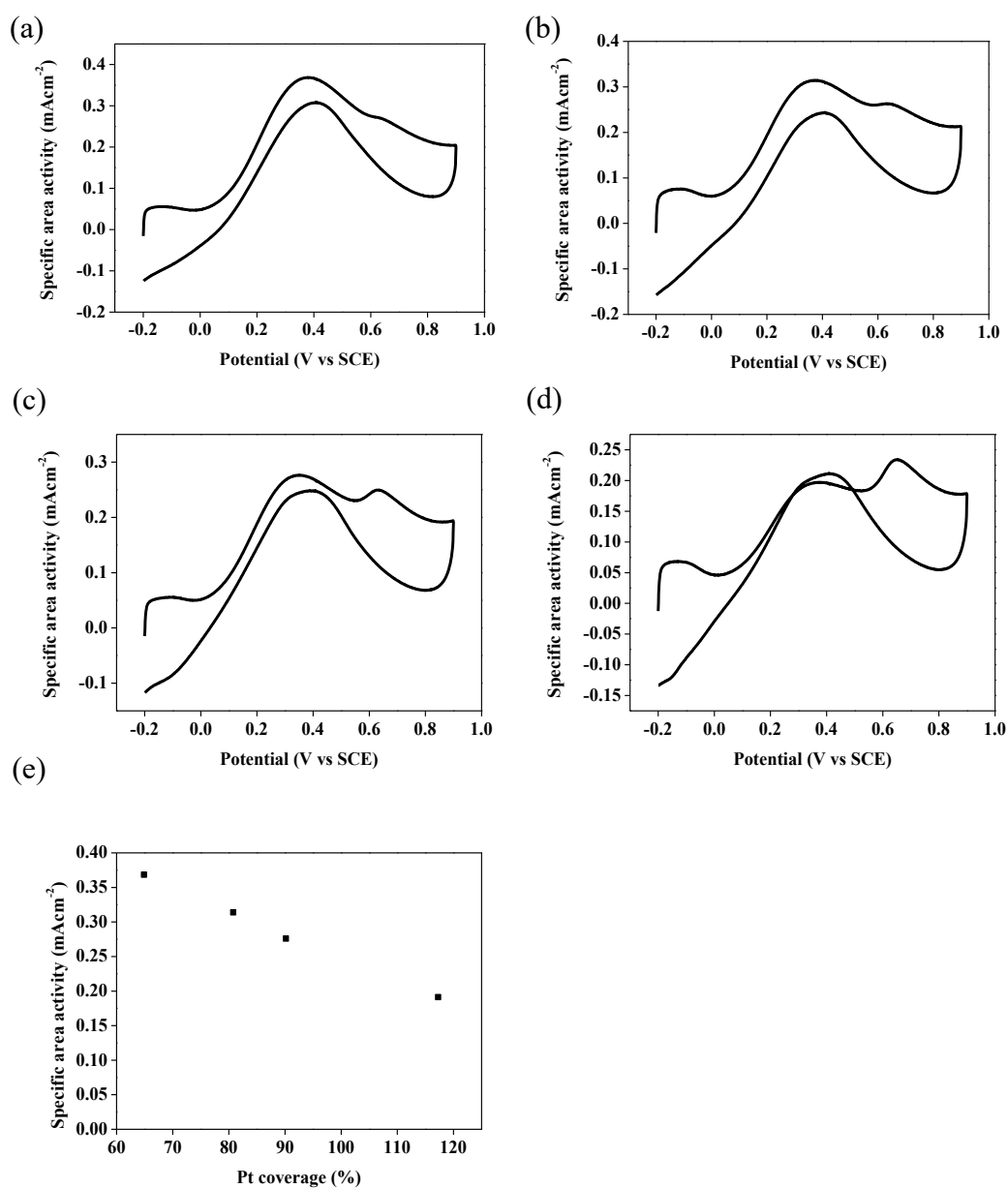


Figure 2.35 CVs of AuNP@Pt/CNTs composite prepared by  $K_2PtBr_4$  solution with Pt coverage of (a) 64.8 %, (b) 80.8 %, (c) 90.2 % and (d) 117.3 % in 0.025 M HCOOH + 0.1 M  $H_2SO_4$  solution. Scan rate,  $50\text{ mVs}^{-1}$ . (e) The relationship between Pt coverage and the electrocatalytic activity towards the oxidation of HCOOH.

Figure 2.36 shows the AuNP@Pt/CNTs composite prepared by  $\text{Pt}(\text{NH}_3)_4(\text{NO}_3)_2$  solution towards the oxidation of formic acid. Higher catalytic activity is achieved towards the direct oxidation of formic acid when compared with  $\text{K}_2\text{PtCl}_4$  solution under same immersion time. Under increasing Pt coverage from 16.1 % to 34.3 %, a decreasing specific area activity is achieved towards the direct oxidation of formic acid from  $1.51 \text{ mAcm}^{-2}$  to  $1.05 \text{ mAcm}^{-2}$ . Due to lower Pt coverage achieved by  $\text{Pt}(\text{NH}_3)_4(\text{NO}_3)_2$  solution, the AuNP@Pt/CNTs composite follows the direct oxidation of formic acid.

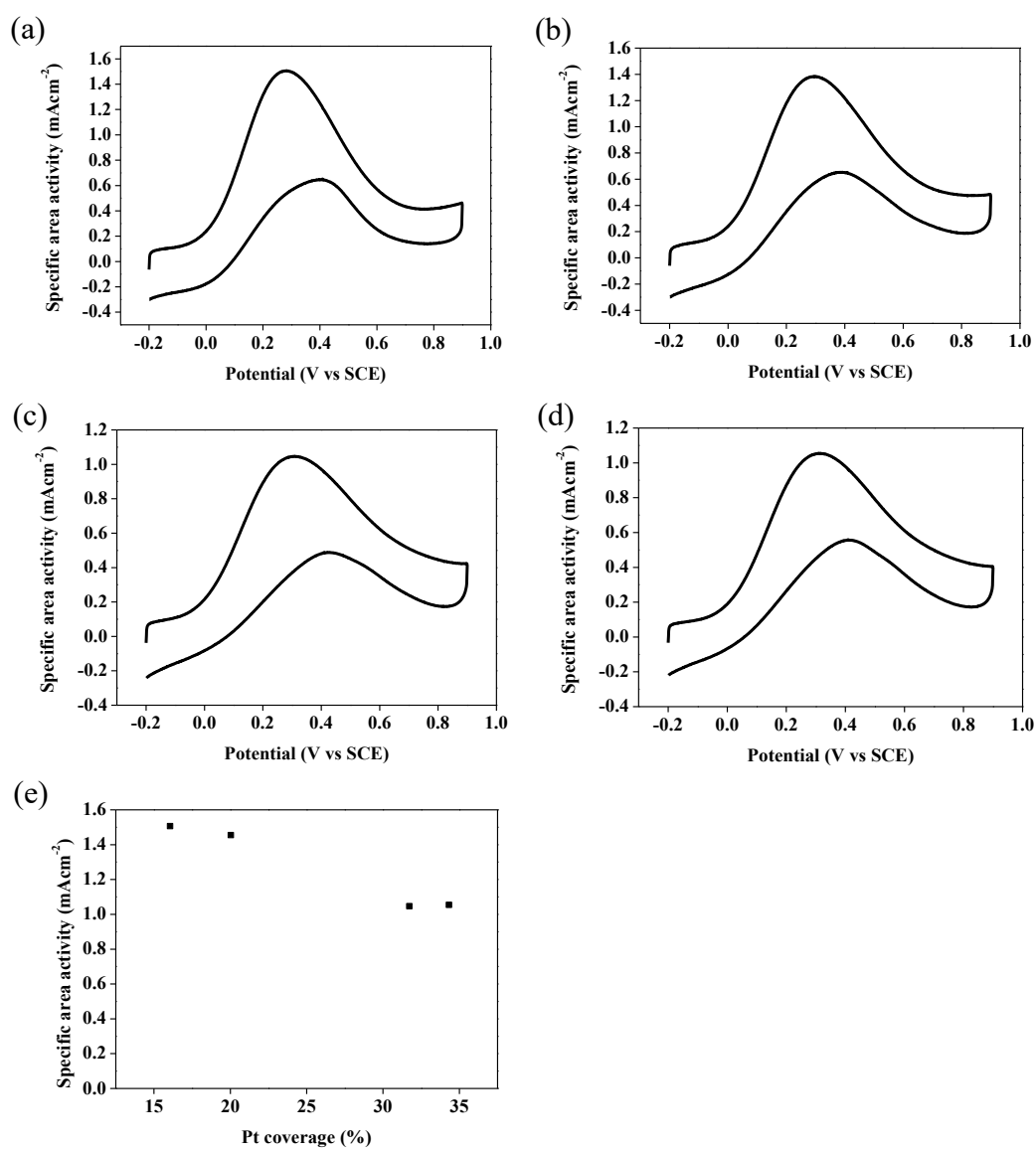


Figure 2.36 CVs of AuNP@Pt/CNTs composite prepared by  $\text{Pt}(\text{NH}_3)_4(\text{NO}_3)_2$  solution with Pt coverage of (a) 16.1 %, (b) 20.0 %, (c) 31.7 % and (d) 34.3 % in 0.025 M  $\text{HCOOH}$  + 0.1 M  $\text{H}_2\text{SO}_4$  solution. Scan rate,  $50 \text{ mVs}^{-1}$ . (e) The relationship between Pt coverage and the electrocatalytic activity towards the oxidation of  $\text{HCOOH}$ .

### Electrooxidation of methanol

The electrooxidation of methanol (MeOH) was investigated by conducting CV of AuNP@Pt/CNTs composites on the GCE in 0.1 M MeOH + 0.1 M H<sub>2</sub>SO<sub>4</sub> solution in the potential region from -0.2 V to 0.9 V with a scan rate of 50 mVs<sup>-1</sup>. It is known that CNTs and Au are not active towards the oxidation of methanol.[61] The specific area activity towards the oxidation of methanol is calculated by normalizing the current to the ECSA of Pt of AuNP@Pt/CNTs composites. The specific area activity towards the oxidation of methanol is presented in Table 2.10 and Figure 2.37. Generally, the specific area activity towards the oxidation of methanol increases with increasing Pt coverage.

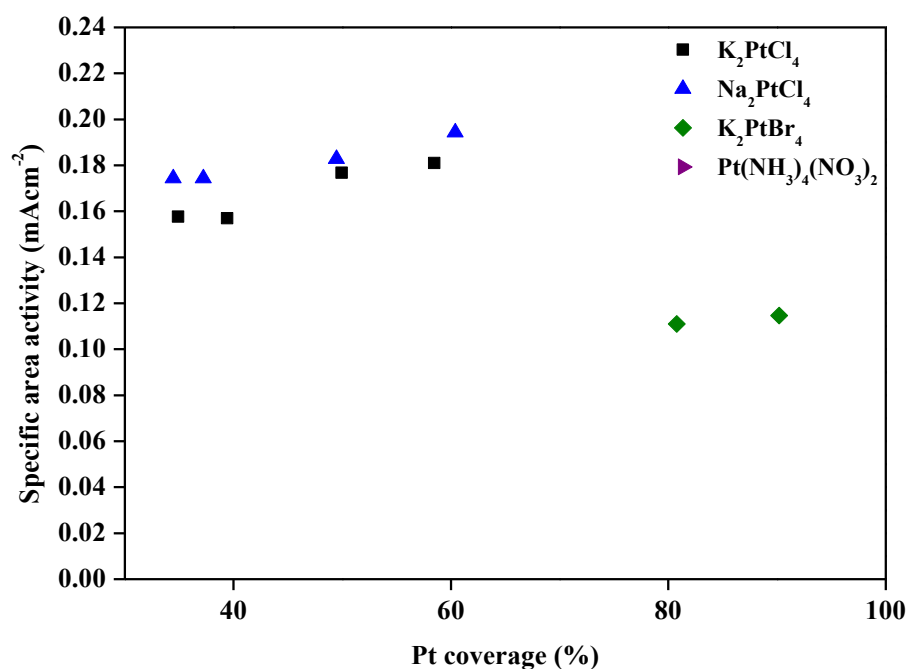


Figure 2.37 The relationship between Pt coverage and specific area activity towards the oxidation of methanol.

Concentration of Pt halides (mM)	Immersion time (min)	K <sub>2</sub> PtCl <sub>4</sub>		Na <sub>2</sub> PtCl <sub>4</sub>		K <sub>2</sub> PtBr <sub>4</sub>		Pt(NH <sub>3</sub> ) <sub>4</sub> (NO <sub>3</sub> ) <sub>2</sub>	
		Specific		Specific		Specific		Specific	
		Pt coverage	area	Pt coverage	area	Pt coverage	area	Pt coverage	area
		(%)	activity (mAcm <sup>-2</sup> )	(%)	activity (mAcm <sup>-2</sup> )	(%)	activity (mAcm <sup>-2</sup> )	(%)	activity (mAcm <sup>-2</sup> )
5.12	10	34.9	0.16	34.5	0.17	64.9	-	16.1	-
	60	39.4	0.16	37.2	0.18	80.8	0.11	20.0	-
	120	49.9	0.18	49.5	0.18	90.2	0.11	31.7	-
	240	58.5	0.18	60.4	0.19	117.3	0.16	34.3	-

Table 2.10 Summary of Pt coverage by different Pt halide solutions with concentration of 5.12 mM under different immersion times and the corresponding specific area activity towards the oxidation of methanol.

Figure 2.38 and Figure 2.39 display the AuNP@Pt/CNTs composites prepared by  $K_2PtCl_4$  and  $Na_2PtCl_4$  solutions of 5.12 mM under different immersion times towards the oxidation of methanol respectively. They achieve similar catalytic activities towards the oxidation of methanol due to similar Pt coverage achieved under same immersion time. For AuNP@Pt/CNTs composites prepared by  $K_2PtCl_4$  and  $Na_2PtCl_4$  solutions, the specific area activity increases from 0.16  $mAcm^{-2}$  to 0.18  $mAcm^{-2}$ ; and from 0.17  $mAcm^{-2}$  to 0.19  $mAcm^{-2}$  under increasing Pt coverage from 34.9 % to 58.5 %; and from 34.5 % to 60.4 % respectively when the immersion time increases from 10 min to 240 min. Both AuNP@Pt/CNTs composites with the Pt coverage over 30 % become active towards the oxidation of MeOH. It is believed that higher Pt coverage increases the availability of continuous Pt sites for the oxidation of methanol.[23, 63]

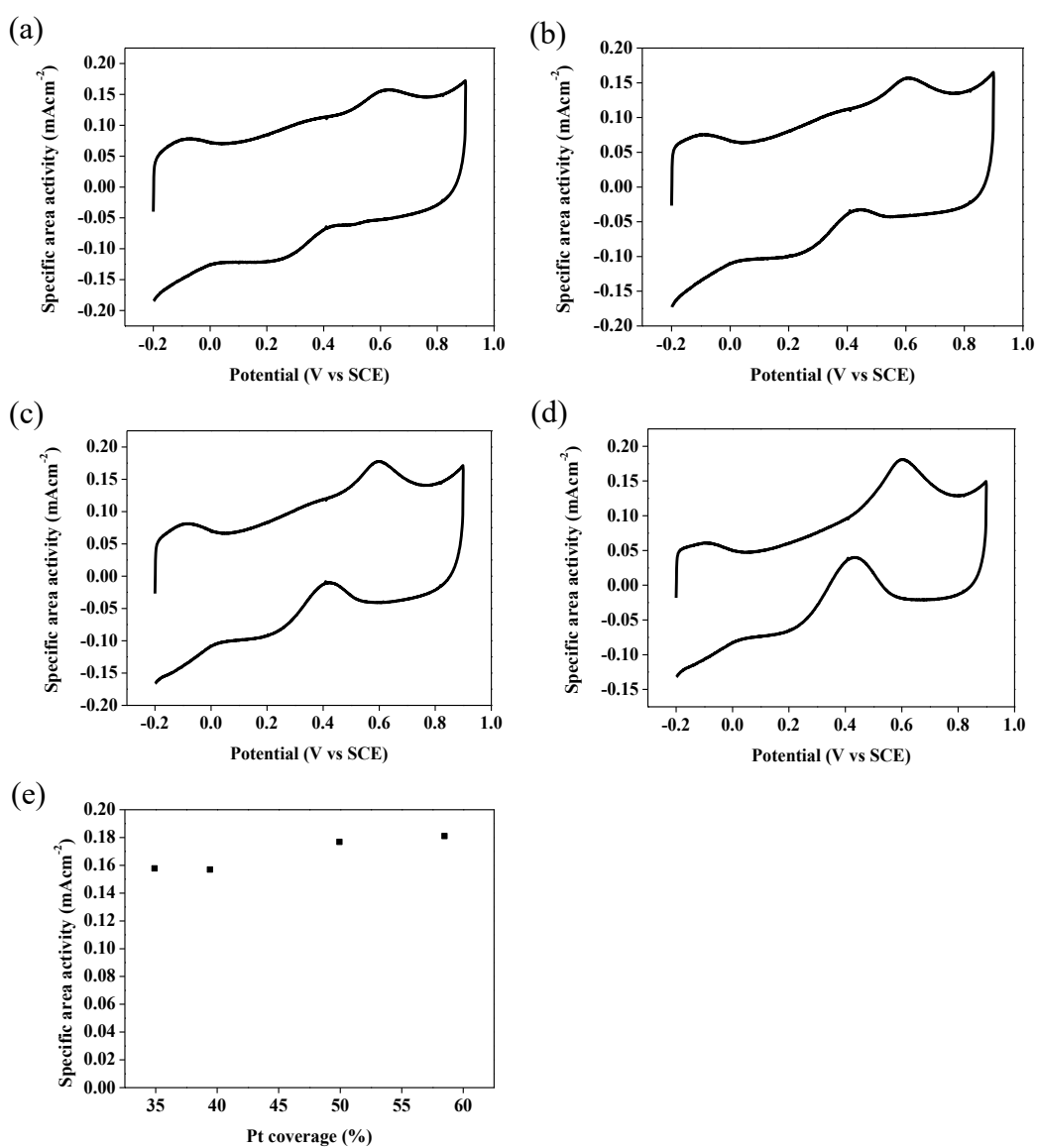


Figure 2.38 CVs of AuNP@Pt/CNTs composite prepared by  $K_2PtCl_4$  solution with Pt coverage of (a) 34.9 %, (b) 39.4 %, (c) 49.9 % and (d) 58.5 % in 0.1 M MeOH + 0.1 M  $H_2SO_4$  solution. Scan rate, 50  $mVs^{-1}$ . (e) The relationship between Pt coverage and the electrocatalytic activity towards the oxidation of MeOH.

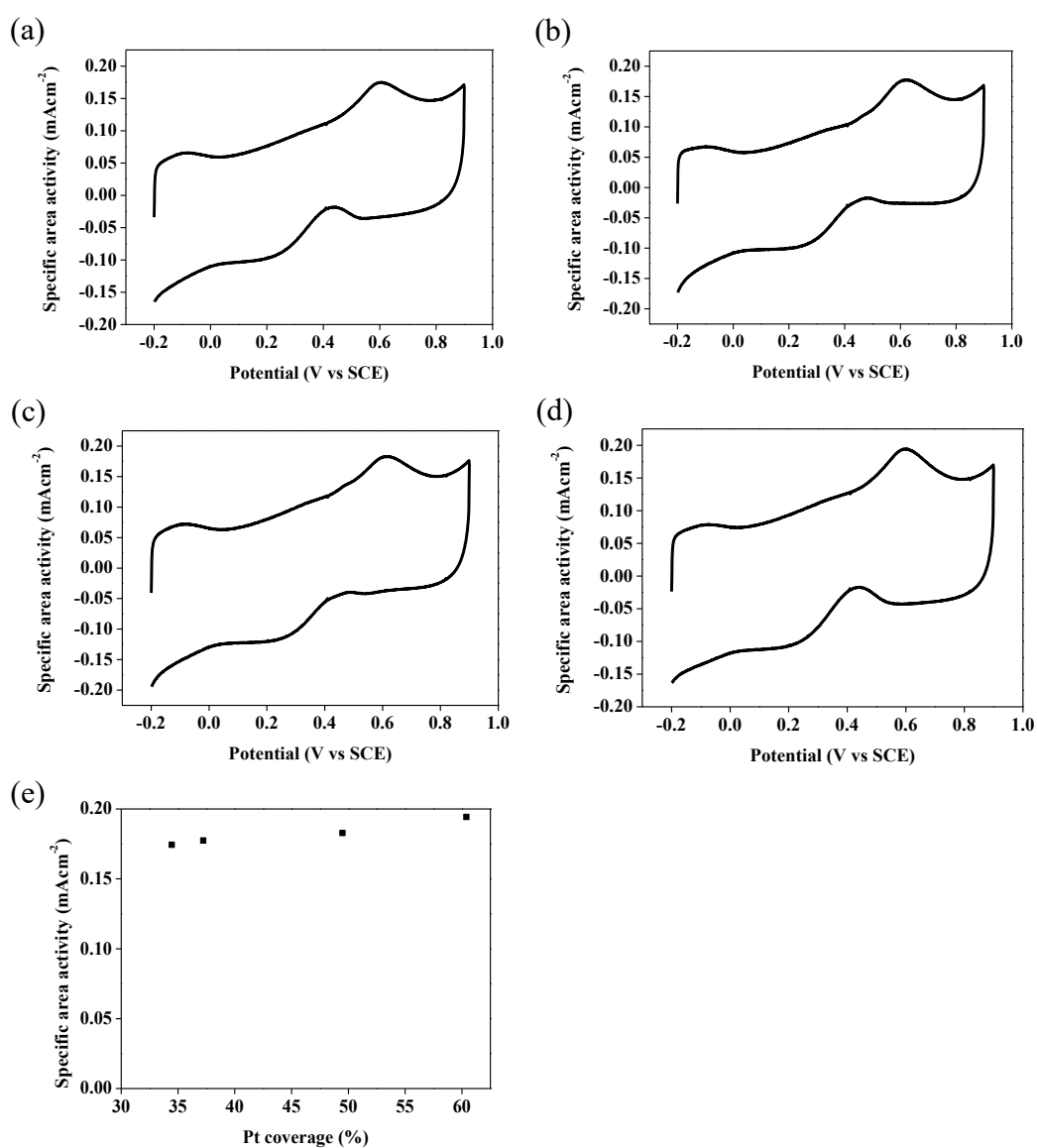


Figure 2.39 CVs of AuNP@Pt/CNTs composite prepared by Na<sub>2</sub>PtCl<sub>4</sub> solution with Pt coverage of (a) 34.5 %, (b) 37.2 %, (c) 49.5 % and (d) 60.4 % in 0.1 M MeOH + 0.1 M H<sub>2</sub>SO<sub>4</sub> solution. Scan rate, 50 mVs<sup>-1</sup>. (e) The relationship between Pt coverage and the electrocatalytic activity towards the oxidation of MeOH.

The AuNP@Pt/CNTs composite prepared by  $K_2PtBr_4$  solution of 5.12 mM under different immersion times towards the oxidation of methanol is shown in Figure 2.40. The AuNP@Pt/CNTs composite with the Pt coverage over 80 % become active towards the oxidation of methanol as displayed in Figure 2.40 (b). The specific area activity decreases from  $0.11 \text{ mAcm}^{-2}$  to  $0.16 \text{ mAcm}^{-2}$  under increasing Pt coverage from 80.8 % to 117.3 % when the immersion time increases from 60 min to 240 min. This differs from the AuNP@Pt/CNTs composites prepared  $K_2PtCl_4$  solution with the Pt coverage over 30 % becoming active towards the oxidation of methanol. Also, their catalytic activity towards the oxidation of methanol is lower when compared with  $K_2PtCl_4$  solution. It is possible that the existence of Br may interrupt the Pt neighboring continuous sites for the oxidation of methanol.  $K_2PtCl_4$  solution may be a better option to synthesize AuNP@Pt/CNTs for methanol oxidation because the usage of Pt is lower.

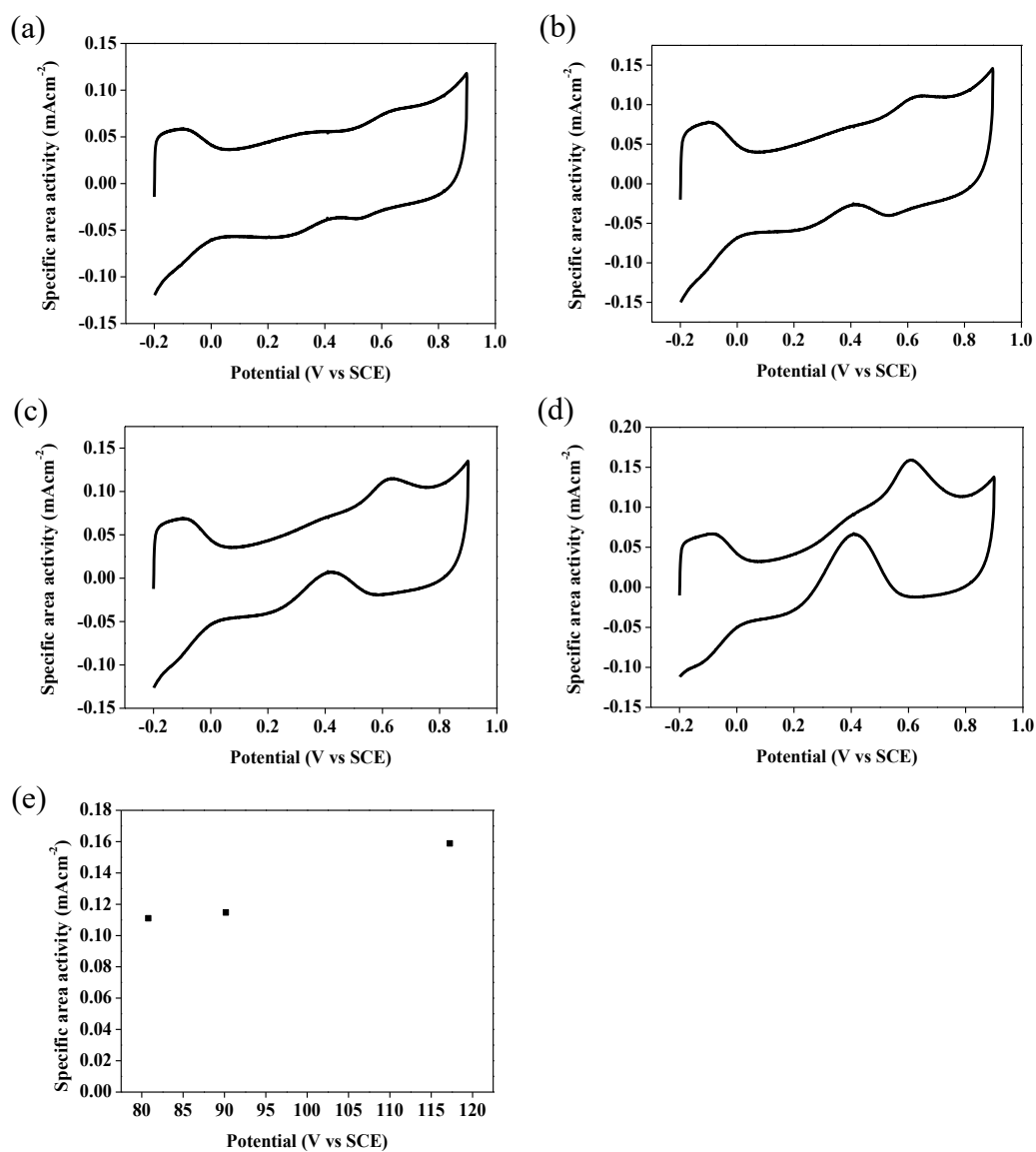


Figure 2.40 CVs of AuNP@Pt/CNTs composite prepared by  $K_2PtBr_4$  solution with Pt coverage of (a) 64.9 %, (b) 80.8 %, (c) 90.2 % and (d) 117.3 % in 0.1M MeOH + 0.1M  $H_2SO_4$  solution. Scan rate, 50  $mVs^{-1}$ . (e) The relationship between Pt coverage and the electrocatalytic activity towards the oxidation of MeOH.

Figure 2.41 displays the CVs of AuNP@Pt/CNTs composite prepared by  $\text{Pt}(\text{NH}_3)_4(\text{NO}_3)_2$  solution of 5.12 mM under different immersion times towards the oxidation of methanol. It is observed that they are inactive towards the oxidation of methanol even the Pt coverage over 30 % when compared with  $\text{K}_2\text{PtCl}_4$  solution.

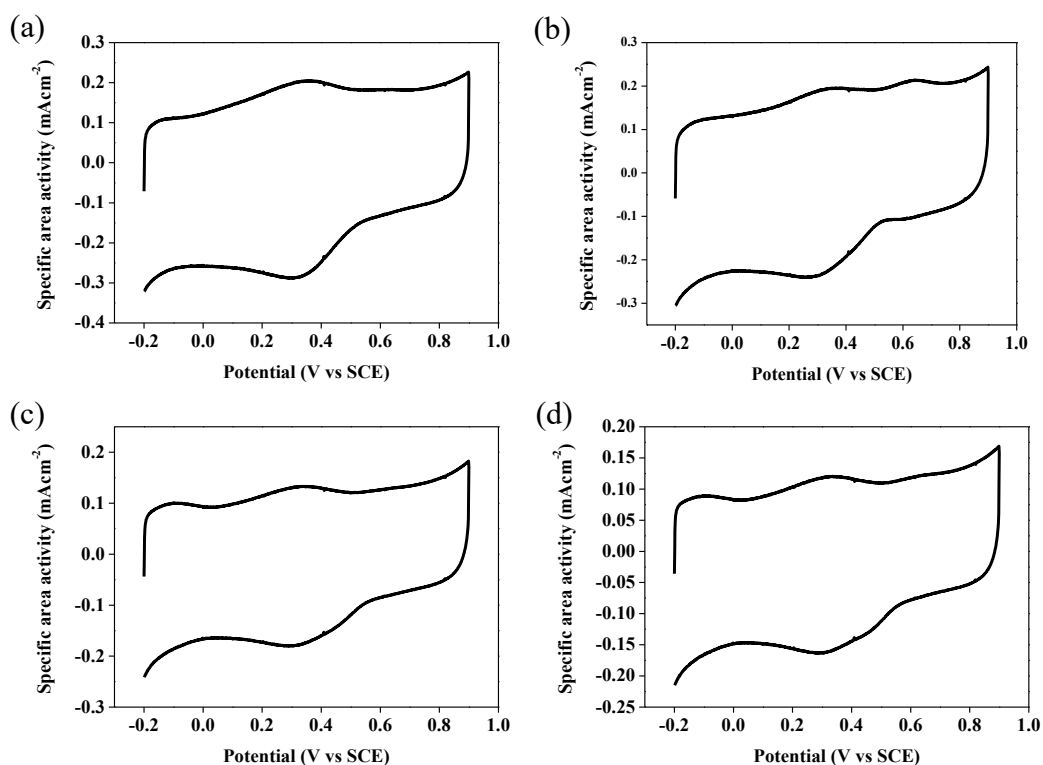


Figure 2.41 CVs of AuNP@Pt/CNTs composite prepared by  $\text{Pt}(\text{NH}_3)_4(\text{NO}_3)_2$  solution with Pt coverage of (a) 16.1 %, (b) 20.0 %, (c) 31.7 % and (d) 34.3 % in 0.1M MeOH + 0.1M  $\text{H}_2\text{SO}_4$  solution. Scan rate,  $50 \text{ mVs}^{-1}$ .

As shown in the results of electrochemical characterizations, the Pt coverages increase under longer immersion time in Pt halide solutions of 5.12 mM. It is suggested that apart from varying the concentration of Pt halide solutions, higher Pt coverage can be achieved by immersion in  $[\text{PtX}_4]^{2-}$  ions solutions with slightly higher concentration of 5.12 mM under longer immersion time. This can reduce the use of Pt, which reduces the cost of catalysts.

However,  $[\text{PtCl}_4]^{2-}$  and  $[\text{PtBr}_4]^{2-}$  ions exhibit different adsorption affinity and electrocatalytic activity towards the oxidation of formic acid and methanol even they have same coordination geometries of square planar. For  $[\text{PtCl}_4]^{2-}$  ions solutions, the AuNP@Pt/CNTs composites with the Pt coverage of greater 30 % start becoming active to indirect oxidation of formic acid and oxidation of methanol. However, for  $[\text{PtBr}_4]^{2-}$  ions solutions, the AuNP@Pt/CNTs composites are not active to indirect oxidation of formic acid and oxidation of methanol until the Pt coverage reaches 80 %. The existence of Br may interrupt the Pt neighboring continuous sites for the oxidation of methanol.

The results demonstrate that the AuNP@Pt/CNTs composites with different Pt coverage were easily synthesized by changing Pt halide solutions, concentrations and immersion time, which reduces the use of Pt and enhances fuel selectivity.

### 2.3 Summary

AuNP/CNTs composite was successfully synthesized and used as a template for adsorption of Pt halides followed by *in-situ* electrochemical reduction to prepare platinum-gold core-shell (AuNP@Pt) nanostructures. Their electrocatalytic activities towards formic acid and methanol oxidations were studied.

1. AuNP/CNTs composite was successfully synthesized with the Au loading of 16.2 %. TEM analysis show the AuNPs are in spherical morphology with the size of  $5.4 \pm 2.0$  nm. Both TEM and XRD analyses suggest that the AuNPs are adopting a fcc structure.
2. AuNP@Pt/CNTs composites were prepared by Pt halide ion adsorption onto AuNP/CNTs composite followed by *in-situ* electrochemical reduction. Electrochemical investigations suggest different Pt halide solutions show different halide ion adsorption affinity and different electrocatalytic activity towards the oxidations of formic acid and methanol.
3. Varying the concentrations of  $[\text{PtX}_4]^{2-}$  ion and  $\text{Pt}(\text{NH}_3)_4(\text{NO}_3)_2$  solutions could control the Pt coverage on AuNP/CNTs composite while  $[\text{PtX}_6]^{2-}$  ion solutions could not. Also, higher Pt coverage could be achieved by  $[\text{PtBr}_4]^{2-}$  ion solution when compared with  $[\text{PtCl}_4]^{2-}$  ion solution due to stronger affinity of Br. It is also confirmed that the ion adsorption process is dependent of Pt halide ions and independent of cations. Also, with the concentrations of  $[\text{PtX}_4]^{2-}$  ion and  $\text{Pt}(\text{NH}_3)_4(\text{NO}_3)_2$  solutions of 5.12 mM, varying the immersion time could also control the Pt coverage on AuNP/CNTs composite.

4. The electrocatalysis studies show that all the AuNP@Pt/CNTs composite with low Pt coverage of lower than 30 % were active to direct oxidation of formic acid. The Pt coverage and specific area activity were optimized to 11.0 % and 1.80 mAcm<sup>-2</sup> respectively. The AuNP@Pt/CNTs composite prepared by [PtCl<sub>4</sub>]<sup>2-</sup> ion solution with Pt coverage of higher than 30 % and prepared by [PtBr<sub>4</sub>]<sup>2-</sup> ion solution with Pt coverage of higher than 80 % start becoming active to indirect oxidations of formic acid and methanol.
  
5. The utilization of Pt and its fuel selectivity are enhanced by simply controlling Pt halide solutions, concentrations and immersion time to synthesize the AuNP@Pt/CNTs composites with different Pt coverage.

## REFERENCES

- [1] P.M. Ajayan, O.Z. Zhou, Applications of carbon nanotubes, Carbon nanotubes, Springer2001, pp. 391-425.
- [2] W. Yang, P. Thordarson, J.J. Gooding, S.P. Ringer, F. Braet, Nanotechnology, 18 (2007) 412001.
- [3] J. Planeix, N. Coustel, B. Coq, V. Brotons, P. Kumbhar, R. Dutartre, P. Geneste, P. Bernier, P. Ajayan, Journal of the American Chemical Society, 116 (1994) 7935-7936.
- [4] K. Balasubramanian, M. Burghard, Small, 1 (2005) 180-192.
- [5] E.T. Thostenson, Z. Ren, T.-W. Chou, Composites science and technology, 61 (2001) 1899-1912.
- [6] M.S. Saha, A. Kundu, Journal of Power Sources, 195 (2010) 6255-6261.
- [7] H. Zhu, C. Xu, D. Wu, B. Wei, R. Vajtai, P. Ajayan, Science, 296 (2002) 884-886.
- [8] P. Jackson, N.R. Jacobsen, A. Baun, R. Birkedal, D. Kühnel, K.A. Jensen, U. Vogel, H. Wallin, Chemistry Central Journal, 7 (2013) 154.
- [9] M.F. De Volder, S.H. Tawfick, R.H. Baughman, A.J. Hart, science, 339 (2013) 535-539.
- [10] T.W. Odom, J.H. Hafner, C.M. Lieber, Scanning probe microscopy studies of carbon nanotubes, Carbon Nanotubes, Springer2001, pp. 173-211.
- [11] I.D. Rosca, F. Watari, M. Uo, T. Akasaka, Carbon, 43 (2005) 3124-3131.
- [12] A. Osorio, I. Silveira, V. Bueno, C. Bergmann, Applied Surface Science, 255 (2008) 2485-2489.
- [13] Y. Peng, H. Liu, Industrial & engineering chemistry research, 45 (2006) 6483-6488.
- [14] K. Balasubramanian, M. Friedrich, C. Jiang, Y. Fan, A. Mews, M. Burghard,

- K. Kern, *Advanced Materials*, 15 (2003) 1515-1518.
- [15] J.L. Bahr, J. Yang, D.V. Kosynkin, M.J. Bronikowski, R.E. Smalley, J.M. Tour, *Journal of the American Chemical Society*, 123 (2001) 6536-6542.
- [16] D.-Q. Yang, B. Hennequin, E. Sacher, *Chemistry of materials*, 18 (2006) 5033-5038.
- [17] R.R. Adzic, J. Zhang, K. Sasaki, M.B. Vukmirovic, M. Shao, J. Wang, A.U. Nilekar, M. Mavrikakis, J. Valerio, F. Uribe, *Topics in Catalysis*, 46 (2007) 249-262.
- [18] Y. Xing, *The Journal of Physical Chemistry B*, 108 (2004) 19255-19259.
- [19] W. Chen, J. Kim, S. Sun, S. Chen, *Langmuir*, 23 (2007) 11303-11310.
- [20] R. Muralidharan, M. McIntosh, X. Li, *Physical Chemistry Chemical Physics*, 15 (2013) 9716-9725.
- [21] N. Kristian, Y. Yan, X. Wang, *Chemical communications*, (2008) 353-355.
- [22] F. Zheng, W.-T. Wong, K.-F. Yung, *Nano Research*, 7 (2014) 410-417.
- [23] N. Kristian, X. Wang, *Electrochemistry Communications*, 10 (2008) 12-15.
- [24] S. Zhang, Y. Shao, G. Yin, Y. Lin, *Angewandte Chemie International Edition*, 49 (2010) 2211-2214.
- [25] S. Zhang, Y. Shao, G. Yin, Y. Lin, *Journal of Power Sources*, 195 (2010) 1103-1106.
- [26] Z. Peng, H. Yang, *Nano Research*, 2 (2009) 406-415.
- [27] I.-S. Park, K.-S. Lee, J.-H. Choi, H.-Y. Park, Y.-E. Sung, *The Journal of Physical Chemistry C*, 111 (2007) 19126-19133.
- [28] R. Xie, M. Chen, J. Wang, S. Mei, Y. Pan, H. Gu, *RSC Advances*, 5 (2015) 650-653.
- [29] C. Xu, R. Wang, M. Chen, Y. Zhang, Y. Ding, *Physical Chemistry Chemical Physics*, 12 (2010) 239-246.

- [30] Z. Zhang, Y. Wang, X. Wang, *Nanoscale*, 3 (2011) 1663-1674.
- [31] J. Xu, C. Zhang, X. Wang, H. Ji, C. Zhao, Y. Wang, Z. Zhang, *Green Chemistry*, 13 (2011) 1914-1922.
- [32] Z. Guo, X. Zhang, H. Sun, X. Dai, Y. Yang, X. Li, T. Meng, *Electrochimica Acta*, 134 (2014) 411-417.
- [33] N. Kristian, Y. Yu, P. Gunawan, R. Xu, W. Deng, X. Liu, X. Wang, *Electrochimica Acta*, 54 (2009) 4916-4924.
- [34] H. Tang, J. Chen, M. Wang, L. Nie, Y. Kuang, S. Yao, *Applied Catalysis A: General*, 275 (2004) 43-48.
- [35] H. Ataee-Esfahani, L. Wang, Y. Nemoto, Y. Yamauchi, *Chemistry of Materials*, 22 (2010) 6310-6318.
- [36] Y.-C. Bai, W.-D. Zhang, C.-H. Chen, J.-Q. Zhang, *Journal of Alloys and Compounds*, 509 (2011) 1029-1034.
- [37] J. Zhu, L. Huang, J. Zhao, Y. Wang, Y. Zhao, L. Hao, Y. Lu, *Materials Science and Engineering: B*, 121 (2005) 199-203.
- [38] K.A. Wepasnick, B.A. Smith, J.L. Bitter, D.H. Fairbrother, *Analytical and bioanalytical chemistry*, 396 (2010) 1003-1014.
- [39] Y. Mu, H. Liang, J. Hu, L. Jiang, L. Wan, *The Journal of Physical Chemistry B*, 109 (2005) 22212-22216.
- [40] G.G. Wildgoose, C.E. Banks, R.G. Compton, *Small*, 2 (2006) 182-193.
- [41] V. Datsyuk, M. Kalyva, K. Papagelis, J. Parthenios, D. Tasis, A. Siokou, I. Kallitsis, C. Galiotis, *Carbon*, 46 (2008) 833-840.
- [42] X. Feng, J. Hu, X. Chen, J. Xie, Y. Liu, *Journal of Physics D: Applied Physics*, 42 (2009) 042001.
- [43] P. Nayak, P. Santhosh, S. Ramaprabhu, *Rsc Advances*, 4 (2014) 41670-41677.

- [44] C. Chen, J. Zhang, Y. Du, X. Yang, E. Wang, *Analyst*, 135 (2010) 1010-1014.
- [45] Y. Dai, S. Chen, *ACS applied materials & interfaces*, 7 (2014) 823-829.
- [46] J.-N. Zheng, S.-S. Li, X. Ma, F.-Y. Chen, A.-J. Wang, J.-R. Chen, J.-J. Feng, *Journal of Materials Chemistry A*, 2 (2014) 8386-8395.
- [47] Y. Kim, H.J. Kim, Y.S. Kim, S.M. Choi, M.H. Seo, W.B. Kim, *The Journal of Physical Chemistry C*, 116 (2012) 18093-18100.
- [48] S. Trasatti, O. Petrii, *Journal of Electroanalytical Chemistry*, 327 (1992) 353-376.
- [49] D.F. Yancey, E.V. Carino, R.M. Crooks, *Journal of the American Chemical Society*, 132 (2010) 10988-10989.
- [50] K. Friedrich, F. Henglein, U. Stimming, W. Unkauf, *Electrochimica acta*, 45 (2000) 3283-3293.
- [51] S. Kim, C. Jung, J. Kim, C.K. Rhee, S.-M. Choi, T.-H. Lim, *Langmuir*, 26 (2010) 4497-4505.
- [52] Y. Nagahara, M. Hara, S. Yoshimoto, J. Inukai, S.-L. Yau, K. Itaya, *The Journal of Physical Chemistry B*, 108 (2004) 3224-3230.
- [53] H.-F. Waibel, M. Kleinert, L. Kibler, D. Kolb, *Electrochimica acta*, 47 (2002) 1461-1467.
- [54] K. Uosaki, S. Ye, Y. Oda, T. Haba, K.-i. Hamada, *Langmuir*, 13 (1997) 594-596.
- [55] K. Uosaki, S. Ye, H. Naohara, Y. Oda, T. Haba, T. Kondo, *The Journal of Physical Chemistry B*, 101 (1997) 7566-7572.
- [56] Z. Zhang, H. Li, F. Zhang, Y. Wu, Z. Guo, L. Zhou, J. Li, *Langmuir*, 30 (2014) 2648-2659.
- [57] J. Wang, S. Zuo, C. Lu, Y. Zu, Z. Chen, *RSC Advances*, 6 (2016)

50315-50321.

[58] J. Kim, C. Jung, C.K. Rhee, T.-h. Lim, *Langmuir*, 23 (2007) 10831-10836.

[59] M.D. Obradović, A.V. Tripković, S.L. Gojković, *Electrochimica Acta*, 55 (2009) 204-209.

[60] S. Yoshimoto, H. Ogata, K. Nishiyama, *Dalton Transactions*, 42 (2013) 15902-15905.

[61] J. Suntivich, Z. Xu, C.E. Carlton, J. Kim, B. Han, S.W. Lee, N.p. Bonnet, N. Marzari, L.F. Allard, H.A. Gasteiger, *Journal of the American Chemical Society*, 135 (2013) 7985-7991.

[62] S. Cherevko, X. Xing, C.-H. Chung, *Electrochimica Acta*, 56 (2011) 5771-5775.

[63] B. Du, Y. Tong, *The Journal of Physical Chemistry B*, 109 (2005) 17775-17780.

## Chapter 3

### Synthesis of Pd@PdPt/CNTs Alloy and Pt@Pd/CNTs

### Phase-separate Catalysts for Direct Liquid Fuel Cells

#### 3.1 Background

##### Overview of core-shell nanoparticles

Pt is commonly used for direct liquid fuel cells. However, Pt is precious, rare and easily poisoned by  $\text{CO}_{\text{ads}}$  during the oxidation of fuels.[1] These drawbacks hinder the large-scale production and commercialization of Pt. Hence, new types of Pt-based electrocatalysts are explored to improve cell performance. Recently, core-shell nanoparticles have attracted increasing attention due to the following reasons. Core-shell nanoparticle consists of a core and a shell, which are inner material and outer layer material respectively.[2] The consumption of Pt metal can be reduced by coating Pt metal onto an inexpensive metal when compared with Pt nanoparticle of same size.[3] The utilization of Pt is improved, which reduces the cost of catalysts. Apart from reducing the cost, the properties can be modified by changing the inner material. Also, as the properties of inner material would be reduced due to the coating of shell, tuning the core-to-shell ratio can control the overall properties.[4] New properties of the catalysts may be offered due to the interactions between the core and shell.[5] Based on different properties, core-shell nanoparticles can be applied in different fields including biomedical,[6] pharmaceutical,[7] electronics [8] and catalysis applications.[9]

## **Synthetic methods**

There are many synthetic methods for synthesizing Pt-based core-shell nanoparticles. The common methods include seed-mediated and galvanic replacement methods.

### **Seed-mediated method**

Seed-mediated method involves the reduction of metal precursor to seeds as a core material. The reduction of metal precursor occurs onto core forming as a shell material, resulting in a core-shell structure.

For instance, Au@Pt core-shell electrocatalysts were synthesized by the reduction of  $\text{HAuCl}_4$ , followed by the addition of  $\text{H}_2\text{PtCl}_6$ .  $[\text{AuCl}_4]^-$  ions were reduced to Au seeds and Pt grew on the Au seeds in the form of dendritic nanowires. Also, the shell thickness of Pt could be controlled by the different Pt-to-Au molar ratios. The Au@Pt core-shell electrocatalysts exhibit higher electrocatalytic activity than the dendritic Pt nanocolloids towards the electrooxidation of methanol. This can reduce the cost and improve the utilization efficiency of Pt.[10]

In seed-mediated method, other metals can be studied and used as core materials.

For example, silver (Ag) is used as a core material to synthesize Ag@Pt core shell nanoparticles.[11] The shell thickness of Pt can also be controlled by tuning the core-to-shell ratios.

### **Galvanic replacement method**

Galvanic replacement reaction is driven by the difference in the standard reduction potentials of two metals. One metal acts as an anode while another one acts as a cathode. The cathode, with higher standard reduction potential, displaces the anode, with lower standard reduction potential, spontaneously.[12]

For example, the facile synthesis of the PtCu intermetallic nanotubes with PtCu@Pt core-shell structure by galvanic replacement using Cu nanowires as template was introduced. Cu nanowires with the length of 20  $\mu\text{m}$  and the average diameter of 245 nm were synthesized by electrodeposition method. The tubular PtCu intermetallic nanotubes with the average diameter of 288 nm and the wall thickness of 20 nm were prepared by galvanic replacement reaction, chemical dealloying with the aid of 10 wt%  $\text{NH}_3$  solution and heat annealing. The electrochemical tests show that the tubular PtCu nanotubes exhibit 4 times higher electrocatalytic activity and 10 times higher durability towards the electrooxidation of formic acid when compared with Pt/C catalyst.[13]

In galvanic replacement method, since cathode is displaced by anode, cathode

and anode act as core and shell materials respectively. Hence, the shell composition can be controlled by varying the cathode-to-anode ratio used in synthesis, so as to control the electrocatalytic property.

### **Development of PtPd-based bimetallic catalysts for electrocatalysis**

It is common to add palladium (Pd) to Pt for direct liquid fuel cells. There are many studies about PdPt bimetallic catalysts for electrocatalysis. It is known that Pd is 50 times more abundant in nature.[14] Also, Pd is cheaper, costing 20 % of the cost of Pt per weight.[15] It is also stated that Pd and Pt have negligible lattice mismatch which is 0.77 %.[14] This not only can reduce the total cost of the electrocatalysts but also alter the electronic effect of the catalysts with enhanced catalytic activity.[16, 17]

For example, Guo and co-workers synthesized Pt-on-Pd bimetallic nanodendrites supported graphene nanosheets by depositing Pd nanoparticles onto PVP-functionalized graphene, followed by the addition of  $K_2PtCl_4$  solution. TEM analysis showed that the Pd nanocrystals with Pt branches dispersed onto the graphene nanosheets. The average size of Pd nanocrystals is 15 nm while the average diameter of Pt branches is ranging from 3 nm to 5 nm. It is also found that the number of Pt branches can be controlled by changing the volumes of graphene solution and  $K_2PtCl_4$  solution. The electrochemical studies show that the Pt-on-Pd bimetallic nanodendrites supported graphene nanosheets exhibit enhanced electrocatalytic activity towards the electrooxidation of methanol when

compared with platinum black and commercial E-TEK Pt/C catalysts.[18]

However, in many studies, synthesizing PtPd-based bimetallic catalysts involves the use of surfactants or other chemical reducing agents. (Table 3.1) It is possible that the surfactants may adsorb on the surface of the catalysts which may decrease the catalytic activity. Therefore, the synthesis of PtPd-based bimetallic catalysts without surfactants was explored.

Catalyst	Morphology	Pd-to-Pt atomic ratio	Fuel	Synthetic method	Surfactant	Specific area activity	Specific mass activity	Ref.
Pt-Pd core-shell	Polyhedral	-	1.0 M MeOH + 0.5 M H <sub>2</sub> SO <sub>4</sub>	Modified polyol method	PVP <sub>Mw = 55,000</sub>	1.5 mAcm <sup>-2</sup>	-	[15]
Pd <sub>75</sub> Pt <sub>25</sub>	Nanodendrite	75 : 25	0.5 M MeOH + 0.5 M H <sub>2</sub> SO <sub>4</sub>	Co-reduction (OAm and H <sub>2</sub> , 1 bar)	-	-	609.565 mA <sub>metal</sub> Pt <sup>-1</sup>	[16]
Pd <sub>80</sub> Pt <sub>20</sub>		80 : 20					321.703 mA <sub>metal</sub> Pt <sup>-1</sup>	
Pd <sub>85</sub> Pt <sub>15</sub>		85 : 15					289.494 mA <sub>metal</sub> Pt <sup>-1</sup>	
PdPt/CNTs	Nanoparticle	1 : 1	1.0 M MeOH + 1.0 M KOH	Co-reduction (NaBH <sub>4</sub> )	-	-	1000 mA <sub>metal</sub> <sup>-1</sup>	[1]
PdPt <sub>3</sub> /CNTs		1 : 3					1100 mA <sub>metal</sub> <sup>-1</sup>	
Pd <sub>3</sub> Pt/CNTs		3 : 1					600 mA <sub>metal</sub> <sup>-1</sup>	

Pd <sub>50</sub> Pt <sub>50</sub> BANs	Sponge	50 : 50	1.0 M MeOH + 1.0 M KOH	Co-reduction (NaBH <sub>4</sub> )	-	-	2200 mA <sub>metal</sub> <sup>-1</sup>	[19]
Pd <sub>45</sub> Pt <sub>55</sub> ANWs	Nanowire	45 : 55	1.0 M EtOH + 0.5 M NaOH	Galvanic replacement reaction	EG	-	900 mA <sub>metal</sub> <sup>-1</sup>	[20]
PdPt/CNTs	Nanoparticle	1 : 1	0.5 M EtOH + 0.5 M KOH	Co-reduction (NaBH <sub>4</sub> )	-	-	1070 mA <sub>metal</sub> <sup>-1</sup>	[1]
PdPt <sub>3</sub> /CNTs		1 : 3					600 mA <sub>metal</sub> <sup>-1</sup>	
Pd <sub>3</sub> Pt/CNTs		3 : 1					800 mA <sub>metal</sub> <sup>-1</sup>	
Pd <sub>50</sub> Pt <sub>50</sub> BANs	Sponge	50 : 50	1.0 M EtOH + 0.5 M NaOH	Co-reduction (NaBH <sub>4</sub> )	-	-	2200 mA <sub>metal</sub> <sup>-1</sup>	[19]

Pd <sub>55</sub> Pt <sub>30</sub> NWs	Nanowire network	55 : 30	0.5 M glycerol + 0.5 M KOH	Co-reduction (NaBH <sub>4</sub> )	PVP, K30	46 mAcm <sup>-2</sup>	1600 mA <sub>metal</sub> <sup>-1</sup>	[21]
Pt <sub>77</sub> Pd <sub>23</sub> ACSNDs/rGOed	Nanoparticle with branches	77 : 23	0.5 M glycerol + 0.5 M KOH	One-pot aqueous method	Biosynthesized polypeptide (colistin sulfate, CS)	2.74 mAcm <sup>-2</sup>	1533.49 mA <sub>metal</sub> <sup>-1</sup>	[22]

---

Table 3.1 Comparison of the previously reported PtPd-based catalysts with respect to their catalytic activities for methanol, ethanol and glycerol oxidations.

### **Aim of the project**

This project is aimed to synthesize two novel models of Pd@PdPt/CNTs and Pt@Pd/CNTs as alloy and phase-separate surface models from the surfactant-free Pd/CNTs and Pt/CNTs composites. Both Pd and Pt metals act as core materials for surface modification to form PdPt alloy and phase-separate shells respectively. Their electrocatalytic activity towards methanol, ethanol and glycerol oxidations are investigated and compared.

## 3.2 Results and Discussions

### 3.2.1 Synthesis of Pd@PdPt/CNTs alloy catalysts

For synthesizing Pd@PdPt/CNTs alloy catalysts, Pd/CNTs composite was firstly prepared by hydrolysis of  $K_2PdCl_4$  to palladium(II) oxide (PdO) on CNTs, followed by hydrogen ( $H_2$ ) reduction. Since the affinity of Pd towards O is high,  $[PdCl_4]^{2-}$  ions attach the oxygen-containing groups on the MWCNTs and then hydrolyze to PdO. After that, PdO was reduced to Pd by reacting with hydrogen to form Pd/CNTs composite.

To confirm the formation of PdO on CNTs before  $H_2$  reduction, XRD was conducted. Figure 3.1 displays the XRD patterns of Pd/CNTs before and after  $H_2$  reduction. Pd/CNTs composite before  $H_2$  reduction exhibits two sets of diffraction peaks. One diffraction peak at  $2\theta$  value of  $26.2^\circ$  is characteristic of the hexagonal structure of graphite, corresponding to the (002) crystal plane (JCPDS Card no. 00-001-0646). The other diffraction peaks at  $2\theta$  values of  $34.2^\circ$ ,  $43.1^\circ$ ,  $55.0^\circ$ ,  $60.5^\circ$  and  $71.8^\circ$  are characteristic of the tetragonal structure of PdO with a  $P4/nmm(129)$  space group, corresponding to the (002), (200), (202), (113) and (004) crystal planes respectively (JCPDS Card no.00-002-1201). This confirms the formation of PdO/CNTs before  $H_2$  reduction.

XRD pattern of Pd/CNTs composite after  $H_2$  reduction also exhibits two sets of diffraction peaks. One diffraction peak is at  $2\theta$  value of  $25.8^\circ$  and is

characteristic of the hexagonal structure of graphite, corresponding to the (002) crystal plane. (JCPDS Card no. 00-001-0646). The other diffraction peaks at  $2\theta$  values of  $39.9^\circ$ ,  $46.6^\circ$ ,  $67.9^\circ$  and  $81.9^\circ$  are characteristic of the face-centered cubic (fcc) structure of Pd with a Fm-3m(225) space group, corresponding to the (111), (222), (220) and (311) crystal planes respectively (JCPDS Card no.00-002-1201), suggesting that PdO is successfully reduced to Pd metal by  $H_2$ .

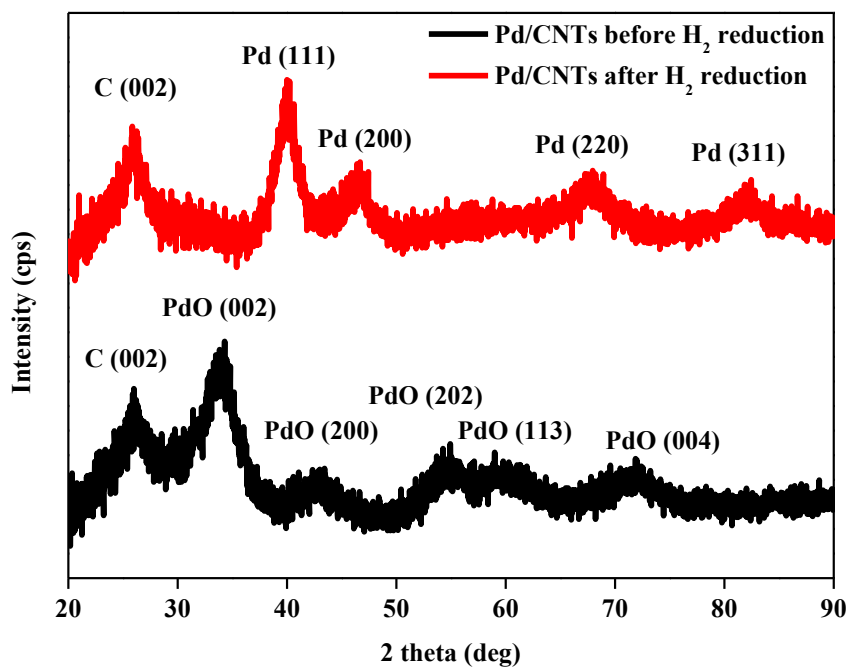


Figure 3.1 XRD patterns of Pd/CNTs composites before and after  $H_2$  reduction.

The morphology of Pd/CNTs composite was investigated by TEM analysis. As displayed in Figure 3.2, the Pd nanoparticles were synthesized in spherical morphology with the average size of  $3.1 \pm 0.5$  nm and successfully deposited on the MWCNTs.

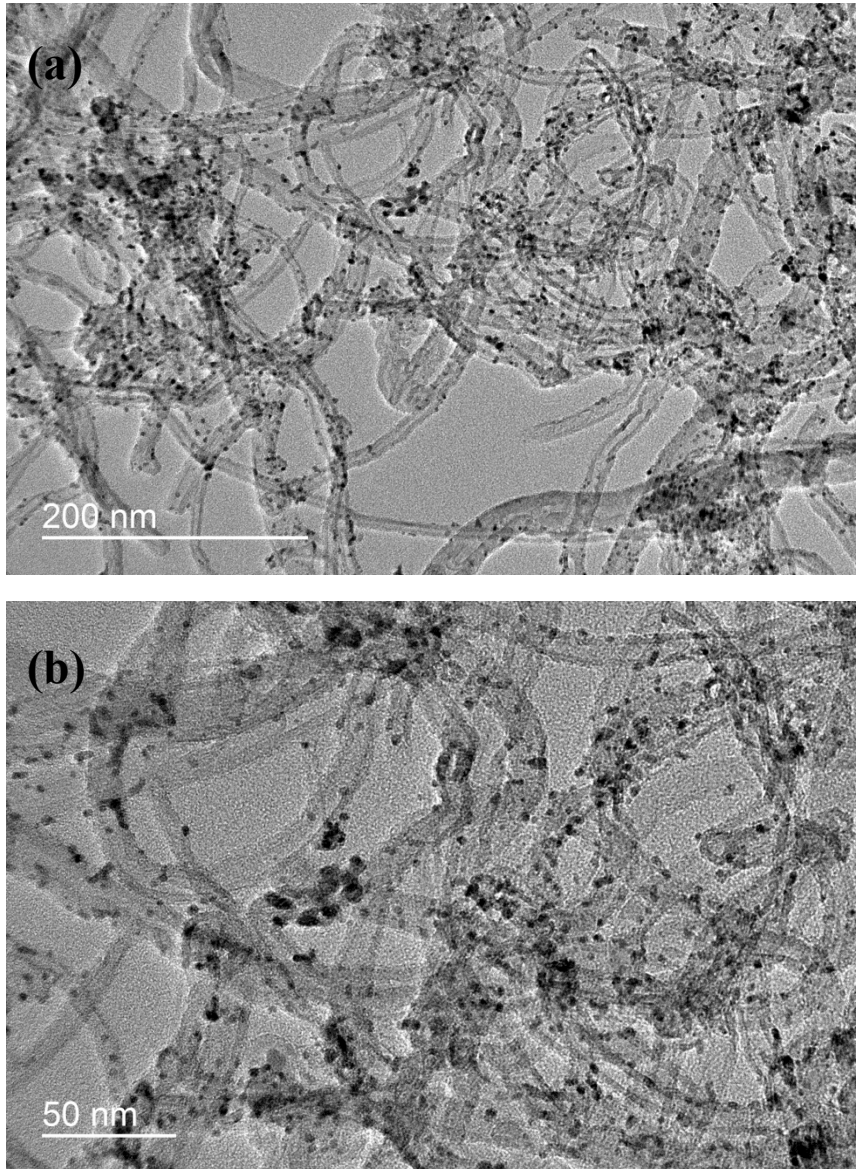


Figure 3.2 (a) LM-TEM and (b) HM-TEM images of Pd/CNTs composite.

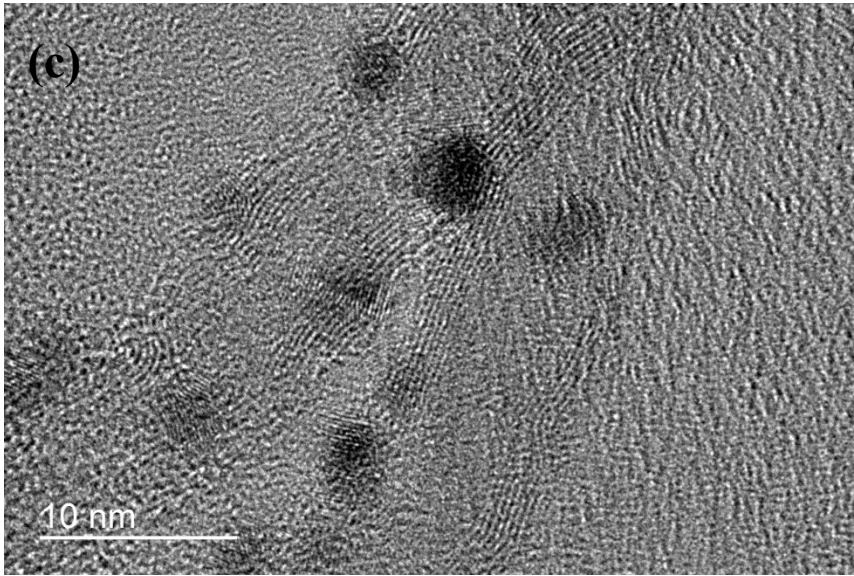
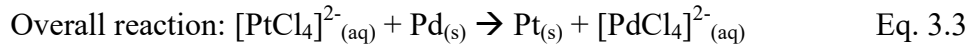
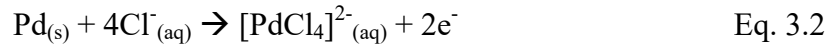
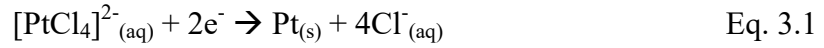


Figure 3.2 (c) HR-TEM image of Pd/CNTs composite.

Since Pd/CNTs composite was synthesized without any introduction of organic surfactant, a clean metal surface is available for later surface modification to form PdPt alloy surface. The Pd@PdPt/CNTs-1 and Pd@PdPt/CNTs-2 composites were synthesized by galvanic replacement reaction between Pd nanoparticles on CNTs and  $[\text{PtCl}_4]^{2-}$  ions. The standard reduction potential of  $[\text{PtCl}_4]^{2-}/\text{Pt}$  pair (0.758 V vs standard hydrogen electrode, SHE) is higher than that of  $[\text{PdCl}_4]^{2-}/\text{Pd}$  pair (0.62 V vs SHE). As a result, the galvanic replacement reaction between Pd and  $[\text{PtCl}_4]^{2-}$  ions takes place spontaneously, as shown by the following equations.



The morphology of Pd@PdPt/CNTs-1 and Pd@PdPt/CNTs-2 composites were studied by TEM analysis.

### **Pd@PdPt/CNTs-1**

As displayed in Figure 3.3, the Pd@PdPt nanoparticles were synthesized in spherical morphology and were successfully deposited on the MWCNTs. The average size of Pd@PdPt nanoparticles from Pd@PdPt/CNTs-1 composite is  $3.5 \pm 0.8$  nm which is slightly larger than the average size of Pd nanoparticles ( $3.1 \pm 0.5$  nm).

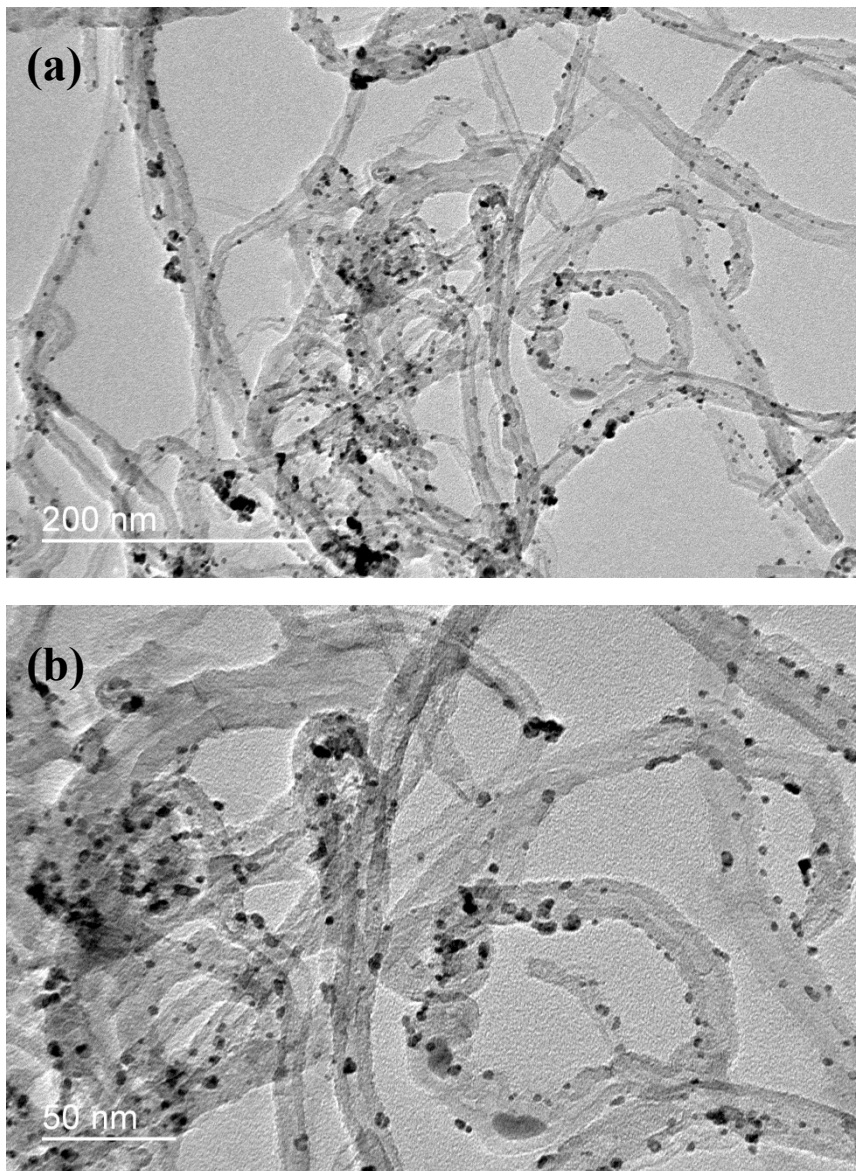


Figure 3.3 (a) LM-TEM and (b) HM-TEM images of Pd@PdPt/CNTs-1 composite.

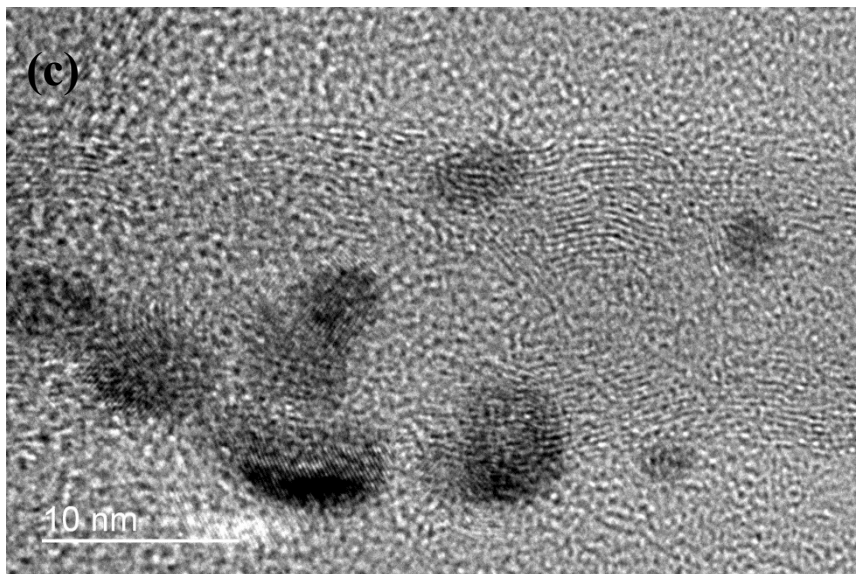


Figure 3.3 (c) HR-TEM image of Pd@PdPt/CNTs-1 composite.

### **Pd@PdPt/CNTs-2**

As displayed in Figure 3.4, the Pd@PdPt nanoparticles were synthesized in spherical morphology and were successfully deposited on the MWCNTs. The average size of Pd@PdPt nanoparticles from Pd@PdPt/CNTs-2 composite is  $3.2 \pm 0.7$  nm, which is slightly larger than the average size of Pd nanoparticles ( $3.1 \pm 0.5$  nm). Compared with Pd@PdPt/CNTs-1 composite ( $3.5 \pm 0.8$  nm), the average size of Pd@PdPt nanoparticles from Pd@PdPt/CNTs-2 composite is smaller because lower amount of  $K_2PtCl_4$  was added to displace Pd metal.

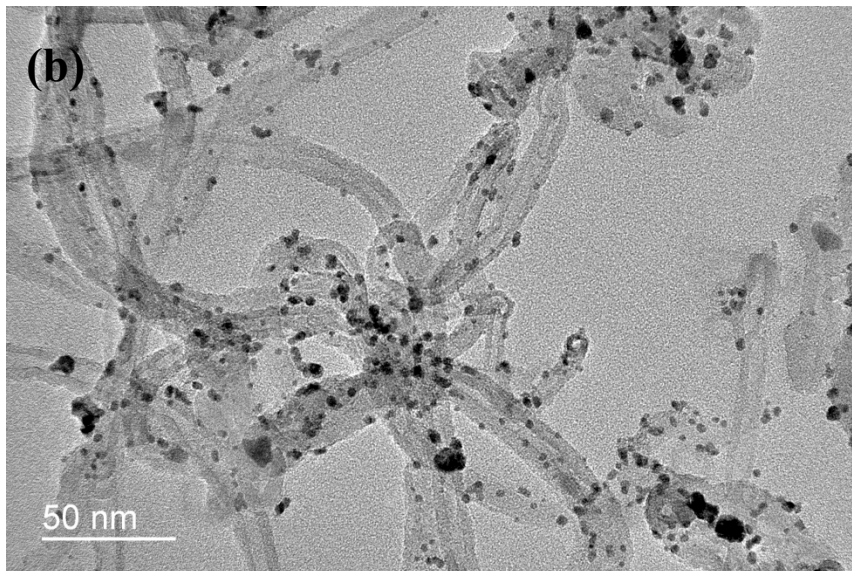
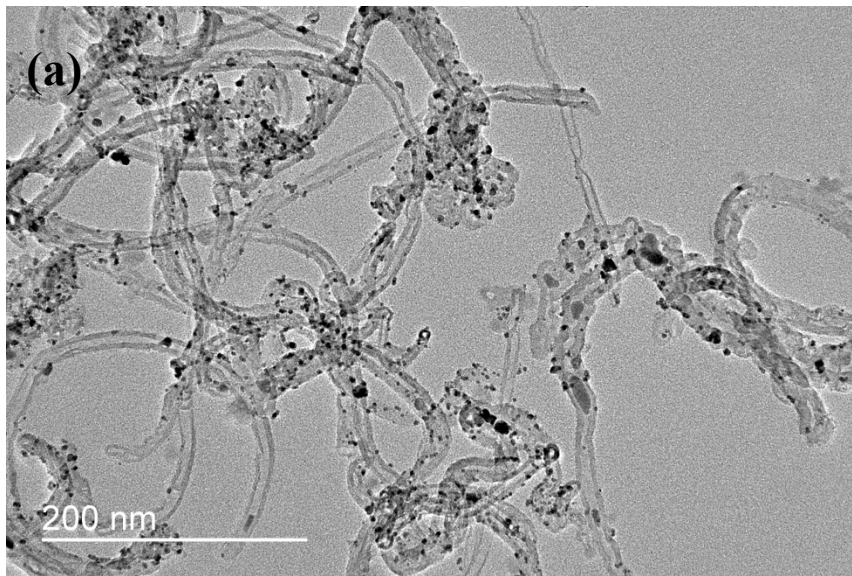


Figure 3.4 (a) LM-TEM and (b) HM-TEM images of Pd@PdPt/CNTs-2 composite.

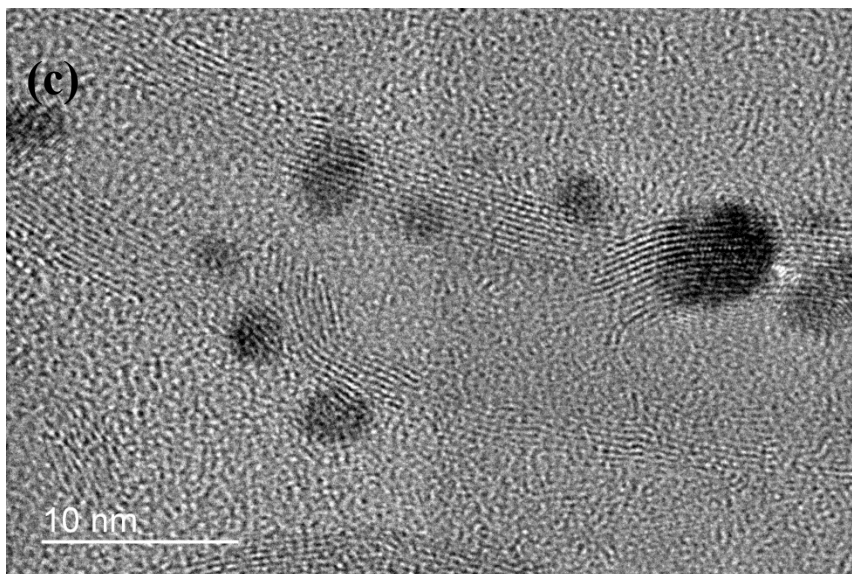


Figure 3.4

(c) HR-TEM image of Pd@PdPt/CNTs-2 composite.

To study the crystalline structures of Pd@PdPt/CNTs composites, XRD was performed. XRD patterns of Pd/CNTs, Pd@PdPt/CNTs-1 and Pd@PdPt/CNTs-2 composites are shown in Figure 3.5 (a). Both Pd@PdPt/CNTs composites exhibit two sets of diffraction peaks. One diffraction peak at  $2\theta$  value of  $26.0^\circ$  is characteristic of the hexagonal structure of graphite, corresponding to the (002) crystal plane (JCPDS Card no. 00-001-0646). For Pd@PdPt-1/CNTs composite, the other diffraction peaks at  $2\theta$  values of  $40.1^\circ$ ,  $46.4^\circ$ ,  $68.3^\circ$  and  $82.1^\circ$  while for Pd@PdPt/CNTs-2 composite, they are at  $2\theta$  values of  $39.5^\circ$ ,  $46.5^\circ$ ,  $67.7^\circ$  and  $82.0^\circ$ . They are characteristic of fcc structure of PdPt with a Fm-3m(225) space group, corresponding to the (111), (200), (220) and (311) crystal planes respectively (JCPDS Card no. 01-072-2839). It can be clearly seen that the position of the (111) peaks of Pd@PdPt/CNTs-1 ( $40.1^\circ$ ) and Pd@PdPt/CNTs-2 ( $39.9^\circ$ ) composites is in between those of Pt ( $39.7^\circ$ ) and Pd ( $40.4^\circ$ ). This indicates the formation of PdPt alloys. [21, 23] Figure 3.5 (b) shows an expanded view of the (111) peaks of Pd/CNTs and Pd@PdPt/CNTs composites. There is a small shift in peak.

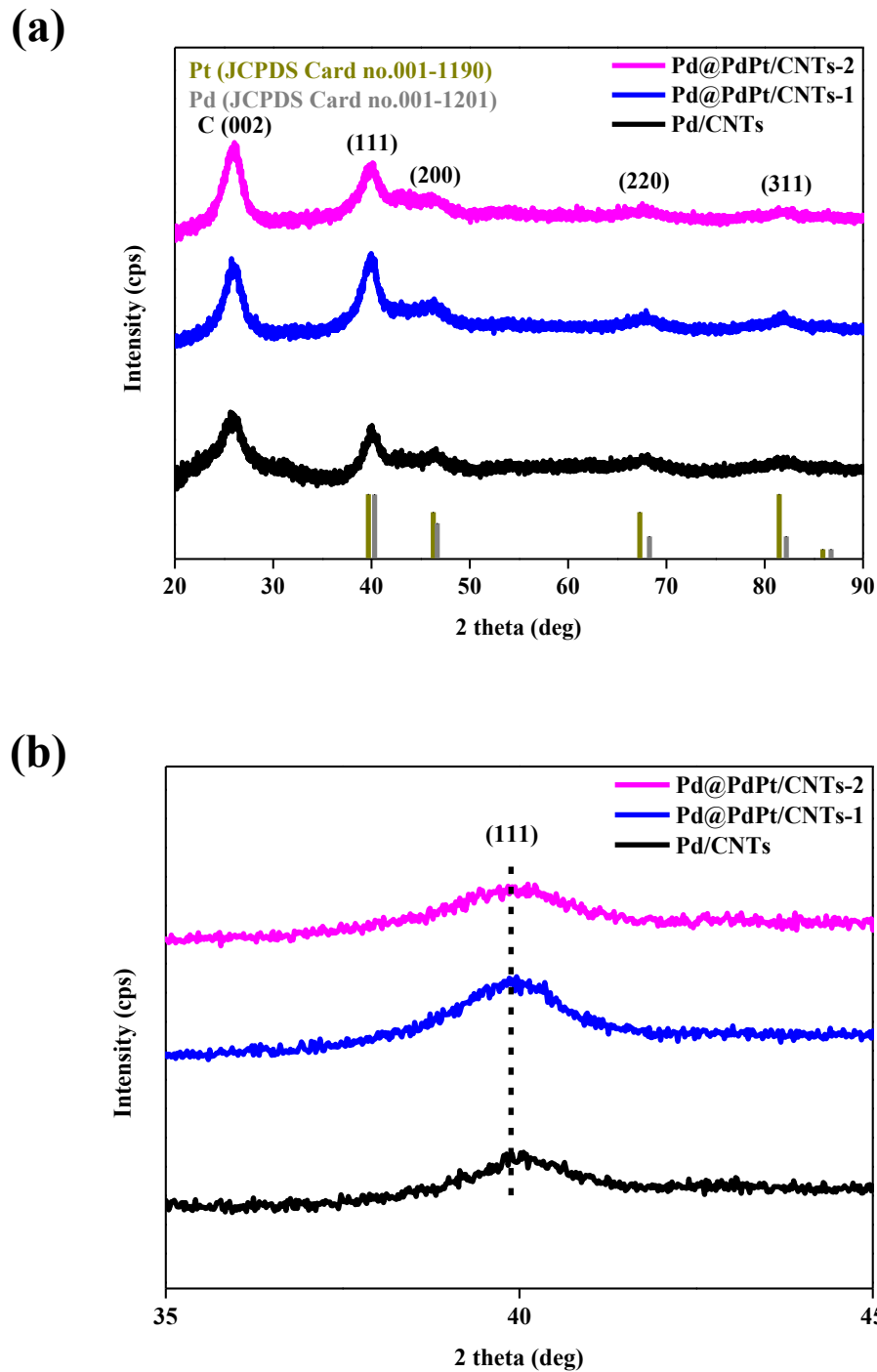


Figure 3.5 (a) XRD patterns and (b) an expanded view (111) peaks of Pd/CNTs, Pd@PdPt/CNTs-1 and Pd@PdPt/CNTs-2 composites.

### 3.2.2 Synthesis of Pt@Pd/CNTs phase-separate catalysts

Pt/CNTs composite was firstly synthesized by stirring  $K_2PtCl_4$  and sonicated acid-treated CNTs at 90 °C for 2 h. It is suggested that  $[PtCl_4]^{2-}/Pt$  exhibit reduction by the electron transfer from CNTs.[24] The morphology of Pt/CNTs composite was studied by TEM analysis. As displayed in Figure 3.6, the Pt nanoparticles were synthesized in spherical morphology with the average size of  $1.6 \pm 0.3$  nm and successfully deposited on the MWCNTs.

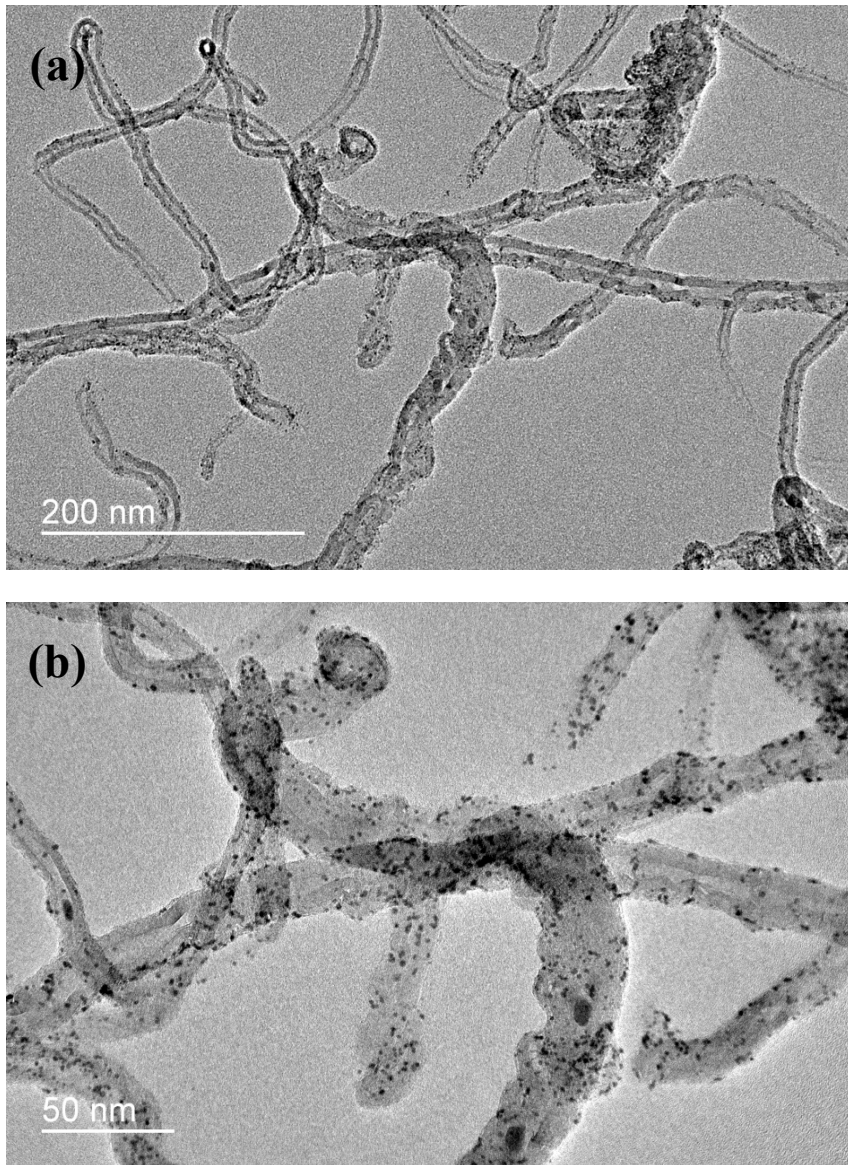


Figure 3.6 (a) LM-TEM and (b) HM-TEM images of Pt/CNTs composite.

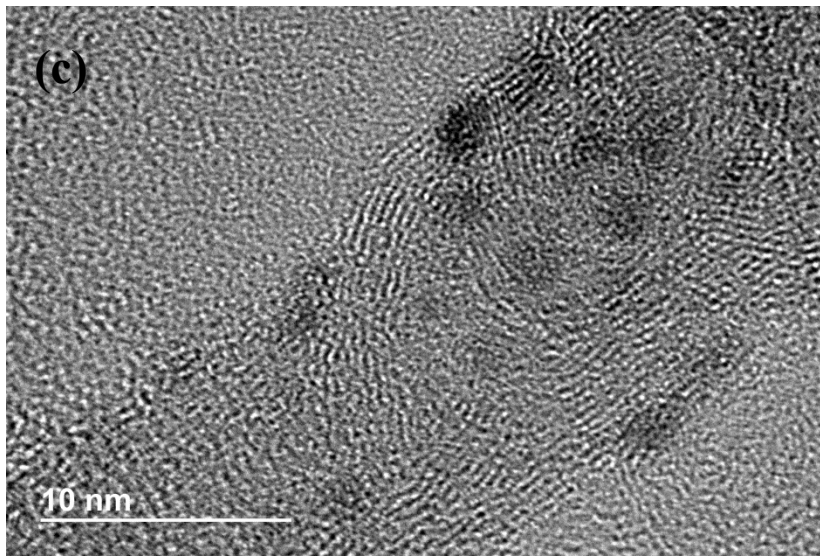


Figure 3.6 (c) HR-TEM image of Pt/CNTs composite.

Similar to Pd/CNTs composite, Pt/CNTs composite was also synthesized without introduction of organic surfactant. Its clean metal surface is available for surface modification to form PdPt phase-separate surface. The Pt@Pd/CNTs composites were synthesized by the adsorption of  $[\text{PdCl}_4]^{2-}$  ions onto Pt surface, followed by  $\text{H}_2$  reduction to form Pd metal. To confirm the adsorption of  $[\text{PdCl}_4]^{2-}$  ions occurs onto Pt surface only, CNTs was used instead of Pt/CNTs composite. As displayed in Figure 3.7, no Pd is formed. Since the standard reduction potential of  $[\text{PdCl}_4]^{2-}/\text{Pd}$  pair (0.62 V vs SHE) is lower than that of  $[\text{PtCl}_4]^{2-}/\text{Pt}$  pair (0.758 V vs SHE), no galvanic replacement reaction between Pt and  $[\text{PdCl}_4]^{2-}$  ions takes place. Therefore, Pt@Pd/CNTs composites are simply in phase-separate structure.

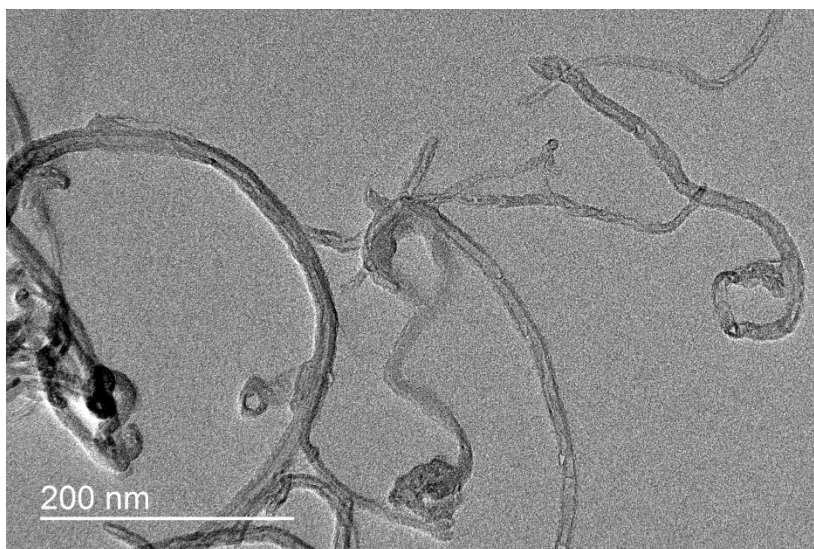


Figure 3.7 LM-TEM image of CNTs immersed in  $\text{K}_2\text{PdCl}_4$  and followed by  $\text{H}_2$  reduction.

The morphology of Pt@Pd/CNTs-1, Pt@Pd/CNTs-2 and Pt@Pd/CNTs-3 composites were studied by TEM analysis.

### **Pt@Pd/CNTs-1**

As displayed in Figure 3.8, the Pt@Pd nanoparticles were synthesized in spherical morphology and were successfully deposited on the MWCNTs. The average size of Pt@Pd nanoparticles from Pt@Pd/CNTs-1 composite is  $2.9 \pm 0.5$  nm, which is larger than the average size of Pt nanoparticles ( $1.6 \pm 0.3$  nm) due to the deposition of Pd on Pt surface.

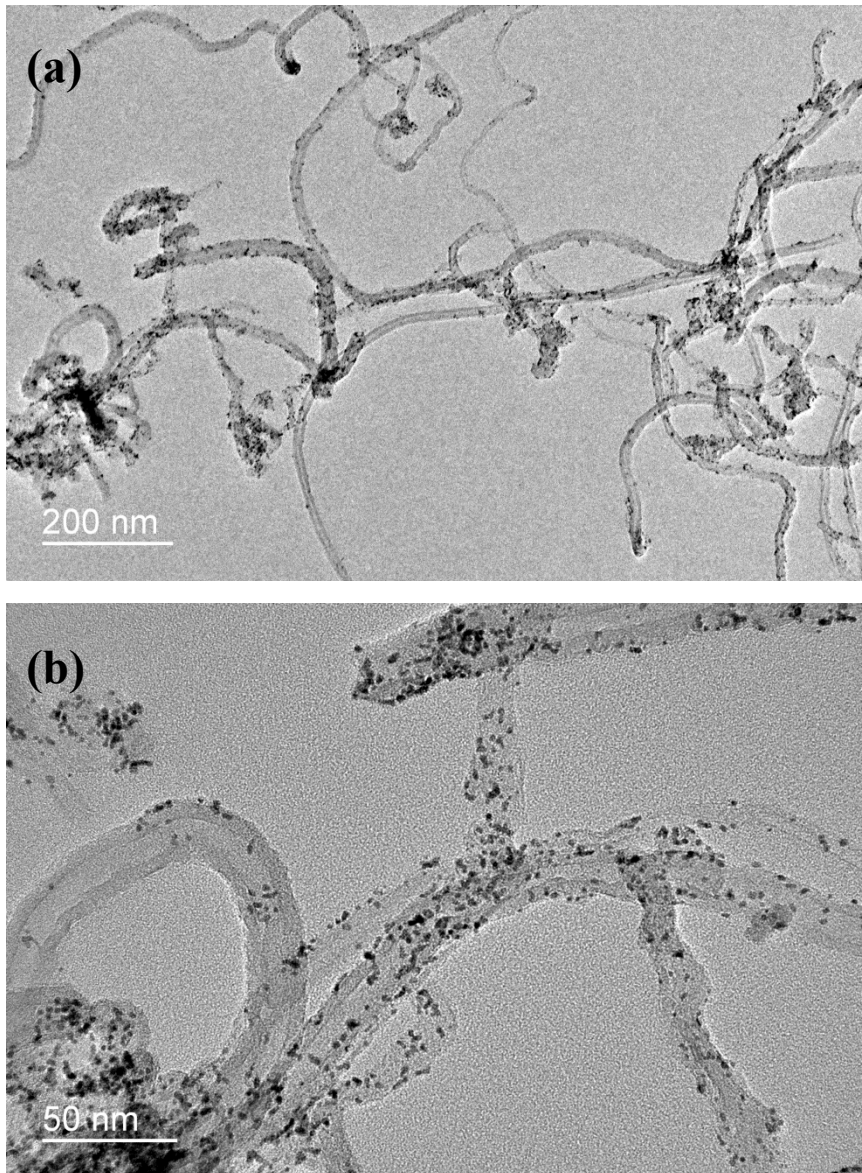


Figure 3.8 (a) LM-TEM and (b) HM-TEM images of Pt@Pd/CNTs-1 composite.

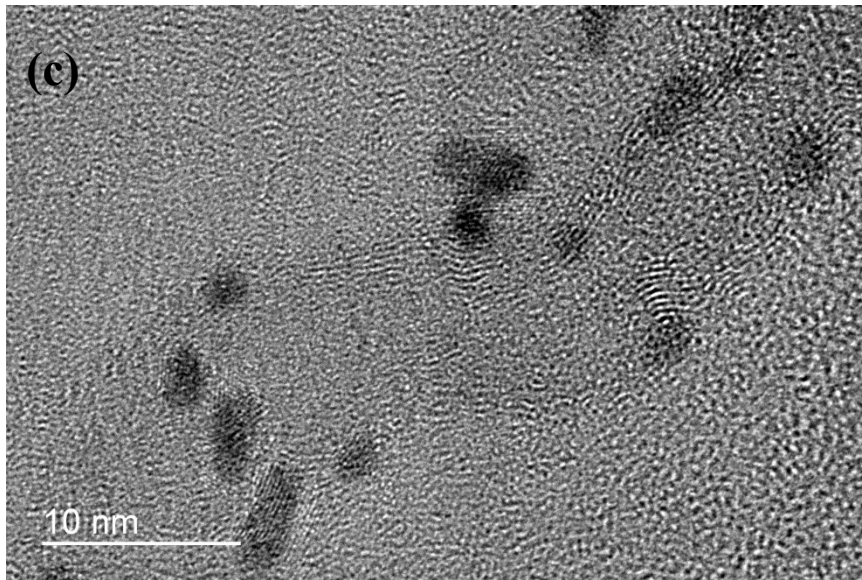


Figure 3.8 (c) HR-TEM image of Pt@Pd/CNTs-1 composite.

### **Pt@Pd/CNTs-2**

As displayed in Figure 3.9, the Pt@Pd nanoparticles were synthesized in spherical morphology and were successfully deposited on the MWCNTs. The average size of Pt@Pd from Pt@Pd/CNTs-2 composite is  $3.0 \pm 0.5$  nm which is larger than the average size of Pt nanoparticles ( $1.6 \pm 0.3$  nm) due to the deposition of Pd onto Pt surface.

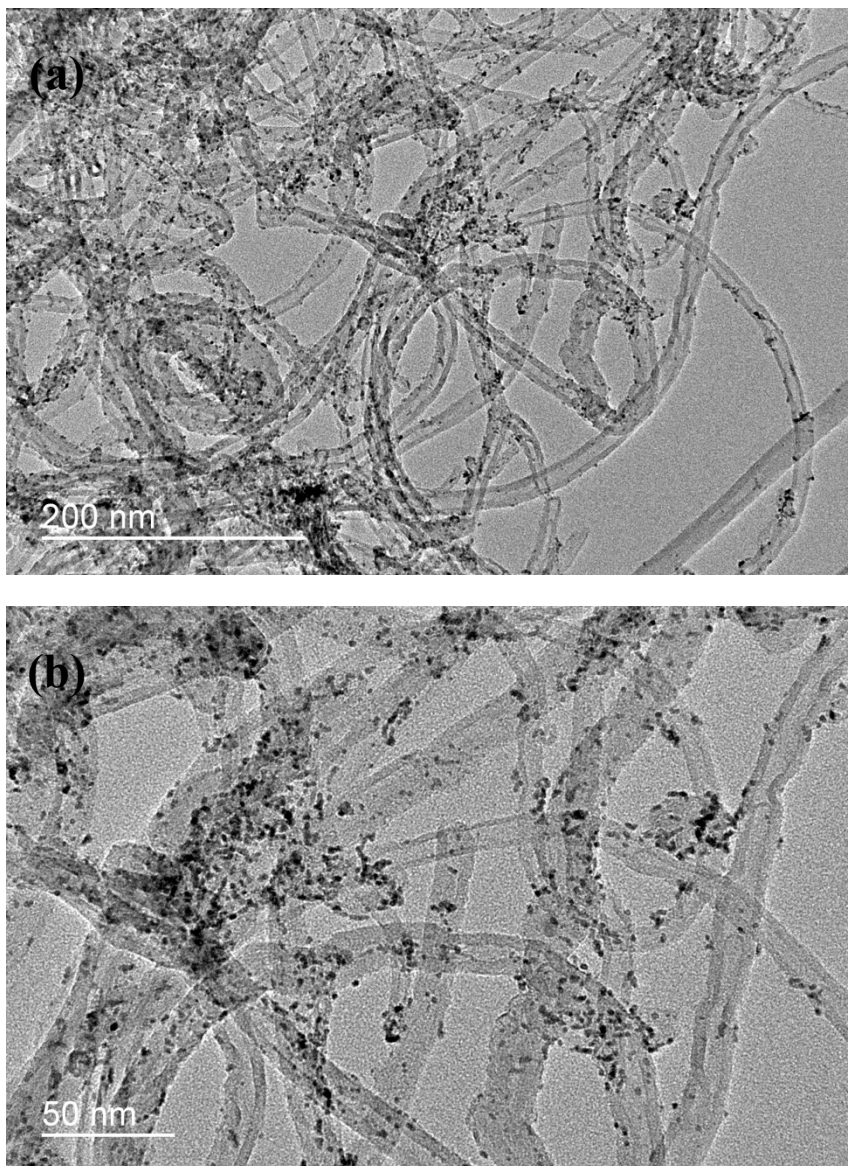


Figure 3.9 (a) LM-TEM and (b) HM-TEM images of Pt@Pd/CNTs-2 composite.

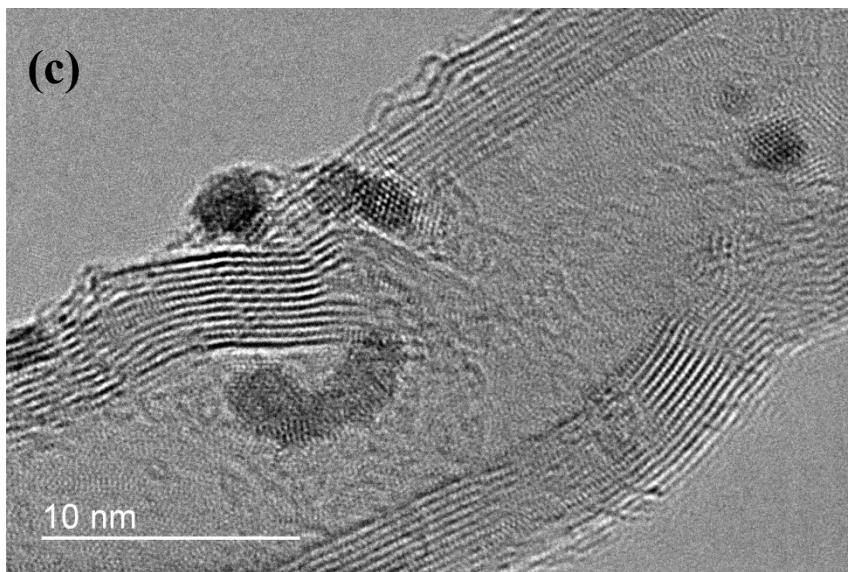


Figure 3.9

(c) HR-TEM image of Pt@Pd/CNTs-2 composite.

### **Pt@Pd/CNTs-3**

As displayed in Figure 3.10, the Pt@Pd nanoparticles were synthesized in spherical morphology and were successfully deposited on the MWCNTs. The average size of Pt@Pd from Pt@Pd/CNTs-3 composite is  $3.0 \pm 0.7$  nm which is larger than the average size of Pt nanoparticles ( $1.6 \pm 0.3$  nm) due to the deposition of Pd onto Pt surface.

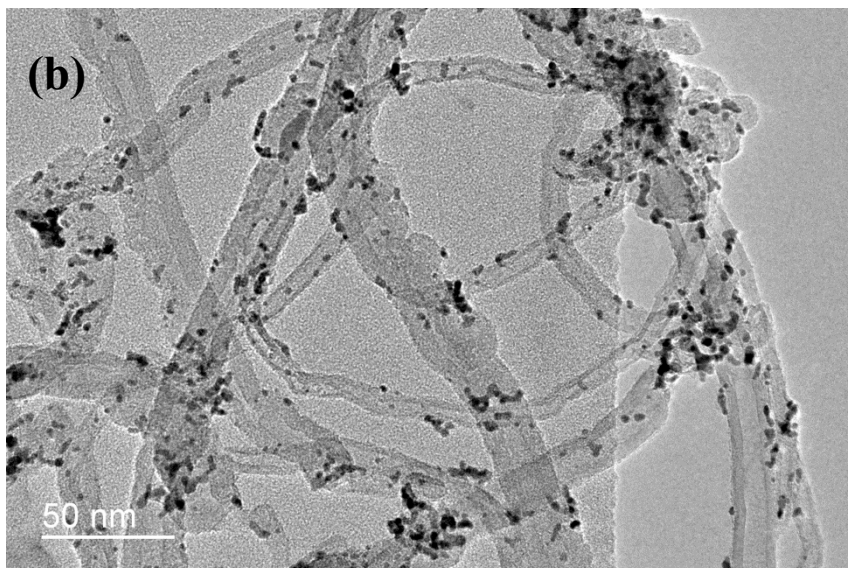
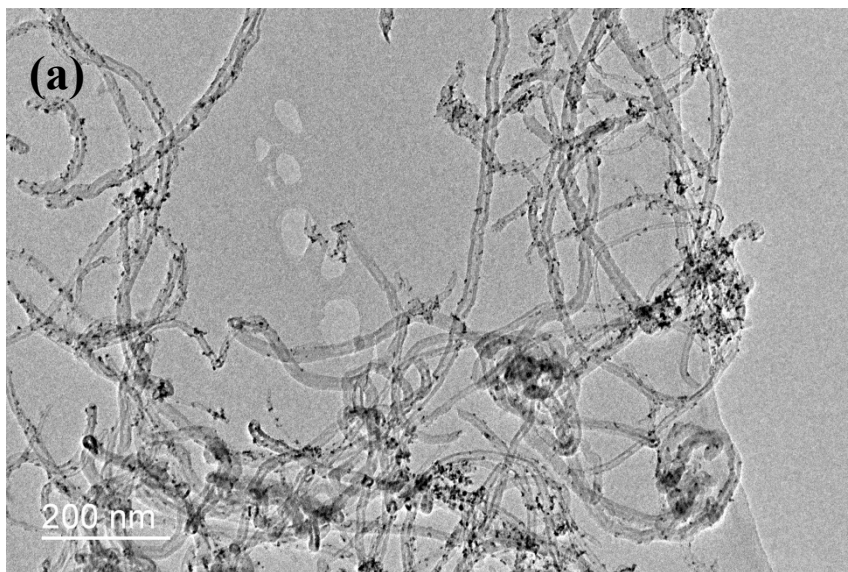


Figure 3.10 (a) LM-TEM and (b) HM-TEM images of Pt@Pd/CNTs-3 composite.

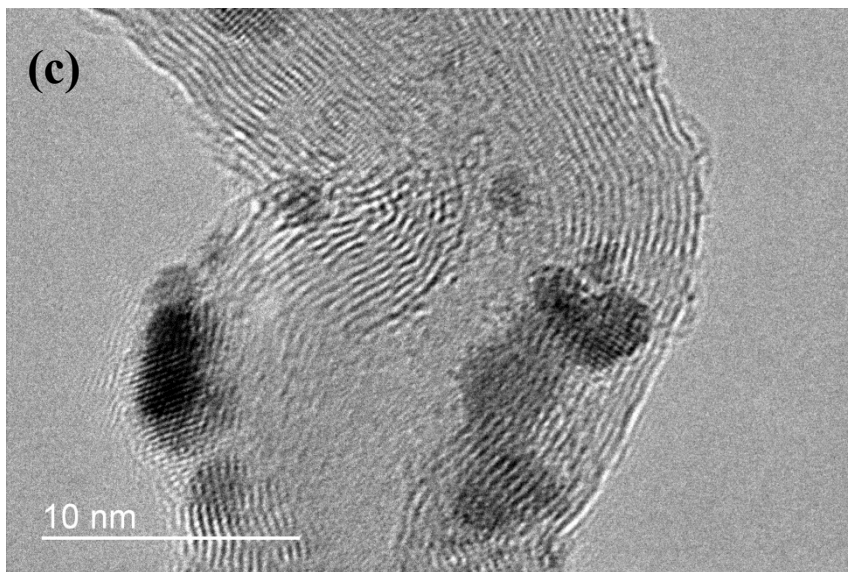


Figure 3.10

(c) HR-TEM image of Pt@Pd/CNTs-3 composite.

To study the crystalline structure, Pt@Pd/CNTs composites were characterized by XRD analysis and compared with Pt/CNTs as displayed in Figure 3.11. Pt/CNTs composite exhibits a diffraction peak at  $2\theta$  value of  $26.2^\circ$ , which is characteristic of the hexagonal structure of graphite, corresponding to the plane (002) (JCPDS Card no. 00-001-0646). No diffractions peaks for Pt were shown due to small particle size. The diffraction peaks of Pt@Pd/CNTs composites become prominent because the particle size increases by depositing of Pd onto Pt. Pt@Pd/CNTs-1, Pt@Pd/CNT-2 and Pt@Pd/CNTs-3 composites exhibit diffraction peaks at  $2\theta$  value of  $25.3^\circ$ ,  $24.7^\circ$  and  $25.6^\circ$  respectively. They are characteristic of the hexagonal structure of graphite, corresponding to the (002) crystal plane (JCPDS Card no. 00-001-0646). Pt@Pd/CNTs-1 composite exhibits other diffraction peaks at  $2\theta$  values of  $39.7^\circ$ ,  $45.5^\circ$ ,  $67.5^\circ$  and  $81.3^\circ$ . Pt@Pd/CNTs-2 composite exhibits other diffraction peaks at  $2\theta$  values of  $39.9^\circ$ ,  $46.4^\circ$ ,  $68.0^\circ$  and  $80.5^\circ$ . Pt@Pd/CNTs-3 composite exhibits other diffraction peaks at  $2\theta$  values of  $39.8^\circ$ ,  $45.8^\circ$ ,  $67.3^\circ$  and  $81.5^\circ$ . These diffraction peaks are characteristic of a fcc structure of PdPt with a Fm-3m(225) space group, corresponding to the (111), (200), (220) and (311) crystal planes respectively (JCPDS Card no. 01-072-2839). All Pt@Pd/CNTs composites exhibit a fcc structure.

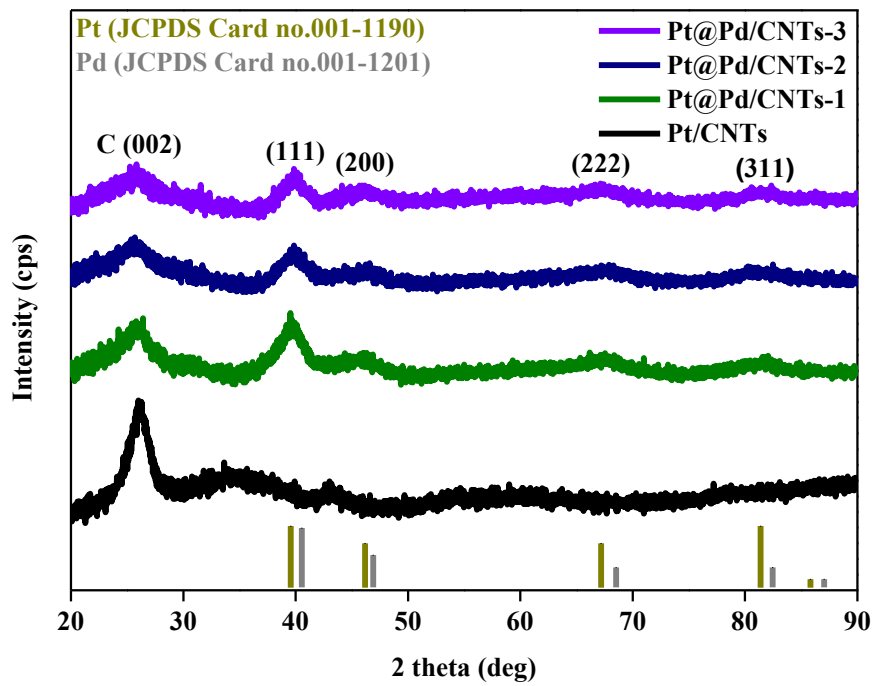


Figure 3.11 XRD patterns of Pt/CNTs, Pt@Pd/CNTs-1, Pt@Pd/CNTs-2 and Pt@Pd/CNTs-3 composites.

### 3.2.3 Elemental and surface composition analysis

The elemental and surface composition analyses of both Pd@PdPt/CNTs and Pt@Pd/CNTs composites were presented in Table 3.2. EDX analysis was conducted to study the elemental composition of the catalysts. The Pd-to-Pt atomic ratio of Pd@PdPt/CNTs-1 composite (1.7 : 1) is lower than that of Pd@PdPt/CNTs-2 composite (3.7 : 1) because higher amount of  $K_2PtCl_4$  was added for synthesizing Pd@PdPt/CNTs-1 composite, and thus higher Pd content is displaced.

ICP-OES was also conducted to study the Pd and Pt loadings of catalysts. The Pd loading of Pd@PdPt/CNTs-1 (5.6 %) and Pd@PdPt/CNTs-2 (9.2 %) composites are lower than that of Pd/CNTs composite (12.1 %) because Pd metal is displaced by  $[PtCl_4]^{2-}$  ions during galvanic replacement reaction. Compared with Pd@PdPt/CNTs-1 composite, the Pd and Pt loadings of Pd@PdPt/CNTs-2 composite are lower and higher respectively. Lower amount of Pd metal is displaced because lower amount of  $K_2PtCl_4$  was added for synthesizing Pd@PdPt/CNTs-2 composite. For Pt@Pd/CNTs composites, the Pt loadings of Pt@Pd/CNTs composites are comparable to Pt/CNTs composite because no replacement reaction takes place in the synthesis of Pt@Pd/CNTs composites and Pt is not displaced by  $[PdCl_4]^{2-}$  ions. Besides, the Pd loading of Pt@Pd/CNTs composites increases from 1.9 % to 6.3 %. Since the cycle number of Pd deposition- $H_2$  reduction increases, more and more Pd content deposit onto Pt surface, resulting in an increasing Pd loading. The ICP-OES result aligns with

the Pd-to-Pt atomic ratios of catalysts detected by EDX analysis.

The surface composition and valence states of Pd and Pt of the catalysts are studied by XPS analysis. The Pd-to-Pt surface ratio of Pd@PdPt/CNTs-1 (1.3 : 1) and Pd@PdPt/CNTs-2 (2.2 : 1) composites are lower than the Pd-to-Pt atomic ratios of Pd@PdPt/CNTs-1 (1.7 : 1) and Pd@PdPt/CNTs-2 (3.2 : 1) composites measured by EDX analysis respectively. Since XPS is a surface-sensitive quantitative spectroscopic technique without detecting the core material, this confirms the formation of Pd@PdPt core-shell structure. This can be further confirmed by high angle annular dark-field scanning transmission electron microscope-energy dispersive spectroscopy (HAADF-STEM-EDS) mappings and line scanning profiles to investigate the composition distribution in catalysts in progress.[25] Also, the Pd-to-Pt surface ratio of Pt@Pd/CNTs composites increases from 1 : 7.2 to 1 : 1.5 because increasing Pd content deposit onto Pt surface with the increasing cycle number of Pd deposition-H<sub>2</sub> reduction.

Catalysts	Average size by TEM (nm)	Crystallite size by XRD (nm)	Pd loading by ICP-OES (%)	Pt loading by ICP-OES (%)	Total metal loading by ICP-OES (%)	Pd-to-Pt atomic ratio by EDX	Pd-to-Pt surface ratio by XPS
Pd/CNTs	3.1 ± 0.5	3.3	12.1	-	12.1	-	-
Pt/CNTs	1.6 ± 0.3	-	-	12.2	12.2	-	-
Pd@PdPt/CNTs-1	3.5 ± 0.8	3.7	5.6	5.7	11.3	1.7 : 1	1.3 : 1
Pd@PdPt/CNTs-2	3.2 ± 0.7	3.5	9.2	2.9	12.1	3.7 : 1	2.2 : 1
Pt@Pd/CNTs-1	2.9 ± 0.5	2.5	1.9	13.0	14.9	1 : 4.9	1 : 7.2
Pt@Pd/CNTs-2	3.0 ± 0.5	2.6	5.4	13.4	18.8	1 : 1.9	1 : 2.3
Pt@Pd/CNTs-3	3.0 ± 0.7	2.6	6.3	12.8	19.1	1 : 1.3	1 : 1.5

Table 3.2 Summary of elemental and surface compositions of Pd/CNTs, Pt/CNTs, Pd@PdPt/CNTs and Pt@Pd/CNTs composites.

As displayed in Figure 3.12, the Pd 3d region of the catalysts is deconvoluted into two doublets which are assigned to metallic Pd(0) and oxidized Pd(II). The more intense doublets correspond to the metallic Pd(0) 3d<sub>3/2</sub> and 3d<sub>5/2</sub> while the less intense doublets correspond to the Pd(II) 3d<sub>3/2</sub> and 3d<sub>5/2</sub>. As summarized in Table 3.3, the amount of Pd species was calculated from the relative intensities of these two doublets. The XPS results suggest that the predominant surface species on the catalysts is metallic Pd(0).

As displayed in Figure 3.12, the Pt 4f region of the catalysts is deconvoluted into two doublets which are assigned to metallic Pt(0) and oxidized Pt(II). The more intense doublets correspond to the metallic Pt(0) 4f<sub>5/2</sub> and 4f<sub>7/2</sub> while the less intense doublets correspond to the Pt(II) 4f<sub>5/2</sub> and 4f<sub>7/2</sub>. As summarized in Table 3.4, the amount of Pt species was calculated from the relative intensities of these two doublets. The XPS results suggest that the predominant surface species on the catalysts is metallic Pt(0).

Extra peaks at 332.1 eV of Pd@PdPt/CNTs, 332.2 eV of Pt@Pd/CNTs-1, 333.6 eV of Pt@Pd/CNTs-2 and 333.5 eV of Pt@Pd/CNTs-3 composites are shown in Figure 3.12 (c) and Figure 3.14. The extra peaks correspond to Pt 4d<sub>3/2</sub>. [26-28]

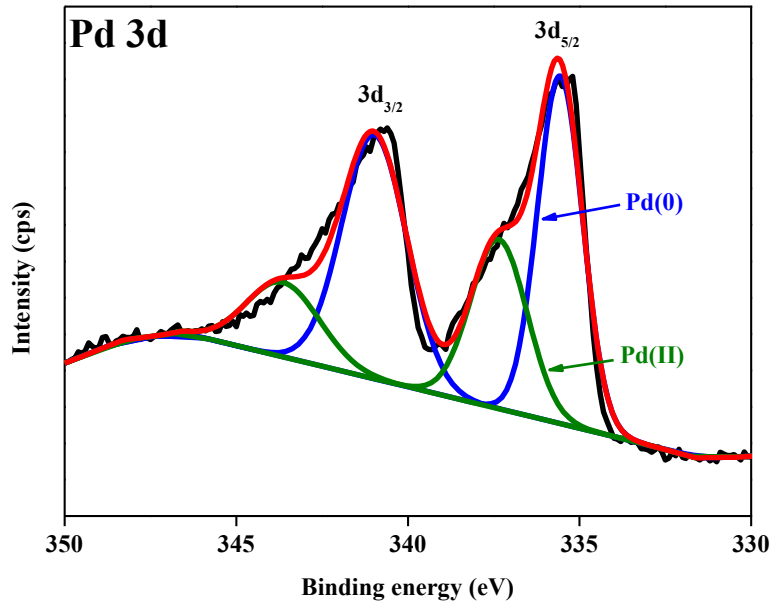
Catalysts	Species	Binding energy (eV) (Pd 3d <sub>3/2</sub> )	Relative intensity (%)	Binding energy (eV) (Pd 3d <sub>5/2</sub> )	Relative intensity (%)
Pd/CNTs	Pd(0)	341.0	74	335.6	62
	Pd(II)	343.6	26	337.4	38
Pd@PdPt/CNTs-1	Pd(0)	340.7	74	335.5	72
	Pd(II)	343.7	26	337.7	28
Pd@PdPt/CNTs-2	Pd(0)	340.9	74	335.7	76
	Pd(II)	343.0	26	337.8	24
Pt@Pd/CNTs-1	Pd(0)	341.4	78	335.8	77
	Pd(II)	344.4	22	338.1	23
Pt@Pd/CNTs-2	Pd(0)	341.4	77	336.0	84
	Pd(II)	344.5	23	338.5	16
Pt@Pd/CNTs-3	Pd(0)	341.5	68	336.2	78
	Pd(II)	344.8	32	338.7	22

Table 3.3 Binding energies and relative intensities of different palladium species of Pd/CNTs, Pd@PdPt/CNTs and Pt@Pd/CNTs composites.

Catalysts	Species	Binding energy (eV) (Pt 4f <sub>5/2</sub> )	Relative intensity (%)	Binding energy (eV) (Pt 4f <sub>7/2</sub> )	Relative intensity (%)
Pt/CNTs	Pt(0)	76.2	74	72.7	71
	Pt(II)	78.0	26	74.4	29
Pd@PdPt/CNTs-1	Pt(0)	74.9	67	71.6	80
	Pt(II)	77.1	33	73.2	20
Pd@PdPt/CNTs-2	Pt(0)	75.0	73	71.6	80
	Pt(II)	77.4	27	73.2	20
Pt@Pd/CNTs-1	Pt(0)	75.0	81	71.6	90
	Pt(II)	77.6	19	72.8	10
Pt@Pd/CNTs-2	Pt(0)	74.7	78	71.5	87
	Pt(II)	76.6	22	73.2	13
Pt@Pd/CNTs-3	Pt(0)	74.7	79	71.3	83
	Pt(II)	76.5	21	72.8	17

Table 3.4 Binding energies and relative intensities of different platinum species of Pt/CNTs, Pd@PdPt/CNTs and Pt@Pd/CNTs composites.

(a)



(b)

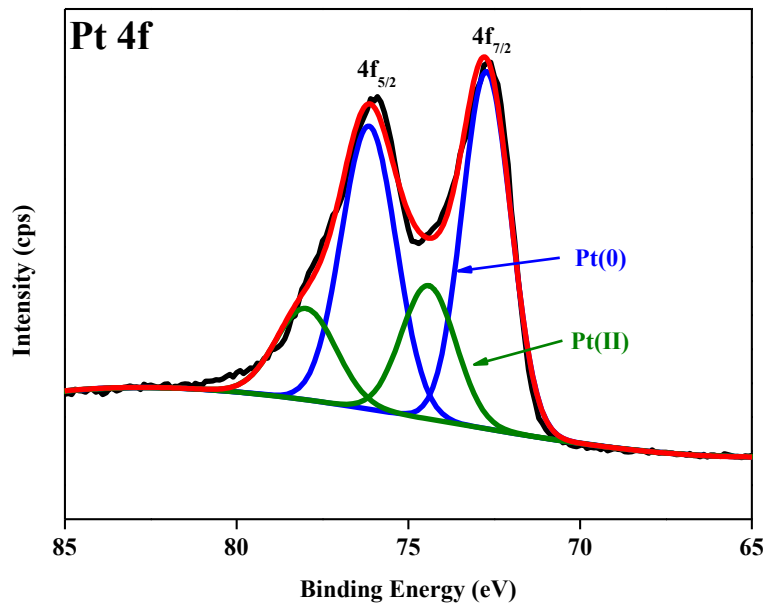
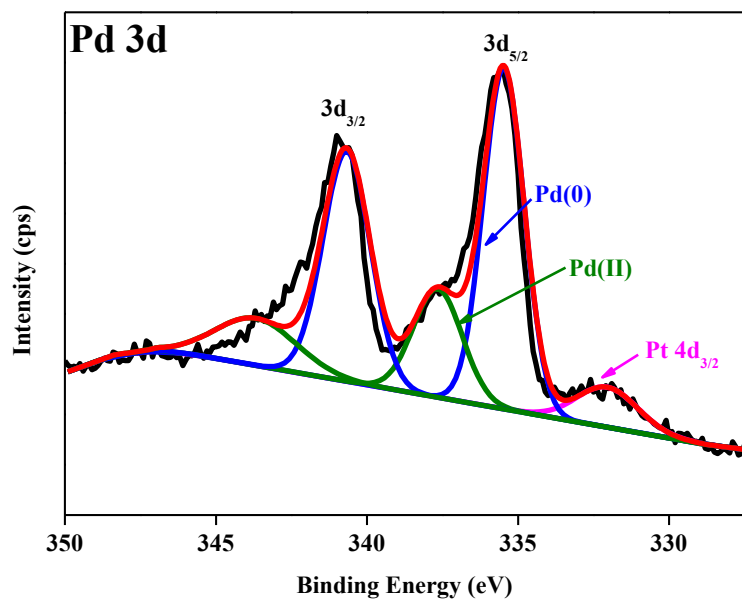


Figure 3.12 XPS spectra of (a) Pd 3d region of Pd/CNTs composite and (b) Pt 4f region of Pt/CNTs composite.

(c)



(d)

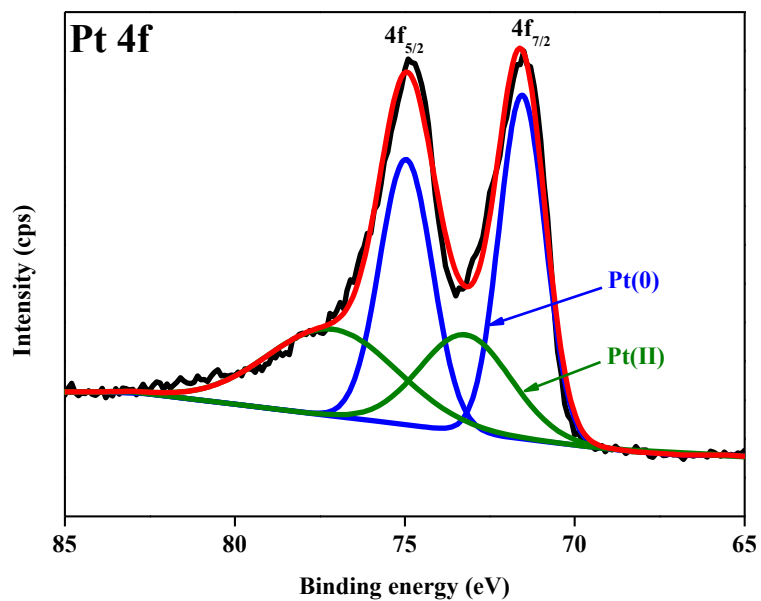
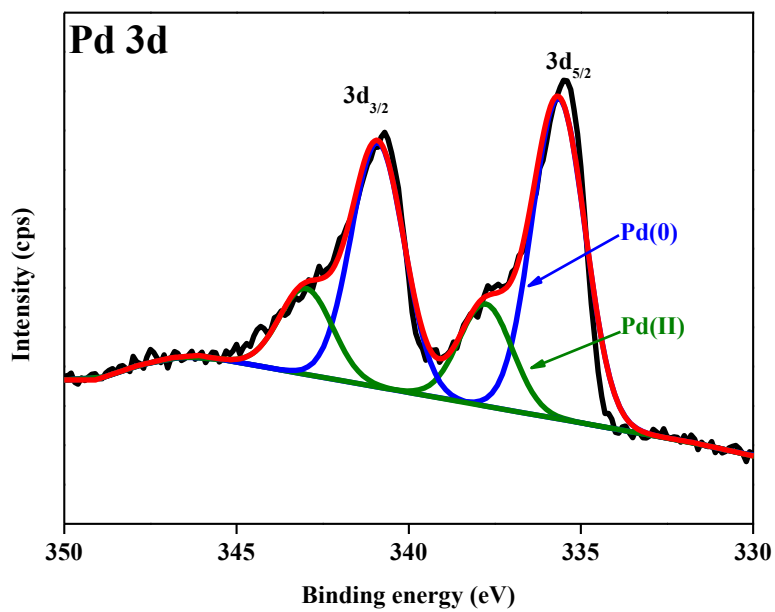


Figure 3.12 XPS spectra of (c) Pd 3d and (d) Pt 4f regions of Pd@PdPt/CNTs-1 composite.

(e)



(f)

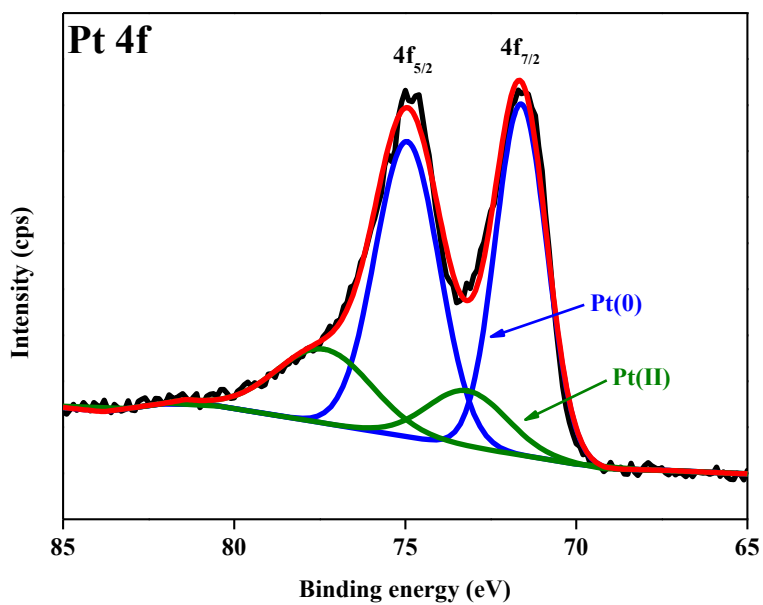
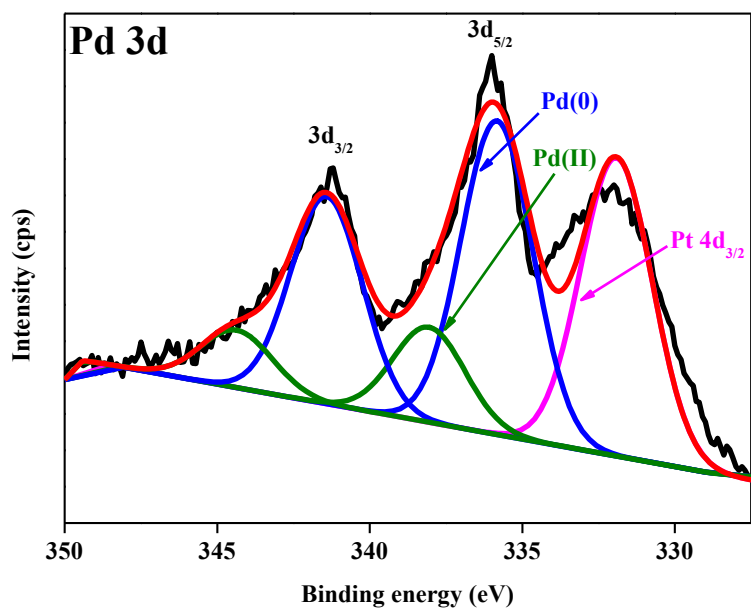


Figure 3.12 XPS spectra of (e) Pd 3d and (f) Pt 4f regions of Pd@PdPt/CNTs-2 composite.

(g)



(h)

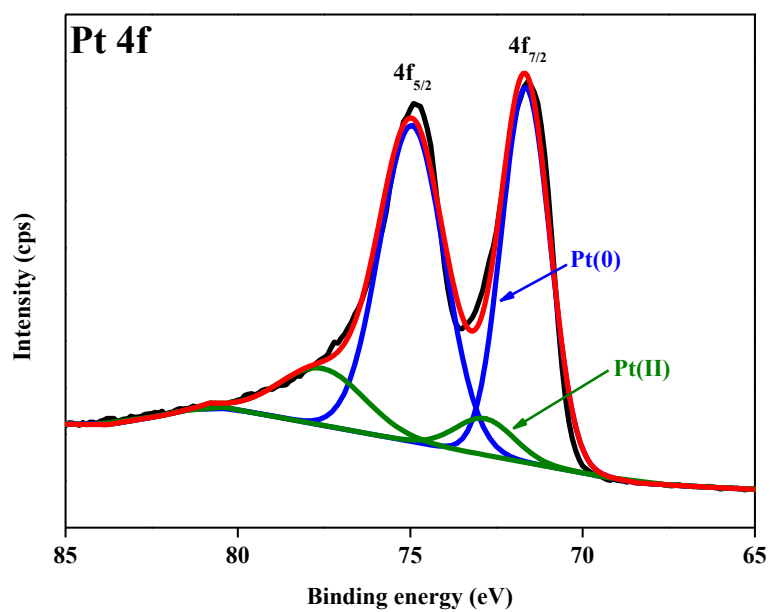
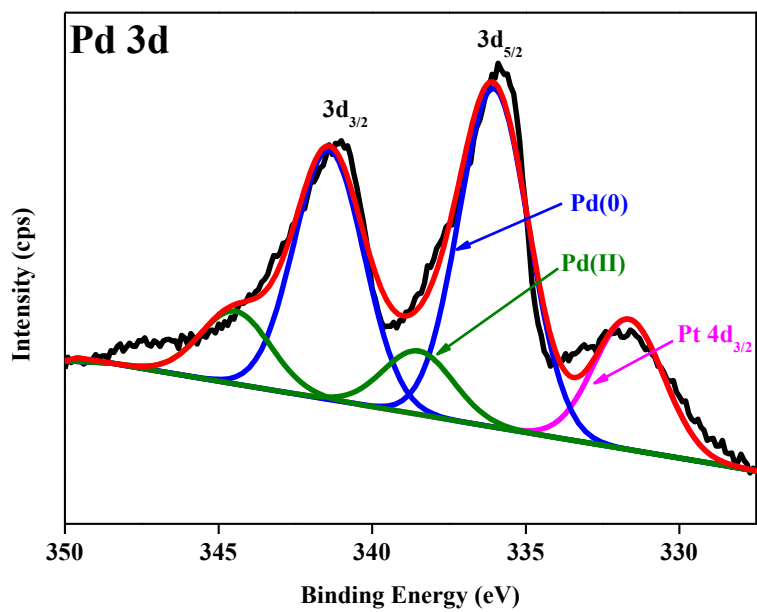


Figure 3.12 XPS spectra of (g) Pd 3d and (h) Pt 4f regions of Pt@Pd/CNTs-1 composite.

(i)



(j)

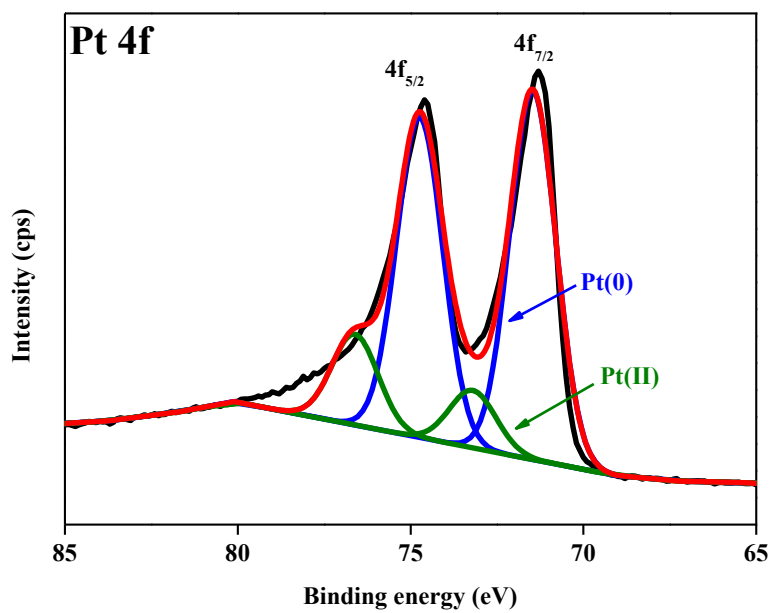
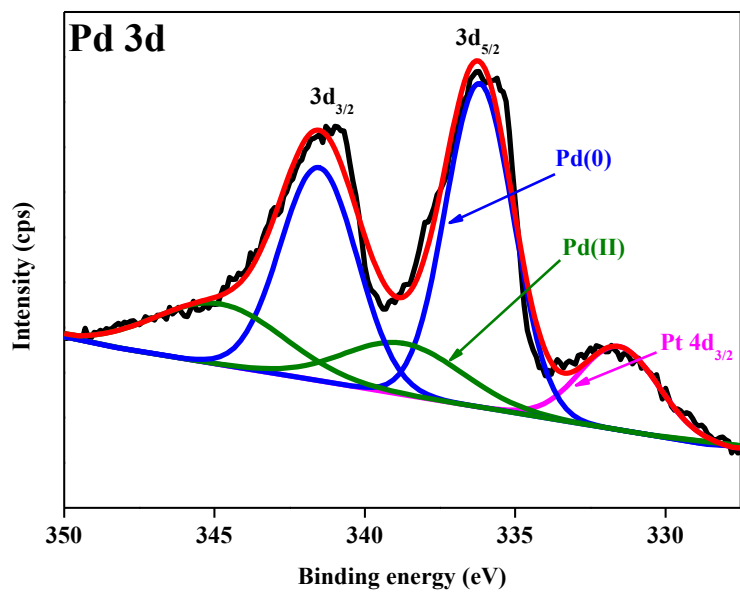


Figure 3.12 XPS spectra of (i) Pd 3d and (j) Pt 4f regions of Pt@Pd/CNTs-2 composite.

(k)



(l)

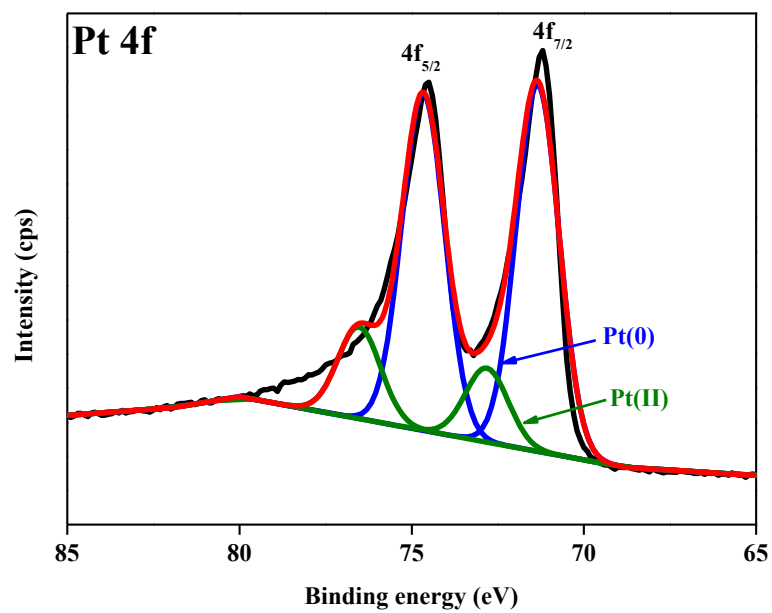


Figure 3.12 XPS spectra of (k) Pd 3d and (l) Pt 4f regions of Pt@Pd/CNTs-3 composite.

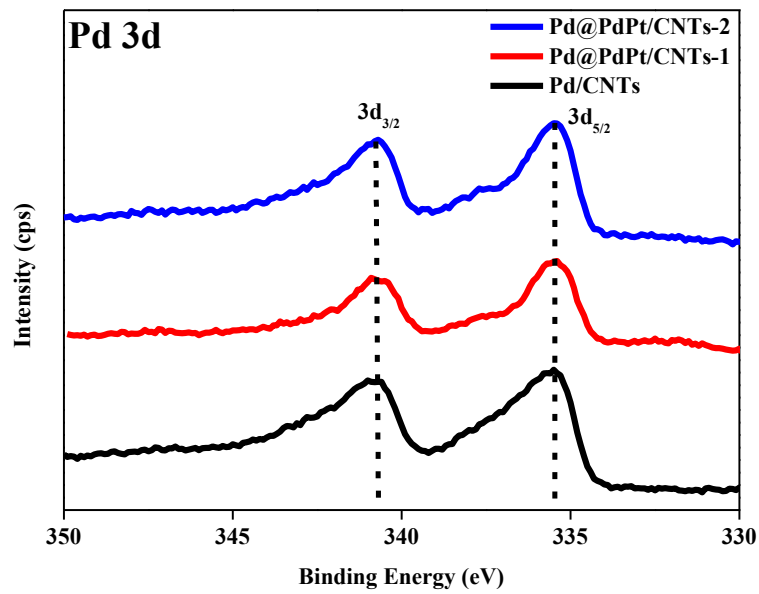
The PdPt alloy formation was confirmed by the shift of binding energy of Pd 3d and Pt 4f peaks. As presented in Table 3.5 and displayed in Figure 3.13 (a), the Pd 3d peaks of Pd@PdPt/CNTs composites are positively shifted when compared with Pd 3d peaks of Pd/CNTs composite. In Figure 3.13 (b), the Pt 4f peaks of Pd@PdPt/CNTs composites are negatively shifted when compared with the Pt 4f region of Pt/CNTs composite. The negatively shifted Pt 4f peaks and the positively shifted Pd 3d peaks suggests the electron transfer from Pd to Pt.[29]

The change of electronic structure confirms the PdPt alloy formation. In Figure 3.14 (a), the Pd 3d peaks of Pt@Pd/CNTs composite are positively shifted when compared with the Pd 3d peaks of Pd/CNTs composite. In Figure 3.14 (b), the Pt 4f peaks of Pt@Pd/CNTs composites are negatively shifted when compared with the Pt 4f peaks of Pt/CNTs composite. The negatively shifted Pt 4f peaks and the positively shifted Pd 3d peaks suggest the electron transfer from Pd to Pt.[29]

	Binding energy of Pd		Binding energy of Pt	
	(eV)		(eV)	
	3d <sub>3/2</sub>	3d <sub>5/2</sub>	4f <sub>5/2</sub>	4f <sub>7/2</sub>
Pd/CNTs	340.6	334.4	-	-
Pt/CNTs	-	-	75.9	72.7
Pd@PdPt/CNTs-1	340.8	335.4	74.8	71.5
Pd@PdPt/CNTs-2	340.9	335.4	74.9	71.5
Pt@Pd/CNTs-1	341.3	336.0	75.0	71.6
Pt@Pd/CNTs-2	341.4	336.0	74.6	71.3
Pt@Pd/CNTs-3	341.5	336.2	74.5	71.2

Table 3.5 Summary of the binding energies of Pd 3d and Pt 4f peaks of Pd/CNTs, Pt/CNTs, Pd@PdPt/CNTs and Pt@Pd/CNTs composites.

(a)



(b)

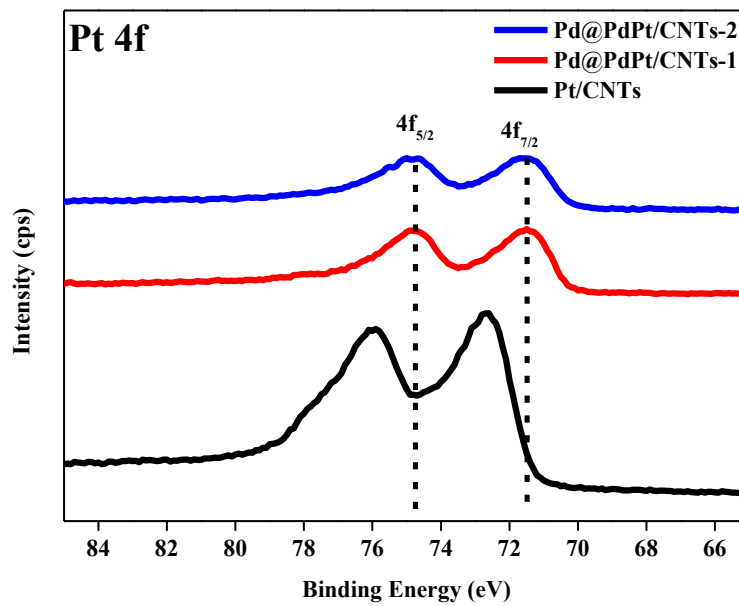


Figure 3.13 XPS spectra of (a) Pd 3d region of Pd/CNTs, Pd@PdPt/CNTs-1 and Pd@PdPt/CNTs-2 composites and (b) Pt 4f region of Pt/CNTs, Pd@PdPt/CNTs-1 and Pd@PdPt/CNTs-2 composites.

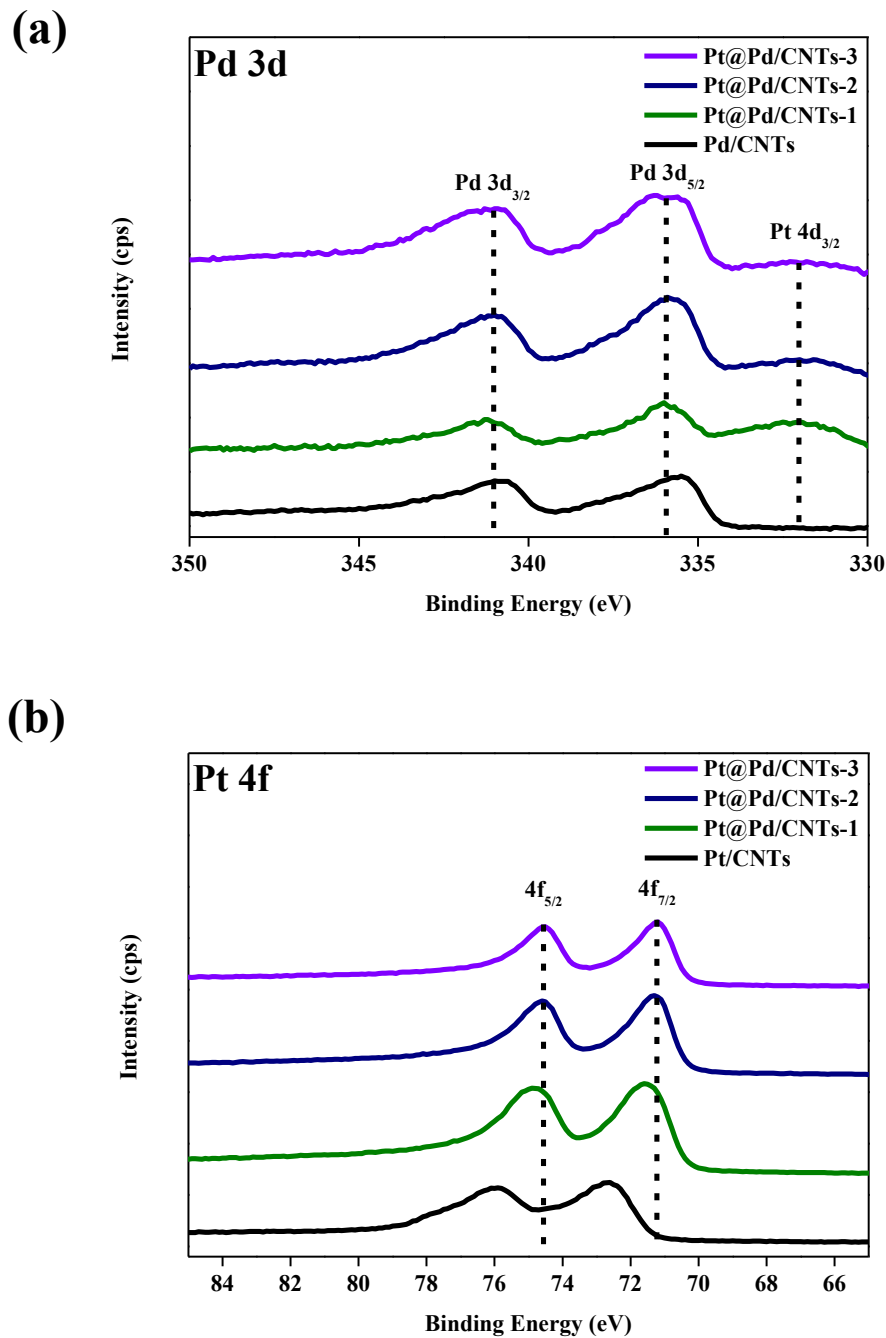


Figure 3.14 XPS spectra of (a) Pd 3d region of Pd/CNTs, Pt@Pd/CNTs-1, Pt@Pd/CNTs-2 and Pt@Pd/CNTs-3 composites and (b) Pt 4f region of Pt/CNTs, Pt@Pd/CNTs-1, Pt@Pd/CNTs-2 and Pt@Pd/CNTs-3 composites.

Compared with Pt, Pd is an oxophilic metal.[30, 31] The oxidative removal of CO<sub>ads</sub> species from catalyst surface by the availability of large number of active oxygen-containing species such as PdO and Pd(OH)<sub>2</sub>. Among the catalysts, Pd@PdPt/CNTs composites exhibit higher O 1s/(Pd 3d + Pt 4f) atomic ratios. (Table 3.6) This suggests that they may have higher density of surface function groups, which is beneficial for the oxidation of intermediates.[32, 33] The faster removal of intermediates releases the catalyst surface for the alcohol oxidations.[34]

Catalysts	O 1s atomic conc. (%)	Pd 3d atomic conc. (%)	Pt 4f atomic conc. (%)	O 1s/(Pd 3d + Pt 4f) atomic ratio
Pd/CNTs	7.40	1.43	-	5.17
Pt/CNTs	7.95	-	1.68	4.73
Pd@PdPt/CNTs-1	5.72	0.46	0.39	6.73
Pd@PdPt/CNTs-2	6.96	0.95	0.27	5.70
Pt@Pd/CNTs-1	5.27	0.17	1.22	3.79
Pt@Pd/CNTs-2	5.58	0.48	1.10	3.53
Pt@Pd/CNTs-3	6.64	0.59	0.91	4.43

Table 3.6 The elemental atomic concentrations of the catalysts.

### 3.2.4 Electrochemical characterizations and electrocatalytic studies

#### 3.2.4.1 Cyclic voltammetry in sulfuric acid

Figure 3.15 exhibits the cyclic voltammograms (CVs) of Pt/CNTs, Pd/CNTs, Pd@PdPt/CNT-1, Pd@PdPt/CNTs-2, Pt@Pd/CNTs-1, Pt@Pd/CNTs-2 and Pt@Pd/CNTs-3 composites in N<sub>2</sub>-purged 0.1 M H<sub>2</sub>SO<sub>4</sub> solution in a potential region between -0.24 V and 1.0 V with a scan rate of 50 mVs<sup>-1</sup>. The typical characteristics of surface oxidation over a wide range of potential,[35] the reduction peak of metal oxides at 0.4 V to 0.5 V and the hydrogen adsorption/desorption (H<sub>ads/des</sub>) peaks in the potential range from 0.0 V to 0.2 V are shown.

A distinct difference is observed in the sharpness of the reduction peak of metal oxides at 0.4 V to 0.5 V of Pd/CNTs and Pt/CNTs composites. For the Pd/CNTs composite in Figure 3.15 (a), the reduction peak of PdO at 0.42 V is sharp and high which is a characteristic feature for Pd surfaces.[35] For the Pt/CNTs composite in Figure 3.15 (b), the reduction peak of PtO at 0.43 V is broad and low. The possible reasons were Pt surface was highly rough and Pt existed in several crystalline facets.[35]

For the Pd/CNTs composite, the peak potential of the reduction peak of PdO is 0.42 V. For Pd@PdPt/CNTs-1 (0.51 V) and Pd@PdPt/CNTs-2 (0.48 V) composites displayed in Figure 3.15 (c), there is a positive shift in the peak

potential of the reduction peaks of metal oxides when compared with Pd/CNTs composite. This may be attributed to the formation of PdPt alloy.

For the Pt/CNTs composite, the peak potential of the reduction peak of PtO is 0.43 V. For Pt@Pd/CNTs-1, Pt@Pd/CNTs-2 and Pt@Pd/CNTs-3 composites in Figure 3.15 (d), there is a positive shift in the peak potentials of the reduction peaks of metal oxides, which are 0.50 V, 0.51 V and 0.51 V respectively, when compared with Pt/CNTs composite. This is probably due to the deposition of Pd on Pt surface. The peak potentials of Pt@Pd/CNTs-1 (0.50 V), Pt@Pd/CNTs-2 (0.52 V) and Pt@Pd/CNTs-3 (0.51 V) composites are not close to Pd/CNTs composite (0.42 V), suggesting that Pt surface is not fully covered by Pd.[35] This further confirms that Pt@Pd/CNTs composites possess a PtPd shell.

The area under the cathodic peaks for the reduction of Pt oxide and Pd oxide are used to determine ECSA of Pt and Pd. The ECSA of Pt and Pd can be calculated by the following equations.

$$ECSA_{Pt} = Q_{Pt}/420 \mu Ccm^{-2} \quad \text{Eq. 3.4}$$

$$ECSA_{Pd} = Q_{Pd}/405 \mu Ccm^{-2} \quad \text{Eq. 3.5}$$

where  $Q_{Pt}$  and  $Q_{Pd}$  are the surface oxide reduction charges of plain Pt and Pd respectively.[36, 37] For monometallic catalysts, the specific area activity is calculated by normalizing the current to  $ECSA_{Pt}$  or  $ECSA_{Pd}$ . For each PtPd-based modified bimetallic catalysts, the mean value of surface oxide reduction charge

was determined based on the Pd-to-Pt surface ratio by XPS [37] and the specific area activity is calculated by normalizing the current to the calculated ECSA of the modified catalysts.

As stated in Table 3.7, the specific area activity of Pd/CNTs ( $0.1571 \text{ mAcm}^{-2}$ ) is highest while that of Pt/CNTs ( $0.080 \text{ mAcm}^{-2}$ ) is lowest. After alloying Pt with Pd/CNTs composite, the specific area activities of Pd@PdPt/CNTs-1 and Pd@PdPt/CNTs-2 composites decrease to  $0.107 \text{ mAcm}^{-2}$  and  $0.119 \text{ mAcm}^{-2}$  respectively when compared with Pd/CNTs composite. After deposition of Pd onto Pt/CNTs, the specific area activities of Pt@Pd/CNTs-1, Pt@Pd/CNTs-2 and Pt@Pd/CNTs-3 composites increase to  $0.090 \text{ mAcm}^{-2}$ ,  $0.105 \text{ mAcm}^{-2}$  and  $0.117 \text{ mAcm}^{-2}$  respectively when compared with Pt/CNTs composite.

The CVs of Pd@PdPt/CNTs and Pt@Pd/CNTs composites in  $\text{H}_2\text{SO}_4$  are not similar. They exhibit similar CV to their metal cores of Pd and Pt respectively. Pd@PdPt/CNTs composites exhibit larger  $\text{H}_{\text{ads/des}}$  peaks when compared with Pt@Pd/CNTs composites due to their Pd metal core. This feature may be used to differentiate alloy and phase-separate structures. To further investigate their potential differences, their electrocatalytic activities towards the oxidations of methanol, ethanol and glycerol were analyzed and compared.

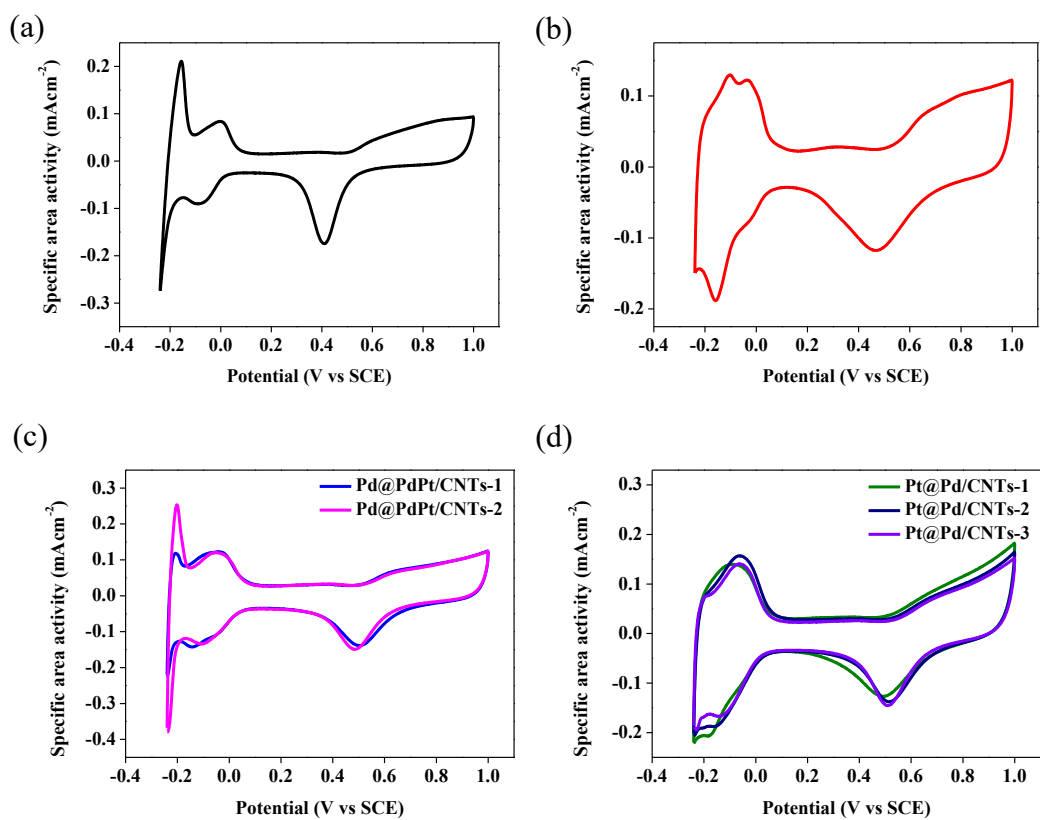


Figure 3.15 CVs of (a) Pd/CNTs, (b) Pt/CNTs, (c) Pd@PdPt/CNTs, and (d) Pt@Pd/CNTs composites in N<sub>2</sub>-purged 0.1 M H<sub>2</sub>SO<sub>4</sub> solution. Scan rate, 50 mVs<sup>-1</sup>.

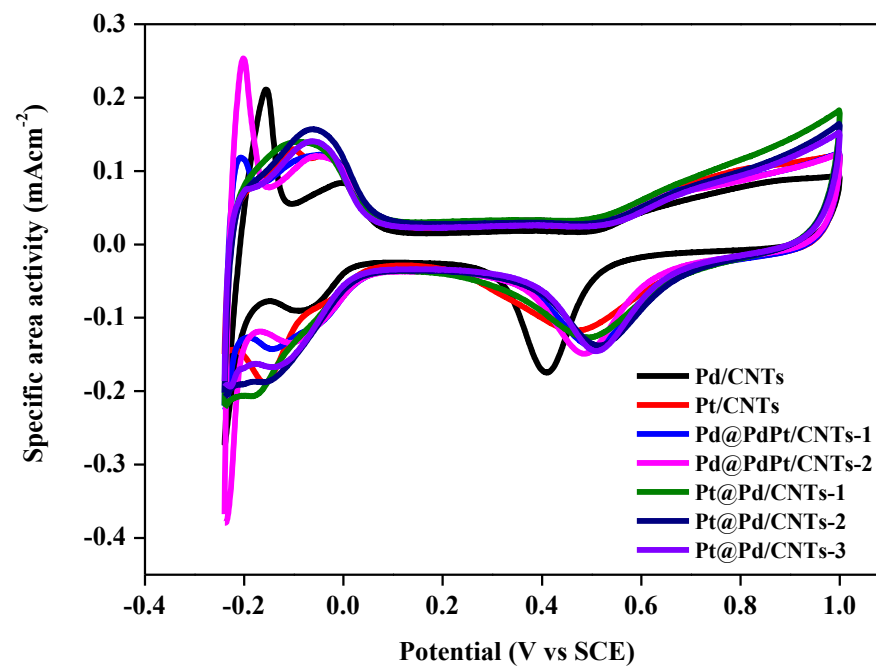


Figure 3.16 CVs of Pd/CNTs, Pt/CNTs, Pd@PdPt/CNTs-1, Pd@PdPt/CNTs-2, Pt@Pd/CNTs-1, Pt@Pd/CNTs-2 and Pt@Pd/CNTs-3 in  $\text{N}_2$ -purged 0.1 M  $\text{H}_2\text{SO}_4$  solution between -0.24 V and 1.0 V. Scan rate,  $50 \text{ mVs}^{-1}$ .

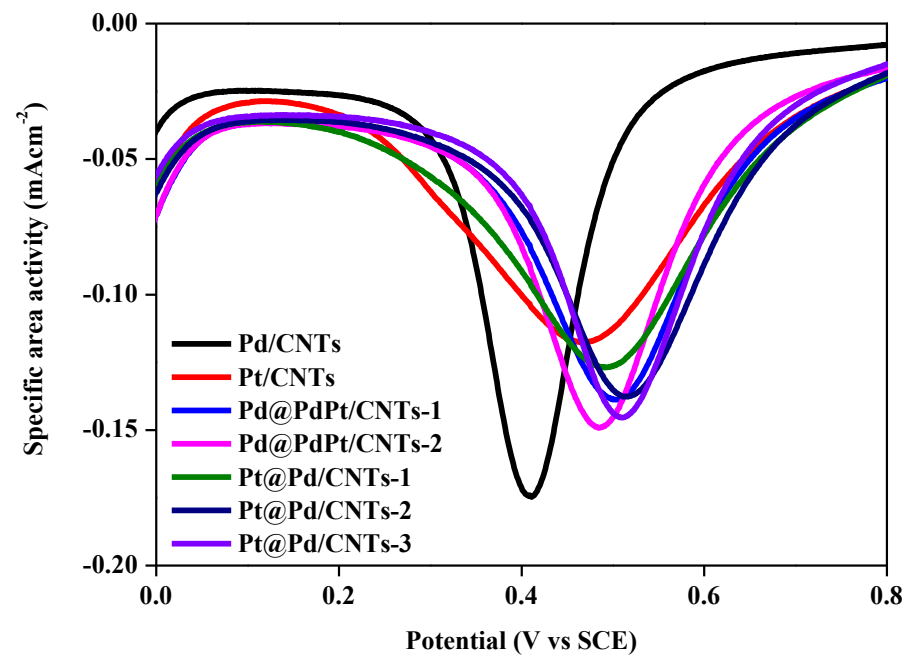


Figure 3.17 CVs of Pd/CNTs, Pt/CNTs, Pd@PdPt/CNTs-1, Pd@PdPt/CNTs-2, Pt@Pd/CNTs-1, Pt@Pd/CNTs-2 and Pt@Pd/CNTs-3 in  $N_2$ -purged 0.1M  $H_2SO_4$  solution between 0.0 V and 0.8 V. Scan rate,  $50 \text{ mVs}^{-1}$ .

Catalysts	Pd-to-Pt surface ratio by XPS	Peak potential (V)	Specific area activity (mAcm <sup>-2</sup> )
Pd/CNTs	-	0.42	0.157
Pt/CNTs	-	0.43	0.079
Pd@PdPt/CNTs-1	1.3 : 1	0.51	0.107
Pd@PdPt/CNTs-2	2.2 : 1	0.48	0.119
Pt@Pd/CNTs-1	1 : 7.2	0.49	0.090
Pt@Pd/CNTs-2	1 : 2.3	0.52	0.105
Pt@Pd/CNTs-3	1 : 1.5	0.51	0.117

Table 3.7 Summary of peak potentials and specific area activities of catalysts in N<sub>2</sub>-purged 0.1 M H<sub>2</sub>SO<sub>4</sub> solution.

### 3.2.4.2 Electrooxidation of methanol and its related chronoamperometric test

#### Electrooxidation of methanol

Figure 3.18 shows the CVs of the catalysts coated on GCE in 0.1 M MeOH + 0.1 M H<sub>2</sub>SO<sub>4</sub> solution in the potential region from 0.0 V to 1.0 V with a scan rate of 50 mVs<sup>-1</sup>. It is known that CNTs is not active towards the oxidation of methanol.[38] The specific area activity towards the oxidation of methanol is calculated by normalizing current to the ECSA of the catalysts.

The Pt/CNTs, Pd@PdPt/CNTs-1, Pt@Pd/CNTs-1 and Pt@Pd/CNTs-2 composites show two anodic peaks in the forward scan and backward scan. In the forward scan, the anodic peak at around 0.6 V is due to the oxidation of methanol. When the voltage applied is higher than the peak potential, the current density decreases because the adsorbed intermediate species block the Pt active sites. In the backward scan, the anodic peak at around 0.4 V is due to the oxidation of CO<sub>ads</sub> or other associated incompletely oxidized carbonaceous intermediates formed during the forward scan.[15, 16, 39]

As shown in Table 3.8, the specific area activity towards the oxidation of methanol decreases in the order of Pt/CNTs (0.62 mAcm<sup>-2</sup>), Pt@Pd/CNTs-1 (0.39 mAcm<sup>-2</sup>), Pd@PdPt/CNTs-1 (0.32 mAcm<sup>-2</sup>) and Pt@Pd/CNTs (0.10 mAcm<sup>-2</sup>) composites while other catalysts including Pd/CNTs, Pd@PdPt/CNTs-2

and Pt@Pd/CNTs-3 composites are inactive to the oxidation of methanol.[16]

Both PtPd-based modified catalysts show lower catalytic activity than Pt/CNTs composite, suggesting that they are inactive mixtures towards methanol oxidation. The Pd@PdPt/CNTs-1 composite ( $0.32 \text{ mAcm}^{-2}$ ) achieve lower specific area activity than Pt/CNTs composite ( $0.62 \text{ mAcm}^{-2}$ ) and Pd@PdPt/CNTs-2 composite is inactive towards the oxidation of methanol. This suggests that catalytic activity towards the oxidation of methanol is not enhanced by alloy structure. Also, Pd@PdPt/CNTs-2 composite has higher Pd content and fewer ensemble Pt sites, resulting in lower catalytic activity.

The specific area activities towards the methanol oxidation of three Pt@Pd/CNTs composites are also inferior to that of Pt/CNTs composite. The reason may be due to the formation of the submonolayer of Pd shell on the Pt nanocore. The specific area activity of Pt@Pd/CNTs-1 ( $0.39 \text{ mAcm}^{-2}$ ) is higher than that of Pt@Pd/CNTs-2 ( $0.10 \text{ mAcm}^{-2}$ ) and Pt@Pd/CNTs-3 composite is inactive towards the oxidation of methanol. As revealed by XPS analysis, the Pt@Pd/CNTs-1 composite has lower Pd-to-Pt surface ratio (1 : 7.2) than Pt@Pd/CNTs-2 (1 : 2.3) and Pt@Pd/CNTs-3 (1 : 1.5) composites. With the increase of Pd-to-Pt surface ratio, more Pd covers on the Pt sites and decreasing Pt active sites are exposed to the oxidation of methanol. As a result, the specific area activity towards the oxidation of methanol decreases with the increasing Pd-to-Pt surface ratio of Pt@Pd/CNTs composites.

In accordance with XPS analysis, Pd@PdPt/CNTs-1 (1.3 : 1) and Pt@Pd/CNTs-3 (1 : 1.5) composites exhibit comparable Pd-to-Pt surface ratio. As shown in Table 3.8, they exhibit significantly different catalytic activity towards methanol oxidation. It is suggested that a structural surface difference is exhibited between Pd@PdPt/CNTs-1 and Pt@Pd/CNTs-3 composites, resulting in a different catalytic activity. For Pd@PdPt-1 composite, a better mixing PdPt alloy surface is exhibited while for Pt@Pd/CNTs-3 composite, Pd adsorb on Pt surface and block Pt active site from the oxidation of methanol. This result indirectly confirms that two different PtPd surface models were successfully established. This can be further confirmed by HAADF-STEM-EDS mappings and line scanning profiles to investigate the composition distribution in catalysts in progress.[25]

Apart from specific area activity, specific mass activity towards methanol oxidation was also estimated by normalizing the current to the Pt metal mass. (Figure 3.19 (b)) Both PtPd-based modified catalysts are less active than monometallic Pt/CNTs composite.

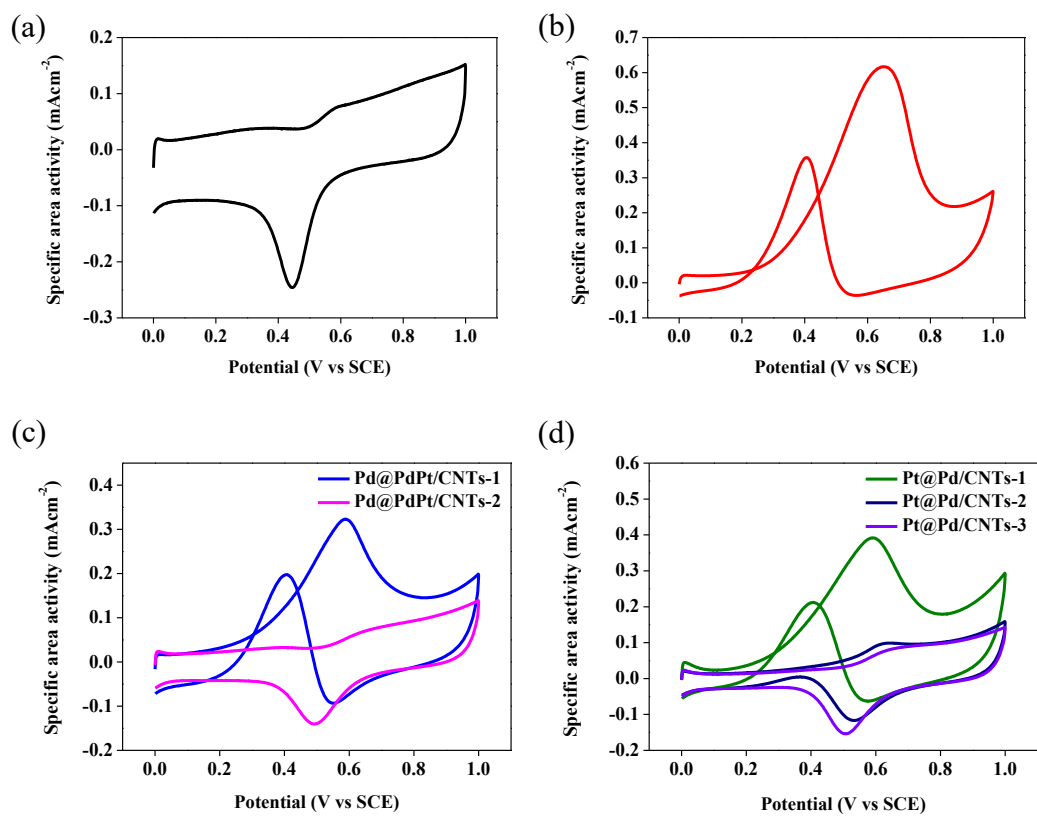


Figure 3.18 CVs of (a) Pd/CNTs, (b) Pt/CNTs, (c) Pd@PdPt/CNTs and (d) Pt@Pd/CNTs composites in 0.1 M MeOH + 0.1 M H<sub>2</sub>SO<sub>4</sub> solution. Scan rate, 50 mVs<sup>-1</sup>.

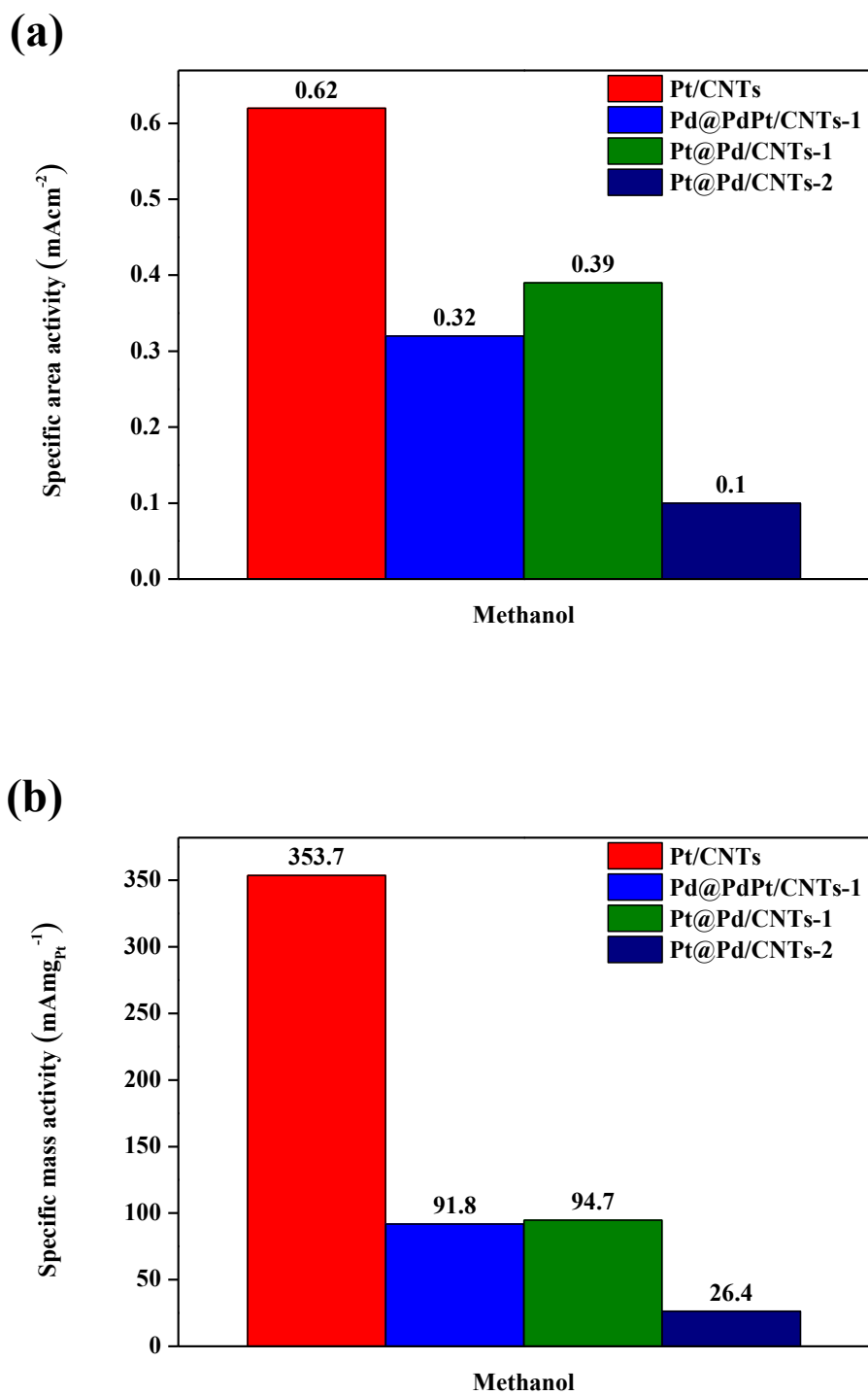


Figure 3.19 (a) The specific area activities and (b) specific mass activities of catalysts towards methanol oxidation.

Catalysts	Specific area activity (mAcm <sup>-2</sup> )	Specific mass activity (mA <sub>mgPt</sub> <sup>-1</sup> )
Pd/CNTs	-	-
Pt/CNTs	0.62	353.7
Pd@PdPt/CNTs-1	0.32	91.8
Pd@PdPt/CNTs-2	-	-
Pt@Pd/CNTs-1	0.39	94.7
Pt@Pd/CNTs-2	0.10	26.4
Pt@Pd/CNTs-3	-	-

Table 3.8 Summary of electrochemical performance of the catalysts towards the electrooxidation of methanol.

### **Chronoamperometric test of methanol oxidation**

To study the stability of the electrocatalysts towards the oxidation of methanol, chronoamperometric tests were performed. Figure 3.20 displays the chronoamperometric curves of the catalysts in 0.1 M MeOH + 0.1 M H<sub>2</sub>SO<sub>4</sub> solution at a fixed potential of 0.45 V for 1000 s. Since Pd/CNTs, Pd@PdPt/CNTs-2 and Pt@Pd/CNTs-3 composites are not active to the oxidation of methanol, chronoamperometric tests were performed only on the Pt/CNTs, Pd@PdPt/CNTs-1, Pt@Pd/CNTs-1, Pt@Pd/CNTs-2 composites.

Initially, the curves of current density decline rapidly owing to the formation and adsorption of poisonous intermediates such as CO<sub>ads</sub> during the oxidation of methanol. Afterwards, the curves of current density become flattened because of the accumulation of poisonous intermediates that blocks the active sites of the electrocatalysts from the oxidation of methanol.[14, 39]

As shown in Table 3.9, the current density retained after chronoamperometric test decreases in the order of Pt/CNTs (69.7 %), Pd@PdPt/CNTs-1 (45.3 %), Pt@Pd/CNTs-1 (40.7 %) and Pt@Pd/CNTs-2 (0.0 %) composites. It is observed that compared with Pt/CNTs composite, other three catalysts achieve lower stability. The possible reason is that the existence of Pd on surface may lower the stability of the catalysts as Pd tends to dissolve in acid during the oxidation of methanol at positive potential.[40]

Pd@PdPt/CNTs-1 and Pt@Pd/CNTs-1 composites achieve comparable stability due to similar comparable catalytic activities achieved towards the oxidation of methanol. Pt@Pd/CNTs-2 composite achieve significantly lower stability than Pt/CNTs composite due to its low surface Pt content.

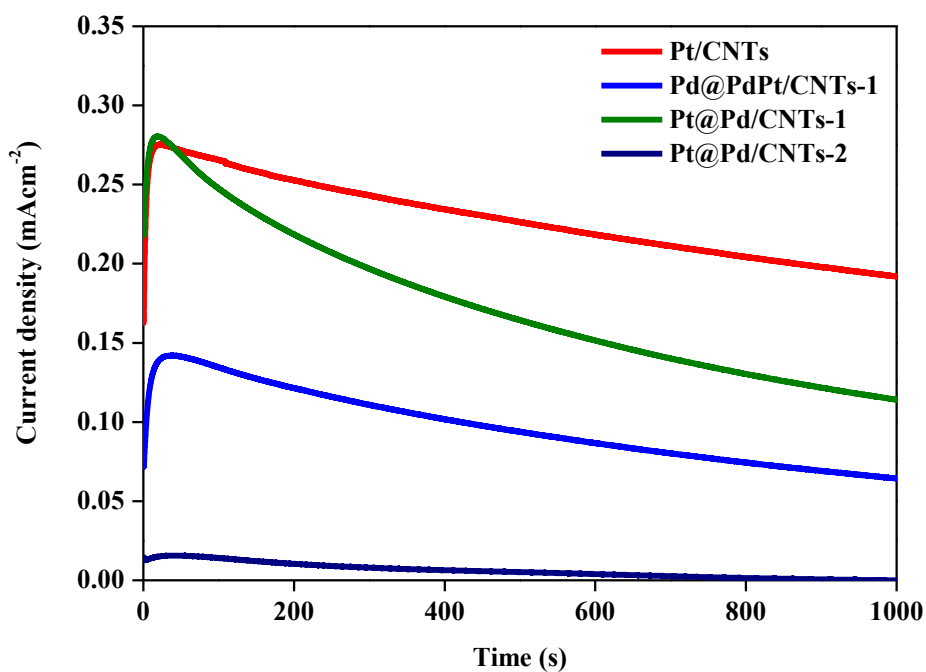


Figure 3.20 Chronoamperometric curves of the catalysts in 0.1 M MeOH + 0.1 M H<sub>2</sub>SO<sub>4</sub> solution at a fixed potential of 0.45 V for 1000 s.

Catalysts	Current density retained after 1000 s chronoamperometric test (%)
Pd/CNTs	-
Pt/CNTs	69.7
Pd@PdPt/CNTs-1	45.3
Pd@PdPt/CNTs-2	-
Pt@Pd/CNTs-1	40.7
Pt@Pd/CNTs-2	0.0
Pt@Pd/CNTs-3	-

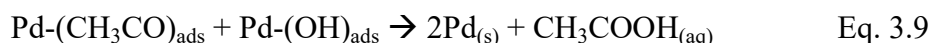
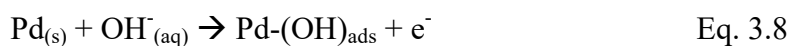
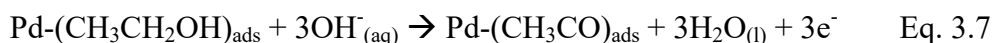
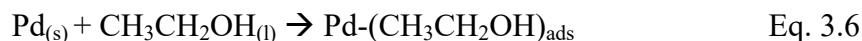
Table 3.9 Summary of electrochemical performance of catalysts towards chronoamperometric test of methanol oxidation.

### 3.2.4.3 Electrooxidation of ethanol and its related chronoamperometric test

#### Electrooxidation of ethanol

Figure 3.21 shows the CVs of the catalysts towards the oxidation of ethanol in 0.1 M EtOH + 0.1 M NaOH solution in the potential region between -0.8 V and 0.6 V with a scan rate of 50 mVs<sup>-1</sup>. It is observed that the anodic peaks in the forward scan are at -0.15 V to 0.0 V and those in the backward scan are at -0.45 V to -0.2 V, relating to the oxidations of ethanol and intermediate carbonaceous species respectively.[1] The specific area activity towards the oxidation of ethanol is calculated by normalizing current to the ECSA of the catalysts.

Mechanistic studies of ethanol oxidation catalyzed by Pd have been proposed as follow. [41-43]



Ethanol is first absorbed on the Pd surface to form Pd-CH<sub>3</sub>CH<sub>2</sub>OH<sub>ads</sub>, which reacts with hydroxide ions (OH<sup>-</sup>) present in the alkaline medium to form Pd-(CH<sub>3</sub>CO)<sub>ads</sub> (Eq. 3.6 and Eq 3.7). The anodic peak in forward scan is due to

the formation of Pd-(CH<sub>3</sub>CO)<sub>ads</sub>, meaning that the oxidation of ethanol is taking place (Eq. 3.7). After reaching the maximum value, the current density decreases with the increasing potential due to the oxidation of Pd to PdO, decreasing the availability of Pd active sites towards the oxidation of ethanol. With the increasing potential in the positive scan, more PdO are formed. As a consequence, the current density further decreases with the increasing potential. During the backward scan, the peak appears at around -0.12 V indicating the reactivation of the electrocatalyst due to the reduction of PdO to Pd as shown by the following equation. (Eq. 3.11)



The Pd surface is then recovered for the adsorption of OH<sup>-</sup>. The Pd-(OH)<sub>ads</sub> reacts with the Pd-(CH<sub>3</sub>CO)<sub>ads</sub> to form acetic acid (CH<sub>3</sub>COOH), which reacts with OH<sup>-</sup> ions to form acetate (CH<sub>3</sub>COO<sup>-</sup>) (Eq. 3.9 and Eq. 3.10).

As shown in Table 3.10, the specific area activity decreases in the order of Pd@PdPt/CNTs-1 (5.00 mAcm<sup>-2</sup>), Pt@Pd/CNTs-2 (2.60 mAcm<sup>-2</sup>), Pt@Pd/CNTs-1 (2.10 mAcm<sup>-2</sup>), Pt@Pd/CNTs-3 (1.94 mAcm<sup>-2</sup>), Pd@PdPt/CNTs-2 (1.85 mAcm<sup>-2</sup>), Pt/CNTs (1.36 mAcm<sup>-2</sup>) and Pd/CNTs (0.50 mAcm<sup>-2</sup>) composites.

Both modified catalysts show higher catalytic activity than monometallic Pd/CNTs and Pt/CNTs composites, suggesting that they are active mixtures

towards ethanol oxidation. The high catalytic activity of Pd@PdPt/CNTs-1 composite ( $5.00 \text{ mAcm}^{-2}$ ) towards the oxidation of ethanol can be attributed to the synergistic effect due to alloy formation. According to XPS analysis, the negative shift of Pt 4f peaks implies an upshift of d-band center. This increases the adsorption of  $\text{OH}^-$  ions and favors the removal of CO species from the catalyst site.[42, 44, 45] However, the electrocatalytic activity of Pd@PdPt/CNTs-2 composite ( $1.89 \text{ mAcm}^{-2}$ ) is not significantly enhanced. The Pd-to-Pt surface ratio of Pd@PdPt/CNTs-2 composite (2.2 : 1) is higher than that of Pd@PdPt/CNTs-1 composite (1.3 : 1). The synergistic effect due to alloying towards the oxidation of ethanol may be reduced. This observation is similar to the study conducted by Zhu et al.,[20] suggesting that increasing Pd content and decreasing Pt content in PdPt alloy catalysts decrease the corresponding catalytic activity towards ethanol oxidation.

It is also observed that the catalytic activities of three Pt@Pd/CNTs composites are enhanced when compared with Pt/CNTs composite. It is suggested that the oxophilicity of Pd is higher than that of Pt, meaning that the tendency of Pd forming oxides is higher. Pd acts as a promoting site for the adsorption of  $\text{OH}^-$  ions from alkaline medium to form Pd- $\text{OH}_{\text{ad}}$  that supplies  $\text{OH}^-$  ions to Pt surface, where the oxidation of ethanol takes place.[30] The specific area activity increases from  $2.10 \text{ mAcm}^{-2}$  to  $2.60 \text{ mAcm}^{-2}$  and then decreases to  $1.94 \text{ mAcm}^{-2}$ . Increasing Pd-to-Pt surface ratio from 1 : 7.2 to 1 : 2.3 enhances the promoting effect by Pd which results in a higher catalytic activity. However, further increase

of Pd-to-Pt surface ratio from 1 : 2.3 to 1 : 1.5 may limit the catalytic role of Pt, resulting in a decreasing catalytic activity.[46]

With a comparable Pd-to-Pt surface ratio, Pd@PdPt/CNTs-1 composite (1.3 : 1) exhibits a more superior performance than Pt@Pd/CNTs-3 composite (1 : 1.5) because a better mixing PdPt alloy surface contributes stronger synergistic effect. For Pt@Pd/CNTs-3 composite, due to the adsorption of Pd onto Pt surface, fewer Pt active sites are exposed to ethanol. Hence, the catalytic role of Pt towards the ethanol oxidation is limited, resulting in a lower catalytic activity. This different catalytic activity further indirectly confirms that the two modified catalysts have different arrangements, resulting in different catalytic activity.

In terms of specific mass activity, Pd@PdPt/CNTs composites are more active than monometallic Pd/CNTs and Pt/CNTs composites while Pt@Pd/CNTs composites are less active than monometallic Pt/CNTs composite towards ethanol oxidation. (Figure 3.22 (b)) This suggests that the alloy structure enhances the utilization of Pt.

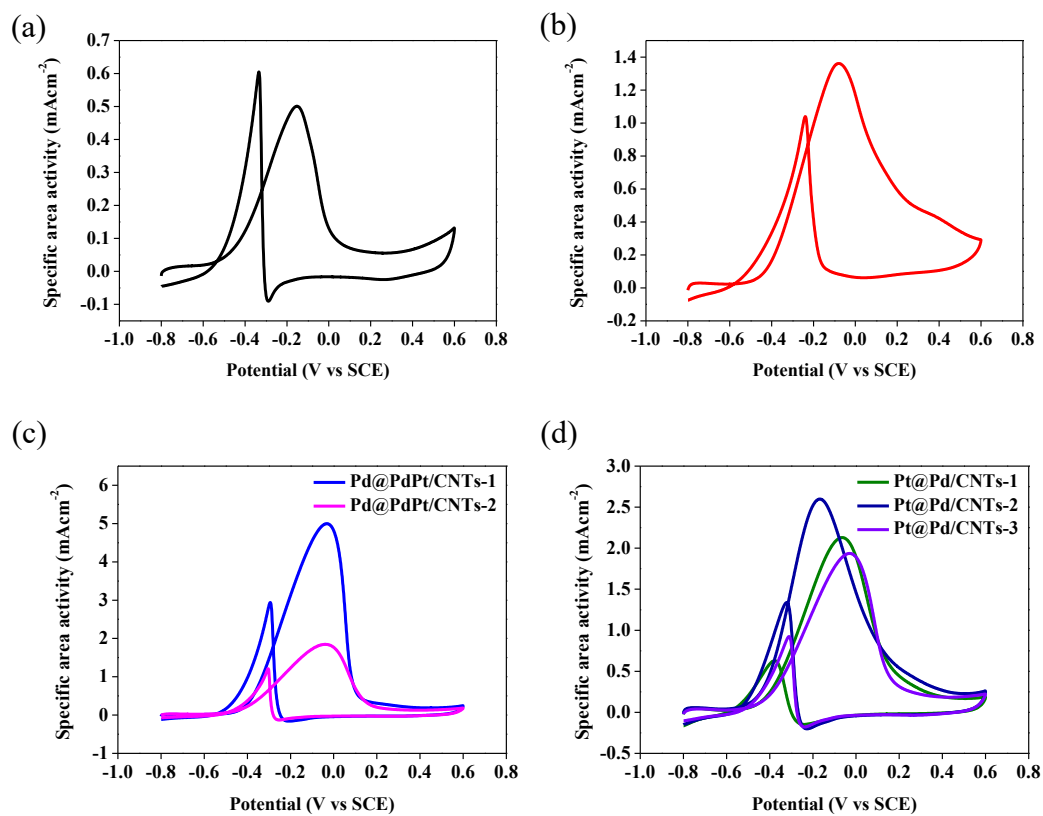


Figure 3.21 CVs of (a) Pd/CNTs, (b) Pt/CNTs, (c) Pd@PdPt/CNTs and (d) Pt@Pd/CNTs composites in 0.1 M EtOH + 0.1 M NaOH solution. Scan rate, 50 mVs<sup>-1</sup>.

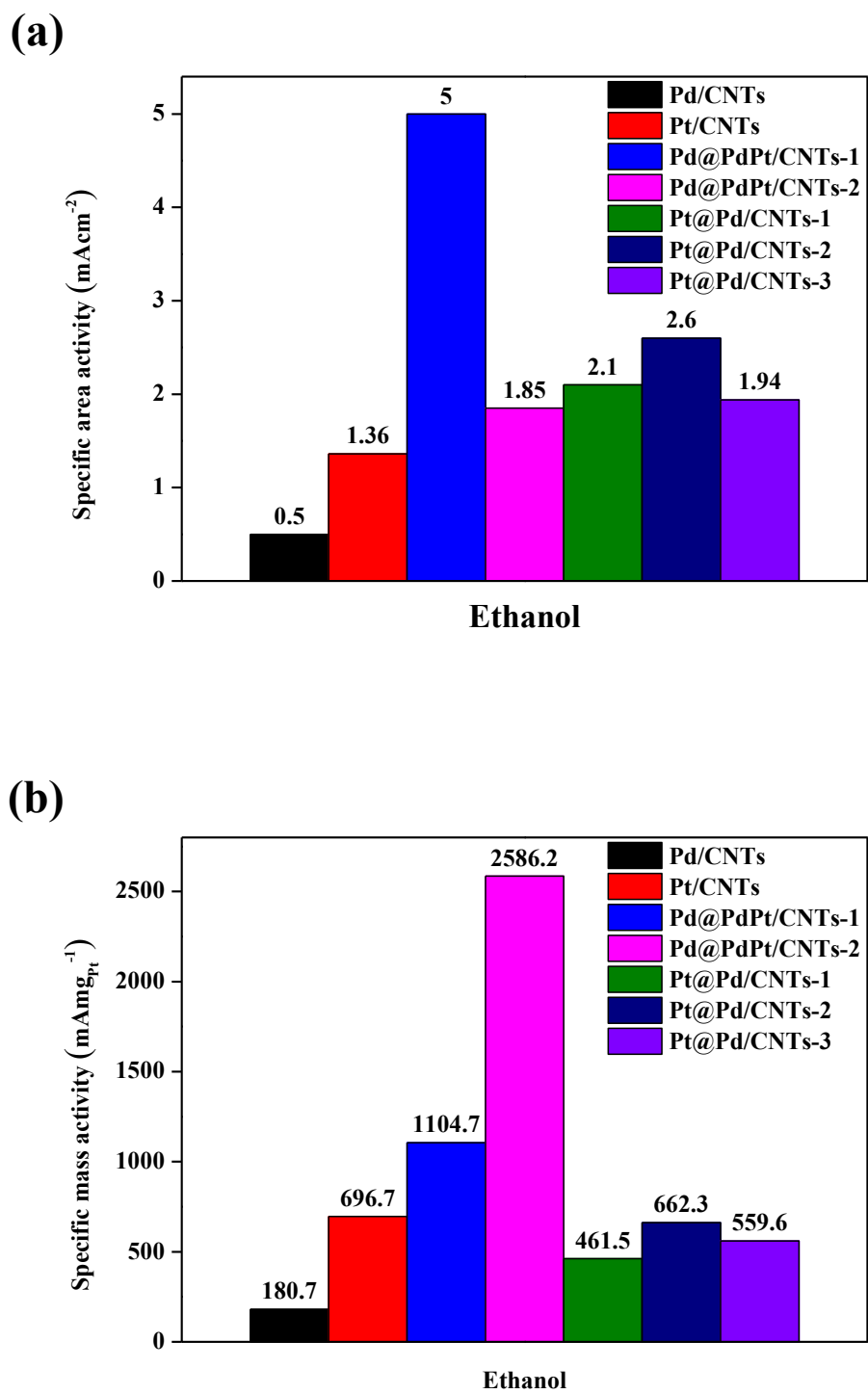


Figure 3.22 The specific area activities and specific mass activities of catalysts towards ethanol oxidation.

Catalysts	Specific area activity (mAcm <sup>-2</sup> )	Specific mass activity (mA <sub>mgPt</sub> <sup>-1</sup> )
Pd/CNTs	0.50	180.7
Pt/CNTs	1.36	696.7
Pd@PdPt/CNTs-1	5.00	1104.7
Pd@PdPt/CNTs-2	1.85	2586.2
Pt@Pd/CNTs-1	2.10	461.5
Pt@Pd/CNTs-2	2.60	662.3
Pt@Pd/CNTs-3	1.94	559.6

Table 3.10 Summary of electrochemical performance of the catalysts towards the electrooxidation of ethanol.

### **Chronoamperometric test of ethanol oxidation**

To study the stability of the catalysts towards the oxidation of ethanol, chronoamperometric tests were performed. Chronoamperometric tests were conducted in 0.1 M ethanol + 0.1 M NaOH solution at a fixed potential of -0.2 V for 1000 s as shown in Figure 3.23.

In the initial stage, the current density decline rapidly due to the adsorption and desorption of intermediates during the oxidation of ethanol. The current density then decline slowly because the intermediates accumulate and block the active sites of the catalysts from the oxidation of ethanol.[45]

As presented in Table 3.11, Pd@PdPt/CNTs composites achieve higher current density retained than Pt@Pd/CNTs composites, indicating their higher stability towards the oxidation of ethanol. The alloying of Pd and Pt is believed to enhance their stability.

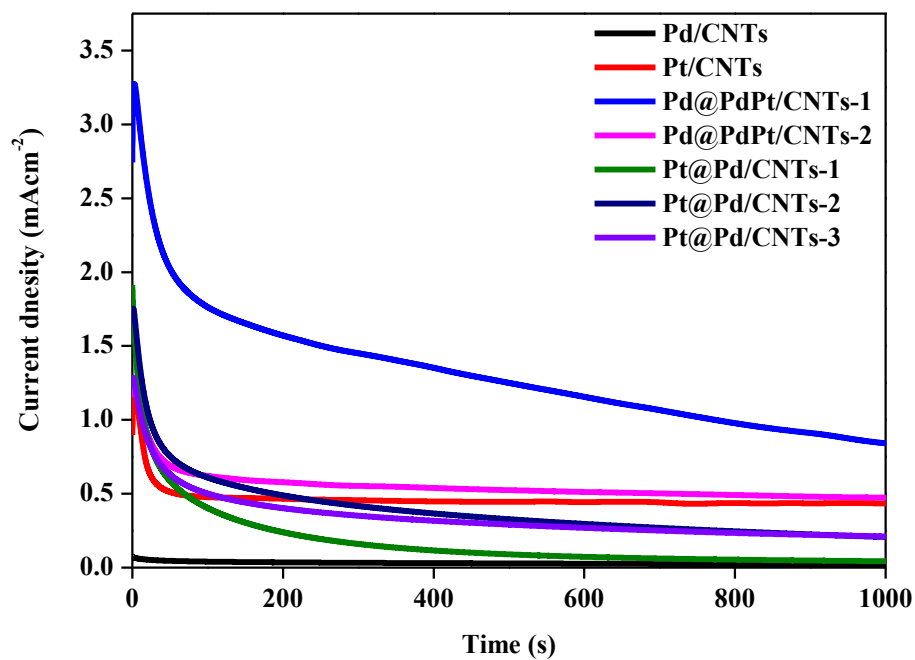


Figure 3.23 Chronoamperometric curves of the catalysts in 0.1 M EtOH + 0.1 M NaOH solution at a fixed potential of -0.2 V for 1000 s.

Catalysts	Current density retained after 1000 s chronoamperometric test (%)
Pd/CNTs	29.0
Pt/CNTs	37.8
Pd@PdPt/CNTs-1	25.7
Pd@PdPt/CNTs-2	38.0
Pt@Pd/CNTs-1	2.3
Pt@Pd/CNTs-2	12.4
Pt@Pd/CNTs-3	16.4

Table 3.11 Summary of electrochemical performance of catalysts towards chronoamperometric test of ethanol oxidation.

### 3.2.4.4 Electrooxidation of glycerol and its related chronoamperometric test

#### Electrooxidation of glycerol

Compared with ethanol oxidation, fewer studies were conducted on glycerol oxidation. Therefore, PtPd-based modified catalysts were further applied on glycerol oxidation. Figure 3.24 shows the CVs of the electrocatalysts towards the oxidation of glycerol in 0.1 M glycerol + 0.1 M NaOH solution in the potential region between -0.6 V and 0.6 V with a scan rate of 50 mVs<sup>-1</sup>. The specific area activity towards the oxidation of glycerol is calculated by normalizing current to the ECSA of the catalysts.

The curves of the oxidation of glycerol show two oxidative peaks in the forward and backward scans respectively. The oxidative peak in forward scan is related to the oxidation of freshly chemisorbed species. Another oxidative peak in reverse scan is related to the removal of intermediate species such as carbonaceous residues CO<sub>ads</sub> which were not completely oxidized in the forward scan.[47, 48]

As shown in Table 3.12, the specific area activity decreases in the order of Pd@PtPt/CNTs-1 (3.20 mAcm<sup>-2</sup>), Pt@Pd/CNTs-1 (2.25 mAcm<sup>-2</sup>), Pt@Pd/CNTs-2 (2.00 mAcm<sup>-2</sup>), Pt@Pd/CNTs-3 (1.82 mAcm<sup>-2</sup>), Pd@PdPt/CNTs-2 (1.31 mAcm<sup>-2</sup>), Pt/CNTs (1.22 mAcm<sup>-2</sup>) and Pd/CNTs (1.21 mAcm<sup>-2</sup>) composites.

Similar to ethanol oxidation, both modified catalysts are more active than monometallic Pd/CNTs and Pt/CNTs composites. The Pd@PdPt/CNTs-1 composite ( $3.20 \text{ mAcm}^{-2}$ ) shows remarkable electrocatalytic activity towards the oxidation of glycerol when compared with Pt/CNTs ( $1.22 \text{ mAcm}^{-2}$ ) and Pd/CNTs ( $1.21 \text{ mAcm}^{-2}$ ) attributing to the synergistic effect due to alloy formation. However, the electrocatalytic activity of Pd@PdPt/CNTs-2 ( $1.31 \text{ mAcm}^{-2}$ ) is not enhanced. According to the XPS analysis, the Pd-to-Pt surface ratio of Pd@PdPt/CNTs-2 composite (2.2 : 1) is higher than that of Pd@PdPt/CNTs-1 composite (1.3 : 1). The synergistic effect due to alloying towards the oxidation of glycerol may be reduced.[30]

The Pt@Pd/CNTs-1 ( $2.25 \text{ mAcm}^{-2}$ ), Pt@Pd/CNTs-2 ( $2.00 \text{ mAcm}^{-2}$ ) and Pt@Pd/CNTs-2 ( $1.82 \text{ mAcm}^{-2}$ ) composites also exhibit higher electrocatalytic activities than with Pt/CNTs ( $1.22 \text{ mAcm}^{-2}$ ) and Pd/CNTs ( $1.21 \text{ mAcm}^{-2}$ ) composites. The oxophilicity of Pd is higher than that of Pt, meaning that the tendency of Pd forming oxides is higher. Pd acts as a promoting site for the adsorption of  $\text{OH}^-$  from alkaline medium and then the formation of  $\text{Pd-OH}_{\text{ad}}$ , transferring  $\text{OH}^-$  species to Pt surface, where the oxidation of glycerol takes place.[30] The specific area activity towards the oxidation of glycerol of Pt@Pd/CNTs composites decreases slightly with the increasing Pd-to-Pt surface ratio from 1 : 7.2 to 1 : 1.5. This suggests that higher Pd content on Pt surface may limit the catalytic role of Pt, resulting in a decreasing catalytic activity.

With a comparable Pd-to-Pt surface ratio, Pd@PdPt/CNTs-1 composite (1.3 : 1) exhibits higher catalytic activity than Pt@Pd/CNTs-3 composite (1 : 1.5) due to a better mixing PdPt alloy surface towards glycerol oxidation, which achieves a similar performance to ethanol oxidation. The existence of Pd on Pt surface of Pt@Pd/CNTs composite limits the catalytic role of Pt towards the glycerol oxidation, resulting in a lower catalytic activity.

Similar to ethanol oxidation, Pd@PdPt/CNTs composites exhibit higher specific mass activity than monometallic Pd/CNTs and Pt/CNTs composites towards glycerol oxidation. (Figure 3.25 (b)) This suggests that the alloy structure enhances the utilization of Pt.

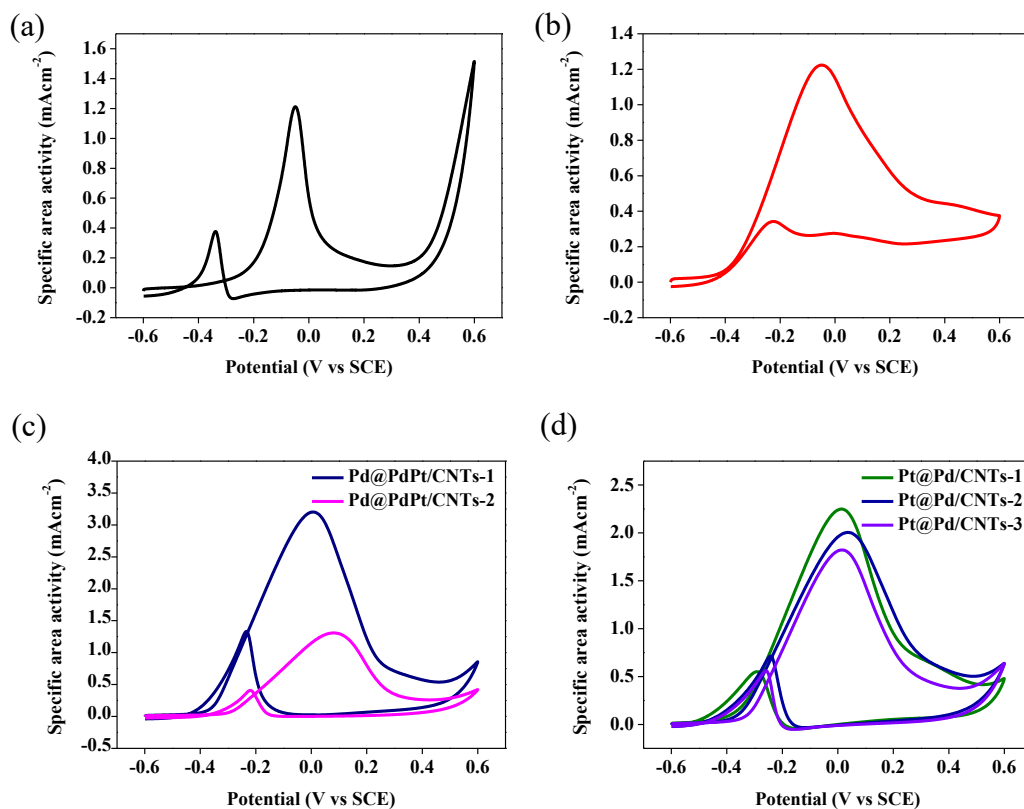


Figure 3.24 CVs of (a) Pd/CNTs, (b) Pt/CNTs, (c) Pd@PdPt/CNTs and (d) Pt@Pd/CNTs composites in 0.1 M glycerol + 0.1 M NaOH solution. Scan rate, 50 mVs<sup>-1</sup>.

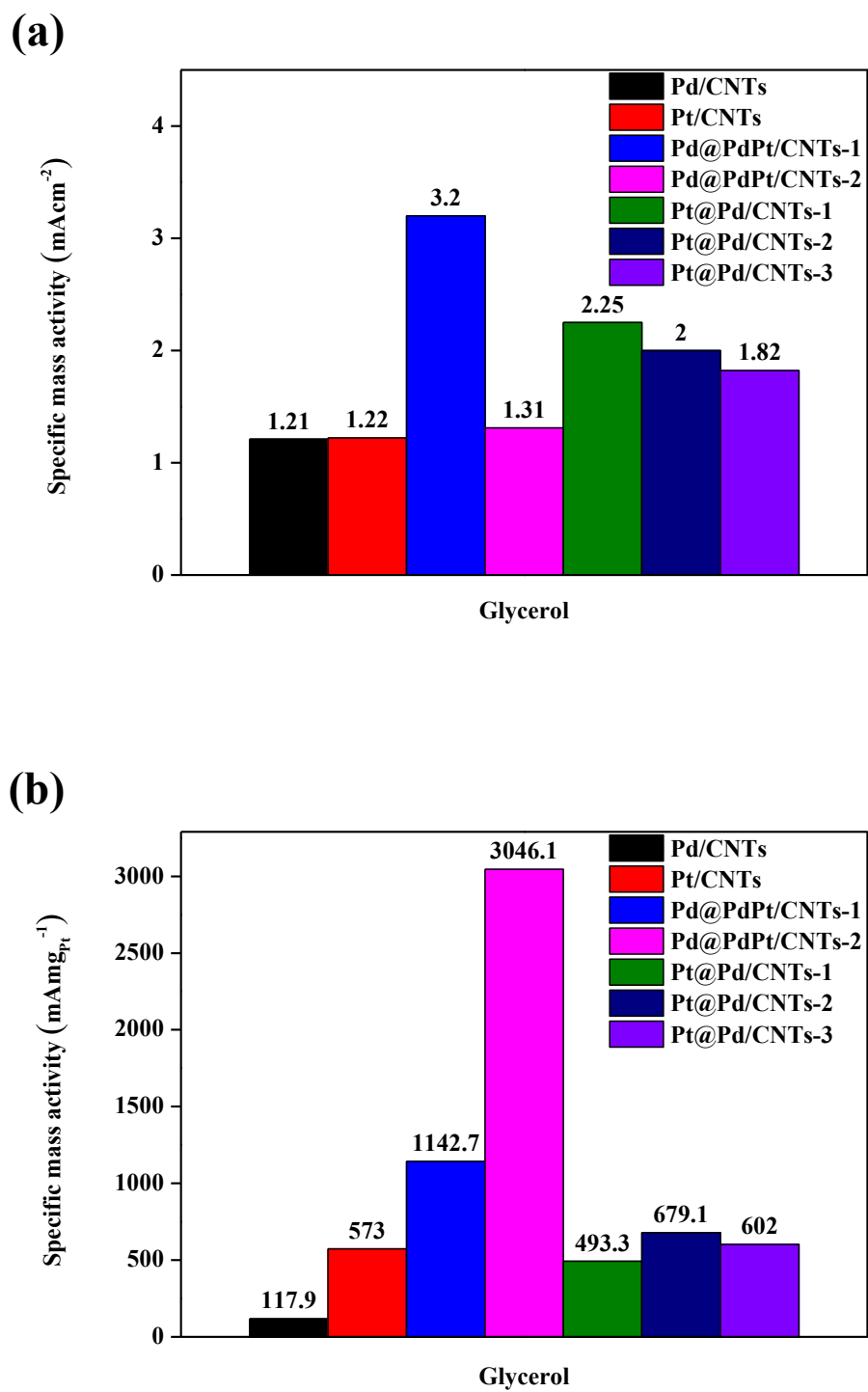


Figure 3.25 (a) The specific area activities and (b) specific mass activities of catalysts towards glycerol oxidation.

Catalysts	Specific area activity (mAcm <sup>-2</sup> )	Specific mass activity (mA <sub>mgPt</sub> <sup>-1</sup> )
Pd/CNTs	1.21	117.9
Pt/CNTs	1.22	573.8
Pd@PdPt/CNTs-1	3.20	1142.7
Pd@PdPt/CNTs-2	1.31	3046.1
Pt@Pd/CNTs-1	2.25	493.3
Pt@Pd/CNTs-2	2.00	679.1
Pt@Pd/CNTs-3	1.82	602.0

Table 3.12 Summary of electrochemical performance of the catalysts towards the electrooxidation of glycerol.

### **Chronoamperometric test of glycerol oxidation**

Chronoamperometric tests were conducted to study the stability of the electrocatalysts for the oxidation of glycerol. Figure 3.26 displays the chronoamperometric curves of the electrocatalysts in 0.1 M glycerol + 0.1 M NaOH solution, by applying a fixed potential of -0.15 V.

The curves of current density rapidly decrease initially due to the generated poisonous intermediate species during the oxidation reactions. The curves of the current density then decrease slower because of the blocking effect of the poisonous intermediates on the catalyst surface from glycerol.[48]

From Table 3.13, it is observed that the current density retained after chronoamperometric tests of Pd@PdPt/CNTs composites are higher, indicating their higher stability than Pt@Pd/CNTs composites towards the oxidation of glycerol. The alloying of Pd and Pt is believed to enhance their stability.

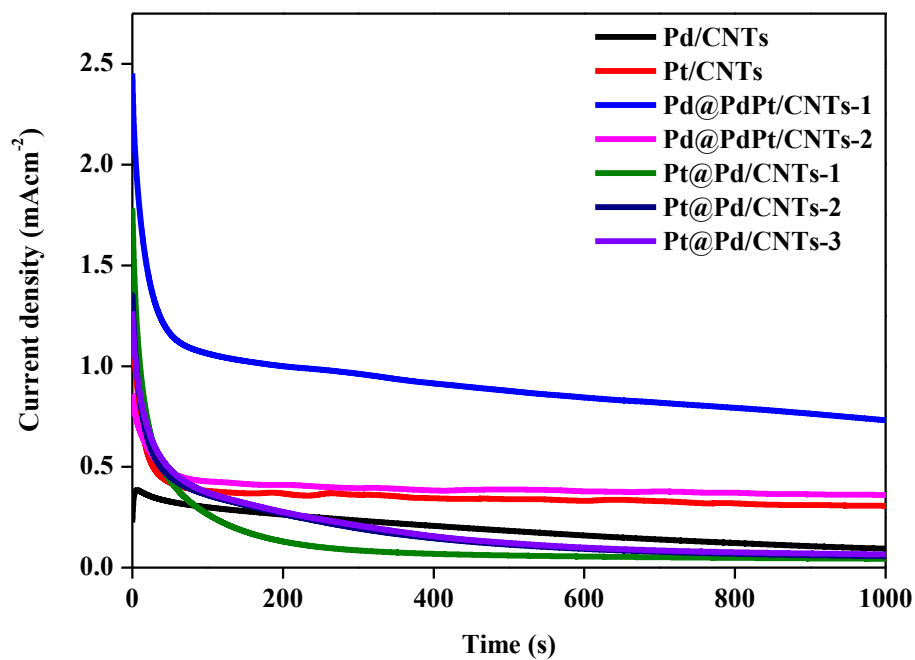


Figure 3.26 Chronoamperometric curves of the catalysts in 0.1 M glycerol + 0.1 M NaOH solution at a fixed potential of -0.15 V for 1000 s.

Catalysts	Current density retained after 1000 s chronoamperometric test (%)
Pd/CNTs	5.5
Pt/CNTs	14.1
Pd@PdPt/CNTs-1	29.8
Pd@PdPt/CNTs-2	41.9
Pt@Pd/CNTs-1	2.5
Pt@Pd/CNTs-2	4.2
Pt@Pd/CNTs-3	5.3

Table 3.13 Summary of electrochemical performance of catalysts towards chronoamperometric test of glycerol oxidation.

### 3.2.4.5 Accelerated durability test in sulfuric acid

To further investigate the stability of the catalysts, the accelerated durability test (ADT) was performed by conducting continued CV cycles (1000 cycles) in N<sub>2</sub>-purged 0.1 M H<sub>2</sub>SO<sub>4</sub> solution in the potential region between -0.24 V and 1.0 V with a scan rate of 50 mVs<sup>-1</sup> as displayed in Figure 3.27. The loss of the ECSA of the catalysts with continued CV cycles is presented in Figure 3.27 (g). Table 3.14 presents the ECSA remained for Pd/CNTs, Pt/CNTs, Pd@PdPt/CNTs-1, Pd@PdPt/CNTs-2, Pt@Pd/CNTs-1, Pt@Pd/CNTs-2 and Pt@Pd/CNTs-3 composites, which are 3.4 %, 64.2 %, 43.2 %, 9.6 %, 43.9 %, 35.1 % and 23.1 % respectively. The Pt/CNTs composite achieve highest stability (64.2 %) while Pd/CNTs composite achieve lowest stability (3.4 %).

The Pd@PdPt/CNTs composites achieve higher stability than Pd/CNTs composite. It is suggested that the existence of Pt on surface may enhance the stability of the catalysts due to alloying effect. It is also found that the stability of Pd@PdPt/CNTs-1 composite (43.2 %) is higher than that of Pd@PdPt/CNTs-2 composite (9.6 %). As confirmed by XPS analysis, the Pt surface content of Pd@PdPt/CNTs-1 composite is higher and thus enhancing the stability of the catalysts.

Three Pt@Pd/CNT composites achieve lower stability than Pt/CNTs composite. It is believed that Pd on the surface of the catalysts would lower the stability of the catalyst because Pd tends to dissolve in H<sub>2</sub>SO<sub>4</sub>.<sup>[49]</sup> This also explains why

the stability of Pt@Pd/CNTs composites decreases with the increasing Pd-to-Pt surface ratio of Pt@Pd/CNTs composites.

With comparable Pd-to-Pt surface ratios, Pd@PdPt/CNTs-1 composite (1.3 : 1) exhibit higher stability than Pt@Pd/CNTs-3 composite (1 : 1.5). The alloy structure of Pd@PdPt/CNTs-1 composite provides a better mixing PdPt surface where the arrangement of PdPt nanoparticles may be reduced during ADT.

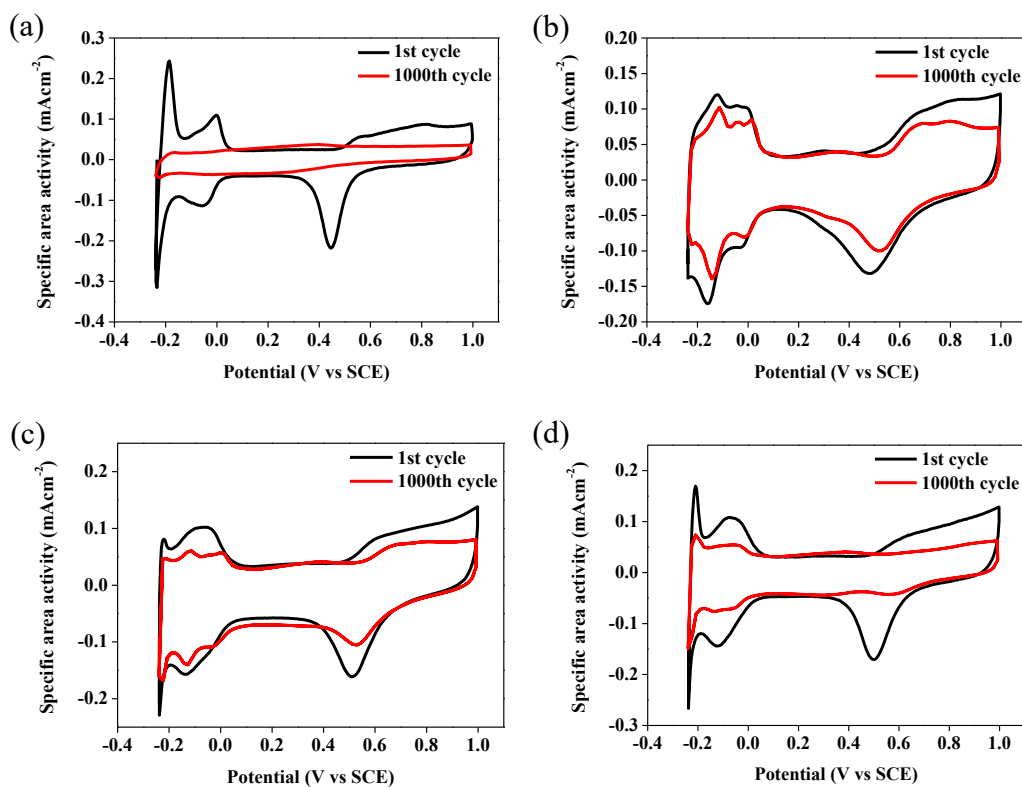


Figure 3.27 ADT of (a) Pd/CNTs, (b) Pt/CNTs, (c) Pd@PdPt/CNTs-1 and (d) Pd@PdPt/CNTs-2 composites in N<sub>2</sub>-purged 0.1 M H<sub>2</sub>SO<sub>4</sub> solution. Scan rate, 50 mVs<sup>-1</sup>.

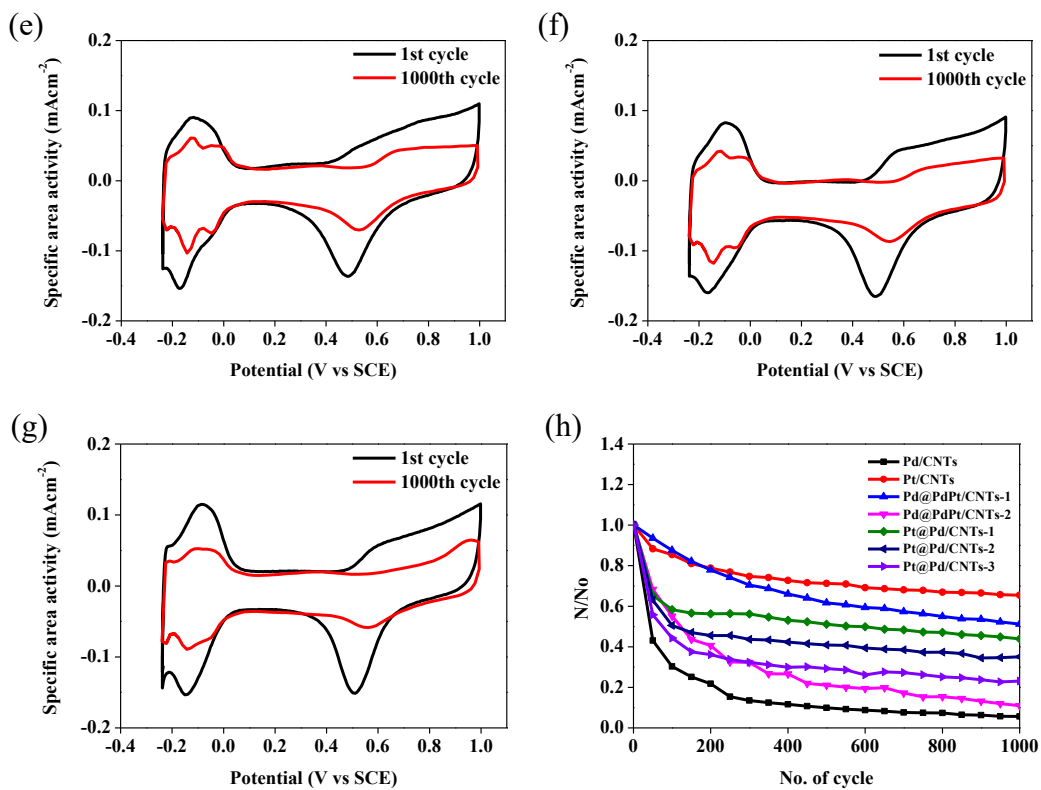


Figure 3.27 ADT of (e) Pt@Pd/CNTs-1, (f) Pt@Pd/CNTs-2 and (g) Pt@Pd/CNTs-3 composites in N<sub>2</sub>-purged 0.1 M H<sub>2</sub>SO<sub>4</sub> solution. Scan rate, 50 mVs<sup>-1</sup>. And (h) their ECSA loss.

Catalysts	ECSA remained after ADT (%)
Pd/CNTs	3.4
Pt/CNTs	64.2
Pd@PdPt/CNTs-1	43.2
Pd@PdPt/CNTs-2	9.6
Pt@Pd/CNTs-1	43.9
Pt@Pd/CNTs-2	35.1
Pt@Pd/CNTs-3	23.1

Table 3.14 Summary of ECSA remained of the catalysts after ADT.

### 3.3 Summary

Two modified electrocatalysts, Pd@PdPt/CNTs alloy and Pt@Pd/CNTs phase-separate composites were successfully developed from the surfactant-free monometallic Pd/CNTs and Pt/CNTs composites respectively. Their electrocatalytic activities towards methanol, ethanol and glycerol oxidations were studied.

1. Pd/CNTs and Pt/CNTs composites were synthesized without introduction of organic surfactants. Pd/CNTs composite was synthesized by hydrolysis of  $[\text{PdCl}_4]^{2-}$  ions to PdO on MWCNTs, followed by  $\text{H}_2$  reduction. Pt/CNTs composite was synthesized by the reduction of  $[\text{PtCl}_4]^{2-}$  ions to Pt due to the electron transfer from MWCNTs.
2. The PdPt shell of Pd@PdPt/CNTs composites were synthesized by the galvanic replacement reaction between Pd and  $[\text{PtCl}_4]^{2-}$  ions. The Pt@Pd/CNTs composites were prepared by adsorption of  $[\text{PdCl}_4]^{2-}$  ions onto Pt surface, followed by hydrogen reduction to Pd metal. XRD analysis shows that both Pd@PdPt/CNTs and Pt@Pd/CNTs composites adopt a fcc structure.
3. Electrocatalytic studies shows that the Pd@PdPt/CNTs alloy and Pt@Pd/CNTs phase-separate composites with particular Pd-to-Pt surface ratio exhibit enhanced catalytic activity towards the oxidations of ethanol and

glycerol except methanol when compared to monometallic Pd/CNTs and Pt/CNTs composites. With comparable Pd-to-Pt surface ratio, Pd@PdPt/CNTs alloy composite exhibits higher catalytic activity than Pt@Pd/CNTs phase-separate composite towards the alcohol oxidations due to a better mixing PdPt alloy surface. The roughly estimated specific mass activity of the catalysts also suggests that the utilization of Pt is enhanced by alloy structure.

4. ADT suggests that the stability of Pd@PdPt/CNTs alloy composites is enhanced when compared with monometallic Pd/CNTs composite while that of Pt@Pd/CNTs phase-separate composites is worsened when compared with monometallic Pt/CNTs composite. With comparable Pd-to-Pt surface ratio, Pd@PdPt/CNTs alloy composite exhibits higher stability than Pt@Pd/CNTs phase-separate composite because the alloy structure may reduce arrangement of PdPt nanoparticles during ADT.

## REFERENCES

- [1] G. Yang, Y. Zhou, H.-B. Pan, C. Zhu, S. Fu, C.M. Wai, D. Du, J.-J. Zhu, Y. Lin, *Ultrasonics sonochemistry*, 28 (2016) 192-198.
- [2] M.B. Gawande, A. Goswami, T. Asefa, H. Guo, A.V. Biradar, D.-L. Peng, R. Zboril, R.S. Varma, *Chemical Society Reviews*, 44 (2015) 7540-7590.
- [3] R. Ghosh Chaudhuri, S. Paria, *Chemical reviews*, 112 (2011) 2373-2433.
- [4] S. Oldenburg, R. Averitt, S. Westcott, N. Halas, *Chemical Physics Letters*, 288 (1998) 243-247.
- [5] H.H. Park, K. Woo, J.-P. Ahn, *Scientific reports*, 3 (2013) 1497.
- [6] S. Balakrishnan, M.J. Bonder, G.C. Hadjipanayis, *Journal of magnetism and magnetic materials*, 321 (2009) 117-122.
- [7] F. Caruso, *Advanced materials*, 13 (2001) 11-22.
- [8] L. Qi, J. Ma, H. Cheng, Z. Zhao, *Colloids and Surfaces A: Physicochemical and Engineering Aspects*, 111 (1996) 195-202.
- [9] S. Phadtare, A. Kumar, V. Vinod, C. Dash, D.V. Palaskar, M. Rao, P.G. Shukla, S. Sivaram, M. Sastry, *Chemistry of materials*, 15 (2003) 1944-1949.
- [10] H. Ataee-Esfahani, L. Wang, Y. Nemoto, Y. Yamauchi, *Chemistry of Materials*, 22 (2010) 6310-6318.
- [11] L. Chen, W. Zhao, Y. Jiao, X. He, J. Wang, Y. Zhang, *Spectrochimica Acta Part A: Molecular and Biomolecular Spectroscopy*, 68 (2007) 484-490.
- [12] X. Wang, J. Feng, Y. Bai, Q. Zhang, Y. Yin, *Chemical reviews*, 116 (2016) 10983-11060.
- [13] C. Du, M. Chen, W. Wang, Q. Tan, K. Xiong, G. Yin, *Journal of Power Sources*, 240 (2013) 630-635.

- [14] T. Xia, H. Shen, G. Chang, Y. Zhang, H. Shu, M. Oyama, Y. He, *Journal of Nanomaterials*, 2014 (2014) 127.
- [15] N.V. Long, M. Ohtaki, T.D. Hien, J. Randy, M. Nogami, *Electrochimica Acta*, 56 (2011) 9133-9143.
- [16] H. Wu, S. Mei, X. Cao, J. Zheng, M. Lin, J. Tang, F. Ren, Y. Du, Y. Pan, H. Gu, *Nanotechnology*, 25 (2014) 195702.
- [17] H. Zhang, M. Jin, Y. Xia, *Chemical Society Reviews*, 41 (2012) 8035-8049.
- [18] S. Guo, S. Dong, E. Wang, *ACS nano*, 4 (2009) 547-555.
- [19] C. Zhu, S. Guo, S. Dong, *Chemistry-A European Journal*, 19 (2013) 1104-1111.
- [20] C. Zhu, S. Guo, S. Dong, *Advanced Materials*, 24 (2012) 2326-2331.
- [21] W. Hong, C. Shang, J. Wang, E. Wang, *Energy & Environmental Science*, 8 (2015) 2910-2915.
- [22] Z.-Z. Yang, X.-X. Lin, X.-F. Zhang, A.-J. Wang, X.-Y. Zhu, J.-J. Feng, *Journal of Alloys and Compounds*, 735 (2018) 2123-2132.
- [23] X. Yang, Q. Yang, J. Xu, C.-S. Lee, *Journal of Materials Chemistry*, 22 (2012) 8057-8062.
- [24] H.C. Choi, M. Shim, S. Bangsaruntip, H. Dai, *Journal of the American Chemical Society*, 124 (2002) 9058-9059.
- [25] X. Weng, Q. Liu, A.-J. Wang, J. Yuan, J.-J. Feng, *Journal of colloid and interface science*, 494 (2017) 15-21.
- [26] T. Wang, R. Yang, S. Ouyang, H. Shi, S. Wang, *RSC Advances*, 5 (2015) 48992-48996.
- [27] B. Veisz, L. Tóth, D. Teschner, Z. Paál, N. Györffy, U. Wild, R. Schlögl,

- Journal of Molecular Catalysis A: Chemical, 238 (2005) 56-62.
- [28] B.I. Boyanov, T.I. Morrison, The Journal of Physical Chemistry, 100 (1996) 16318-16326.
- [29] F. Zheng, S.-Y. Luk, T.-L. Kwong, K.-F. Yung, RSC advances, 6 (2016) 44902-44907.
- [30] C. Jin, J. Zhang, R. Dong, Q. Huo, Int. J. Electrochem. Sci, 9 (2014) 5743-5750.
- [31] A.J. Zhang, M. Gaur, V.I. Birss, Journal of Electroanalytical Chemistry, 389 (1995) 149-159.
- [32] Y.-N. Wu, S.-J. Liao, Z.-X. Liang, L.-J. Yang, R.-F. Wang, Journal of Power Sources, 194 (2009) 805-810.
- [33] H. Wang, C. Xu, F. Cheng, M. Zhang, S. Wang, S.P. Jiang, Electrochemistry Communications, 10 (2008) 1575-1578.
- [34] C. Jin, X. Ma, J. Zhang, Q. Huo, R. Dong, Electrochimica Acta, 146 (2014) 533-537.
- [35] I.M. Al-Akraa, A.M. Mohammad, M.S. El-Deab, B.E. El-Anadouli, International Journal of Hydrogen Energy, 40 (2015) 1789-1794.
- [36] K. Friedrich, F. Henglein, U. Stimming, W. Unkauf, Electrochimica acta, 45 (2000) 3283-3293.
- [37] S. Mahapatra, J. Datta, International Journal of Electrochemistry, 2011 (2011).
- [38] J. Suntivich, Z. Xu, C.E. Carlton, J. Kim, B. Han, S.W. Lee, N.p. Bonnet, N. Marzari, L.F. Allard, H.A. Gasteiger, Journal of the American Chemical Society, 135 (2013) 7985-7991.

- [39] Y. Li, L. Tang, J. Li, *Electrochemistry Communications*, 11 (2009) 846-849.
- [40] D.A.J. Rand, R. Woods, *Journal of Electroanalytical Chemistry and Interfacial Electrochemistry*, 35 (1972) 209-218.
- [41] Z. Liang, T. Zhao, J. Xu, L. Zhu, *Electrochimica Acta*, 54 (2009) 2203-2208.
- [42] S.-C. Lin, J.-Y. Chen, Y.-F. Hsieh, P.-W. Wu, *Materials letters*, 65 (2011) 215-218.
- [43] J. Liu, J. Ye, C. Xu, S.P. Jiang, Y. Tong, *Electrochemistry Communications*, 9 (2007) 2334-2339.
- [44] M. Wakisaka, S. Mitsui, Y. Hirose, K. Kawashima, H. Uchida, M. Watanabe, *The Journal of Physical Chemistry B*, 110 (2006) 23489-23496.
- [45] S.T. Nguyen, H.M. Law, H.T. Nguyen, N. Kristian, S. Wang, S.H. Chan, X. Wang, *Applied Catalysis B: Environmental*, 91 (2009) 507-515.
- [46] K. Ding, Y. Wang, H. Yang, C. Zheng, YanliCao, H. Wei, Y. Wang, Z. Guo, *Electrochimica Acta*, 100 (2013) 147-156.
- [47] A. Dector, F. Cuevas-Muñiz, M. Guerra-Balcázar, L.A. Godínez, J. Ledesma-García, L. Arriaga, *International Journal of Hydrogen Energy*, 38 (2013) 12617-12622.
- [48] S.-S. Li, Y.-Y. Hu, J.-J. Feng, Z.-Y. Lv, J.-R. Chen, A.-J. Wang, *International Journal of Hydrogen Energy*, 39 (2014) 3730-3738.
- [49] N.V. Rees, R.G. Compton, *Journal of Solid State Electrochemistry*, 15 (2011) 2095-2100.

## **Chapter 4**

# **Synthesis of Hollow PtAg Nanowires for Direct Liquid Fuel Cells**

### **4.1 Background**

#### **Overview of hollow nanostructures**

Over the past few decades, hollow nanostructures have attracted a growing attention. “Hollow nanostructure” means a solid structure with an empty space with the size in nanometer. There is a wide range of morphologies for the hollow nanostructures including hollow spheres,[1-3] hollow nanotubes,[4, 5] hollow nanocubes[6-8] and hollow octahedrons.[9, 10] Compared with the solid counterparts, hollow nanostructures have numerous advantages including larger surface area to volume ratio, lower density, higher loading capacity, higher catalytic activity and improved utilization of Pt.[11] Based on these advantages, a wide range of applications including catalysis,[12] sensing,[13, 14] imaging,[15, 16] biomedicine,[17] energy storage[18] and environmental remediation[19] are developed.

#### **Synthetic methods**

The synthetic methods for hollow nanostructures are divided into three categories, which are hard template-mediated method, soft template-mediated method and self-templating synthesis.

#### **Hard template-mediated method**

In hard template-mediated method, a hard template is firstly prepared. Hard

templates usually involve polymer, silica, carbon or metal. The coating process is conducted by sol-gel process or hydrothermal reactions. The hollow structure is synthesized by the removal of the inside template by chemical etching, thermal treatment, calcination or dissolving in specific solvents.[11, 20]

One of the advantages of this method is that large scale production of hollow structures by hard templating synthesis is easily achieved. Also, it is easy to control the morphology of the hollow structure because its morphology is determined by the morphology of the template. However, it may be difficult to remove the hard template. The removal of hard template may also destroy the hollow structure.[20] The production cost of silica and polystyrene (PS), which are commonly used as hard templates, is high, limiting the scale-up production.[21]

Hollow zinc oxide (ZnO) microspheres were synthesized by templating against mono-sized sulfonated polystyrene (PS). PS microspheres were synthesized by dispersion polymerization. The purified and dried PS microspheres were sulfonated with concentrated sulfuric acid to obtain sulfonated PS. A  $[\text{Zn}(\text{en})_2]^{2+}$  complex solution is formed by mixing zinc acetate dehydrate, sulfonated PS, anhydrous ethylenediamine (en) and water. The PS-ZnO core-shell microspheres were prepared by heating the  $[\text{Zn}(\text{en})_2]^{2+}$  complex solution in autoclave at 160 °C. Finally, the PS-ZnO core-shell microspheres were mixed with *N,N*-dimethylformamide (DMF) to dissolve the PS cores and obtain hollow ZnO structures.[22]

Hollow Pt spheres with nanosponge shell were prepared by templating against

silica particles. Silica nanoparticles were modified with amino group for the attachment of the initial seeds. The modified silica nanoparticles and pluronic F127 were dispersed in  $K_2PtCl_4$  solution, followed by the addition of ascorbic acid. The centrifuged and washed product was mixed with 10 wt% hydrofluoric acid solution to obtain the hollow Pt spheres by removing the silica core.[23]

### **Soft template-mediated method**

In soft template-mediated method, soft templates are prepared. Soft templates are commonly in fluid form such as emulsion droplets, vesicles, micelles and gas bubbles. After preparing the soft templates, a layer of material is then coated on the surface of the templates, followed by removing the templates. Complicated hierarchical structures can be produced by soft template-mediated method. However, the hollow structures produced are less uniform.[20, 21] The removal of the templates may also destroy the hollow structure.[11]

Both hollow zinc peroxide ( $ZnO_2$ ) or zinc oxide ( $ZnO$ ) spheres were synthesized by templating against gas bubbles. The mixture of  $ZnO$  powder ultrasonically dispersed in water and 30 wt% hydrogen peroxide ( $H_2O_2$ ) aqueous solution is heated in autoclave at 150 °C for 20 h. Due to the decomposition of  $H_2O_2$ , *in-situ* oxygen ( $O_2$ ) gas bubbles generated and acted as soft templates. Hollow  $ZnO_2$  spheres were obtained after drying the mixture while hollow  $ZnO$  spheres were obtained after heating the hollow  $ZnO_2$  spheres at 180 °C for 10 h. During heating, hollow  $ZnO$  spheres were obtained due to the decomposition of  $ZnO_2$  into  $ZnO$  with the loss of  $O_2$ .[24]

Hollow titania spheres were synthesized by templating against

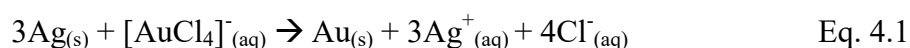
surfactant-stabilized non-aqueous emulsion droplets. The emulsions were prepared by ultrasonating the mixture of sodium dodecyl sulfate (SDS), formamide and titanium(IV) ethoxide in hexadecane solution. After that, the mixture of formamide and water was added to the emulsions. It is necessary to control water-to-alkoxide molar ratio in 4 : 1 in order to complete the reaction. Hollow titania spheres with the size ranging from 500  $\mu\text{m}$  to 3000  $\mu\text{m}$  could be obtained after centrifuging and washing formamide away with water.[25]

### **Self-templating synthesis**

In self-templating synthesis, the templates are synthesized to create hollow structure and integrate into the shell of the hollow structure. There are several advantages including lower production cost, simple synthetic procedure and easy to scale up. However, there is no general self-templating method for synthesizing hollow structure. It usually requires a particular combination of experimental parameters.[20]

One of the self-templating methods is galvanic replacement reaction. This is an electrochemical process involving the oxidation and reduction of metals. The driving force is the difference in the electrochemical potentials between two metals. One metal acts as reducing agent (anode) while another metal acts as oxidizing agent (cathode). The anode metal template, which is also called sacrificial template, with lower standard reduction potential is synthesized first. When contacting with the cathode metal of higher standard reduction potential, the anode metal dissolves and is oxidized into the solution. The cathode metal ions are reduced and deposit on the surface of anode metal. The shape and interior void size of hollow structures are determined by anode metal.[20, 21, 26]

Sun and Xia synthesized hollow gold nanoboxes with the silver nanocubes as sacrificial templates. The silver nanocubes were prepared by reducing silver nitrate with ethylene glycol (EG) in the existence of poly(vinylpyrrolidone) (PVP). Gold nanoboxes were then synthesized by templating against silver nanocubes.[27] As the standard reduction potential of  $[\text{AuCl}_4]^-/\text{Au}$  (1.00 V vs standard hydrogen electrode, SHE) is more positive than that of  $\text{Ag}^+/\text{Ag}$  (0.80 V vs SHE), the silver nanoboxes were oxidized by gold(III) chloride ( $\text{HAuCl}_4$ ) according to the following equation. [28]



When silver nanoboxes react with insufficient amount of  $\text{HAuCl}_4$ , pinholes were formed on the surface. The pinholes allow the transport of silver and  $[\text{AuCl}_4]^-$  ions in and out of the cubes until the galvanic replacement reaction completes. Finally, hollow gold nanostructures were formed.[27]

### **Development of PtAg-based bimetallic catalysts for electrocatalysis**

Apart from Au and Pd, Ag is also commonly used to synthesize PtAg-based catalysts. Ag is a metal which is much cheaper and more abundant than Pt.[29] Also, Ag is an oxophilic element, [30] which facilitates the adsorption of  $\text{OH}^-$  ions onto the NP surfaces enhanced catalytic activity and CO tolerance.[31] There are many studies exploring the synthesis of PtAg-based bimetallic catalysts with different morphologies. (Table 4.1)

Catalyst	Morphology	Pt-to-Ag atomic ratio	Fuel	Synthetic method	Specific area activity	Specific mass activity	Ref.
PtMFs	Porous structure	55 : 45	0.1 M MeOH +	Galvanic replacement	1.34 mAcm <sup>-2</sup>	102.43 mA <sub>gPt</sub> <sup>-1</sup>	[32]
Porous PtAg mesoflowers	composed of nanoparticles	72 : 28	0.1 M HClO <sub>4</sub>	reaction	1.57 mAcm <sup>-2</sup>	222.2 mA <sub>gPt</sub> <sup>-1</sup>	
PtAg alloyed nanocrystals	multi-petals and multioctahedra	70 : 30 76 : 24 66 : 34	1.0 M MeOH + 0.5 M H <sub>2</sub> SO <sub>4</sub>	Co-reduction, seed-mediated method	1.91 mAcm <sup>-2</sup> 0.6 mAcm <sup>-2</sup> 1.4 mAcm <sup>-2</sup>	237 mA <sub>gPt</sub> <sup>-1</sup> 384 mA <sub>gPt</sub> <sup>-1</sup> 161.5 mA <sub>gPt</sub> <sup>-1</sup>	[33]
Hollow PtAg alloy nanospheres	Hollow sphere	4.77 : 1	0.1 M MeOH + 0.1 M H <sub>2</sub> SO <sub>4</sub>	Galvanic replacement reaction	-	180 mA <sub>gPt</sub> <sup>-1</sup>	[1]
PtAg PNTs porous nanotubes	Tube	5.7 : 1	1.0 M EtOH + 1.0 M NaOH	Alloying-dealloying approach	2.0 mAcm <sup>-2</sup>	-	[34]
PtAg nanotubes	Tube	3 : 1	0.5 M glycerol + 0.5 M NaOH	Galvanic replacement reaction	-	~ 1500 mA <sub>gPt</sub> <sup>-1</sup>	[35]

PtAg NCs Solid-core@porous- shell alloyed PtAg nanocrystals	Solid-core@porous- shell structure	1 : 1	0.5 M glycerol + 0.5 M NaOH	Co-reduction	77.91 mAcm <sup>-2</sup>	1303 mA <sub>gPt</sub> <sup>-1</sup>	[36]
PtAg nanoflowers	Each nanoflower has several ultrathin fan-shaped petals	3 : 1	1.0 M HCOOH + 1.0 M KOH	Solvothermal method	~ 37 mAcm <sup>-2</sup>	-	[37]
Hollow PtAg alloy nanospheres	Hollow sphere	4.77 : 1	0.05 M HCOOH + 0.1 M H <sub>2</sub> SO <sub>4</sub>	Galvanic replacement reaction	-	~ 110 mA <sub>g</sub> <sup>-1</sup>	[1]

---

Table 4.1 Comparison of the previously reported PtAg-based catalysts with respect to their catalytic activities for methanol, ethanol, glycerol and formic acid oxidations.

Compared with solid PtAg catalysts, hollow tube morphology consists of an inter-connected 3D porous shell structure. This allows the free transport of electrons and medium molecules, resulting in superior electrocatalytic performance.[30] Nanospheres is one of the typical PtAg nanostructures. Hollow PtAg alloy nanospheres synthesized by Zheng et al. consist of rougher shell surface with the development of aggregated nanoparticles on the shell surface. The aggregation of nanoparticles on the shell surface may decrease the accessible surface area, decreasing the specific mass activity towards the both direct and indirect oxidations of formic acid.[1] The absence of aggregated particles on shell surface on hollow tube morphology may also facilitate the transport of fuel molecules.

According to other literatures, other special PtAg nanostructures were explored. Porous PtAg mesoflowers (PtMFs) synthesized by Zhuang et al. consist of porous structure and composed of nanoparticles less than 5 nm. PtMFs exhibit high catalytic activity towards methanol oxidation due to their unique 3-dimensional architecture, where the interconnected interstices and channels extending in all three dimensions allow the rapid diffusion and mass transport of external reagents directly to the surface of Pt catalysts, as well as unblocked transport of electrons.[32] PtAg alloyed nanocrystals synthesized by Fang et al. consist of porous and a roughly spherical shape with multipetals. The enhancement in electrocatalytic performance may be due to its porous structure and multipetals, which increase the ECSA for electrocatalysis. Also, the negative charges accumulate at the sharp sites of catalysts is beneficial for the electrocatalytic enhancement due to sharp-tip effect.[33]

### **Aim of the project**

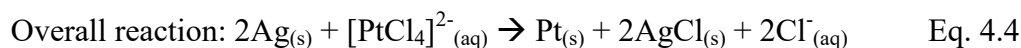
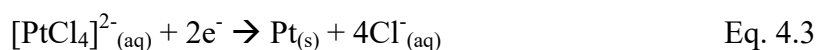
The project is to synthesize hollow PtAg nanowires (NWs) under the galvanic replacement reaction between silver nanowires (AgNWs) as a sacrificial template and potassium tetrachloroplatinate(II) ( $K_2PtCl_4$ ). Hollow PtAg NWs with different Pt-to-Ag atomic ratios are investigated and characterized. Also, their electrocatalytic activity towards the oxidations of methanol, ethanol, glycerol and formic acid are explored.

## 4.2 Results and Discussions

### 4.2.1 Synthesis of AgNWs and PtAg NWs

The AgNWs were synthesized by reducing silver nitrate ( $\text{AgNO}_3$ ) by EG in the presence of PVP. It is proposed that silver nanoparticles (AgNPs) were formed initially and acted as seeds for the growth of nanowires.[38]

The PtAg NWs composites were synthesized by galvanic replacement reaction between  $[\text{PtCl}_4]^{2-}$  ions and AgNWs which acted as sacrificial template. Since the standard reduction potential of  $[\text{PtCl}_4]^{2-}/\text{Pt}$  pair (0.758 V vs standard hydrogen electrode, SHE) is higher than that of  $\text{AgCl}/\text{Ag}$  pair (0.2233 V vs SHE), silver is more likely oxidized to AgCl by reacting with  $\text{Cl}^-$  ions. Hence, the galvanic replacement reaction proceeded spontaneously.[39] It is proposed that Pt deposited onto AgNWs surface and Ag core disappeared, resulting in the formation of hollow structure.[1]



Hollow PtAg NWs prepared by controlling different volumes of 80 mM K<sub>2</sub>PtCl<sub>4</sub> solution were presented in Table 4.2. To study the surface plasmon resonance (SPR) of AgNWs and PtAg NWs composites, UV-Vis spectroscopy was performed. As displayed in Figure 4.1, the AgNWs solution shows two absorption bands at 355 nm and 393 nm, which are ascribed to the surface plasmon resonance bands of the transverse and longitudinal modes of the AgNWs respectively.[40, 41] It is observed that the intensity of the AgNWs absorption peak decreases and become a flat line with increasing volumes of 80 mM K<sub>2</sub>PtCl<sub>4</sub> solution.

PtAg NWs	Volume of 80 mM K <sub>2</sub> PtCl <sub>4</sub> solution (μL)
PtAg-1 NWs	313
PtAg-2 NWs	326
PtAg-3 NWs	1250
PtAg-4 NWs	2500

Table 4.2 Synthesis of hollow PtAg NWs with different volumes of 80 mM K<sub>2</sub>PtCl<sub>4</sub> solution.

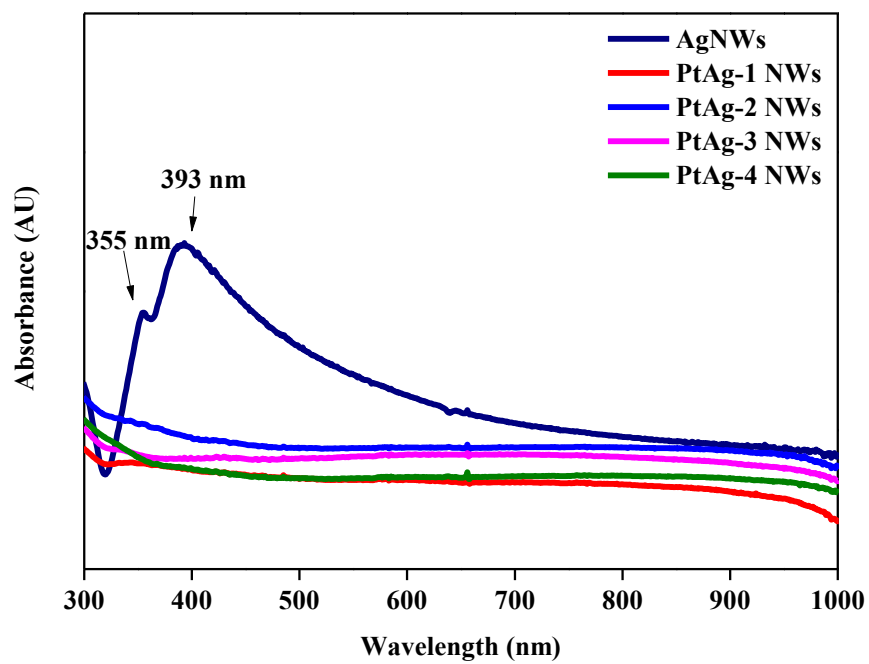


Figure 4.1

UV-vis spectra of AgNWs and PtAg NWs solutions.

After investigating their SPR property, morphological studies were conducted to confirm the morphology of AgNWs and PtAg NWs composites.

### AgNWs

The morphology and size of AgNWs composite were studied by TEM analysis. As displayed in Figure 4.2, the AgNWs was successfully synthesized with the length of  $4.4 \pm 2.5 \mu\text{m}$  and the width of  $0.2 \pm 0.1 \mu\text{m}$ . The detailed structure of AgNWs composite was analyzed by selective area electron diffraction (SAED) and high resolution transmission electron microscopy (HR-TEM) as displayed in Figure 4.2 (c) and (d) respectively. Figure 4.2 (c) shows that the diffraction rings obtained from (111), (200), (220) and (311) crystal planes which are consistent to the d-spacing of silver. It is suggested that the AgNWs composite is adopting a face-centered cubic (fcc) structure with a Fm-3m(225) space group (JCPDS Card no.00-001-1164). From Figure 4.2 (d), the crystal plane with d-spacing of 2.37 Å is found which corresponds to the (111) crystal plane of silver.

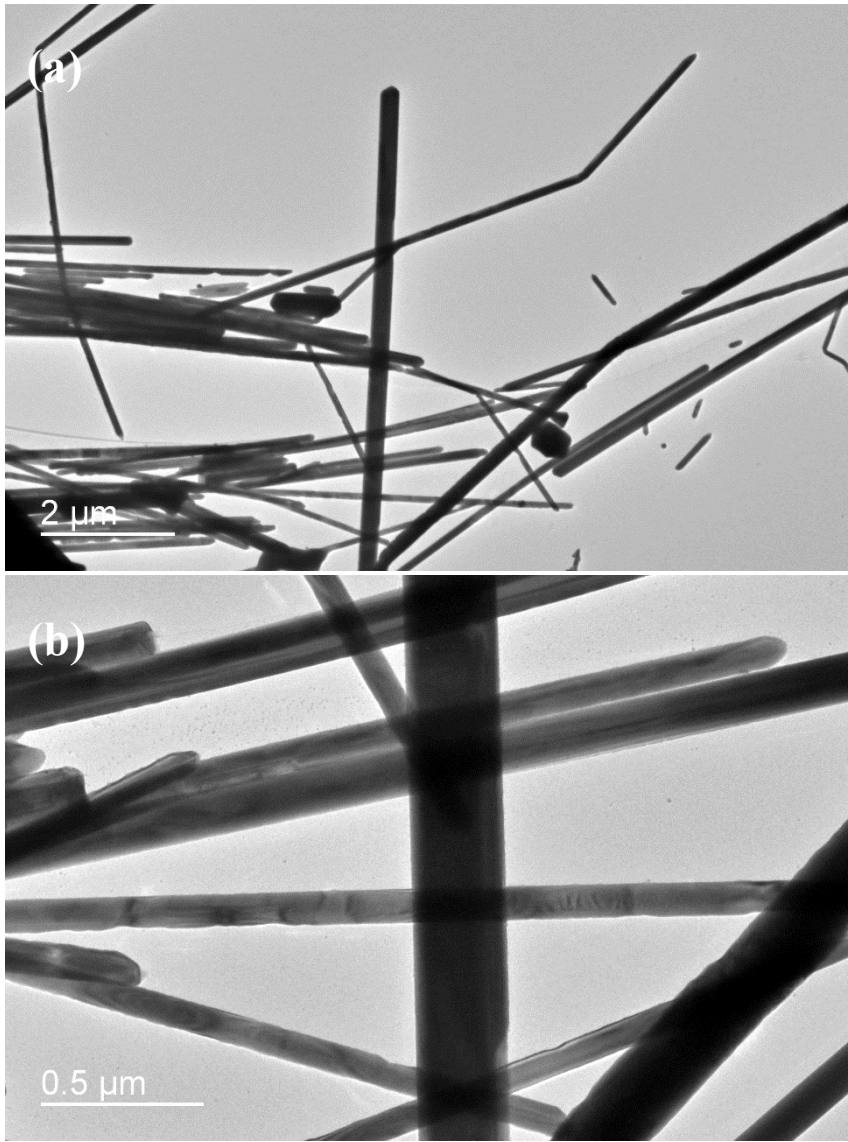


Figure 4.2 (a) LM-TEM and (b) HM-TEM images of AgNWs composite.

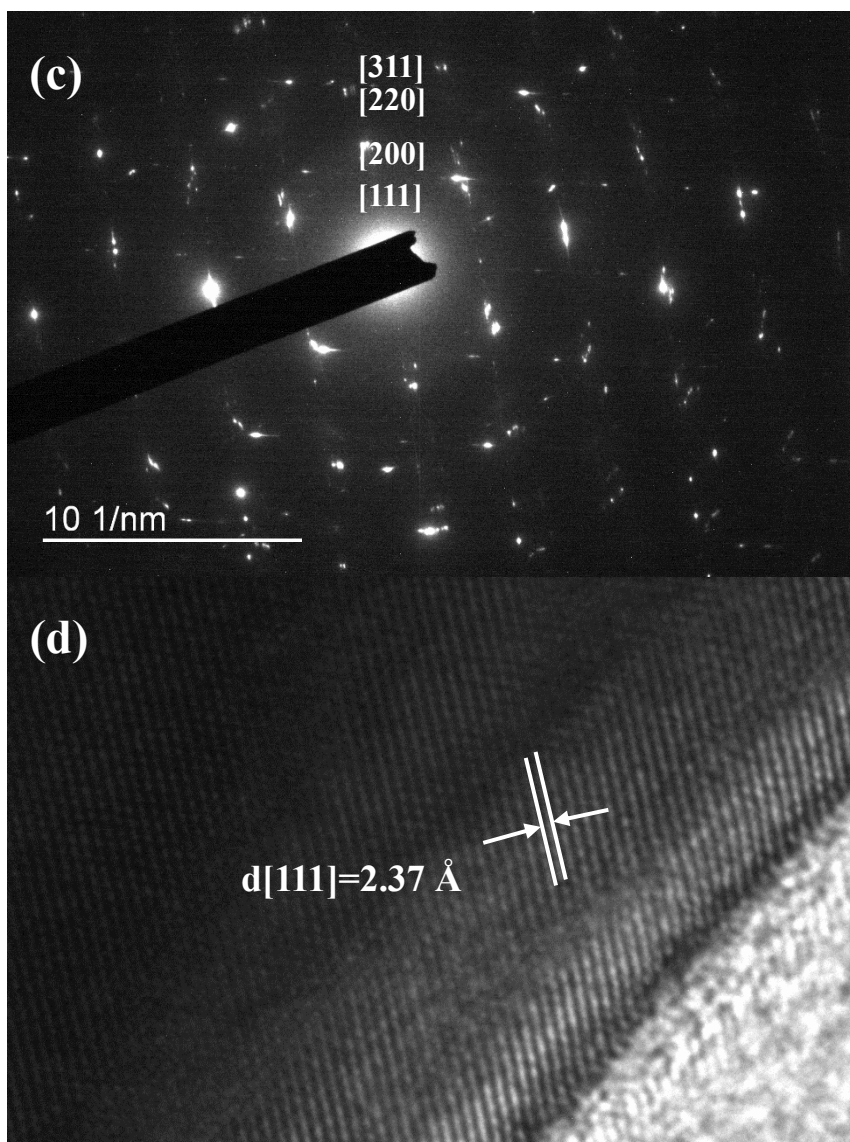


Figure 4.2 (c) SAED and (d) HR-TEM images of AgNWs composite.

### **PtAg-1 NWs**

The morphology of PtAg-1 NWs composite was studied by TEM analysis. As displayed in Figure 4.3, the hollow PtAg-1 NWs with the shell thickness of  $10.5 \pm 3.1$  nm were successfully synthesized with porous surface. The structure of PtAg-1 NWs composite was analyzed by SAED and HR-TEM as displayed in Figure 4.3 (c) and (d) respectively. Figure 4.3 (c) shows that the diffraction rings are assigned to the (111), (200), (220) and (311) crystal planes which are consistent to the d-spacing of PtAg. It is suggested that the PtAg-1 NWs composite is adopting a fcc structure with a Fm-3m(225) space group (JCPDS Card no. 01-071-9228). From Figure 4.3 (d), the crystal plane with d-spacing of 1.33 Å is found which corresponds to the (222) crystal plane of PtAg.

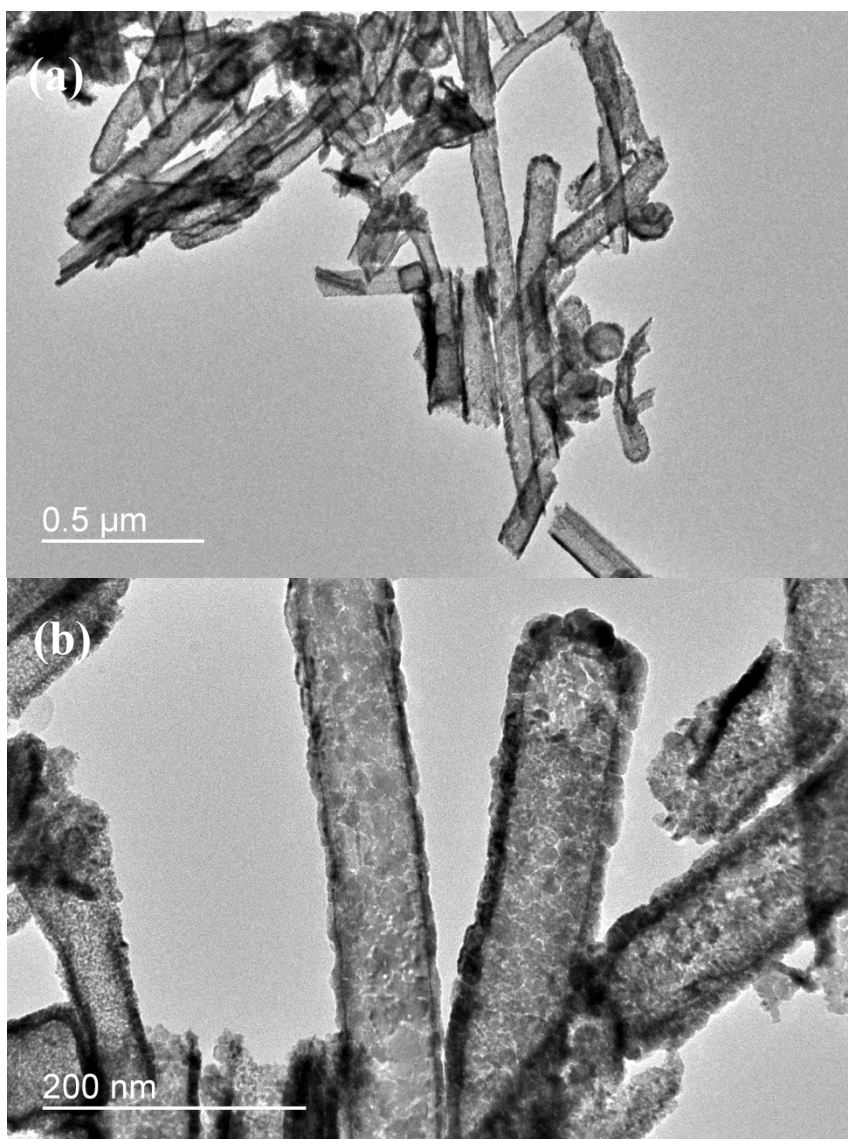


Figure 4.3 (a) LM-TEM and (b) HM-TEM images of PtAg-1 NWs composite.

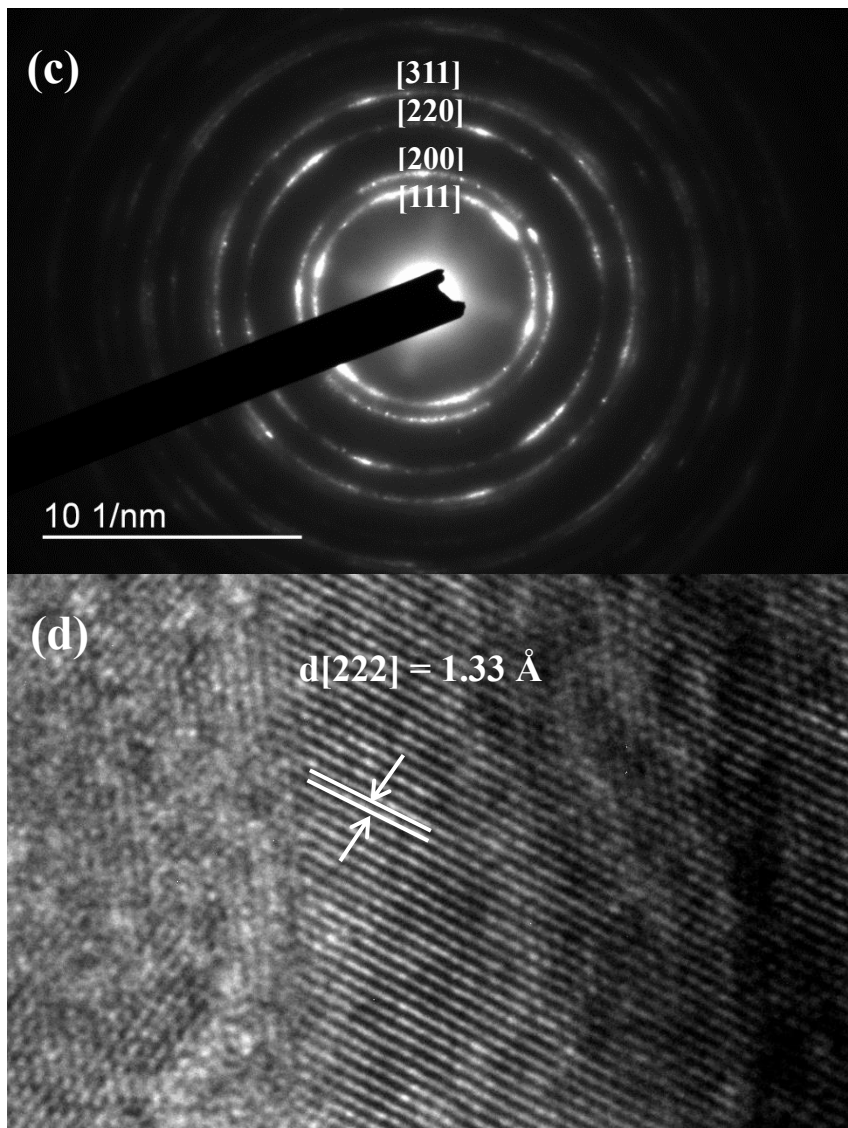


Figure 4.3 (c) SAED and (d) HR-TEM images of PtAg-1 NWs composite.

### **PtAg-2 NWs**

The morphology of PtAg-2 NWs composite was studied by TEM analysis. As displayed in Figure 4.4, the hollow PtAg-2 NWs with the shell thickness of  $11.4 \pm 3.0$  nm were successfully synthesized with porous surface. The structure of PtAg-2 NWs composite was analyzed by SAED and HR-TEM as displayed in Figure 4.4 (c) and (d) respectively. Figure 4.4 (c) shows that the diffraction rings are assigned to the (111), (200), (220) and (311) crystal planes which are consistent to the d-spacing of PtAg. It is suggested that the PtAg-2 NWs composite is adopting a fcc structure with a Fm-3m(225) space group (JCPDS Card no. 01-071-9228). From Figure 4.4 (d), the crystal plane with d-spacing of 2.49 Å is found which corresponds to the (111) crystal plane of PtAg.

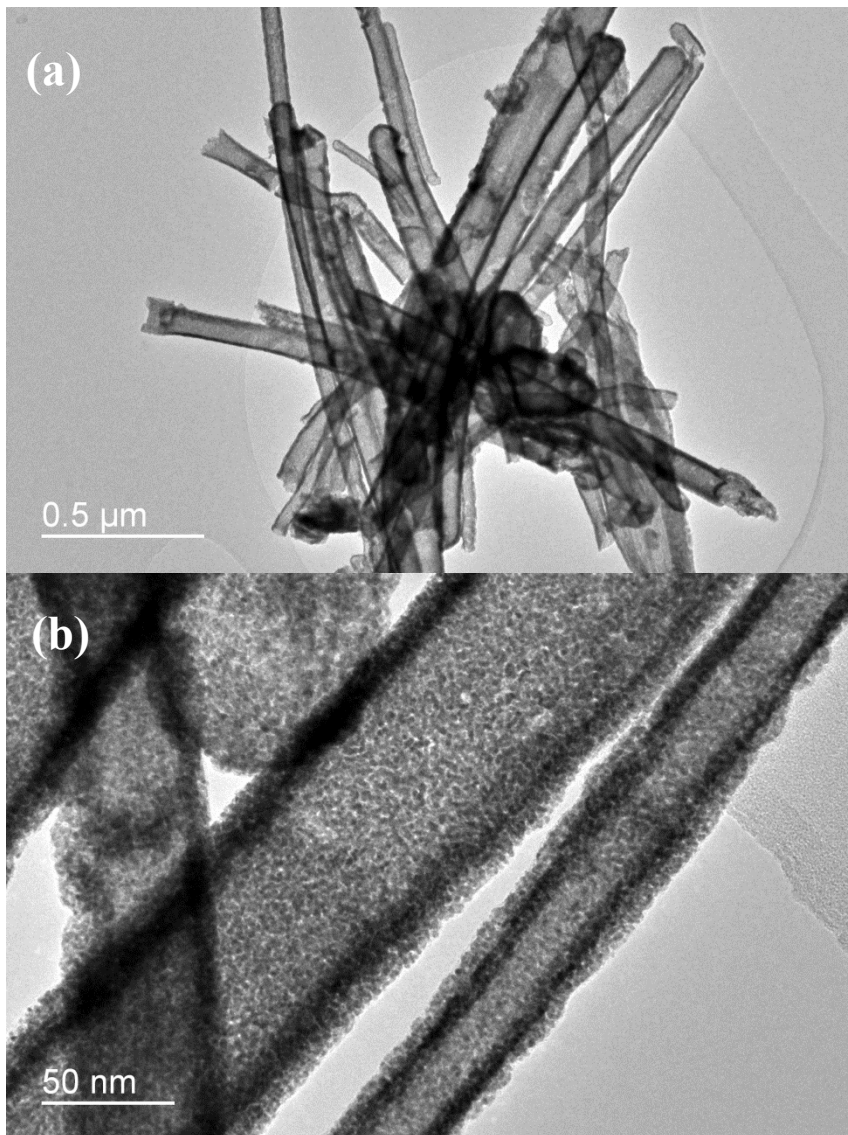


Figure 4.4 (a) LM-TEM and (b) HM-TEM images of PtAg-2 NWs composite.

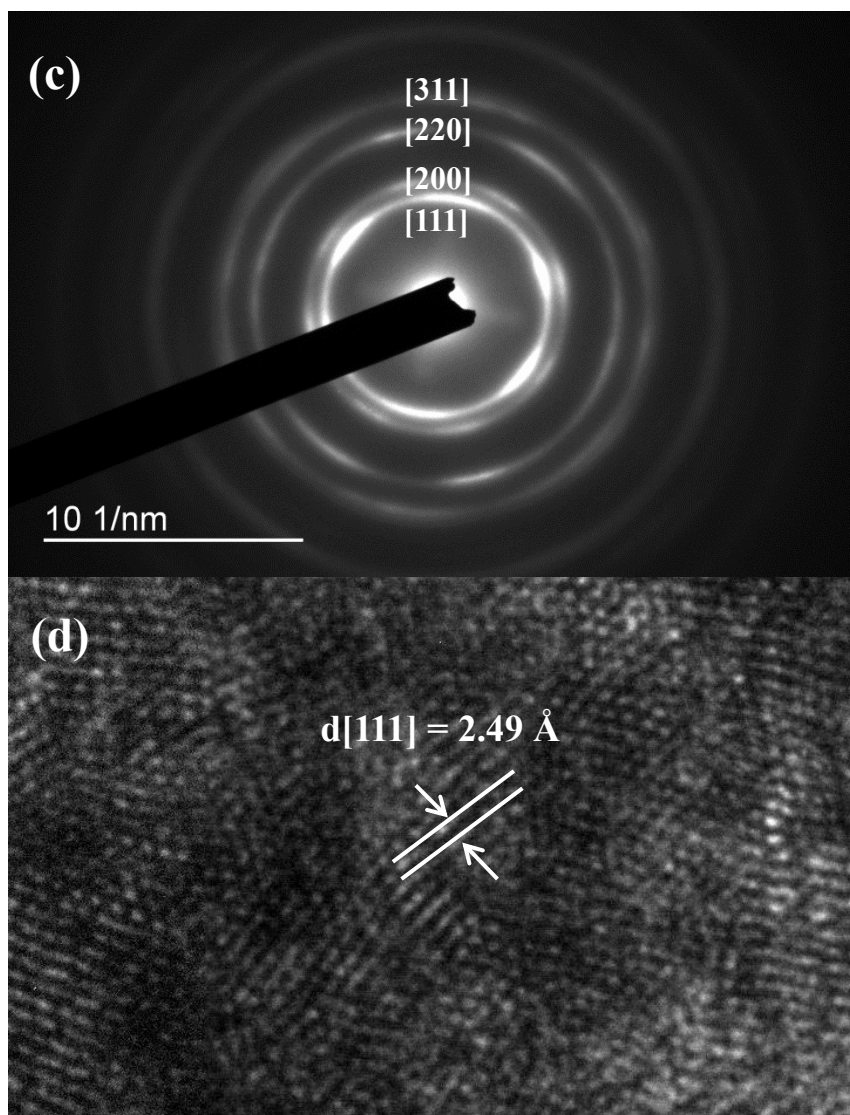


Figure 4.4 (c) SAED and (d) HR-TEM images of PtAg-2 NWs composite.

### **PtAg-3 NWs**

The morphology of PtAg-3 NWs composite was studied by TEM analysis. As displayed in Figure 4.5, the hollow PtAg-3 NWs with the shell thickness of  $11.3 \pm 3.9$  nm were successfully synthesized with porous surface. The structure of PtAg-3 NWs composite was analyzed by SAED and HR-TEM as displayed in Figure 4.5 (c) and (d) respectively. Figure 4.5 (c) shows that the diffraction rings are assigned to the (111), (200), (220) and (311) crystal planes which are consistent to the d-spacing of PtAg. It is suggested that the PtAg-3 NWs composite is adopting a fcc structure with a Fm-3m(225) space group (JCPDS Card no. 01-071-9228). From Figure 4.5 (d), the crystal plane with d-spacing of 2.06 Å is found which corresponds to the (200) crystal plane of PtAg.

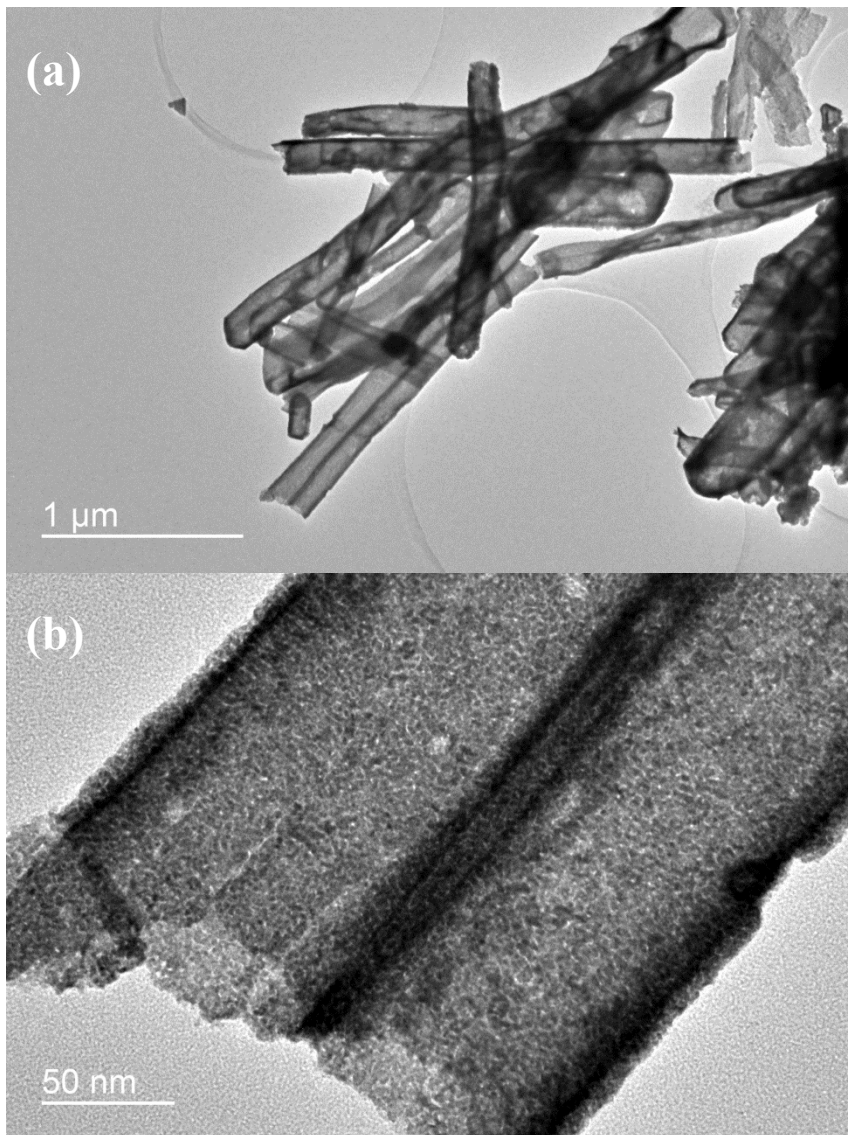


Figure 4.5 (a) LM-TEM and (b) HM-TEM images of PtAg-3 NWs composite.

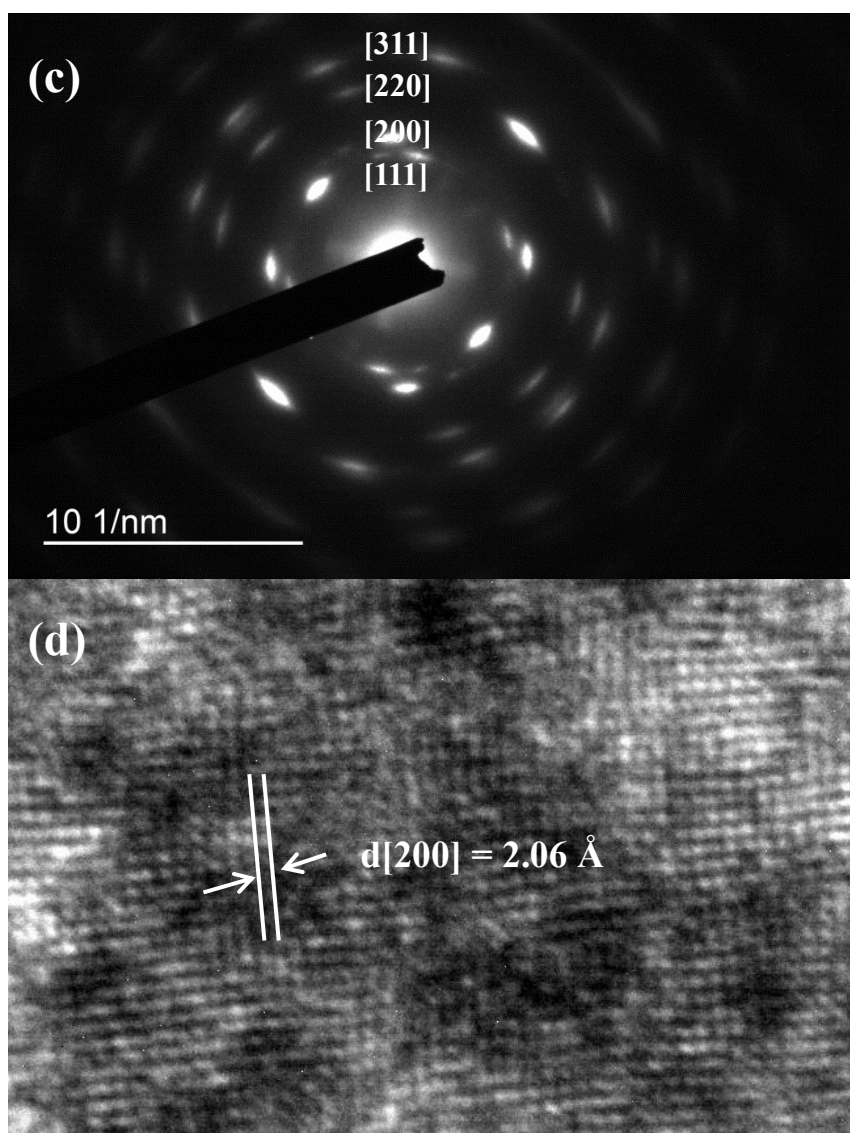


Figure 4.5 (c) SAED and (d) HR-TEM images of PtAg-3 NWs composite.

### **PtAg-4 NWs**

The morphology of PtAg-4 NWs composite was studied by TEM analysis. As displayed in Figure 4.6, the hollow PtAg-4 NWs with the shell thickness of  $10.7 \pm 1.2$  nm were successfully synthesized with porous surface. The structure of PtAg-4 NWs composite was analyzed by SAED and HR-TEM as displayed in Figure 4.6 (c) and (d) respectively. Figure 4.6 (c) shows that the diffraction rings are assigned to the (111), (200), (220) and (311) crystal planes which are consistent to the d-spacing of PtAg. It is suggested that the PtAg-4 NWs composite is adopting a fcc structure with a Fm-3m(225) space group (JCPDS Card no. 01-071-9228). From Figure 4.6 (d), the crystal plane with d-spacing of 2.72 Å is found which corresponds to the (111) crystal plane of PtAg.

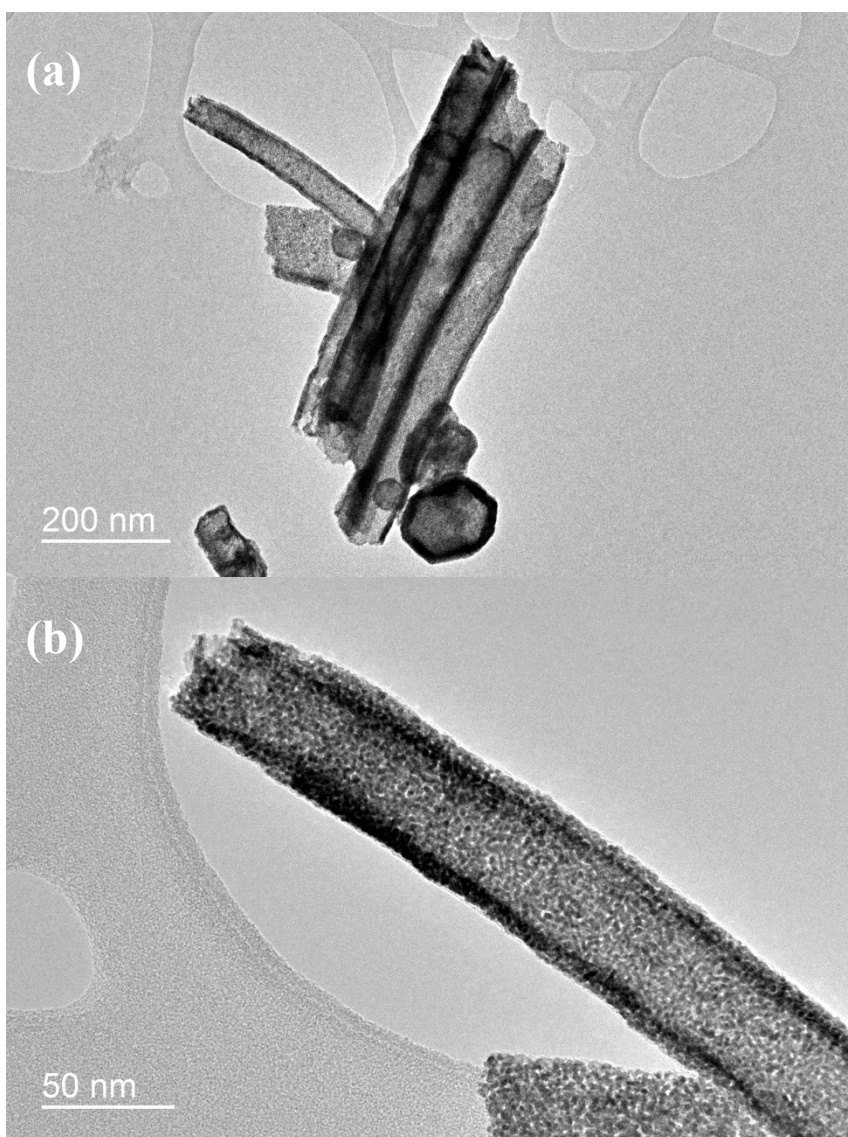


Figure 4.6 (a) LM-TEM and (b) HM-TEM images of PtAg-4 NWs composite.

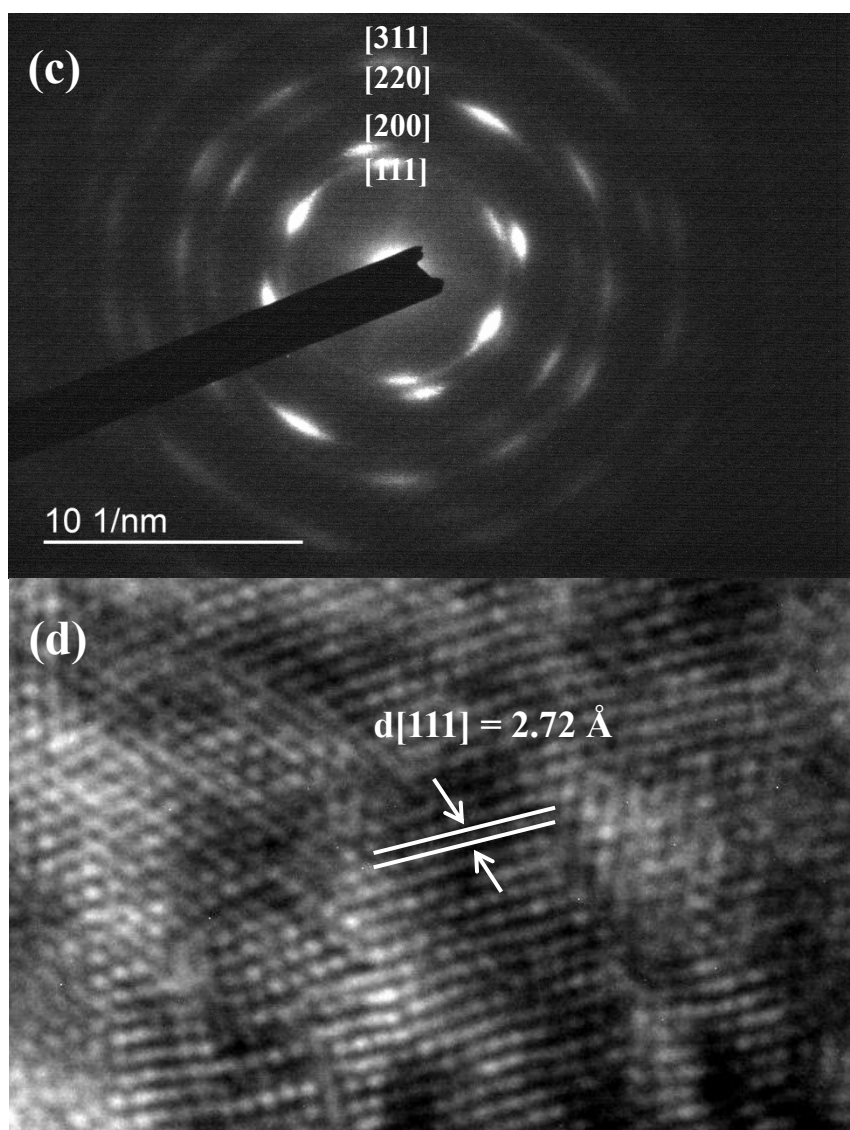


Figure 4.6 (c) SAED and (d) HR-TEM images of PtAg-4 NWs composite.

As shown in Table 4.3, the shell thickness of PtAg NWs composites mainly range from  $10.5 \pm 3.1$  nm to  $11.4 \pm 3.0$  nm, which is not an obvious change with the increase of addition volume of 80 mM  $K_2PtCl_4$  solution. EDX analysis demonstrates that Pt-to-Ag atomic ratio increases from 1 : 3.0 to 3.5 : 1 with the increase of volume of  $K_2PtCl_4$  solution from 313  $\mu$ L to 2500  $\mu$ L. With more  $K_2PtCl_4$  solution added, more Ag is displaced by  $[PtCl_4]^{2-}$  ions. Also, the remaining unreacted pure Ag metal was washed by 5 M  $HNO_3$  solution.

Catalysts	Shell thickness (nm)	Pt-to-Ag atomic ratio by EDX
PtAg-1 NWs	$10.5 \pm 3.1$	1 : 3.0
PtAg-2 NWs	$11.4 \pm 3.0$	1.2 : 1
PtAg-3 NWs	$11.3 \pm 3.9$	2.4 : 1
PtAg-4 NWs	$10.7 \pm 1.2$	3.5 : 1

Table 4.3 Summary of shell thickness and Pt-to-Ag atomic ratio of PtAg NWs composites.

To study the crystalline structure, the AgNWs, PtAg NWs and Pt black composites were characterized by XRD analysis as shown in Figure 4.7. The AgNWs composite exhibits diffraction peaks at  $2\theta$  values of  $38.2^\circ$ ,  $44.4^\circ$ ,  $64.5^\circ$ ,  $77.5^\circ$  and  $81.6^\circ$  which are characteristic of a fcc structure of Ag with a 225:Fm-3m space group, corresponding to the (111), (200), (220), (311) and (222) crystal planes respectively (JCPDS Card no.00-001-1164). The PtAg NWs composites exhibit diffraction peaks as stated in Table 4.4, which are characteristic of a fcc structure of PtAg with a 225:Fm-3m space group, corresponding to the (111), (200), (220), (311) and (222) crystal planes respectively (JCPDS Card no.01-071-9228). The Pt black composite exhibits diffraction peaks at  $2\theta$  values of  $39.8^\circ$ ,  $46.1^\circ$ ,  $67.5^\circ$ ,  $81.2^\circ$  and  $86.1^\circ$  which are characteristic of a fcc structure of Pt with a 225:Fm-3m space group, corresponding to the (111), (200), (220), (311) and (222) crystal planes respectively (JCPDS Card no.00-001-1190). As displayed in Figure 4.7, the diffraction peaks of PtAg NWs composites are slightly shifted from standard diffraction peaks of Ag as indicated by dotted lines. Besides, as presented in Table 4.4, the diffraction peaks of PtAg NWs composites are located in between the standard diffraction peaks of Ag and Pt and no characteristic Ag or Pt diffraction peaks are found, implying the formation of PtAg alloy.[1, 34, 36, 37, 42, 43]

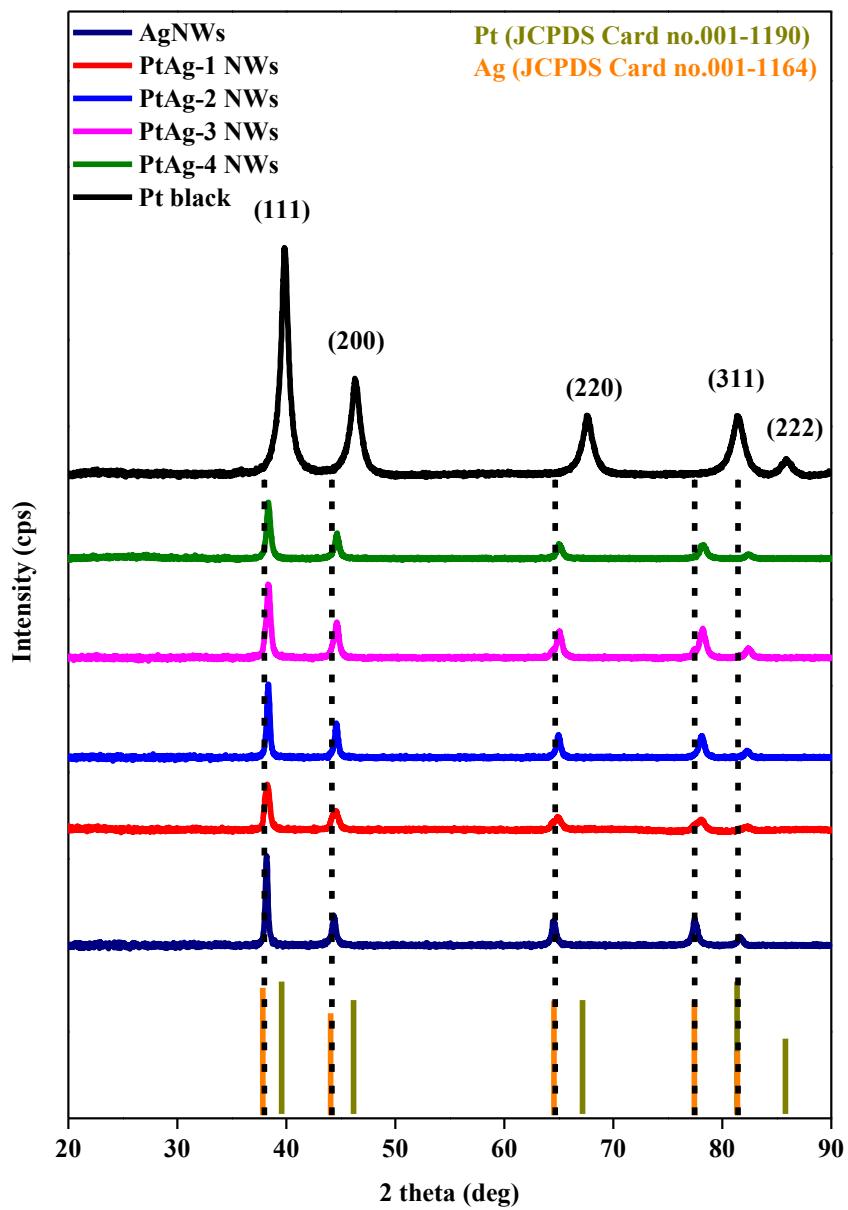


Figure 4.7 XRD patterns of AgNWs, PtAg NWs and Pt black composites.

Crystal plane	Standard Pure Ag	AgNWs	PtAg-1 NWs	PtAg-2 NWs	PtAg-3 NWs	PtAg-4 NWs	Pt black	Standard Pure Pt
(111)	37.9 °	38.2 °	38.2 °	38.3 °	38.4 °	38.3 °	39.8 °	39.7 °
(200)	44.1 °	44.4 °	44.5 °	44.6 °	44.7 °	44.6 °	46.1 °	46.3 °
(220)	64.7 °	64.5 °	64.9 °	64.9 °	65.0 °	65.0 °	67.5 °	67.3 °
(311)	77.6 °	77.5 °	78.1 °	78.1 °	77.4 °	78.1 °	81.2 °	81.5 °
(222)	81.5 °	81.6 °	82.3 °	82.2 °	82.3 °	82.5 °	86.1 °	86.0 °

Table 4.4 Diffraction peaks of AgNWs, PtAg NWs and Pt black composites.

X-ray photoelectron spectroscopy (XPS) is a surface sensitive quantitative technique. Since EDX and XRD analyses confirm the existence of Pt of PtAg NWs and alloy formation respectively, XPS was performed to further confirm the existence of Pt on the catalyst surface. The chemical composition and valence states of Ag and Pt were also studied. The XPS spectra of AgNWs, PtAg NWs and Pt black composites are displayed in Figure 4.9.

For Ag NWs composite, the Ag 3d region shows two peaks at 374.2 eV and 368.2 eV corresponding to the metallic Ag(0) 3d<sub>3/2</sub> and 3d<sub>5/2</sub> respectively. For PtAg NWs composites, the Ag 3d region shows two peaks at 374.1 eV and 368.1 eV corresponding to the metallic Ag(0) 3d<sub>3/2</sub> and 3d<sub>5/2</sub> respectively.

As displayed in Figure 4.8, the Pt 4f region of the catalysts is deconvoluted into two doublets assigned to metallic Pt(0) and oxidized Pt(II). The more intense doublets correspond to the metallic Pt(0) 4f<sub>5/2</sub> and 4f<sub>7/2</sub> while the less intense doublets at correspond to the oxidized Pt(II) 4f<sub>5/2</sub> and 4f<sub>7/2</sub>. As summarized in Table 4.5, the amount of Pt species was calculated from the relative intensities of these two doublets. The XPS results suggest that the predominant surface species on the catalysts is metallic Pt(0).

The binding energies of Ag and Pt of PtAg NWs composites are presented in Table 4.6. Compared with standard pure Ag, the Ag 3d peaks of PtAg NWs composites are slightly negatively shifted of 0.1 eV to 0.2 eV.[33] As shown in Figure 4.10 (a) and (b), it is observed that both Ag 3d<sub>3/2</sub> and 3d<sub>5/2</sub> peaks are slightly negatively shifted with increasing Pt-to-Ag atomic ratio by EDX analysis. It is suggested that the increasing Pt content of PtAg NWs composites causes the

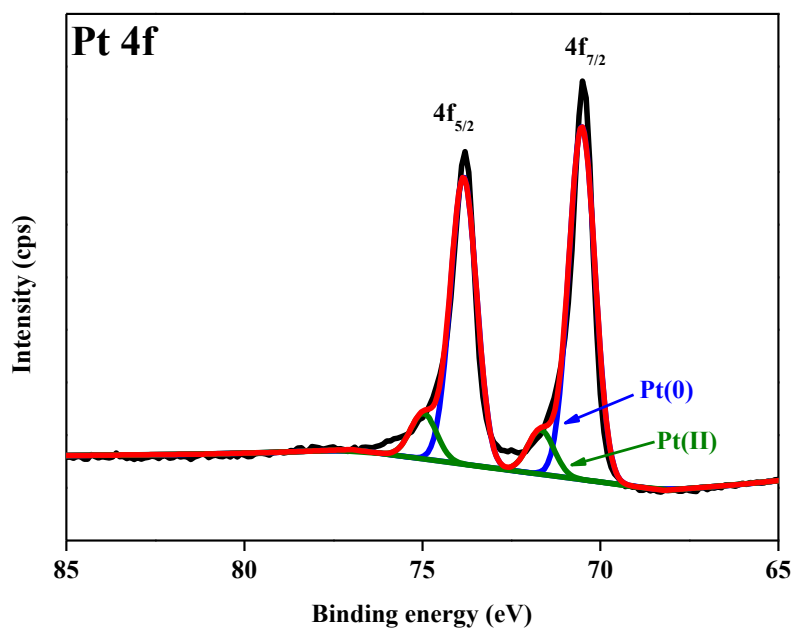
negative shift of binding energy.

Compared with standard pure Pt, the Pt 4f peaks of PtAg NWs composites are negatively shifted of 0.7 eV. The significantly negative shift of Pt 4f peaks implies that the electronic structure of Pt is modified, further confirming the formation of PtAg alloy.[35, 44, 45]

Catalysts	Species	Binding energy (eV) (Pt 4f <sub>5/2</sub> )	Relative intensity (%)	Binding energy (eV) (Pt 4f <sub>7/2</sub> )	Relative intensity (%)
PtAg-1 NWs	Pt(0)	73.8	86	70.5	89
	Pt(II)	75.0	14	71.6	11
PtAg-2 NWs	Pt(0)	73.9	87	70.5	88
	Pt(II)	75.0	13	71.8	12
PtAg-3 NWs	Pt(0)	73.9	85	70.6	87
	Pt(II)	75.0	15	71.7	13
PtAg-4 NWs	Pt(0)	73.9	79	70.6	80
	Pt(II)	75.2	21	71.9	20
Pt black	Pt(0)	74.6	66	71.3	75
	Pt(II)	76.5	34	72.8	25

Table 4.5 Binding energies and relative intensities of different platinum species of Pt black and PtAg NWs composites.

(a)



(b)

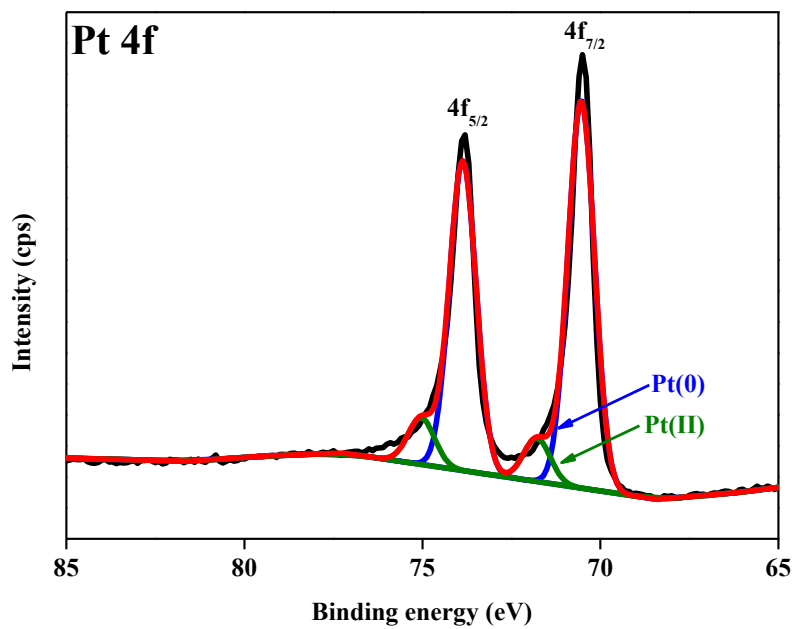
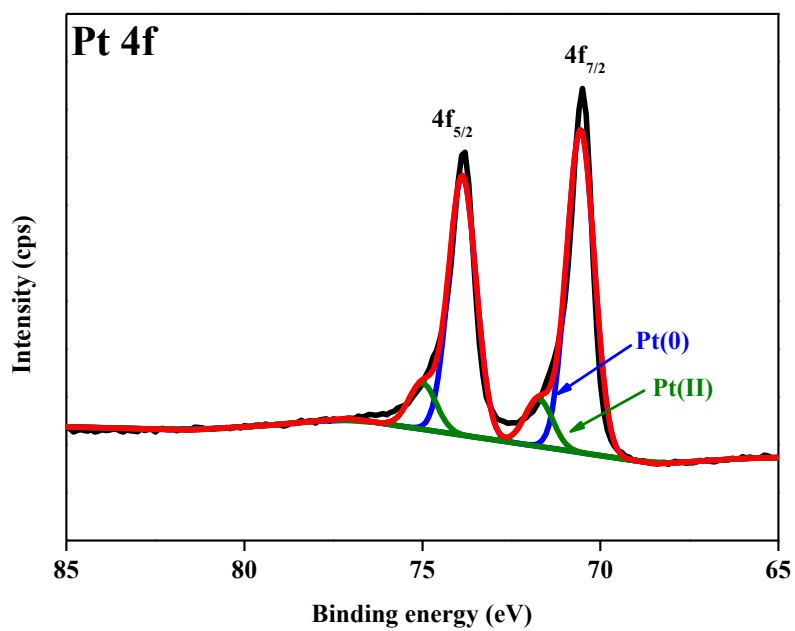


Figure 4.8

XPS spectra of Pt 4f region of (a) PtAg-1 and (b) PtAg-2 NWs composites.

(c)



(d)

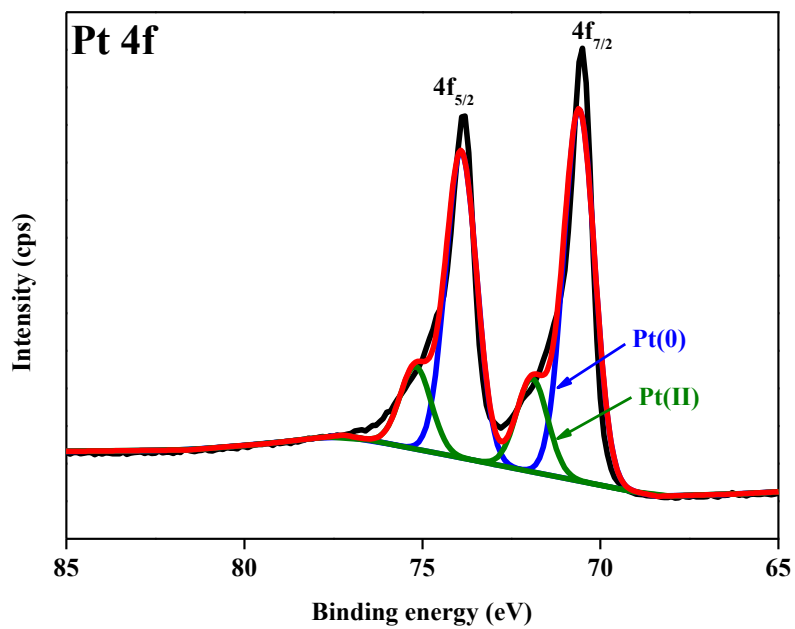


Figure 4.8 XPS spectra of Pt 4f region of (c) PtAg-3 and (d) PtAg-4 NWs composites.

(e)

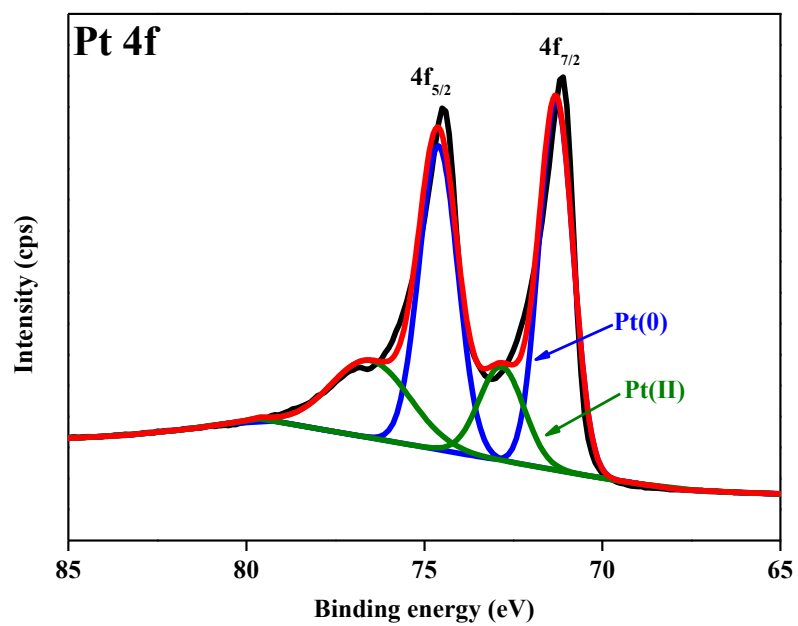


Figure 4.8 XPS spectra of Pt 4f region of (e) Pt black composite.

	Binding energy of Ag		Binding energy of Pt	
	(eV)		(eV)	
	3d <sub>3/2</sub>	3d <sub>5/2</sub>	4f <sub>5/2</sub>	4f <sub>7/2</sub>
Standard Pure Ag	374.3	368.3	-	-
Standard Pure Pt	-	-	74.5	71.2
AgNWs	374.2	368.2	-	-
PtAg-1 NWs	374.1	368.1	73.8	70.5
PtAg-2 NWs	374.1	368.1	73.8	70.5
PtAg-3 NWs	374.1	368.1	73.8	70.5
PtAg-4 NWs	374.1	368.1	73.8	70.5
Pt black	-	-	73.8	70.5

Table 4.6 Summary of the binding energies of Ag 3d and Pt 4f of PtAg NWs composites.

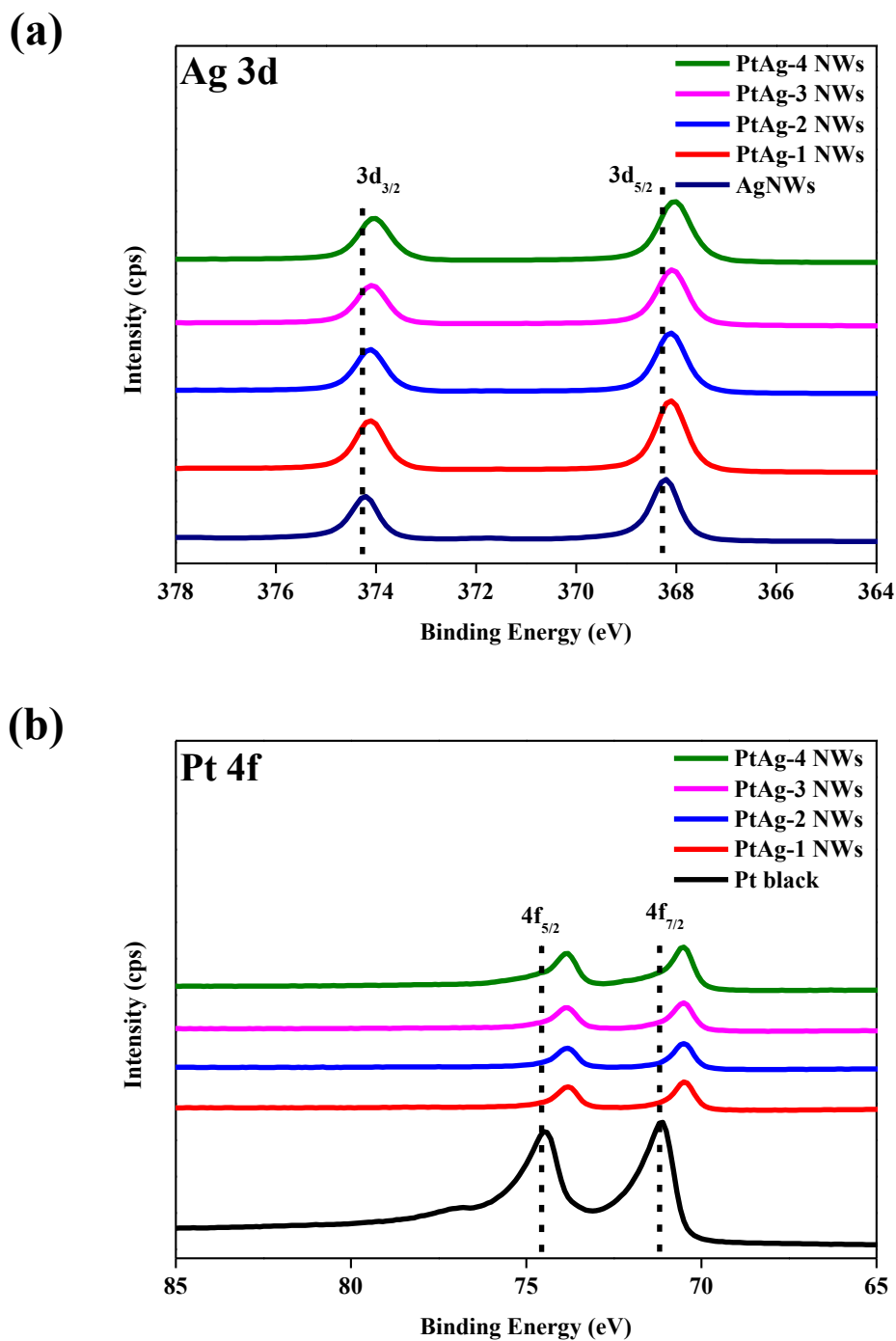


Figure 4.9 XPS spectra of (a) Ag 3d region of AgNWs and PtAg NWs composites and (b) Pt 4f region of Pt black and PtAg NWs composites. The dotted lines indicate the binding energy of standard pure Ag and Pt.

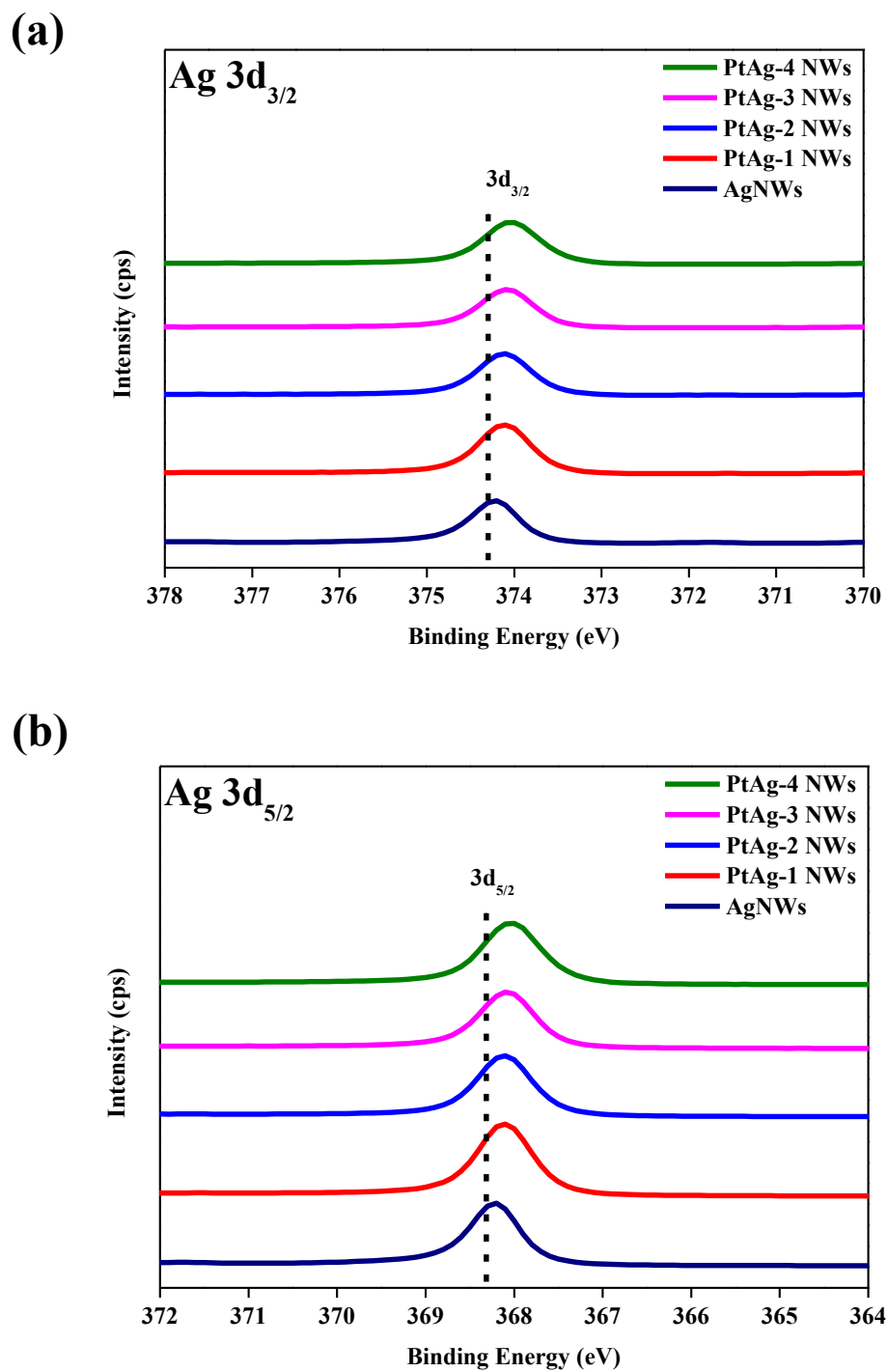


Figure 4.10 XPS spectra of (a) Ag 3d<sub>3/2</sub> and (b) Ag 3d<sub>5/2</sub> peaks of AgNWs and PtAg NWs composites. The dotted lines indicate the binding energy of standard pure Ag 3d<sub>3/2</sub> and 3d<sub>5/2</sub> peaks.

XPS analysis also shows an increasing trend of Pt-to-Ag surface ratio with an increasing volume of  $K_2PtCl_4$  solution added as shown in Table 4.7. Since an increasing volume of  $K_2PtCl_4$  solution was added, more Pt deposited on the surface of Ag NWs and displaced Ag. This results in an increasing trend of Pt-to-Ag surface ratio from 1 : 8.0 to 1 : 3.5.

Catalysts	Pt-to-Ag surface ratio by XPS
PtAg-1 NWs	1 : 8.0
PtAg-2 NWs	1 : 6.2
PtAg-3 NWs	1 : 5.5
PtAg-4 NWs	1 : 3.5

Table 4.7 Summary of Pt-to-Ag surface ratio of PtAg NWs composites.

## 4.2.2 Electrochemical Characterizations and Electrocatalytic Studies

### 4.2.2.1 Cyclic voltammetry in sulfuric acid

Figure 4.12 displays the cyclic voltammograms (CVs) of Pt black and PtAg NWs composites in N<sub>2</sub>-purged 0.1 M H<sub>2</sub>SO<sub>4</sub> solution in a potential region between -0.24 V and 1.0 V with a scan rate of 50 mVs<sup>-1</sup>. The typical characteristics of surface oxidation over a wide range of potential,[46] the reduction peak of oxidized Pt at 0.4 V to 0.6 V in cathodic scan and the hydrogen adsorption/desorption (H<sub>ads/des</sub>) peaks in the potential range from -0.24 V to 0.0 V are shown.

In anodic scan, the PtAg NWs composites exhibit the anodic peak at 0.8 V to 1.0 V which is related to the formation of the oxides species of Pt and Ag.[47] On the contrary, Pt black exhibits an anodic peak at around 0.6 V due to the formation of Pt oxide. In cathodic scan, both Pt black and PtAg NWs composites show the reduction peak of oxidized Pt at 0.4 V to 0.6 V.

It is observed that there are two resolved peaks in the H<sub>ads/des</sub> region of Pt black. They are related to the weakly and strongly bonded hydrogen species on different crystal planes of Pt.[48, 49] The peaks with more negative potential correspond to (111) plane while those with more positive potential correspond to (100) plane. [1, 50] The PtAg NWs composites show no resolved peaks in the H<sub>ads/des</sub> region. It is believed that the incorporation of Ag into Pt lattice decreases the crystallinity of the Pt surface.[1]

The peak area under the cathodic peak for the reduction of Pt oxide is used to determine ECSA of Pt. The ECSA of Pt can be calculated by the following

equation.

$$ECSA_{Pt} = Q_{Pt}/420 \mu Ccm^{-2} \quad \text{Eq. 4.5}$$

where  $Q_{Pt}$  is the surface oxide reduction charges of plain Pt.[51, 52] The specific area activity is calculated by normalizing the current to  $ECSA_{Pt}$ . As shown in Table 4.8, the specific area activities of PtAg-2 NWs, PtAg-3 NWs and PtAg-4 NWs composites are of similar values ranging from 0.094  $mAcm^{-2}$  to 0.097  $mAcm^{-2}$  which are calculated from the reduction peak of oxidized Pt at 0.4 V to 0.6 V. It is indicated that similar specific area activities were achieved in  $H_2SO_4$  solution. PtAg-1 NWs composite has a slightly lower specific area activity of 0.090  $mAcm^{-2}$  due to the lower Pt content on catalyst surface as shown by XPS analysis.

Catalysts	Specific area activity ( $mAcm^{-2}$ )
PtAg-1 NWs	0.090
PtAg-2 NWs	0.097
PtAg-3 NWs	0.094
PtAg-4 NWs	0.095
Pt black	0.088

Table 4.8 Summary of specific area activities of PtAg NWs and Pt black composites in  $N_2$ -purged 0.1 M  $H_2SO_4$  solution.

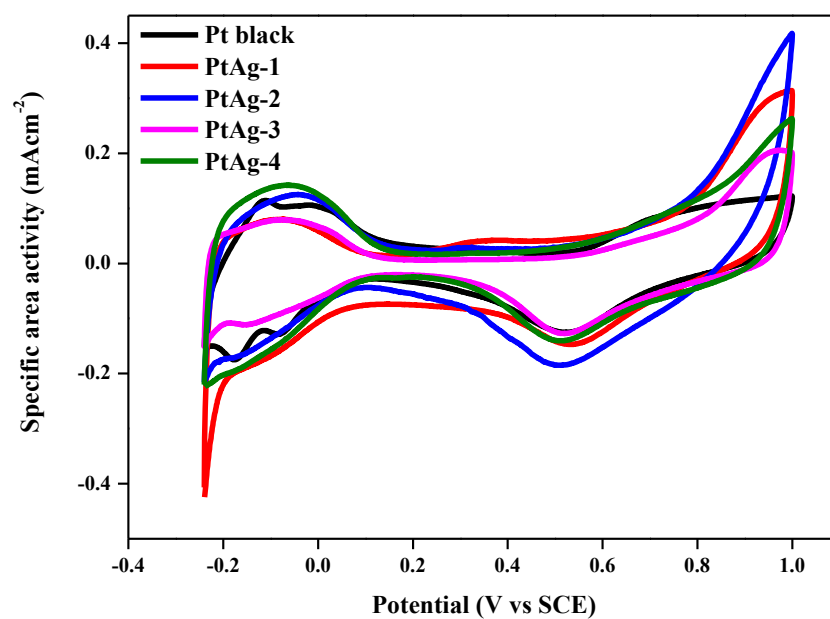


Figure 4.11 CVs of PtAg NWs and Pt black composites in  $N_2$ -purged  $0.1\text{ M H}_2\text{SO}_4$  solution. Scan rate,  $50\text{ mVs}^{-1}$ .

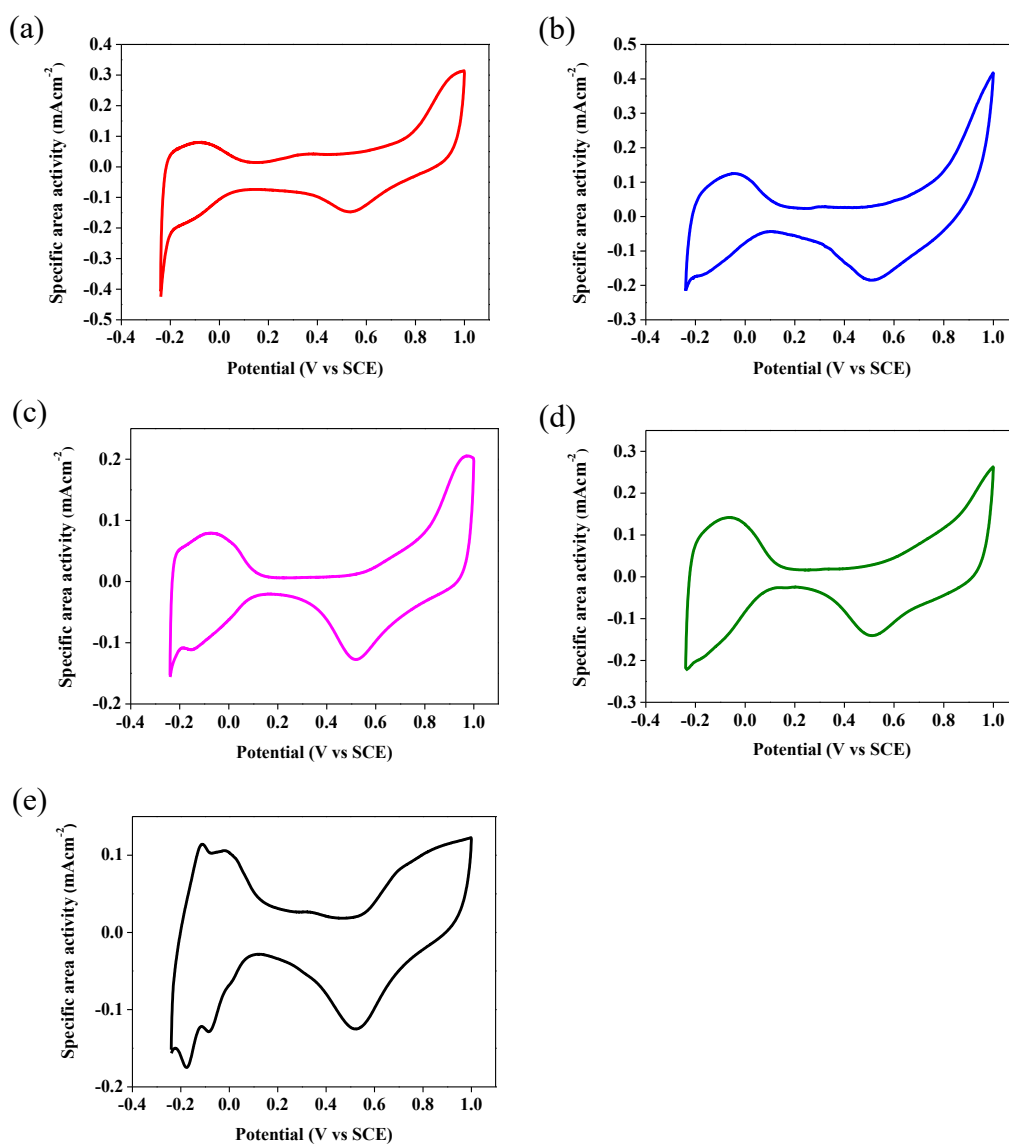


Figure 4.12 CVs of (a) PtAg-1 NWs (b) PtAg-2 NWs, (c) PtAg-3 NWs, (d) PtAg-4 NWs and (e) Pt black composites in  $N_2$ -purged 0.1 M  $H_2SO_4$  solution. Scan rate,  $50 \text{ mVs}^{-1}$ .

#### 4.2.2.2 Electrooxidation of methanol and its related chronoamperometric test

##### Electrooxidation of methanol

Figure 4.13 displays the CVs of the catalysts on GCE in 0.1M MeOH + 0.1M H<sub>2</sub>SO<sub>4</sub> solution in the potential region from 0.0 V to 1.0 V with a scan rate of 50 mVs<sup>-1</sup>. It is known that Ag is not active towards the oxidation of methanol.[53] The specific area activity towards the oxidation of methanol is calculated by normalizing the current to the ECSA of Pt in the catalysts.

The CVs show typical features of the oxidation of methanol. The PtAg NWs and Pt black composites exhibit two anodic peaks in the both forward and backward scans. The anodic peak at around 0.6 V in the forward scan is due to the oxidation of methanol. With the increasing potential, the current density decreases. This is probably because of the blockage of Pt active sites by the adsorbed intermediate species such as CO<sub>ads</sub> hindering further methanol oxidation. In backward scan, the anodic peak at around 0.4 V is due to the oxidation of CO<sub>ads</sub> or other associated incompletely oxidized carbonaceous intermediates generated during the forward scan.[32, 54, 55]

In Table 4.9, the specific area activity towards the oxidation of methanol increases from 0.12 mAcm<sup>-2</sup> to 0.59 mAcm<sup>-2</sup> with the increasing Pt-to-Ag surface ratio. The increasing Pt-to-Ag surface ratio indicates the increasing availability of Pt neighboring continuous sites for the oxidation of methanol due to ensemble effect. All PtAg NWs composites achieve lower specific area activity than Pt black composite except PtAg-4 NWs composite which achieves comparable catalytic activity to Pt black.[33]

Apart from specific area activity, the ratio of anodic peak current density in forward scan ( $I_f$ ) to that in backward scan ( $I_b$ ) is also regarded as another parameter to determine the performance of the catalysts. The  $I_f/I_b$  ratio indicates poison tolerating ability of the catalysts towards the adsorbed carbonaceous species such as  $CO_{ads}$ .

To study the poison tolerating ability of the PtAg NWs and Pt black composites, the PtAg-4 NWs and Pt black composites with comparable catalytic activities were compared. It is observed that the PtAg-4 NWs composite ( $I_f/I_b = 2.68$ ) exhibit higher  $I_f/I_b$  ratio than Pt black composite ( $I_f/I_b = 1.02$ ) indicating higher poison tolerating ability of PtAg-4 NWs composite. This is probably due to the modification of electronic structure of Pt by alloying with Ag as confirmed by XRD and XPS analysis. [32, 33]

Catalysts	Specific area activity ( $mAcm^{-2}$ )	$I_f/I_b$
PtAg-1 NWs	0.12	2.65
PtAg-2 NWs	0.14	2.70
PtAg-3 NWs	0.20	2.41
PtAg-4 NWs	0.59	2.68
Pt black	0.55	1.03

Table 4.9 Summary of electrochemical performance of PtAg NWs and Pt black composites towards the electrooxidation of methanol.

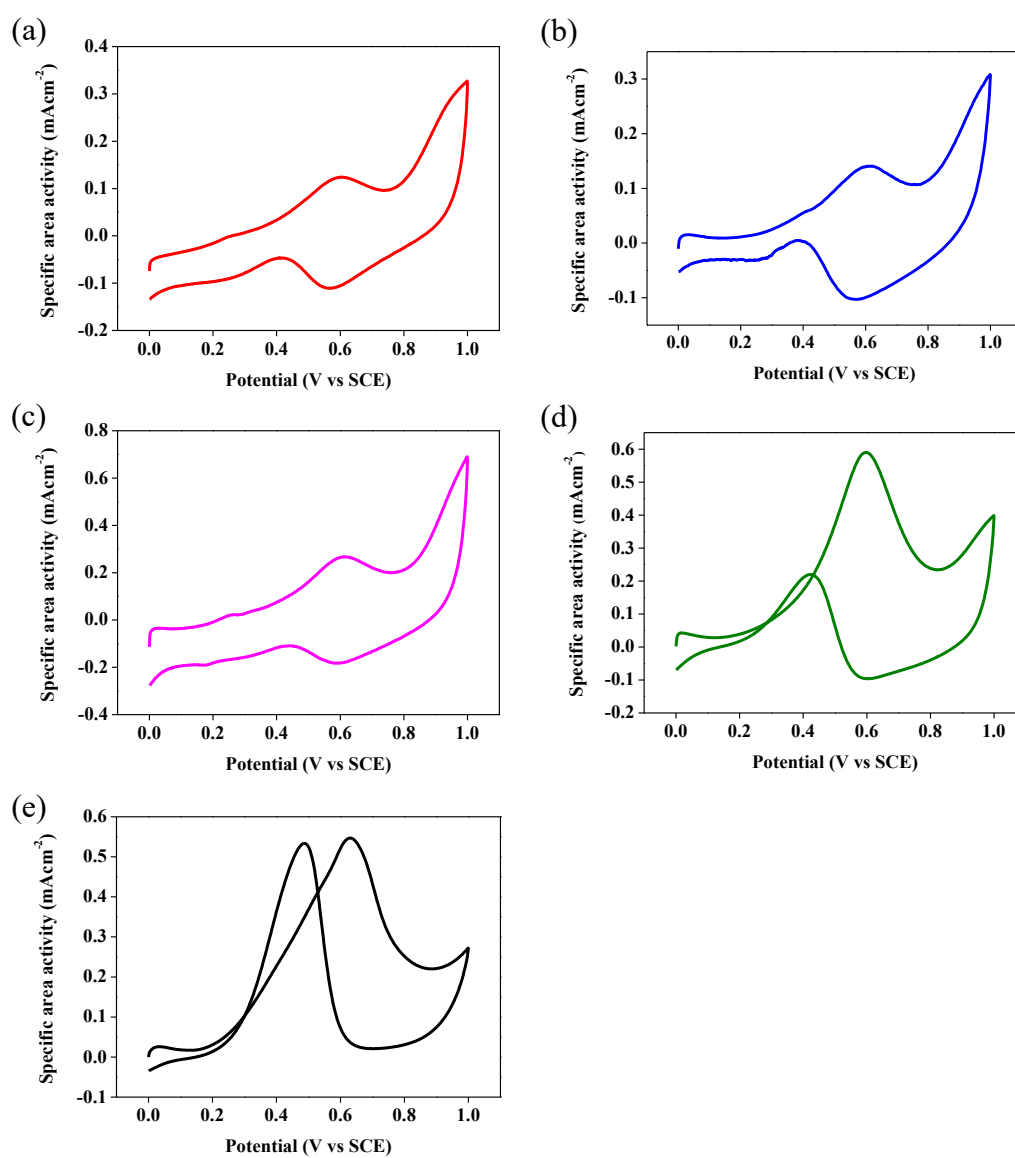


Figure 4.13 CVs of (a) PtAg-1 NWs, (b) PtAg-2 NWs, (c) PtAg-3 NWs, (d) PtAg-4 NWs and (e) Pt black composites in 0.1 M MeOH + 0.1 M H<sub>2</sub>SO<sub>4</sub> solution. Scan rate, 50 mVs<sup>-1</sup>.

### **Chronoamperometric test of methanol oxidation**

To study the stability of the electrocatalysts towards the oxidation of methanol, chronoamperometric tests were conducted. Figure 4.14 displays the chronoamperometric curves of the catalysts in 0.1 M MeOH + 0.1 M H<sub>2</sub>SO<sub>4</sub> solution at a fixed potential of 0.45 V for 3600 s.

Initially, the curves of current density decrease fast because of the formation and adsorption of poisonous intermediates such as CO<sub>ads</sub> during the oxidation of methanol. After that, the curves of current density decrease slowly and become flattened because the poisonous intermediates accumulate and block the active sites of the catalysts from the oxidation of methanol.[32, 34]

In Table 4.10, the current density retained after chronoamperometric test decreases in the order of Pt black (31.6 %), PtAg-4 NWs (20.3 %), PtAg-1 NWs (20.1 %), PtAg-2 NWs (4.2 %) and PtAg-3 NWs (1.8 %) composites. It is suggested that the PtAg NWs composites achieve lower stability than Pt black composite towards the oxidation of methanol. This implies that the alloying of Ag and Pt of the catalysts does not enhance their stability.

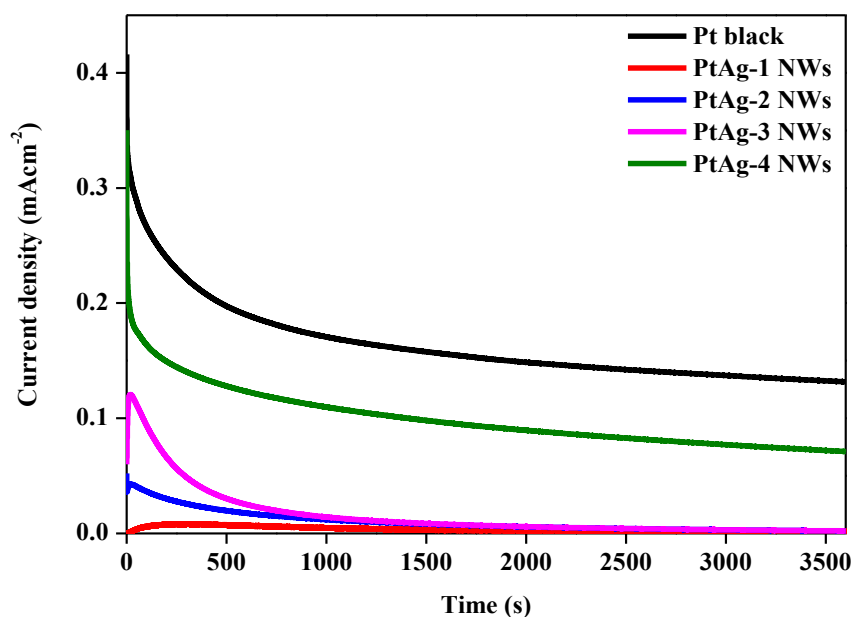


Figure 4.14 Chronoamperometric curves of PtAg NWs and Pt black composites in 0.1 M MeOH + 0.1 M H<sub>2</sub>SO<sub>4</sub> solution at a fixed potential of 0.45 V for 3600 s.

Catalysts	Current density retained after 3600 s chronoamperometric test (%)
PtAg-1 NWs	20.1
PtAg-2 NWs	4.2
PtAg-3 NWs	1.8
PtAg-4 NWs	20.3
Pt black	31.6

Table 4.10 Summary of electrochemical performance of PtAg NWs and Pt black composites towards chronoamperometric test of methanol oxidation.

### 4.2.2.3 Electrooxidation of ethanol and its related chronoamperometric test

#### Electrooxidation of ethanol

Figure 4.15 shows the CVs of the catalysts towards the oxidation of ethanol (EtOH) in 0.1 M EtOH + 0.1 M NaOH solution in the potential region between -0.8 V and 0.6 V with a scan rate of 50 mVs<sup>-1</sup>. It is known that Ag is not active towards the oxidation of ethanol.[29, 56] The specific area activity towards the oxidation of ethanol is calculated by normalizing the current to the ECSA of Pt in the catalysts.

The Pt black and PtAg NWs composites exhibit two anodic peaks in the both forward and backward scans. As displayed in Figure 4.15, it is observed that the anodic peaks in the forward scan are at -0.15 V to 0.02 V and those in the backward scan are at -0.45 V to -0.2 V. They are related to the oxidations of ethanol and intermediate carbonaceous species respectively.[57, 58]

As shown in Table 4.11, the specific area activity towards the oxidation of ethanol decreases from 1.56 mAcm<sup>-2</sup> to 0.43 mAcm<sup>-2</sup> with the increasing Pt-to-Ag surface ratios.[59] The maximum enhancement is achieved at the Pt-to-Ag surface ratio of 1 : 8.0. This may be explained by the incorporation of Ag into Pt. It is proposed that Ag offers oxygen-containing species by forming Ag-OH<sub>ads</sub>. This favors the faster removal of CO<sub>ads</sub> species from Pt active sites. As a result, more Pt active sites are released for the oxidation of ethanol, which increases the oxidation rate.[56]

It is also found that the PtAg NWs composites exhibit higher I<sub>f</sub>/I<sub>b</sub> than Pt black composite suggesting that the PtAg NWs composites are more tolerant to CO<sub>ads</sub>

due to the alloy effect.

Catalysts	Specific area activity (mAcm <sup>-2</sup> )	I <sub>f</sub> /I <sub>b</sub>
PtAg-1 NWs	1.56	6.33
PtAg-2 NWs	1.00	6.00
PtAg-3 NWs	0.77	6.53
PtAg-4 NWs	0.43	2.63
Pt black	0.46	1.48

Table 4.11 Summary of electrochemical performance of PtAg NWs and Pt black composites towards the electrooxidation of ethanol.

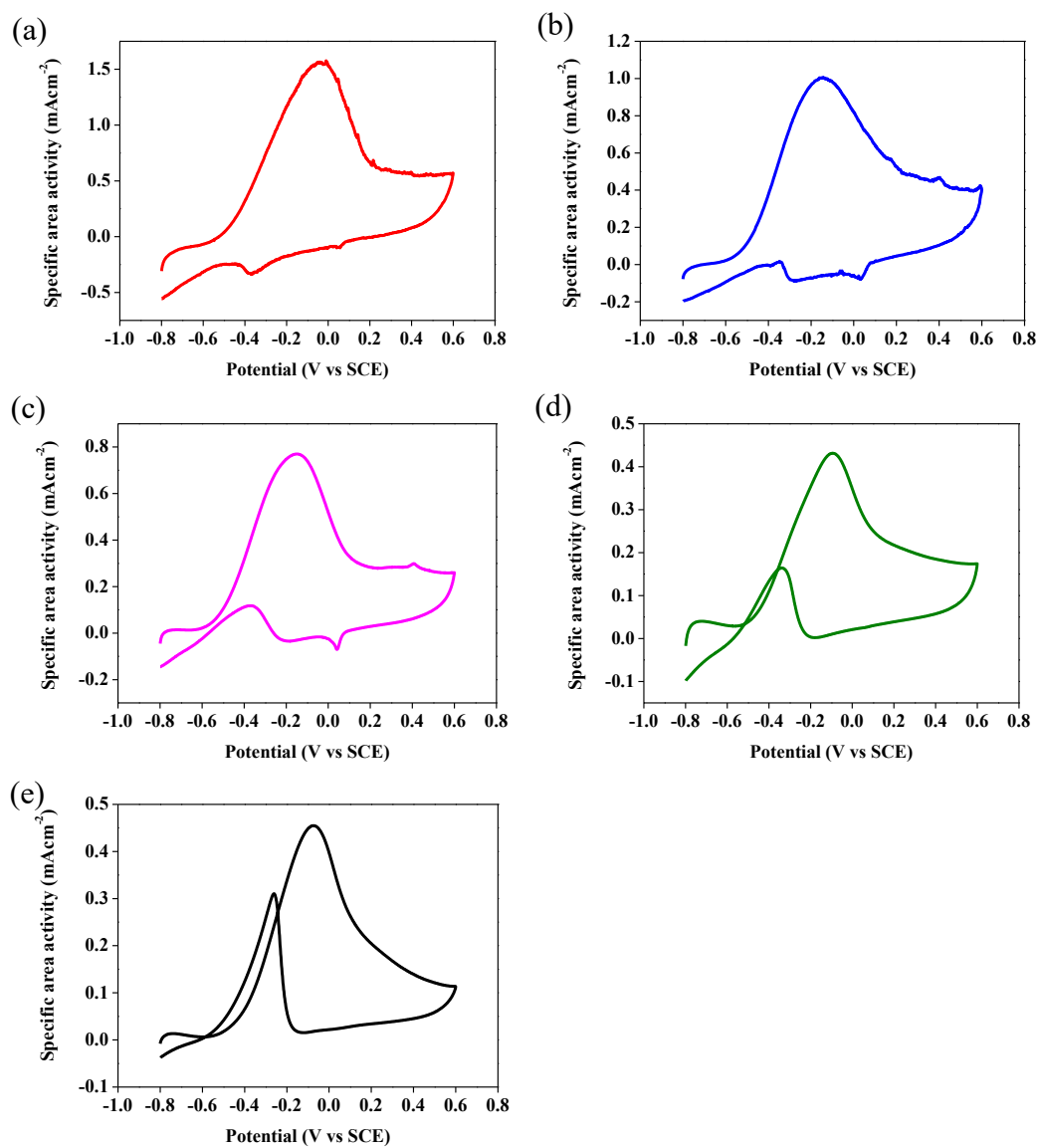


Figure 4.15 CVs of (a) PtAg-1 NWs, (b) PtAg-2 NWs, (c) PtAg-3 NWs, (d) PtAg-4 NWs and (e) Pt black composites in 0.1 M EtOH + 0.1 M NaOH solution. Scan rate, 50 mVs<sup>-1</sup>.

### **Chronoamperometric test of ethanol oxidation**

To explore the stability of the catalyst towards the oxidation of ethanol, chronoamperometric tests were conducted in 0.1 M EtOH + 0.1 M NaOH solution at a fixed potential of -0.3 V for 3600 s as shown in Figure 4.16.

Initially, the current densities drop rapidly because of the adsorption and desorption of intermediates during the oxidation of ethanol. The current densities then drop slowly because the intermediates accumulate and block the Pt active sites of the catalysts from the oxidation of ethanol.[29, 58]

As shown in Table 4.12, all the catalysts exhibit comparable current density retained after chronoamperometric test ranging from 11.2 % to 15.0 %, indicating comparable stability towards the oxidation of ethanol except PtAg-1 NWs composite (0.0 %). The lowest stability of PtAg-1 NWs composite is probably due to its high catalytic activity causing faster stability loss. This also implies that the alloying of Ag and Pt of the catalysts does not enhance their stability.

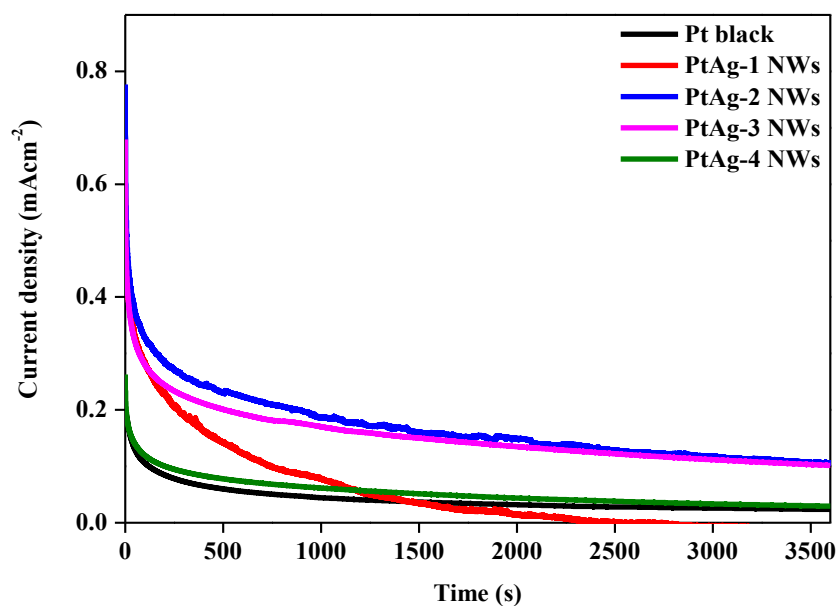


Figure 4.16 Chronoamperometric curves of PtAg NWs and Pt black composites in 0.1 M EtOH + 0.1 M NaOH solution at a fixed potential of -0.3 V for 3600 s.

Catalysts	Current density retained after 3600 s
	chronoamperometric test (%)
PtAg-1 NWs	0.0
PtAg-2 NWs	13.6
PtAg-3 NWs	15.0
PtAg-4 NWs	11.2
Pt black	13.4

Table 4.12 Summary of electrochemical performance of Pt black and PtAg NWs composites towards chronoamperometric test of ethanol oxidation.

#### 4.2.2.4 Electrooxidation of glycerol and its related chronoamperometric test

##### Electrooxidation of glycerol

Figure 4.17 displays the CVs of the catalysts towards the oxidation of glycerol in 0.1 M glycerol + 0.1 M NaOH solution in the potential region between -0.6V and 0.6 V with a scan rate of 50 mVs<sup>-1</sup>. It is known that Ag is not active towards the oxidation of glycerol.[60, 61] The specific area activity towards the oxidation of glycerol is calculated by normalizing the current to the ECSA of Pt in the catalysts.

The curves of the oxidation of glycerol show an oxidative peak in both forward and backward scans respectively. In forward scan, the oxidative peak at -0.1 V to 0.0 V is associated with the oxidation of glycerol molecules. In reverse scan, the oxidative peak at -0.3 V to 0.4 V is related to the removal of CO-like intermediate species. [36, 61]

Table 4.13 shows that the specific area activity towards the oxidation of glycerol of PtAg NWs composites. The order of PtAg-2 > PtAg-1 > PtAg-3 > PtAg-4 NWs composites in terms of peak current density is observed. This indicates that the specific area activity towards the oxidation of glycerol increases from 1.09 mAcm<sup>-2</sup> to 1.64 mAcm<sup>-2</sup> and then decreases from 1.64 mAcm<sup>-2</sup> to 0.67 mA<sup>-2</sup> with the increasing Pt-to-Ag surface ratio. The maximum enhancement of glycerol oxidation is achieved at Pt-to-Ag surface ratio of 1 : 6.2. Also, the specific area activities of all PtAg NWs composites are higher than that of Pt black composite indicating higher catalytic activity.

The Pt-to-Ag surface ratio increases from 1 : 8.0 for PtAg-1 NWs to 1 : 6.2 for

PtAg-2 NWs composite, suggesting that the increase of Pt active sites enhances the catalytic activity for glycerol oxidation. For PtAg-2 NWs, PtAg-3 NWs and PtAg-4 NWs composites, the Pt-to-Ag surface ratio increases from 1 : 6.2 to 1 : 3.5. The possible reason is that the increasing Pt composition may cause easy aggregation of Pt, which reduces the ECSA of Pt. This may decrease Pt utilization, which lowers the catalytic activity. For PtAg-4 NWs composite, high content of Pt make its catalytic behavior close to Pt black composite.[61]

It is also proposed that Ag has both promoting and inhibiting effects towards glycerol oxidation. Ag has stronger promoting effect when the Pt-to-Ag surface ratio decreases from 1 : 3.5 for PtAg-4 NWs to 1:6.2 for PtAg-2 NWs. Glycerol oxidation is a complex oxidation reaction, which generates multiple carbonyl intermediates. They adsorb and block the active sites of the catalysts. [62, 63] This requires more Ag to get rid of strong binding intermediates from the catalysts. Ag offer oxygen-containing species by forming Ag-OH<sub>ads</sub> and oxidize CO<sub>ads</sub> species from Pt active sites efficiently. The catalytic activity is enhanced by releasing more Pt active sites. However, the inhibiting effect of Ag becomes stronger when the Pt-to-Ag surface ratio decreases form 1 : 6.2 for PtAg-2 NWs to 1 : 8.0 for PtAg-1 NWs. Excessive adsorption of OH<sup>-</sup> ions onto catalyst may compete with glycerol molecules, resulting in a decreasing catalytic activity.[56]

Also, the PtAg NWs composites exhibit higher  $I_f/I_b$  ratio than Pt black composite suggesting that the PtAg NWs composites are more tolerant to CO<sub>ads</sub> species due to the alloy effect.

Catalysts	Specific area activity (mAcm <sup>-2</sup> )	I <sub>f</sub> /I <sub>b</sub>
PtAg-1 NWs	1.09	8.65
PtAg-2 NWs	1.64	4.00
PtAg-3 NWs	0.80	3.40
PtAg-4 NWs	0.67	2.58
Pt black	0.65	2.24

Table 4.13 Summary of electrochemical performance of PtAg NWs and Pt black composites towards the electrooxidation of glycerol.

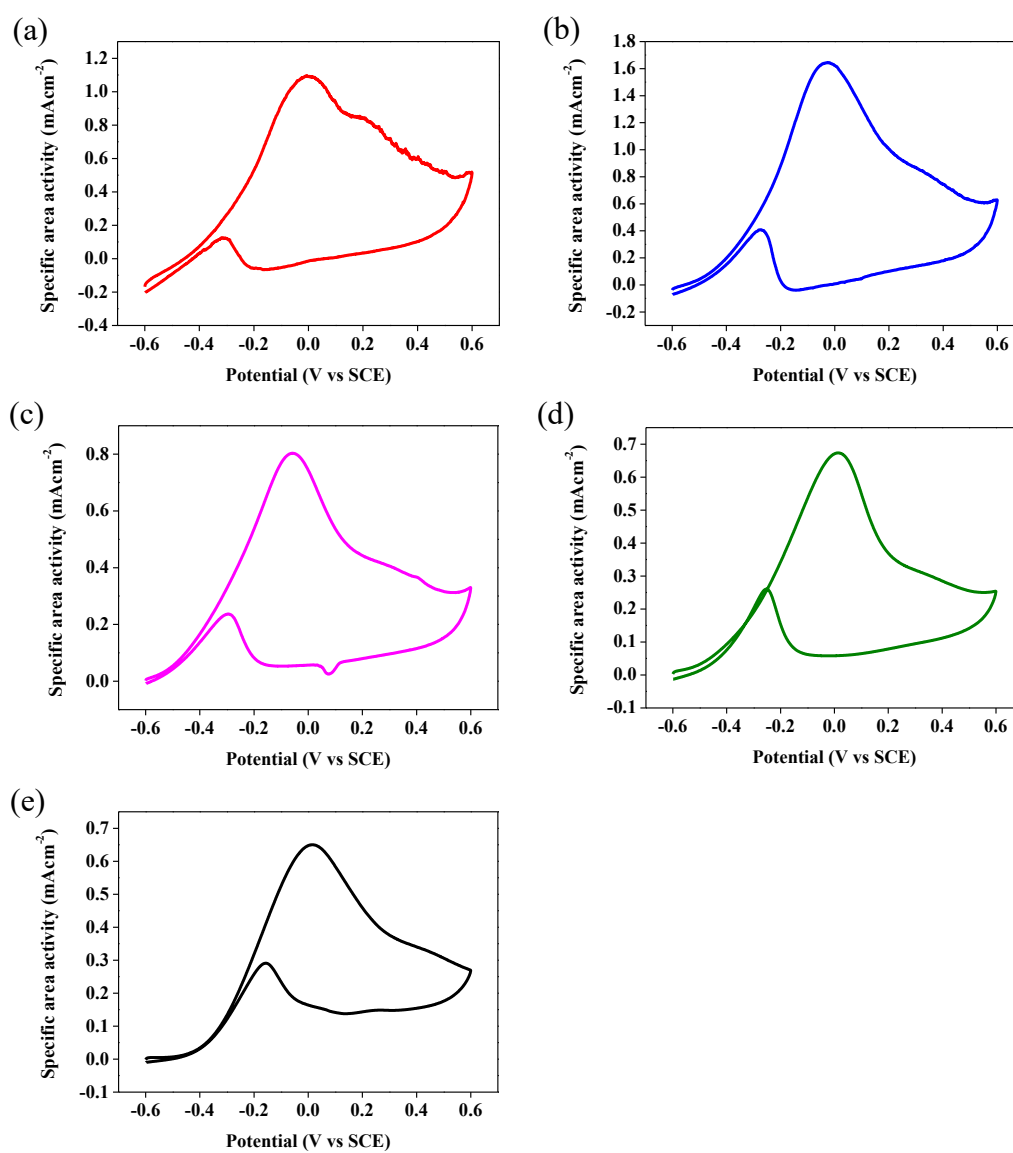


Figure 4.17 CVs of (a) PtAg-1 NWs, (b) PtAg-2 NWs, (c) PtAg-3 NWs, (d) PtAg-4 NWs and (e) Pt black composites in 0.1 M glycerol + 0.1 M NaOH solution. Scan rate,  $50 \text{ mVs}^{-1}$ .

### **Chronoamperometric test of glycerol oxidation**

Chronoamperometric tests were conducted to study the stability of the catalysts for the oxidation of glycerol. Figure 4.18 displays the chronoamperometric curves of the catalysts in 0.1 M glycerol + 0.1 M NaOH solution, by applying a fixed potential of -0.15 V.

Initially, the curves of current density drop rapidly owing to the generated poisonous intermediate species during the catalytic reactions. The curves of the current density then decrease gradually because the generated poisonous intermediates cover on the Pt active sites and hinder them from glycerol oxidation.[36, 60]

As shown in Table 4.14, the current density retained after chronoamperometric test of Pt black and PtAg-4 NWs composites are 6.6 % and 6.1 % respectively, indicating similar stability. Due to similar catalytic behavior between Pt black and PtAg-4 NWs composites, similar stability are achieved. Besides, their stability are slightly higher than those of PtAg-1, PtAg-2 and PtAg-3 NWs composites, which were 3.1 %, 3.5 % and 3.6 % respectively. Generally, PtAg NWs and Pt black composites exhibit low stability towards the oxidation of glycerol. This implies that the alloying of Ag and Pt of the catalysts does not enhance their stability.

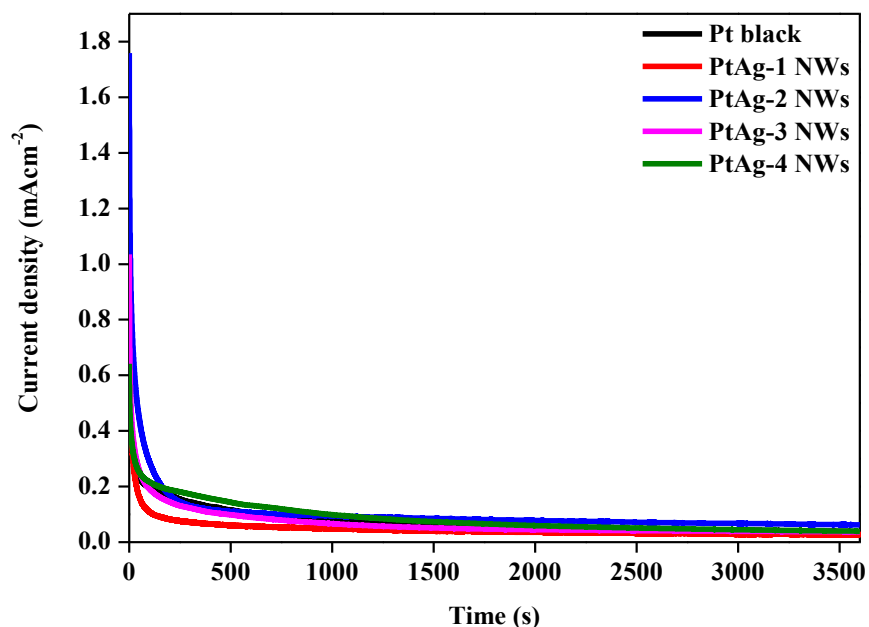


Figure 4.18 Chronoamperometric curves of PtAg NWs and Pt black composites in 0.1 M glycerol + 0.1 M NaOH solution at a fixed potential of -0.15 V for 3600 s.

Catalysts	Current density retained after 3600 s chronoamperometric test (%)
PtAg-1 NWs	3.1
PtAg-2 NWs	3.5
PtAg-3 NWs	3.6
PtAg-4 NWs	6.1
Pt black	6.6

Table 4.14 Summary of electrochemical performance of PtAg NWs and Pt black composites towards chronoamperometric test of glycerol oxidation.

#### 4.2.2.5 Electrooxidation of formic acid and its related chronoamperometric test

##### Electrooxidation of formic acid

Figure 4.19 displays the CVs of the catalysts towards the oxidation of formic acid (HCOOH) in 0.025M HCOOH + 0.1M H<sub>2</sub>SO<sub>4</sub> solution in the potential region between -0.2 V and 0.9 V with a scan rate of 50 mVs<sup>-1</sup>. It is believed that Ag is inactive towards the oxidation of formic acid. The specific area activity towards the oxidation of formic acid is calculated by normalizing the current to the ECSA of Pt in the catalysts.

In the forward scan, the oxidative peaks at 0.3 V to 0.4 V and 0.5 V to 0.6 V are related to the dehydrogenation and dehydration of formic acid oxidation respectively. In the backward scan, the oxidative peak at 0.2 V to 0.3 V is related to the oxidation of CO<sub>ads</sub> and other residual carbon species generated in forward scan.[37]

As shown in Table 4.15, all the PtAg NWs composites exhibit comparable specific area activity in both dehydrogenation and dehydration of formic acid oxidation but higher than Pt black composite. The existence of Ag may assist in eliminating CO and enhancing the oxidation of formic acid.[1, 64] However, the PtAg NWs composites with different Pt-to-Ag surface ratios do not show significant difference in the specific area activity towards formic acid oxidation.

Catalysts	Specific area activity	Specific area activity
	towards dehydrogenation (mAcm <sup>-2</sup> )	towards dehydration (mAcm <sup>-2</sup> )
PtAg-1 NWs	0.33	0.38
PtAg-2 NWs	0.37	0.35
PtAg-3 NWs	0.31	0.33
PtAg-4 NWs	0.34	0.37
Pt black	0.15	0.24

Table 4.15 Summary of electrochemical performance of PtAg NWs and Pt black composites towards the electrooxidation of formic acid.

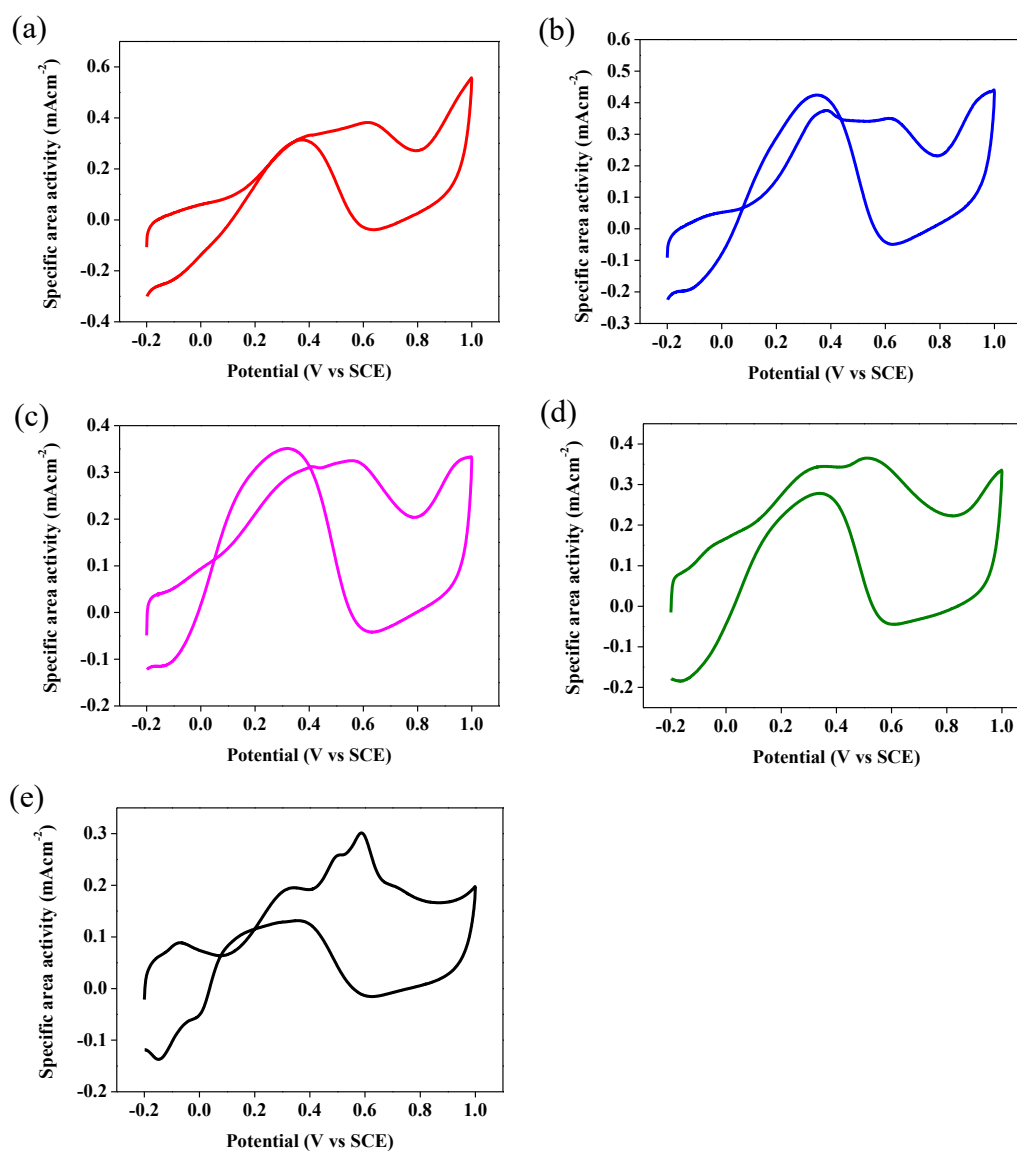


Figure 4.19 CVs of (a) PtAg-1 NWs, (b) PtAg-2 NWs, (c) PtAg-3 NWs, (d) PtAg-4 NWs and (e) Pt black composites in 0.025 M HCOOH + 0.1 M H<sub>2</sub>SO<sub>4</sub> solution. Scan rate, 50 mVs<sup>-1</sup>.

### **Chronoamperometric test of formic acid oxidation**

Chronoamperometric tests were conducted to study the stability of the catalysts for the oxidation of formic acid. Figure 4.20 displays the chronoamperometric curves of the catalysts in 0.025 M HCOOH + 0.1 M H<sub>2</sub>SO<sub>4</sub> solution, by applying a fixed potential of 0.2 V.

Initially, the current density decreases fast because intermediate species were formed during the catalytic reactions. The curves of the current density then decrease slowly because the generated intermediates species may accumulate on the Pt active sites and block them from the oxidation of formic acid.[1]

As shown in Table 4.16, the current density retained after chronoamperometric test of PtAg NWs composites ranging from 2.8 % to 12.9 %, are lower than that of Pt black composite, indicating poor stability towards the oxidation of formic acid. That implies that the alloying of Ag and Pt of the catalysts does not enhance their stability.

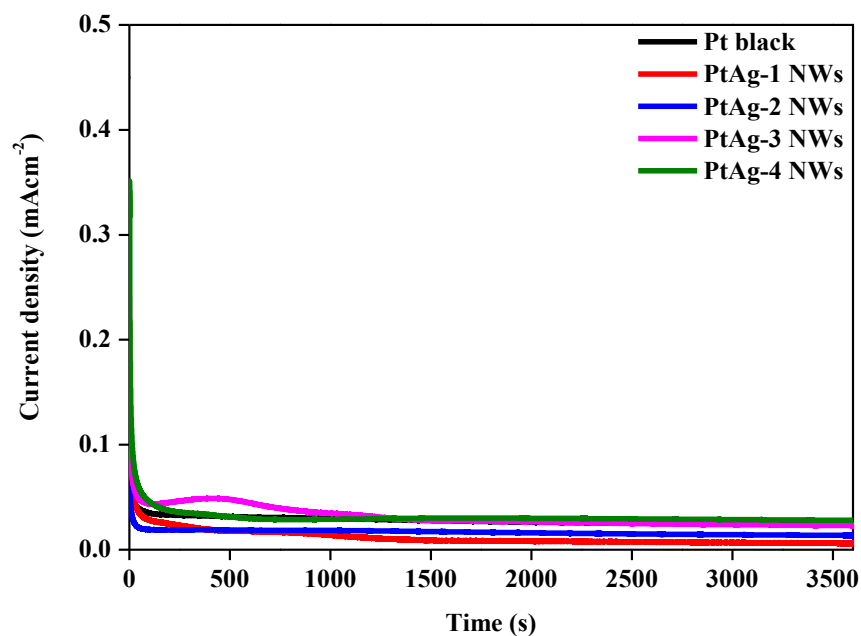


Figure 4.20 Chronoamperometric curves of PtAg NWs and Pt black composites in 0.025 M HCOOH + 0.1 M H<sub>2</sub>SO<sub>4</sub> solution at a fixed potential of 0.2 V for 3600 s.

Catalysts	Current density retained after 3600 s chronoamperometric test (%)
PtAg-1 NWs	2.8
PtAg-2 NWs	12.9
PtAg-3 NWs	9.5
PtAg-4 NWs	8.2
Pt black	24.5

Table 4.16 Summary of electrochemical performance of PtAg NWs and Pt black composites towards chronoamperometric test of formic acid oxidation.

### 4.3 Summary

AgNWs composite was successfully synthesized and used as a sacrificial template for synthesizing hollow PtAg NWs through the galvanic replacement reaction. Their electrocatalytic activities towards methanol, ethanol, glycerol and formic acid oxidations were studied.

1. AgNWs composite was successfully synthesized with  $\text{AgNO}_3$  as a metal precursor, PVP as a surfactant and EG as a reducing agent at  $170\text{ }^\circ\text{C}$ .
2. Hollow PtAg NWs composites were successfully synthesized in the galvanic replacement reaction between AgNWs as sacrificial template and  $\text{K}_2\text{PtCl}_4$  as metal precursor at  $30\text{ }^\circ\text{C}$ . The alloying of Ag and Pt was confirmed by XRD and XPS analysis. It is also discovered that varying the volumes of  $\text{K}_2\text{PtCl}_4$  solution could control the Pt-to-Ag atomic ratio and surface ratio as shown by EDX and XPS analyses respectively but not the shell thickness of PtAg NWs composites as shown by TEM analysis.
3. Electrocatalytic studies show that the PtAg NWs composites with specific Pt-to-Ag surface ratio exhibit enhanced catalytic activity and higher poison tolerance but poor stability towards the oxidations of methanol, ethanol and glycerol when compared with Pt black composite. Also, the catalytic activity does not change significantly towards the oxidation of formic acid at different Pt-to-Ag surface ratios. The fine adjustment of Pt-to-Ag surface ratio is vital for the oxidations of different alcohols.

## REFERENCES

- [1] F. Zheng, S.-Y. Luk, T.-L. Kwong, K.-F. Yung, *RSC Advances*, 6 (2016) 44902-44907.
- [2] H.-P. Liang, H.-M. Zhang, J.-S. Hu, Y.-G. Guo, L.-J. Wan, C.-L. Bai, *Angewandte Chemie*, 116 (2004) 1566-1569.
- [3] B. Liu, H.Y. Li, L. Die, X.H. Zhang, Z. Fan, J.H. Chen, *Journal of Power Sources*, 186 (2009) 62-66.
- [4] J. Yuanyuan, L. Yizhong, H. Dongxue, Z. Qixian, N. Li, *Nanotechnology*, 23 (2012) 105609.
- [5] S.O. Obare, N.R. Jana, C.J. Murphy, *Nano Letters*, 1 (2001) 601-603.
- [6] J.J. Teo, Y. Chang, H.C. Zeng, *Langmuir*, 22 (2006) 7369-7377.
- [7] G. Chen, C. Xu, X. Song, S. Xu, Y. Ding, S. Sun, *Crystal Growth & Design*, 8 (2008) 4449-4453.
- [8] Y. Xu, X. Jiao, D. Chen, *The Journal of Physical Chemistry C*, 112 (2008) 16769-16773.
- [9] W. Wang, T. Yang, G. Yan, H. Li, *Materials Letters*, 82 (2012) 237-239.
- [10] X. Zhang, W. Qin, D. Li, D. Yan, B. Hu, Z. Sun, L. Pan, *Chemical Communications*, 51 (2015) 16413-16416.
- [11] X. Zhou, Y. Gan, J. Du, D. Tian, R. Zhang, C. Yang, Z. Dai, *Journal of Power Sources*, 232 (2013) 310-322.
- [12] H.M. Chen, R.-S. Liu, M.-Y. Lo, S.-C. Chang, L.-D. Tsai, Y.-M. Peng, J.-F. Lee, *The Journal of Physical Chemistry C*, 112 (2008) 7522-7526.
- [13] H. Zhu, J. Wang, G. Xu, *Crystal Growth & Design*, 9 (2009) 633-638.
- [14] C. Li, Y. Liu, L. Li, Z. Du, S. Xu, M. Zhang, X. Yin, T. Wang, *Talanta*, 77 (2008) 455-459.
- [15] Y. Chen, H. Chen, D. Zeng, Y. Tian, F. Chen, J. Feng, J. Shi, *ACS Nano*, 4

(2010) 6001-6013.

[16] J. Chen, F. Saeki, B.J. Wiley, H. Cang, M.J. Cobb, Z.-Y. Li, L. Au, H. Zhang, M.B. Kimmey, Li, Y. Xia, *Nano Letters*, 5 (2005) 473-477.

[17] J.Z. Zhang, *The Journal of Physical Chemistry Letters*, 1 (2010) 686-695.

[18] X.W. Lou, Y. Wang, C. Yuan, J.Y. Lee, L.A. Archer, *Advanced Materials*, 18 (2006) 2325-2329.

[19] J.B. Fei, Y. Cui, X.H. Yan, W. Qi, Y. Yang, K.W. Wang, Q. He, J.B. Li, *Advanced Materials*, 20 (2008) 452-456.

[20] X. Wang, J. Feng, Y. Bai, Q. Zhang, Y. Yin, *Chemical Reviews*, 116 (2016) 10983-11060.

[21] Q. Zhang, W. Wang, J. Goebel, Y. Yin, *Nano Today*, 4 (2009) 494-507.

[22] Y. Yang, Y. Chu, Y. Zhang, F. Yang, J. Liu, *Journal of Solid State Chemistry*, 179 (2006) 470-475.

[23] H. Atae-Esfahani, Y. Nemoto, L. Wang, Y. Yamauchi, *Chemical Communications*, 47 (2011) 3885-3887.

[24] S. Cheng, D. Yan, J.T. Chen, R.F. Zhuo, J.J. Feng, H.J. Li, H.T. Feng, P.X. Yan, *The Journal of Physical Chemistry C*, 113 (2009) 13630-13635.

[25] A.M. Collins, C. Spickermann, S. Mann, *Journal of Materials Chemistry*, 13 (2003) 1112-1114.

[26] X. Xia, Y. Wang, A. Ruditskiy, Y. Xia, *Advanced Materials*, 25 (2013) 6313-6333.

[27] Y. Sun, Y. Xia, *Science*, 298 (2002) 2176-2179.

[28] Q. Zhang, J.Y. Lee, J. Yang, C. Boothroyd, J. Zhang, *Nanotechnology*, 18 (2007) 245605.

[29] S.T. Nguyen, H.M. Law, H.T. Nguyen, N. Kristian, S. Wang, S.H. Chan, X. Wang, *Applied Catalysis B: Environmental*, 91 (2009) 507-515.

- [30] X. Gu, C. Wang, L. Yang, C. Yang, *Journal of Nanoscience and Nanotechnology*, 17 (2017) 2843-2847.
- [31] T. Miao, Y. Song, C. Bi, H. Xia, D. Wang, X. Tao, *The Journal of Physical Chemistry C*, 119 (2015) 18434-18443.
- [32] L. Zhuang, W. Wang, F. Hong, S. Yang, H. You, J. Fang, B. Ding, *Journal of Solid State Chemistry*, 191 (2012) 239-245.
- [33] C. Fang, J. Zhao, G. Zhao, L. Kuai, B. Geng, *Nanoscale*, 8 (2016) 14971-14978.
- [34] Y.-Y. Feng, L.-X. Bi, Z.-H. Liu, D.-S. Kong, Z.-Y. Yu, *Journal of catalysis*, 290 (2012) 18-25.
- [35] Y. Kim, H. Kim, W.B. Kim, *Electrochemistry Communications*, 46 (2014) 36-39.
- [36] X. Weng, Q. Liu, A.-J. Wang, J. Yuan, J.-J. Feng, *Journal of Colloid and Interface Science*, (2017).
- [37] J.-J. Lv, S.-S. Li, J.-N. Zheng, A.-J. Wang, J.-R. Chen, J.-J. Feng, *International Journal of Hydrogen Energy*, 39 (2014) 3211-3218.
- [38] Y. Sun, Y. Xia, *Advanced Materials*, 14 (2002) 833-837.
- [39] G.W. Sławiński, F.P. Zamborini, *Langmuir*, 23 (2007) 10357-10365.
- [40] C.M. Copley, S.E. Skrabalak, D.J. Campbell, Y. Xia, *Plasmonics*, 4 (2009) 171-179.
- [41] Y. Jiang, Y. Lu, D. Han, Q. Zhang, L. Niu, *Nanotechnology*, 23 (2012) 105609.
- [42] C. Xu, Y. Liu, F. Su, A. Liu, H. Qiu, *Biosensors and Bioelectronics*, 27 (2011) 160-166.
- [43] Z. Peng, H. Yang, *Journal of Solid State Chemistry*, 181 (2008) 1546-1551.
- [44] J. Zeng, J. Yang, J.Y. Lee, W. Zhou, *The Journal of Physical Chemistry B*,

110 (2006) 24606-24611.

[45] W. Hong, C. Shang, J. Wang, E. Wang, *Energy & Environmental Science*, 8 (2015) 2910-2915.

[46] I.M. Al-Akraa, A.M. Mohammad, M.S. El-Deab, B.E. El-Anadouli, *International Journal of Hydrogen Energy*, 40 (2015) 1789-1794.

[47] J. Xu, T. Zhao, Z. Liang, *The Journal of Physical Chemistry C*, 112 (2008) 17362-17367.

[48] S. Yu, Q. Lou, K. Han, Z. Wang, H. Zhu, *International journal of hydrogen energy*, 37 (2012) 13365-13370.

[49] J. Zhao, A. Manthiram, *Applied Catalysis B: Environmental*, 101 (2011) 660-668.

[50] P.N. Ross, *Surface Science*, 102 (1981) 463-485.

[51] S. Kim, C. Jung, J. Kim, C.K. Rhee, S.-M. Choi, T.-H. Lim, *Langmuir*, 26 (2010) 4497-4505.

[52] K. Friedrich, F. Henglein, U. Stimming, W. Unkauf, *Electrochimica acta*, 45 (2000) 3283-3293.

[53] C. Li, Y. Yamauchi, *Physical Chemistry Chemical Physics*, 15 (2013) 3490-3496.

[54] Y. Li, L. Tang, J. Li, *Electrochemistry Communications*, 11 (2009) 846-849.

[55] L. Feng, G. Gao, P. Huang, X. Wang, C. Zhang, J. Zhang, S. Guo, D. Cui, *Nanoscale research letters*, 6 (2011) 551.

[56] C. Jin, X. Ma, J. Zhang, Q. Huo, R. Dong, *Electrochimica Acta*, 146 (2014) 533-537.

[57] G. Yang, Y. Zhou, H.-B. Pan, C. Zhu, S. Fu, C.M. Wai, D. Du, J.-J. Zhu, Y. Lin, *Ultrasonics sonochemistry*, 28 (2016) 192-198.

[58] Y.-Y. Feng, Z.-H. Liu, W.-Q. Kong, Q.-Y. Yin, L.-X. Du, *International*

Journal of Hydrogen Energy, 39 (2014) 2497-2504.

[59] C. Jin, J. Zhang, Q. Huo, R. Dong, Journal of Electroanalytical Chemistry, 736 (2015) 112-116.

[60] B.T.X. Lam, M. Chiku, E. Higuchi, H. Inoue, Advances in Nanoparticles, 5 (2016) 167.

[61] C. Jin, Z. Zhang, Z. Chen, Q. Chen, Int. J. Electrochem. Sci, 8 (2013) 4215-4224.

[62] S. Carrettin, P. McMorn, P. Johnston, K. Griffin, C.J. Kiely, G.J. Hutchings, Physical Chemistry Chemical Physics, 5 (2003) 1329-1336.

[63] A. Falase, M. Main, K. Garcia, A. Serov, C. Lau, P. Atanassov, Electrochimica Acta, 66 (2012) 295-301.

[64] X. Jiang, X. Yan, W. Ren, Y. Jia, J. Chen, D. Sun, L. Xu, Y. Tang, ACS Applied Materials & Interfaces, 8 (2016) 31076-31082.

## Chapter 5

### Conclusions

Pt and Pt-based electrocatalysts are widely used in direct liquid fuel cells. However, the high cost and limited reserve of Pt constrains its massive applications. Our ultimate goal is to develop low-Pt-content catalysts with improved Pt utilization and enhanced catalytic activity.

Platinum-gold core-shell (AuNP@Pt) nanostructures supported on MWCNTs composites were prepared by Pt halide ion adsorption onto AuNPs surface, followed by *in-situ* electrochemical reduction. AuNP/CNTs composite, with the Au loading of 16.2 % and size of  $5.4 \pm 2.0$  nm, was synthesized as a template for depositing Pt. Both TEM and XRD analyses suggest that the AuNPs are adopting a fcc structure. Electrochemical investigations suggest that different Pt halide solutions show different halide ion adsorption affinity and different electrocatalytic activity towards the oxidations of formic acid and methanol. Pt coverage can be controlled by varying the concentrations of  $[\text{PtX}_4]^{2-}$  ion and  $\text{Pt}(\text{NH}_3)_4(\text{NO}_3)_2$  solutions but not  $[\text{PtX}_6]^{2-}$  ion solution, and the immersion time with the concentrations of  $[\text{PtX}_4]^{2-}$  ion and  $\text{Pt}(\text{NH}_3)_4(\text{NO}_3)_2$  solutions of 5.12 mM. The electrocatalytic studies show that the direct oxidation of formic acid occurs on the AuNP@Pt/CNTs composite with low Pt coverage of lower than 30 %. Indirect oxidation of formic acid and oxidation of methanol start occurring on the AuNP@Pt/CNTs composite prepared by  $[\text{PtCl}_4]^{2-}$  ion solution with Pt coverage of higher than 30 % and prepared by  $[\text{PtBr}_4]^{2-}$  ion solution with Pt coverage of higher than 80 %. The utilization of Pt and its fuel selectivity are enhanced by

simply controlling Pt halide solutions, concentrations and immersion time to synthesize the AuNP@Pt/CNTs with different Pt coverages.

Pd@PdPt/CNTs alloy and Pt@Pd/CNTs phase-separate composites were successfully developed from the surfactant-free monometallic Pd/CNTs and Pt/CNTs composites respectively. Pd/CNTs composite was synthesized by hydrolysis of  $[\text{PdCl}_4]^{2-}$  ions on MWCNTs, followed by  $\text{H}_2$  reduction while Pt/CNTs composite was synthesized by the reduction of  $[\text{PtCl}_4]^{2-}$  ions to Pt due to the electron transfer from MWCNTs. Since Pd/CNTs and Pt/CNTs composites were synthesized without any introduction of organic surfactants, their clean metal surfaces were modified to form alloy and phase-separate PdPt shells respectively. The PdPt shell of Pd@PdPt/CNTs composites were synthesized by the galvanic replacement reaction between Pd and  $[\text{PtCl}_4]^{2-}$  ions while that of Pt@Pd/CNTs composites were prepared by adsorption of  $[\text{PdCl}_4]^{2-}$  ions onto Pt surface, followed by  $\text{H}_2$  reduction to Pd metal. XRD analysis shows that both Pd@PdPt/CNTs and Pt@Pd/CNTs composites adopt a fcc structure. XPS analysis also confirms the formation of PdPt alloy structure. As revealed by electrocatalytic studies, the Pd@PdPt/CNTs alloy and Pt@Pd/CNTs phase-separate composites with particular Pd-to-Pt surface ratio exhibit enhanced catalytic activity towards the oxidations of ethanol and glycerol when compared to monometallic Pd/CNTs and Pt/CNTs composites.

Hollow PtAg NWs composites were synthesized under the galvanic replacement reaction between AgNWs as sacrificial template and  $\text{K}_2\text{PtCl}_4$  as metal precursor. AgNWs composite was synthesized with  $\text{AgNO}_3$  as a metal precursor, PVP as a

surfactant and EG as a reducing agent at 170 °C. It is found that varying the volumes of  $K_2PtCl_4$  solution could control the Pt-to-Ag atomic ratio and surface ratio as studied by EDX and XPS analyses respectively. Also, both XRD and XPS analyses confirm the formation of PtAg alloy in hollow PtAg NWs. Electrochemical investigations show that the hollow PtAg NWs composites with specific Pt-to-Ag surface ratio exhibit enhanced catalytic activity towards the oxidations of methanol, ethanol, glycerol and formic acid when compared with Pt black composite.

In my research, bimetallic Pt-based catalysts were explored. Trimetallic Pt-based catalysts will be further researched for the electrocatalysis of direct liquids oxidations.

## Chapter 6

### Experimental Section

#### 6.1 General Section

##### 6.1.1 Materials

Multi-walled carbon nanotubes (MWCNTs) was purchased from Fortune. Ethylene glycol (EG,  $(\text{CH}_2\text{OH})_2$ , purity 95 %) and glycerol (purity 99+ %) were purchased from Acros Organics. Methanol (MeOH) was purchased from Anaqua Chemicals Supply. Sulfuric acid ( $\text{H}_2\text{SO}_4$ ) was purchased from Arkonic Scientific. Acetone ( $\text{CH}_3\text{COCH}_3$ ) was purchased from Duksan Pure Chemicals. Conc. nitric acid ( $\text{HNO}_3$ , purity 65 %) and conc. hydrochloric acid (HCl, purity 37 %) were purchased from Fisher Chemical. Gold(III) chloride trihydrate ( $\text{HAuCl}_4 \cdot 3\text{H}_2\text{O}$ ), sodium citrate ( $\text{Na}_3\text{C}_6\text{H}_5\text{O}_7$ ), sodium borohydride ( $\text{NaBH}_4$ ), potassium tetrachloroplatinate(II) ( $\text{K}_2\text{PtCl}_4$ , purity 98 %), potassium hexachloroplatinate(IV) ( $\text{K}_2\text{PtCl}_6$ , purity 99.9 %), tetraammineplatinum(II) nitrate ( $\text{Pt}(\text{NH}_3)_4(\text{NO}_3)_2$ ), potassium tetrachloropalladate(II) ( $\text{K}_2\text{PdCl}_4$ , purity 98 %), polyvinylpyrrolidone (PVP,  $M_w = 40,000$ ), Nafion and formic acid ( $\text{HCOOH}$ , purity >88 %) were purchased from Sigma Aldrich. Sodium tetrachloroplatinate(II) hydrate ( $\text{Na}_2\text{PtCl}_4$ ), sodium hexachloroplatinate(IV) hexahydrate ( $\text{Na}_2\text{PtCl}_6 \cdot 6\text{H}_2\text{O}$ ), potassium tetrabromoplatinate(II) ( $\text{K}_2\text{PtBr}_4$ ) and potassium hexabromoplatinate(IV) ( $\text{K}_2\text{PtBr}_6$ ) were purchased from Strem Chemicals. Silver nitrate ( $\text{AgNO}_3$ ), ammonium hydroxide ( $\text{NH}_4\text{OH}$ , purity 35 %) and sodium hydroxide ( $\text{NaOH}$ ) were purchased from UNI-CHEM. Ethanol (EtOH) was purchased from VWR Chemicals.

## **6.1.2 Physical characterization techniques**

### UV-Vis spectroscopy

UV-vis spectroscopy is commonly used to characterize the surface plasmon resonance (SPR) of the samples.[1, 2] The samples diluted with water were measured for UV-Vis spectroscopic analysis on a HEWLETT PACKARD Spectrometer.

### Inductively coupled plasma optical emission spectroscopy

Inductively coupled plasma optical emission spectroscopy (ICP-OES) is used to analyze the metal loadings on supports. Sample solution is first pumped into nebulizer. Nebulizer converts sample solution into mist. ICP atomizes the metal compounds into gaseous atoms and excites them from ground state to excited state. The excited metal atoms return to ground state and emit light. Wavelength selector selects emitted light. Detector finally measures the intensity of emitted light. The intensity of emitted light is compared with that of elements of known concentration. The metal loadings of samples were analyzed by ICP-OES on a Agilent Technologies 700 Series ICP-OES. The samples were digested by conc. HNO<sub>3</sub> (250  $\mu$ L) and conc. HCl (750  $\mu$ L). The mixture was diluted to 10 mL with water. The diluted sample (1 mL) was further diluted to 25 mL with 1000 ppm indium solution (125  $\mu$ L) and 1 % HNO<sub>3</sub> solution.

### Powder X-ray diffraction

Powder X-ray diffraction (XRD) is used to investigate the crystal structure of the samples. It is also used to identify the crystal planes and estimate the crystalline size. X-ray is directed on to the sample and interacts with the sample. The X-rays are diffracted off the atoms that form various crystal planes. The diffracted

X-rays are detected and processed. After that, they are converted to count rate which is displayed in XRD patterns. The samples were measured by XRD on a Rigaku SmartLab X-ray diffractometer using Cu K $\alpha$  radiation ( $\lambda = 1.54056 \text{ \AA}$ , 45 kV, 200 mA) with scattering angles ( $2\theta$ ) ranging from  $20^\circ$  to  $90^\circ$  with a step width  $0.02^\circ$  in a scanning rate of  $2.5^\circ \text{ min}^{-1}$ . The crystalline sizes could be calculated by Debye-Scherrer's equation (Eq. 6.1).

$$D = \frac{K\lambda}{B\cos\theta} \quad \text{Eq. 6.1}$$

where D is crystalline size, K is Scherrer constant,  $\lambda$  is X-ray wavelength, B is full width at half maximum (FWHM) and  $\theta$  is Bragg angle.

#### Transmission electron microscopy

To study the morphology of the samples, transmission electron microscopy (TEM) is used. The filament is connected a high-voltage source (around 200 kV) and emits electrons into vacuum. Vacuum system prevents the collisions between the electrons and other gas atoms and reduces energy loss. The lenses focus the electron beam and guide them to the sample. The electrons transmit through and interact with the sample. The projector lenses expand the beam and project the image onto an imaging device. The samples were dispersed in ethanol and dropped on copper grids for TEM analysis on a Field Emission Electron Microscope STEM (JEOL Model JEM-2100F).

#### Selected area electron diffraction

To study the crystalline structure of the sample, selected area electron diffraction (SAED) is adopted. The electron beam is directed to the specific area of the sample. The specific area is selected by an aperture. The crystal planes in the

samples act as diffraction gratings to diffract the electrons. The image with many spot which is SAED pattern is projected onto the screen.

#### Energy dispersive X-ray spectroscopy

To analyze the elemental composition, energy dispersive X-ray spectroscopy (EDX) is used. The incoming electron with high energy excites and ejects an electron from inner electron shell, resulting in a vacancy. An electron at higher energy electron shell falls down and fills the vacancy. Owing to the energy difference between higher and lower energy shell, energy is released in the form of X-ray which is measured by an energy-dispersive spectrometer. The samples were dispersed in ethanol and dropped on copper grids for EDX analysis on a Field Emission Electron Microscope STEM (JEOL Model JEM-2100F).

#### X-ray photoelectron spectroscopy

To study the surface composition and valence states of the samples, X-ray photoelectron spectroscopy (XPS) is used. X-rays excite the atoms and electrons eject out. Each element produces a characteristic set of XPS peaks at characteristic binding energy values. The surface oxidation states of each element of the composites were analyzed by a Axis Ultra DLD XPS using monochromatic AlK $\alpha$  radiation of 1486.6 eV with an electron take off angle at 90° under the pressure in the sample chamber of 10<sup>-8</sup> Torr.

## 6.2 Experimental Catalysts Preparation

### 6.2.1 Catalysts preparation for Chapter 2

#### Functionalization of multi-walled carbon nanotubes (MWCTs)

MWCNTs (100 mg) was refluxed in conc. HNO<sub>3</sub> (100 mL) under 80 °C for 16 h. The acid-treated MWCNTs was centrifuged and washed until pH value of around 6 was achieved. The acid-treated MWCNTs was dried under 60 °C for 16 h.

#### Preparation of AuNPs

1 % HAuCl<sub>4</sub>·3H<sub>2</sub>O (85 μL), EG (70 μL) and 0.1 M sodium citrate (250 μL) were added into water (100 mL) in a round-bottom flask. 0.1 M NaBH<sub>4</sub> solution (85 μL) was added dropwise into the mixture under stirring. The mixture was stirred for 5 min, resulting in a pale pink AuNPs solution.

#### Preparation of AuNP/CNTs composite

Acid-treated MWCNTs (2.0 mg) was added into the AuNPs solution and the mixture was sonicated for 30 min. Sodium citrate (0.2955 g) was added to the mixture under stirring and stirred for 3 h. The mixture was centrifuged and washed with water three times. The AuNP/CNTs composite was dried under 60 °C for 16 h.

#### Preparation of AuNP@Pt/CNTs composite

AuNP@Pt/CNTs composites were prepared by immersing the GCE with coated AuNP/CNTs composite into Pt halide solutions (K<sub>2</sub>PtCl<sub>4</sub>, K<sub>2</sub>PtCl<sub>6</sub>, Na<sub>2</sub>PtCl<sub>4</sub>, Na<sub>2</sub>PtCl<sub>6</sub>·6H<sub>2</sub>O, K<sub>2</sub>PtBr<sub>4</sub>, K<sub>2</sub>PtBr<sub>6</sub>, Pt(NH<sub>3</sub>)<sub>4</sub>(NO<sub>3</sub>)<sub>2</sub>) followed by *in-situ* electrochemical reduction.

## 6.2.2 Catalysts preparation for Chapter 3

### Preparation of Pd/CNTs composite

Acid-treated MWCNTs (4.0 mg) was sonicated in water (100 mL) for 30 min.  $K_2PdCl_4$  (0.0020 g) was added into the mixture and stirred for 2 h under 60 °C. The mixture was centrifuged and washed with water three times, resulting in PdO/CNTs composite. The PdO/CNTs composite was dispersed in water (100 mL) and stirred for 2 h under 60 °C with  $H_2$  purge. The mixture was centrifuged and washed with three times, and dried under 60 °C for 16 h, resulting in Pd/CNTs composite.

### Preparation of Pt/CNTs composite

Acid-treated MWCNTs (4.0 mg) was sonicated in water (100 mL) for 30 min.  $K_2PtCl_4$  (0.0016 g) was added into the mixture and stirred for 2 h under 90 °C. The mixture was centrifuged and washed with water three times, and dried under 60 °C for 16 h to obtain Pt/CNTs composite.

### Preparation of Pd@PdPt/CNTs composites

Pd/CNTs composite (2 mg) was sonicated in 0.01 M  $H_2SO_4$  solution (20 mL) for 30 min. Different amounts of  $K_2PtCl_4$  (83.0 mg and 8.3 mg) were added into the mixture and stirred for 1 h under 90 °C to obtain Pd@PdPt/CNTs composites (labelled as Pd@PdPt/CNTs-1 and Pd@PdPt/CNTs-2 respectively). The mixture was centrifuged and washed with water three times, and dried under 60 °C for 16 h to obtain Pd@PdPt/CNTs composites.

### Preparation of Pt@Pd/CNTs composites

Pt/CNTs composite (2 mg) was sonicated in 0.1 M  $H_2SO_4$  solution (20 mL) for

30 min.  $K_2PdCl_4$  (0.2000 g) was added into the mixture and stirred for 1 h at room temperature. The mixture was centrifuged and washed with water three times. The mixture was dispersed in water (20 mL) and stirred for 2 h at room temperature with  $H_2$  purge, resulting in Pt@Pd/CNTs composite (labelled as Pt@Pd/CNTs-1). The mixture was centrifuged and washed with water three times, and dried under 60 °C for 16 h, resulting in Pt@Pd/CNTs composites.

Pt@Pd/CNTs-2 and Pt@Pd/CNTs-3 composites were prepared under the same procedures by using Pt@Pd/CNTs-1 and Pt@Pd/CNTs-2 composites respectively, instead of Pd/CNTs composite.

### 6.2.3 Catalysts preparation for Chapter 4

#### Preparation of silver nanowires (AgNWs)

In a typical synthesis, PVP (0.0889 g) and EG (5 mL) were prepared and heated for 10 min at 170 °C. 0.08 M AgNO<sub>3</sub> in EG solution (2.5 mL) was added dropwise into the mixture by an injection pump (KDS-200, Stoelting Co., Wood Dale, IL) at a rate of 0.0025 mLs<sup>-1</sup>. After injection, the reaction mixture was further heated at 170 °C for 2 h, resulting in a greyish white AgNWs solution.

#### Preparation of PtAg nanowires (PtAg NWs)

The PtAg NWs with different Pt-to-Ag nominal ratios of 1 : 8, 1 : 4, 1 : 2 and 1 : 1 were prepared by cooling the AgNWs solution to 30 °C, followed by the dropwise addition of 80 mM K<sub>2</sub>PtCl<sub>4</sub> solution (313 μL, 625 μL, 1.250 mL and 2.5 mL; labelled as PtAg-1, PtAg-2, PtAg-3, PtAg-4) and heated for 1 h, resulting in black PtAg NWs solution. The final solution was washed by acetone and water several times through centrifugation. It was then washed with NH<sub>4</sub>OH (3 mL) and water to remove AgCl, followed by washing with 5 M HNO<sub>3</sub> (3 mL) and water to remove unreacted silver. The final product was dried at 60 °C for 16 h, resulting in black PtAg NWs solid powder.

### **6.3 Electrochemical Characterizations and Electrocatalytic Studies**

The electrochemical measurements were conducted on a CHI660D electrochemical working station with a standard three-electrode system consisting of a glassy carbon electrode (GCE) (5 mm in diameter) as a working electrode, a platinum strip as a counter electrode and a saturated calomel electrode (SCE) as a reference electrode. The GCE was polished with 0.3  $\mu\text{m}$  and 0.05  $\mu\text{m}$  alumina powder, followed by washing with water. The catalyst was dispersed in solvent and a portion of the mixture was pipetted and dropped on the GCE. The GCE coated with catalysts was dried in vacuum overnight.

### 6.3.1 Electrochemical characterizations and electrocatalytic studies for Chapter 2

AuNP/CNTs composite (1 mg) was dispersed in ethanol (250  $\mu\text{L}$ ). A portion of the mixture (10  $\mu\text{L}$ ) was pipetted and dropped on the GCE and dried in vacuum overnight.

#### Cyclic voltammetry in sulfuric acid

The cyclic voltammetry (CV) measurement of AuNP/CNTs composite was conducted at room temperature and in  $\text{N}_2$ -purged 0.1 M  $\text{H}_2\text{SO}_4$  solution in the potential range between -0.24 V and 1.5 V at a scan rate of  $50 \text{ mVs}^{-1}$ .

#### Preparation of AuNP@Pt/CNTs composites

The AuNP@Pt/CNTs composites were prepared by immersing the GCE with coated AuNP/CNTs composite into Pt halide solutions ( $\text{K}_2\text{PtCl}_4$ ,  $\text{K}_2\text{PtCl}_6$ ,  $\text{Na}_2\text{PtCl}_4$ ,  $\text{Na}_2\text{PtCl}_6 \cdot 6\text{H}_2\text{O}$ ,  $\text{K}_2\text{PtBr}_4$ ,  $\text{K}_2\text{PtBr}_6$ ,  $\text{Pt}(\text{NH}_3)_4(\text{NO}_3)_2$ ) followed by *in-situ* electrochemical reduction.

#### Electrooxidation of formic acid and its related chronoamperometric test

The electrocatalysis of formic acid ( $\text{HCOOH}$ ) oxidation was studied by conducting CV measurement in 0.025 M  $\text{HCOOH}$  + 0.1 M  $\text{H}_2\text{SO}_4$  solution in the potential range between -0.2 V and 0.9 V at a scan rate of  $50 \text{ mVs}^{-1}$ . The chronoamperometric test was performed in 0.025 M  $\text{HCOOH}$  + 0.1 M  $\text{H}_2\text{SO}_4$  solution at a fixed potential of 0.15 V for 3600 s.

#### Electrooxidation of methanol

The electrocatalysis of methanol ( $\text{MeOH}$ ) oxidation was studied by conducting

CV measurement in 0.1 M MeOH + 0.1 M H<sub>2</sub>SO<sub>4</sub> solution in the potential range between -0.2 V and 0.9 V at a scan rate of 50 mVs<sup>-1</sup>.

### 6.3.2 Electrochemical characterizations and electrocatalytic studies for Chapter 3

The Pd/CNTs, Pt/CNTs, Pd@PdPt/CNTs and Pt@Pd/CNTs composites (1 mg) were dispersed in ethanol (250  $\mu\text{L}$ ). A portion of the mixture (10  $\mu\text{L}$ ) was pipetted and dropped on the GCE and dried in vacuum overnight.

#### Cyclic voltammetry in sulfuric acid

The CV measurements of Pd/CNTs, Pt/CNTs, Pd@PdPt/CNTs and Pt@Pd/CNTs composites were conducted at room temperature and in  $\text{N}_2$ -purged 0.1M  $\text{H}_2\text{SO}_4$  solution in the potential range between -0.24 V and 1.0 V at a scan rate of 50  $\text{mVs}^{-1}$ .

#### Electrooxidation of methanol and its related chronoamperometric test

The electrocatalysis of methanol oxidation was studied by conducting CV measurement in 0.1 M MeOH + 0.1 M  $\text{H}_2\text{SO}_4$  solution in the potential range between 0.0 V and 1.0 V at a scan rate of 50  $\text{mVs}^{-1}$ . The chronoamperometric test was performed in 0.1 M MeOH + 0.1 M  $\text{H}_2\text{SO}_4$  solution at a fixed potential of 0.45 V for 1000 s.

#### Electrooxidation of ethanol and its related chronoamperometric test

The electrocatalysis of ethanol (EtOH) oxidation was studied by conducting CV measurement in 0.1 M EtOH + 0.1 M NaOH solution in the potential range between -0.8 V and 0.6 V at a scan rate of 50  $\text{mVs}^{-1}$ . The chronoamperometric test was performed in 0.1 M EtOH + 0.1 M NaOH solution at a fixed potential of -0.2 V for 1000 s.

### Electrooxidation of glycerol and its related chronoamperometric test

The electrocatalysis of glycerol oxidation was studied by conducting CV measurement in 0.1 M glycerol + 0.1 M NaOH solution in the potential range between -0.6 V and 0.6 V at a scan rate of  $50 \text{ mVs}^{-1}$ . The chronoamperometric test was performed in 0.1 M glycerol + 0.1 M NaOH solution at a fixed potential of -0.15 V for 1000 s.

### Accelerated durability test in sulfuric acid

Accelerated durability test (ADT) was performed by conducting continued CV cycles (1000 cycles) in  $\text{N}_2$ -purged 0.1 M  $\text{H}_2\text{SO}_4$  solution in the potential region between -0.24 V and 1.0 V with a scan rate of  $50 \text{ mVs}^{-1}$ .

### 6.3.3 Electrochemical characterizations and electrocatalytic studies for Chapter 4

PtAg NWs and Pt black composites (1 mg) were dispersed in ethanol (250  $\mu\text{L}$ ). A portion of the mixture (10  $\mu\text{L}$ ) was pipetted and dropped on the GCE and dried in vacuum. The catalysts on the GCE were coated with 0.05 % Nafion solution (5  $\mu\text{L}$ ) and dried in vacuum.

#### Cyclic voltammetry in sulfuric acid

The CV measurements of PtAg NWs and Pt black composites were conducted at room temperature and in  $\text{N}_2$ -purged 0.1 M  $\text{H}_2\text{SO}_4$  solution in the potential range between -0.24 V and 1.0 V at a scan rate of 50  $\text{mVs}^{-1}$ .

#### Electrooxidation of methanol and its related chronoamperometric test

The electrocatalysis of methanol oxidation was studied by conducting CV measurement in 0.1 M MeOH + 0.1 M  $\text{H}_2\text{SO}_4$  solution in the potential range between 0.0 V and 1.0 V at a scan rate of 50  $\text{mVs}^{-1}$ . The chronoamperometric test was performed in 0.1 M MeOH + 0.1 M  $\text{H}_2\text{SO}_4$  solution at a fixed potential of 0.45 V for 3600 s.

#### Electrooxidation of ethanol and its related chronoamperometric test

The electrocatalysis of ethanol oxidation was studied by conducting CV measurement in 0.1 M EtOH + 0.1 M NaOH solution in the potential range between -0.8 V and 0.6 V at a scan rate of 50  $\text{mVs}^{-1}$ . The chronoamperometric test was performed in 0.1 M EtOH + 0.1 M NaOH solution at a fixed potential of -0.3 V for 3600 s.

#### Electrooxidation of glycerol and its related chronoamperometric test

The electrocatalysis of glycerol oxidation was studied by conducting CV measurement in 0.1 M glycerol + 0.1 M NaOH solution in the potential range between -0.6 V and 0.6 V at a scan rate of  $50 \text{ mVs}^{-1}$ . The chronoamperometric test was performed in 0.1 M glycerol + 0.1 M NaOH solution at a fixed potential of -0.15 V for 3600 s.

#### Electrooxidation of formic acid and its related chronoamperometric test

The electrocatalysis of formic acid oxidation was studied by conducting CV measurement in 0.025 M HCOOH + 0.1 M H<sub>2</sub>SO<sub>4</sub> solution in the potential range between -0.2 V and 1.0 V at a scan rate of  $50 \text{ mVs}^{-1}$ . The chronoamperometric test was performed in 0.025 M HCOOH + 0.1 M H<sub>2</sub>SO<sub>4</sub> solution at a fixed potential of 0.15 V for 3600 s.

## REFERENCES

- [1] L.J. Sherry, S.-H. Chang, G.C. Schatz, R.P. Van Duyne, B.J. Wiley, Y. Xia, Nano letters, 5 (2005) 2034-2038.
- [2] K.A. Willets, R.P. Van Duyne, Annu. Rev. Phys. Chem., 58 (2007) 267-297.